UNIVERSITY OF CALIFORNIA SAN DIEGO

Defining the epigenetic landscape and functional dependencies of pancreatic cancer stem cells

A dissertation submitted in partial satisfaction of
the requirements for the degree Doctor of Philosophy

in

Biomedical Sciences

by

Lesley Paige Ferguson

Committee in charge:

Professor Tannishtha Reya, Chair
Professor Diana Hargreaves
Professor Scott Lippman
Professor Andrew Lowy
Professor Maike Sander
Professor Jing Yang

2021

The thesis of Lesley Paige Ferguson is approved and it is acceptable in quality and form for publication on microfilm and electronically.

University of California San Diego

2021

DEDICATION

This dissertation is dedicated to my dad, Ken Ferguson III, and all other pancreatic cancer patients who have deserved a longer future. This work is also dedicated to everyone in my life who has supported me along the way. Thank you for shaping who I am, and holding me up when I needed encouragement. To my mom Robyn, who showed me I had the grit to do anything. To my husband Adam, who always knows how to make me smile (especially by getting me ice cream). To my younger sisters Bailey and Phoebe, who are my best friends. To all my best friends, who are my family. And to our work from home French bulldog co-workers, Belli and Clo.

EPIGRAPH

We were neither what we had been nor what we would be become once we reached our destination.

Jeff VanderMeer

TABLE OF CONTENTS

LIST OF ABBREVIATIONS

AdCre: adenoviral Cre
AML: acute myeloid leukemia
CDK: cyclin-dependent kinase
ChIP-seq: Chromatin immunoprecipitation followed by sequencing
CML: chronic myeloid leukemia
CRISPR: clustered regularly interspaced short palindromic repeats
CSC: cancer stem cell
ESC: embryonic stem cell
EMT: epithelial to mesenchymal transition
FACS: fluorescence-activated cell sorting
GC-MS: gas chromatography mass spectrometry
GEMM: genetically engineered mouse model
GFP: green fluorescent protein
GO: gene ontology
GPCR: G-coupled protein receptor
GSEA: gene set enrichment analysis
H3K27ac: histone H3 lysine-27 acetylation
H3K4me: histone H3 lysine-4 monomethylation
H3K4me3: histone H3 lysine-4 trimethylation
Hh: Hedgehog signaling pathway
HDAC: histone deacetylase
HR: hazard ratio
HSC: hematopoietic stem cell
KC: Kras$^{LSL/+}$; Ptf1a-Cre
KPF: FSF-Kras$^{G12D/+}$; p53$^{frt/frt}$; Pdx-Flp
KP$^{f/f}$C: Kras$^{LSL/G12D+}$, Trp53$^{fl/fl}$, Ptf1a-Cre
KP$^{R172H/+}$C: Kras$^{LSL/G12D}$ Trp$^{R127H/+}$, Ptf1a-Cre
MDSC: myeloid derived suppressor cell
MEK: Mitogen-activated protein kinase kinase
Msi: Musashi
mTOR: mammalian target of rapamycin
NSG: NOD-*scid* IL2Rgamma^{null}
OXPHOS: oxidative phosphorylation
PanIN: pancreatic intraepithelial neoplasia
PDX: patient-derived xenograft
PDAC: pancreatic ductal adenocarcinoma
PI3K: phosphatidylinositol-3-kinase
Msi2-GFP reporter mice
qPCR: quantitative polymerase chain reaction
RNA-seq: RNA sequencing
RORγ: retinoic-acid-receptor-related orphan receptor gamma
scRNA-seq: single cell RNA-seq
sgRNA: single guide RNA
shRNA: short hairpin RNA
SWI/SNF: SWItch/Sucrose Non-Fermentable nucleosome remodeling complex
Th17 cell: T helper 17 cell
TMA: tissue microarray
TME: tumor microenvironment

LIST OF FIGURES

LIST OF TABLES

LIST OF SUPPLEMENTAL FILES

ACKNOWLEDGEMENTS

I would like to acknowledge Professor Tannishtha Reya for her support in my scientific training and career development throughout my time in the lab, and thank her for giving me the freedom to work independently and develop confidence in my own ideas. I would also like to acknowledge my thesis committee for their support and input over the years, as they helped shape and improve this work and my own outlook as a scientist.

Chapter 1, in part, is a reprint of the material as it appears in Trends in Cancer, 2021. Ferguson LP†, Diaz E, and Reya T*. “The role of the microenvironment in regulating stem cell fate in cancer”. The dissertation author was the primary author of this review.

Chapter 2, is a reprint of the material as it appears in Cell, 2019. Lytle NK†, Ferguson LP†, Rajbhandari N, Gilroy K, Fox RG, Deshpande A, Schürch CM, Hamilton M, Robertson N, Lin W, Noel P, Wartenberg M, Zlobec I, Eichmann M, Galván JA, Karamitopoulou E, Gilderman T, Esparza LA, Shima Y, Spahn P, French R, Lewis NE, Fisch KM, Sasik R, Rosenthal SB, Kritzik M, Von Hoff D, Han H, Ideker T, Deshpande AL, Lowy AM, Adams PD, and Reya T*. “A multiscale map of the stem cell state in pancreatic adenocarcinoma”. The dissertation author was co-first author and a primary contributor to this paper.

Chapter 3 has been submitted as it may appear in Nature Communications, 2022. Ferguson LP†, Gatchalian J, Chambers K, McDermott ML, Rajbhandari N, Lytle NK, Rosenthal SB, Schürch CM, Hamilton M, Albini S, Wartenberg M, Zlobec I, Galván JA, Karamitopoulou E, Puri PL, Bruneau BG, Lowy AM, Hargreaves DC*, and Reya T*. “SMARCD3 is a key epigenetic dependency for pancreatic adenocarcinoma”**.** The dissertation author was the primary investigator and author of this paper.

Chapter 4 is co-authored with Chambers KC, McDermott ML, Fisher C, Heyen-Genel S, and Jackson M, and Reya TR. The dissertation author was primary author of this chapter.

VITA

2010 Bachelor of Science, Northeastern University

2021 Doctor of Philosophy, University of California San Diego

ABSTRACT OF THE DISSERTATION

Defining the epigenetic landscape and functional dependencies
of pancreatic cancer stem cells

by

Lesley Paige Ferguson

Doctor of Philosophy in Biomedical Sciences

University of California San Diego, 2021

Professor Tannishtha Reya, Chair

Despite recent advances in cancer treatment, resistance to therapy and metastatic progression remain critical drivers of mortality. One central mechanism underlying therapy resistance and metastasis is tumor heterogeneity. Within the tumor bulk, genetic and epigenetic diversity fuel variable responses to therapy and a spectrum of invasive potential. In particular, rare subpopulations of tumor cells that reactivate developmental signals are

uniquely primed for therapy resistance and metastatic success. These cells, often referred to as cancer stem cells, are enriched for the ability to self-renew in the face of therapy, driving eventual relapse. Deepening our understanding of the molecular dependencies of these aggressive cells may provide new opportunities for therapeutic intervention. In collaboration with a fellow graduate student (Nikki Lytle) who led this project, we used transcriptional and epigenetic profiling paralleled by a genome-wide CRISPR analysis to map the molecular dependencies of pancreatic cancer stem cells. This integrated approach revealed an unexpected utilization of immuno-regulatory signals by pancreatic cancer cells, and identified the nuclear hormone receptor (RORγ) as a targetable dependency in pancreatic cancer stem cells. We expanded preclinical work to test RORγ inhibitors, providing new evidence that clinical grade RORγ inhibitors can block pancreatic cancer growth and deplete cancer stem cells *in vivo*. These studies also revealed a unique epigenetic landscape in cancer stem cells, suggesting upstream epigenetic regulation of stem cell fate. Thus, to follow this work, I used a curated functional screen for stem cell-enriched epigenetic factors, ultimately identifying the SWI/SNF subunit SMARCD3 as an epigenetic dependency in pancreatic cancer stem cells. Using diverse genetic mouse models, I showed that *Smarcd3* dependency is bimodal, with a preferential impact in established tumors, improving survival and chemosensitivity *in vivo*. Finally, I leveraged genetically engineered mouse models to identify and test clinical inhibitors that target cancer stem cells. Using a genetic reporter for the stem cell signal Msi2, I helped conduct an image-based screen and found that clinical inhibitors of MEK signaling inhibited *Msi2* and blocked CSC growth *in vivo*. Together, these studies generate a comprehensive molecular profile of the landscape and functional requirements of pancreatic cancer stem cells that may be used to identify new therapeutic targets in the future.

Chapter 1. Introduction

1.1. Stem cell signals in cancer

Despite advances in cancer treatment and management, a large fraction of patients with both metastatic and local disease still face primary or acquired resistance to therapy and eventually succumb to disease. To develop more effective strategies to treat cancer, there is a great need to define the mechanisms underlying both resistance and metastatic progression. One central mechanism by which cells acquire these malignant features is the activation of developmental signaling pathways. Within the tumor, classic stem cell signals such as Oct4, Sox2, Wnt, or Notch are often aberrantly reactivated within subpopulations of cancer cells that, like embryonic stem cells, are enriched in their ability to self-renew[1,2,3,4]. These aggressive cancer cells, referred to as cancer stem cells (CSCs)[1], co-opt the survival and self-renewal mechanisms of normal stem cells to initiate or fuel tumor propagation and heterogeneity, resist therapy, and contribute to metastatic outgrowth. Together, these clinically-relevant functional features make CSCs core contributors to disease relapse and critical targets for cancer therapy (Figure 1.1).

Origin of the cancer stem cell concept in hematologic malignancies

Historically, the CSC concept first emerged from observations that only a small fraction of “tumor-initiating cells” within the tumor bulk were exclusively responsible for tumor outgrowth in the transplant setting, recapitulating the heterogeneity of the original tumor[2,5,6]. These tumor-initiating cells shared molecular and phenotypic features of stem cells[7], leading to the hypothesis that normal stem cells might act as the cellular origin of cancer. The robust activation of self-renewal and survival pathways in stem cells might provide a cellular landscape uniquely primed for transformation in the context of genetic mutation. In theory, this

transformed tumorigenic stem cell would sit at the apex of the tumor hierarchy, fueling tumor heterogeneity just as normal stem cells give rise to the differentiated progeny within a tissue hierarchy[1,4,5,8,9,10]. This concept framed the tumor as an aberrant tissue, with tumorigenicity driven primarily by phenotypically and molecularly unique “cancer stem cells”. Cancer stem cells were thus originally defined as the rare subset of tumorigenic cancer cells with the unlimited proliferative potential and the ability to form tumors[1].

A great deal of early support for the CSC concept came from the study of hematologic malignancies, in part because hierarchical relationships among normal hematopoietic stem cells (HSCs) and their differentiated lineages are relatively well-defined[5]. In acute myeloid leukemia (AML), leukemic cells sufficient to form tumors are defined by the cell surface expression of CD34+CD38-, lineage-specific markers of normal HSCs[11,12]. These rare leukemic stem cells hierarchically give rise to differentiated myeloid cells constituting the bulk malignancy, and represent a bona fide cancer stem cell population[11,12].

The identification of a leukemic cancer stem cell with phenotypic similarities to a normal HSC suggested that in leukemia, perhaps the HSC acted as the cellular origin of cancer. Genetic modeling of leukemic driver mutations in mice demonstrated that oncogenic mutations in HSCs could indeed drive leukemogenesis, supporting the HSC as the leukemic cell of origin[13,14,15,16]. Providing further evidence for the HSC as the clonal origin of leukemia, genomic sequencing has identified leukemic driver mutations within normal human HSCs in leukemia patients[13,17,18,19,20]. These studies suggested that the cancer stem cell could act not only as a driver of tumor propagation, but as the cellular origin of cancer, historically framing the CSC as not only important for tumor growth but as a potential source of tumor initiation[2].

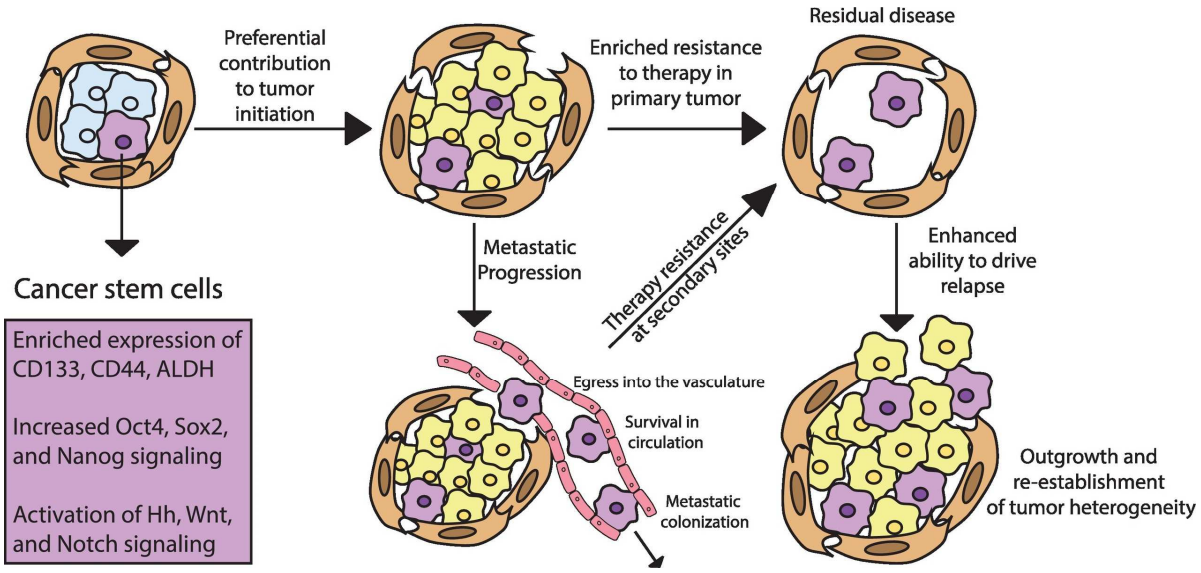

Figure 1.1. Cancer cells enriched for stem cell programs drive features of progressive disease. Within the tumor bulk, rare subpopulations of cancer cells are often enriched for the expression of CD133, CD44, and ALDH and the activation of classical development transcription factors and signals such as Oct4, Sox2, Nanog, Hedgehog (Hh), Notch, and Wnt. These cells, enriched for stem cell signals, preferentially contribute to tumor initiation, metastatic progression, and therapy resistance, driving relapse.

Cancer stem cells in solid tumors

Unlike hematologic malignancies, most solid tumors have less well-defined lineage relationships and their cellular origin is often less clear[5,21]. Nonetheless, transplantation assays and lineage tracing strategies have been used to identify putative cancer stem cell populations in a wide range of solid tumors[2,3,5,9,22] including cancers of the breast[23], brain[24,25], skin[26,27,28], intestine[29,30,31], colon[32,33,34], and pancreas[35,36,37]. Cancer stem cells that preferentially contribute to tumor propagation in solid tumors have been identified using various tissue-specific markers[5] that include CD133, CD44, and ALDH[3] among others. Genetically engineered mouse models (GEMMs) have provided some evidence that stem cells may also act as the clonal cell of origin in solid tumors[38,39,40]. For example, targeted genetic deletion of the tumor suppressor APC specifically in Lgr5+ intestinal crypt stem cells, but not more differentiated transit-amplifying cells, drove rapid adenoma development in mice[40]. Emerging evidence, however, suggests that the CSC concept may be more flexible than originally thought, especially in some

solid tumors[2,41]. Recent work in GEMMs showed that Lgr5- non-stem cells of the intestine were also competent to drive intestinal tumorigenesis in the context of chronic inflammation[42]. Constitutive NF-kB activation restricted to Lgr5- cells was sufficient to give rise to Lgr5+ stem cells and intestinal adenomatous polyps through the activation of Wnt signaling[42]. These results and others[43,44,45] challenge the hierarchical nature of CSCs in solid tumors, and suggest that stem cell fate in cancer may be plastic and dependent at least in part on the surrounding tumor microenvironment (TME)[2,3,46,47].

1.2. Cancer stem cells as key drivers of disease progression and relapse

Cancer stem cells and therapy resistance

Whether or not cancer stem cells represent a fixed entity or a plastic state, there is abundant evidence that aggressive cells with a stem cell fate exist and are functionally distinct from their more differentiated counterparts in the tumor[1,2,3,5]. Most simply, cancer stem cells can be defined by their clinically relevant functional features: the enriched ability to drive tumor propagation, resist standard therapies[1,9,35,37,48,49,50], and contribute to metastasis[3,2,51,52,53,54]. Co-opting the features of normal stem cells that shield them from apoptosis, CSCs evade cytotoxic and targeted therapies though quiescence, enhanced DNA damage repair, resistance to ROS-induced cell damage, and upregulation of drug transporters[2,3,4]. The role of cancer stem cells in therapy resistance and relapse has been thoroughly explored in chronic myeloid leukemia (CML). Treatment with the targeted inhibitor imatinib (a BCR-ABL inhibitor) is standard of care for CML. Although an effective therapy, imatinib does not eradicate leukemic stem cells which can drive disease relapse if therapy is discontinued[55,56,57]. CSCs are also enriched after treatment with either standard of care radiation[58] or chemotherapy (temozolomide)[59] in glioblastoma, evading therapeutic targeting through DNA damage repair or quiescence respectively. Cancer stem cells have broadly been found to be enriched after therapy across

cancers[2,60,61,62], suggesting that they act as key drivers of resistance and represent an important therapeutic target.

As immunotherapy has risen to the forefront of cancer therapy, early evidence suggests that stem cell fate may also mediate sensitivity to immunotherapy. Response to immunotherapy can hinge on the expression of surface molecules, antigenicity, and T-cell infiltration[63]. Modulation of these factors by CSCs may mediate sensitivity to immunotherapy[64]. In some cases, CSCs have been found to preferentially up-regulate the adaptive immune checkpoint PD-L1[65,66], suggesting that checkpoint blockade may be an effective strategy for eradicating this subfraction. CSCs in pancreatic cancer also upregulate CD47 (the “don’t eat me” signal) to evade innate immune killing, making them a good target for CD47 blocking antibodies[67]. However, in other cases stem cell fate has been associated with resistance to immunotherapy. For example, tumor-intrinsic up-regulation of Wnt/beta-catenin in melanoma is associated with reduced T-cell infiltration and poor clinical response to immunotherapy[68]. CSCs have also been found to drive resistance to adoptive T-cell transfer, where patient-derived T-cells are engineered to target a cancer antigen and drive an immune response upon re-transplant. In the context of squamous cell carcinoma, a population of cancer stem cells preferentially evaded adoptive T-cell transfer through expression of CD80, driving T-cell exhaustion and relapse[69]. Thus, as the use of immunotherapies expands, it will remain pertinent to assess the mechanisms by which CSCs may mediate response to immune-targeted therapies.

Cancer stem cells and metastasis

In addition to driving therapy resistance, cancer stem cells have also been found to preferentially contribute to metastasis. Metastatic outgrowth is a core contributor to overall cancer mortality[70], and is often closely associated with the activation of stem programs[2,3,4,51].

The metastatic process can be thought of as occurring in several steps: the acquisition of invasive potential at the primary site and egress into the blood stream, colonization and survival at the metastatic site, followed by eventual outgrowth and relapse[70]. Cancer cells are required to survive harsh conditions through each step, selecting for cells with both enhanced invasive programs and the ability to self-renew. Though not completely congruent, metastasis-initiating cells often draw parallels to functionally defined cancer stem cell populations[51] and the acquisition of a stem cell fate often coincides with the induction of an epithelial-to-mesenchymal transition (EMT) phenotype[3,2,4,51,54,71]. Disseminated cancer cells are frequently enriched for stem programs, supporting a role for cancer stem cells in metastasis[51,52,53,54,72,73]. Some functional studies have also demonstrated that cancer stem cells preferentially give rise to metastases. In colon cancer, for example, the vast majority of metastases arose from a highly self-renewing population of long-term CSCs[74]. Similarly, a population of CD26+ CSCs were identified in colorectal cancer; CD26+ cancer cells were enriched in their ability to form metastases and CD26 expression in primary patient tumors was predictive of distant metastasis formation[75]. These findings and others[35,76,77] further emphasize the importance of stem cell fate in disease progression and clinical outcome.

1.3. Targeting stem cell signals and cancer stem cells in cancer

Inhibitors of stem cell signals for cancer therapy

Together, the ability to fuel tumor growth and metastasis in the face of therapy makes cancer stem cells key drivers of aggressive disease. Consistent with this, the upregulation of stem cell signals is often predictive of worse clinical prognosis[3,7,9,51,78,79,80,81] and there is evidence that genetic ablation of the cancer stem cell fraction can improve disease prognosis in mouse models[3,59,82,83]. Thus, cancer cells with a stem cell fate drive progressive disease and represent a critical target for therapy. To this end, inhibitors of some classic stem cell signals

have been developed, yielding some clinical successes[84,85]. Hedgehog (Hh) pathway inhibitors, for example, have been approved for the treatment of basal cell carcinoma[86,87], and acute myeloid leukemia[88]. Inhibitors of Notch, Wnt, and Hippo signaling are also in various stages of clinical development[84]. There have also been significant efforts to develop inhibitory antibodies that target CSC-associated cell surface molecules including CD20, CD52, CD123, CD44, and EpCAM[85]. In addition to these cell surface markers and developmental signals, cancer stem cells are likely to rely on a wide range of distinct intrinsic pathways that could be exploited therapeutically.

Targeting cancer stem cell metabolism

Unique metabolism is one such intrinsic feature of CSCs that may have important therapeutic implications[2,89,90,91]. In embryonic development, metabolic changes accompany the shift between a stem cell state and differentiated fate. Embryonic stem cells (ESCs) exhibit enhanced glycolytic activity and reduced oxidative phosphorylation (OXPHOS), likely limiting ROS levels and promoting self-renewal[92]. Cancer stem cells possess similarly unique metabolic features[90,93]. Like ESCs, CSCs have been found to be primarily glycolytic in nasopharyngeal[94], breast[95], and liver cancer[96]. Conversely, CSCs in lung cancer[97], pancreatic cancer[98], and glioblastoma[99] have been shown to prefer OXPHOS, demonstrating the tissue-specificity of cancer stem cell metabolism. Several strategies to disrupt CSC metabolism have been pursued clinically. Metformin, an electron transport chain inhibitor targeting OXPHOS, has shown promising results in some cancers[100] including lung[101], ovarian[102], and breast[103]. Metabolic inhibitors targeting redox homeostasis such as disulfiram[104,105,106,107] have also been tested in an attempt to induce oxidative stress in cancer stem cells. CSCs have also been shown to preferentially upregulate lipid metabolism[91,108], fatty acid oxidation[109,110], and glutamine import[111]. Among these metabolic pathways, an inhibitor of the lipogenic enzyme

FASN[112] has made it to the clinic so far. However, a wealth of promising preclinical data[91] suggests that further clinical development of compounds targeting various arms of CSC metabolism is warranted.

Epigenetics in cancer stem cells

Another emerging strategy for targeting cancer stem cell populations is through the inhibition of epigenetic regulators[113]. Epigenetic regulation comprises the interactions between DNA and histone modifications and the repertoire of enzymes and complexes that orchestrate and interpret them. These carefully coordinated changes to the chromatin landscape function as a dynamic mechanism for redefining transcriptionally accessible genomic regions in a specific cellular context, enabling the emergence of diverse phenotypes from cells of identical genotype[114,115]. Epigenetic regulatory mechanisms are crucial to embryogenesis and fate determination in development[114,115,116,117,118] and also function in the self-renewal of adult somatic cells[119,120,121,122]. Therefore, it is not surprising that many epigenetic processes are co-opted by cancer cells to transition to a more plastic and stem-like state that contributes to tumor heterogeneity, therapeutic resistance, and metastasis[123,124,125,126,127,128]. In fact, cancer stem cells have been shown to depend on the activity of epigenetic enzymes including DNA methyltransferase[120,129,130], lysine demethylase[131,132], histone deacetylases (HDACs)[133], and the histone methyltransferase EZH2[134,135] among others[127]. Several epigenetic therapies have gained FDA approval so far, primarily in hematologic malignancies[128,136,137]. However, mounting preclinical evidence supports the activity of epigenetic drugs against CSCs; the clinical use of epigenetic therapies is likely to continue to grow and may represent a promising strategy to improve sensitivity to existing therapies[113,128,137].

Regulation of stem cell fate by the tumor microenvironment

Stem cell fate in cancer is regulated not only by the intrinsic molecular pathways outlined above, but also by the extrinsic microenvironmental context. Growing evidence supports a role for the tumor microenvironment in supporting stem cell fate, suggesting that direct targeting of stem cell signals may not be sufficient to eradicate CSCs[2,3]. Secreted factors produced by immune cells, fibroblasts, and endothelial cells in the TME can directly promote the acquisition of a stem cell fate or the expansion of the CSC fraction, supporting therapy resistance and metastasis[46]. Defining the microenvironmental signals that support stemness may point us towards new strategies that leverage TME modulation to ablate CSCs, block tumor progression, and sensitize to current therapies. For example, in pancreatic cancer, tumor associated macrophages were found to support CSC function through the activation of STAT3, a central effector pathway implicated in cell survival[138]. Macrophage depletion effectively reduced the $Aldh^{Bright}$ CSC fraction, sensitizing to chemotherapy *in vivo*[138]. Similarly, a distinct population of stem cell-supportive CD10+GPR77+ CAFs were recently identified in breast cancer[139]. Treatment of patient-derived xenografts with a GPR77 neutralizing antibody reduced the Aldh+ stem fraction and enhanced chemotherapy-induced apoptosis[139]. Thus, targeting distinct CSC-TME signaling pathways may be an effective approach to ablate the stem fraction and improve therapeutic sensitivity in cancer.

1.4. Pancreatic cancer and the role of stem cell signals

Pancreatic ductal adenocarcinoma, referred to here as pancreatic cancer or PDAC, accounts for over 95% of pancreatic cancers and represents a serious unmet medical need today[140]. Although it represented only 3% of new cancer cases in 2020, pancreatic cancer is currently the third leading cause of cancer death in the United States[141,142]. This is driven by the disease's five-year survival rate of only 10%[142], the lowest of any cancer. High mortality in

PDAC can be attributed in part to late diagnosis; there are no current diagnostics capable of detecting the premalignant pancreatic intraepithelial neoplasia (PanIN) stage that precedes progression to frank adenocarcinoma[143,144,145]. Furthermore, pancreatic cancer is characterized by early metastatic dissemination[146,147] and broad resistance to therapy. The only potentially curable treatment for pancreatic cancer is surgical resection; however, only 20% of patients are diagnosed with local disease amenable to resection[148,149]. Instead, the vast majority of patients are diagnosed with inoperable and often systemic disease which is notoriously refractory to chemotherapy[150,151], radiation, and targeted therapies including immunotherapy[152,153]. Due to the lack of improvement in time to diagnosis and therapy, as well as increasing incidence[142] pancreatic cancer is projected to become the second leading cause of cancer death by 2030[141].

Molecular features of pancreatic cancer

Given the current state of pancreatic cancer treatment, the search for mediators of PDAC pathogenesis and therapy resistance remains of great significance. Pancreatic cancer is characterized by the common alteration of several genes: activating mutations of KRAS2 are found in >90% of tumors, while the tumor suppressors p16/INK4A, p53, and SMAD4 are commonly inactivated[140,154]. Genes implicated in SWI/SNF chromatin remodeling, axon guidance, and DNA damage repair pathways are also commonly targeted for genetic alterations in PDAC, indicating their importance to disease etiology[155,156]. Identification of actionable genetic mutations across these pathways holds some promise for precision medicine in pancreatic cancer[157]. Furthermore, recent work has demonstrated that pancreatic cancer can also be stratified at the epigenetic and transcriptional level, rather than by genetic diversity alone. PDAC can now be classified into two molecular subtypes (classical and basal)[158,159,160,161,162]; each subtype is associated with specific cis-regulatory networks[163] and

epigenetic features[162,164] that contribute to differential prognosis[158,159,160,161,162,165]. These subtypes may soon be used stratify patients into personalized therapies in the clinic, and the identification of subtype-specific functional dependencies may reveal new targets for future therapy[165].

Stem cell signals in pancreatic cancer

As in many other cancers, it has become clear that the reactivation of stem cell signals contributes significantly to pancreatic cancer heterogeneity and progression. The stem cell signals Hedgehog, Wnt, and Notch have all been implicated in various aspects of pancreatic cancer biology[140,166]. The basal PDAC subtype, associated with poor prognosis and chemoresistance[165], was found to be enriched for Wnt signaling and genetic alterations in the developmental transcription factor Myc[167,162,154,168]. Therapy-resistant and preferentially metastatic cancer stem cell populations have also been identified in pancreatic cancer using various markers[49,169]. Pancreatic CSCs were first identified by the cell surface expression of CD44+CD24+ESA+. CD44+CD24+ESA+ cancer stem cells, enriched for Hh signaling, were identified in human patient-derived xenografts; these CSCs were highly tumorigenic compared to CD44-CD24-ESA- cancer cells[36]. Soon after, CD133+ was shown to define a pancreatic cancer stem cell fraction enriched for tumorigenicity and resistance to chemotherapy (gemcitabine), while a specific CXCR4+CD133+ subpopulation was critical for metastasis[35]. Enriched ALDH activity[170] and cMet expression[171] have also been used to identify pancreatic cancer stem cell populations, and our lab has more recently identified the Musashi RNA-binding proteins as markers of therapy-resistant and metastatic pancreatic CSCs[172]. Expression of many of these cancer stem cell markers has been associated with metastasis and poor prognosis in patients[49,173,174,175,176,177,178].

Given the growing evidence for pancreatic cancer stem cells as important contributors to resistance and metastasis, these cells remain an important target for therapy. As in many other cancers, efforts are underway to inhibit CSC function or deplete CSCs in pancreatic cancer clinically[37,49,]. One stem cell signal that has been targeted clinically in PDAC is the Hh pathway. Although preclinical studies suggested that Hh inhibitors could inhibit CSC function and block metastasis[179], the results of a clinical trial testing Hh inhibition in pancreatic cancer were disappointing[180]. Hh inhibition surprisingly drove worse clinical outcomes in patients[180], presumably due to unanticipated effects on the stromal biology of tumors[181]. Inhibitors of Notch signaling have also been tested in PDAC, though with little success to date[153]. Currently, clinical trials are ongoing to test the effect of a CSC-targeted inhibitor of STAT3 (napabucasin) in PDAC[182]. Despite these clinical explorations, targeting pancreatic CSCs in the clinic remains a significant challenge to meet in the years to come[183]. Extending our understanding of the intrinsic and extrinsic molecular dependencies of pancreatic CSCs may provide new opportunities for therapeutic intervention in the future.

1.5. Acknowledgements

Chapter 1, in part, is a reprint of the material as it appears in Trends in Cancer, 2021. Ferguson LP†, Diaz E, and Reya T*. “The role of the microenvironment in regulating stem cell fate in cancer”. The dissertation author was the primary author of this review.

1.6. References

1. Reya, T., Morrison, S. J., Clarke, M. F. and Weissman, I. L. Stem cells, cancer, and cancer stem cells. *Nature* **414**, 105–111 (2001).

2. Batlle, E. & Clevers, H. Cancer stem cells revisited. *Nat. Med.* **23**, 1124–1134 (2017).

3. Nassar, D. & Blanpain, C. Cancer stem cells: basic concepts and therapeutic implications. *Annu. Rev. Pathol. Mech. Dis.* **11**, 47–76 (2016).

4. Lytle, N.K., Barber, A.G., and Reya, T. Stem cell fate in cancer growth, progression and therapy resistance. *Nat. Rev. Cancer* **18**, (2018).

5. Clevers, H. The cancer stem cell: Premises, promises and challenges. *Nat. Med.* **17**, 313–319 (2011).

6. Kleinsmith, L. J. & Pierce, G. B. Multipotentiality of single embryonal carcinoma cells. *Cancer Res.* **24**, (1964).

7. Eppert, K., Takenaka, K., Lechman, E.R., Waldron, L., Nilsson, B., Van Galen, P., Metzeler, K.H., Poeppl, A., Ling, V., Beyene, J. and Canty, A.J. Stem cell gene expression programs influence clinical outcome in human leukemia. *Nat. Med.* **17**, 1086–1093 (2011).

8. Furth, J., Kahn, M. C. and Breedis, C. The transmission of leukemia of mice with a single cell. *Am. J. Cancer* **31**, 276–282 (1937).

9. Kreso, A. & Dick, J. E. Evolution of the cancer stem cell model. *Cell Stem Cell* **14**, 275–291 (2014).

10. Hanoun, M., Zhang, D., Mizoguchi, T., Pinho, S., Pierce, H., Kunisaki, Y., Lacombe, J., Armstrong, S.A., Dührsen, U. and Frenette, P.S. Acute myelogenous leukemia-induced sympathetic neuropathy promotes malignancy in an altered hematopoietic stem cell niche. *Cell Stem Cell* **15**, 365–375 (2014).

11. Bonnet, D. & Dick, J. E. Human acute myeloid leukemia is organized as a hierarchy that originates from a primitive hematopoietic cell. *Nat. Med.* **3**, 730–737 (1997).

12. Lapidot, T., Sirard, C., Vormoor, J., Murdoch, B., Hoang, T., Caceres-Cortes, J., Minden, M., Paterson, B., Caligiuri, M.A. and Dick, J.E. A cell initiating human acute myeloid leukaemia after transplantation into SCID mice. *Nature* **367**, 645–648 (1994).

13. Corces-Zimmerman, M. R. & Majeti, R. Pre-leukemic evolution of hematopoietic stem cells – the importance of early mutations in leukemogenesis. *Leukemia* **28**, 2276 (2014).

14. Stavropoulou, V., Kaspar, S., Brault, L., Sanders, M.A., Juge, S., Morettini, S., Tzankov, A., Iacovino, M., Lau, I.J., Milne, T.A. and Royo, H. MLL-AF9 expression in hematopoietic stem cells drives a highly invasive AML expressing EMT-related genes linked to poor outcome. *Cancer Cell* **30**, 43–58 (2016).

15. Chu, S.H., Heiser, D., Li, L., Kaplan, I., Collector, M., Huso, D., Sharkis, S.J., Civin, C. and Small, D. FLT3-ITD knockin impairs hematopoietic stem cell quiescence/homeostasis, leading to myeloproliferative neoplasm. *Cell Stem Cell* **11**, 346–358 (2012).

16. Daley, G. Q., Van Etten, R. A. and Baltimore, D. Induction of chronic myelogenous leukemia in mice by the P210 bcr/abl gene of the Philadelphia chromosome. *Science* **247**, 824–830 (1990).

17. Jan, M., Snyder, T.M., Corces-Zimmerman, M.R., Vyas, P., Weissman, I.L., Quake, S.R. and Majeti, R. Clonal evolution of preleukemic hematopoietic stem cells precedes human acute myeloid leukemia. *Sci. Transl. Med.* **4**, (2012).

18. Welch, J.S., Ley, T.J., Link, D.C., Miller, C.A., Larson, D.E., Koboldt, D.C., Wartman, L.D., Lamprecht, T.L., Liu, F., Xia, J. and Kandoth, C. The origin and evolution of mutations in acute myeloid leukemia. *Cell* **150**, 264–278 (2012).

19. Miyamoto, T., Weissman, I. L. and Akashi, K. AML1/ETO-expressing nonleukemic stem cells in acute myelogenous leukemia with 8;21 chromosomal translocation. *Proc. Natl. Acad. Sci.* **97**, 7521–7526 (2000).

20. Shlush, L.I., Zandi, S., Mitchell, A., Chen, W.C., Brandwein, J.M., Gupta, V., Kennedy, J.A., Schimmer, A.D., Schuh, A.C., Yee, K.W. and McLeod, J.L. Identification of pre-leukaemic haematopoietic stem cells in acute leukaemia. *Nature* **506**, 328–333 (2014).

21. Blanpain, C. Tracing the cellular origin of cancer. *Nat. Cell Biol.* **15**, 126–134 (2013).

22. Ebben, J.D., Treisman, D.M., Zorniak, M., Kutty, R.G., Clark, P.A. and Kuo, J.S. The cancer stem cell paradigm: a new understanding of tumor development and treatment. *Expert Opin. Ther. Targets* **14**, 621–632 (2010).

23. Al-Hajj, M., Wicha, M. S., Benito-Hernandez, A., Morrison, S. J. and Clarke, M. F. Prospective identification of tumorigenic breast cancer cells. *Proc. Natl. Acad. Sci. U. S. A.* **100**, 3983–3988 (2003).

24. Singh, S.K., Hawkins, C., Clarke, I.D., Squire, J.A., Bayani, J., Hide, T., Henkelman, R.M., Cusimano, M.D. and Dirks, P.B. Identification of human brain tumour initiating cells. *Nature* **432**, 396–401 (2004).

25. Ignatova, T.N., Kukekov, V.G., Laywell, E.D., Suslov, O.N., Vrionis, F.D. and Steindler, D.A. Human cortical glial tumors contain neural stem-like cells expressing astroglial and neuronal markers in vitro. *Glia*, **39**, 193-206 (2002).

26. Mascré, G., Dekoninck, S., Drogat, B., Youssef, K.K., Brohée, S., Sotiropoulou, P.A., Simons, B.D. and Blanpain, C. Distinct contribution of stem and progenitor cells to epidermal maintenance. *Nature* **489**, 257–262 (2012).

27. Driessens, G., Beck, B., Caauwe, A., Simons, B.D. and Blanpain, C. Defining the mode of tumour growth by clonal analysis. *Nature* **488**, 527–530 (2012).

28. White, A.C., Tran, K., Khuu, J., Dang, C., Cui, Y., Binder, S.W. and Lowry, W.E.. Defining the origins of Ras/p53-mediated squamous cell carcinoma. *Proc. Natl. Acad. Sci.* **108**, 7425–7430 (2011).

29. Barker, N., Ridgway, R.A., Van Es, J.H., Van De Wetering, M., Begthel, H., Van Den Born, M., Danenberg, E., Clarke, A.R., Sansom, O.J. and Clevers, H. Crypt stem cells as the cells-of-origin of intestinal cancer. *Nature* **457**, 608–611 (2009).

30. Schepers, A.G., Snippert, H.J., Stange, D.E., van den Born, M., van Es, J.H., van de

Wetering, M. and Clevers, H. Lineage tracing reveals Lgr5+ stem cell activity in mouse intestinal adenomas. *Science* **337**, 730–735 (2012).

31. Kozar, S., Morrissey, E., Nicholson, A.M., van der Heijden, M., Zecchini, H.I., Kemp, R., Tavare, S., Vermeulen, L. and Winton, D.J. Continuous clonal labeling reveals small numbers of functional stem cells in intestinal crypts and adenomas. *Cell Stem Cell* **13**, 626–633 (2013).

32. Dalerba, P., Dylla, S., Park, I., Liu, R., Wang, X., Cho, R.W., Hoey, T., Gurney, A., Huang, E.H., Simeone, D.M., Sheltong, A.A., Parmiani, G., Castelli, C., and Clarke, M.F. Phenotypic characterization of human colorectal cancer stem cells. *Proc. Natl. Acad. Sci.* **104,** 10158-10163 (2007).

33. O'Brien, C.A., Pollett, A., Gallinger, S. and Dick, J.E., A human colon cancer cell capable of initiating tumour growth in immunodeficient mice. *Nature* **445**, 106-110 (2007).

34. Ricci-Vitiani, L., Lombardi, D.G., Pilozzi, E., Biffoni, M., Todaro, M., Peschle, C. and De Maria, R. Identification and expansion of human colon-cancer-initiating cells. *Nature* **445**, 111-115 (2007).

35. Hermann, P.C., Huber, S.L., Herrler, T., Aicher, A., Ellwart, J.W., Guba, M., Bruns, C.J. and Heeschen, C. Distinct populations of cancer stem cells determine tumor growth and metastatic activity in human pancreatic cancer. *Cell Stem Cell* **1**, 313–323 (2007).

36. Li, C., Heidt, D.G., Dalerba, P., Burant, C.F., Zhang, L., Adsay, V., Wicha, M., Clarke, M.F. and Simeone, D.M. Identification of pancreatic cancer stem cells. *Cancer Res.* **67**, 1030–1037 (2007).

37. Hermann, P. C. & Sainz, B. Pancreatic cancer stem cells: A state or an entity? *Sem. Cancer Biol.* **53**, 223–231 (2018).

38. Gimple, R. C., Bhargava, S., Dixit, D. and Rich, J. N. Glioblastoma stem cells: lessons from the tumor hierarchy in a lethal cancer. *Genes Dev.* **33**, 591–609 (2019).

39. Lapouge, G., Youssef, K.K., Vokaer, B., Achouri, Y., Michaux, C., Sotiropoulou, P.A. and Blanpain, C. Identifying the cellular origin of squamous skin tumors. *Proc. Natl. Acad. Sci.* **108**, 7431–7436 (2011).

40. Barker, N., Ridgway, R.A., Van Es, J.H., Van De Wetering, M., Begthel, H., Van Den Born, M., Danenberg, E., Clarke, A.R., Sansom, O.J. and Clevers, H. Crypt stem cells as the cells-of-origin of intestinal cancer. *Nature* **457**, 608–611 (2008).

41. Medema, J. P. Cancer stem cells: The challenges ahead. *Nat. Cell Biol.* **15**, 338–344 (2013).

42. Schwitalla, S., Fingerle, A.A., Cammareri, P., Nebelsiek, T., Göktuna, S.I., Ziegler, P.K., Canli, O., Heijmans, J., Huels, D.J., Moreaux, G. and Rupec, R.A. Intestinal tumorigenesis initiated by dedifferentiation and acquisition of stem-cell-like properties.

Cell **152**, 25–38 (2013).

43. Gupta, P.B., Fillmore, C.M., Jiang, G., Shapira, S.D., Tao, K., Kuperwasser, C. and Lander, E.S. Stochastic state transitions give rise to phenotypic equilibrium in populations of cancer cells. *Cell* **146**, 633–644 (2011).

44. Roesch, A., Fukunaga-Kalabis, M., Schmidt, E.C., Zabierowski, S.E., Brafford, P.A., Vultur, A., Basu, D., Gimotty, P., Vogt, T. and Herlyn, M. A temporarily distinct subpopulation of slow-cycling melanoma cells Is required for continuous tumor growth. *Cell* **141**, 583–594 (2010).

45. Chaffer, C.L., Brueckmann, I., Scheel, C., Kaestli, A.J., Wiggins, P.A., Rodrigues, L.O., Brooks, M., Reinhardt, F., Su, Y., Polyak, K. and Arendt, L.M. Normal and neoplastic nonstem cells can spontaneously convert to a stem-like state. *Proc. Natl. Acad. Sci.* **108**, 7950–7955 (2011).

46. Ferguson, L. P., Diaz, E. and Reya, T. The role of the microenvironment and immune system in regulating stem cell fate in cancer. *Trends in Cancer* **7**, 624–634 (2021).

47. Valent, P., Bonnet, D., De Maria, R., Lapidot, T., Copland, M., Melo, J.V., Chomienne, C., Ishikawa, F., Schuringa, J.J., Stassi, G. and Huntly, B. Cancer stem cell definitions and terminology: the devil is in the details. *Nat. Rev. Cancer* **12**, 767–775 (2012).

48. García-Silva, S., Frias-Aldeguer, J. and Heeschen, C. Stem cells & pancreatic cancer. in *Pancreatology* **13**, 110–113 (2013).

49. Zhan, H.X., Xu, J.W., Wu, D., Zhang, T.P. and Hu, S.Y. Pancreatic cancer stem cells: New insight into a stubborn disease. *Cancer Lett.* **357**, 429–437 (2015).

50. Fox, R.G., Lytle, N.K., Jaquish, D.V., Park, F.D., Ito, T., Bajaj, J., Koechlein, C.S., Zimdahl, B., Yano, M., Kopp, J.L. and Kritzik, M. Image-based detection and targeting of therapy resistance in pancreatic adenocarcinoma. *Nature* **534**, 407–411 (2016).

51. Oskarsson, T., Batlle, E. and Massagué, J. Metastatic stem cells: Sources, niches, and vital pathways. *Cell Stem Cell* **14**, 306–321 (2014).

52. Fessler, E., Dijkgraaf, F. E., De Sousa E Melo, F. and Medema, J. P. Cancer stem cell dynamics in tumor progression and metastasis: Is the microenvironment to blame? *Cancer Lett.* **341**, 97–104 (2013).

53. Steinbichler, T.B., Savic, D., Dudás, J., Kvitsaridze, I., Skvortsov, S., Riechelmann, H. and Skvortsova, I.I. Cancer stem cells and their unique role in metastatic spread. In *Semin. Cancer Biol.* **60,** 148-156 (2020).

54. Mani, S.A., Guo, W., Liao, M.J., Eaton, E.N., Ayyanan, A., Zhou, A.Y., Brooks, M., Reinhard, F., Zhang, C.C., Shipitsin, M. and Campbell, L.L. The epithelial-mesenchymal transition generates cells with properties of stem cells. *Cell* **133**, 704–715 (2008).

55. Corbin, A.S., Agarwal, A., Loriaux, M., Cortes, J., Deininger, M.W. and Druker, B.J.

Human chronic myeloid leukemia stem cells are insensitive to imatinib despite inhibition of BCR-ABL activity. *J. Clin. Invest.* **121**, 396–409 (2011).

56. Chomel, J.C., Bonnet, M.L., Sorel, N., Bertrand, A., Meunier, M.C., Fichelson, S., Melkus, M., Bennaceur-Griscelli, A., Guilhot, F. and Turhan, A.G. Leukemic stem cell persistence in chronic myeloid leukemia patients with sustained undetectable molecular residual disease. *Blood* **118**, 3657–3660 (2011).

57. Bhatia, R., Holtz, M., Niu, N., Gray, R., Snyder, D.S., Sawyers, C.L., Arber, D.A., Slovak, M.L. and Forman, S.J. Persistence of malignant hematopoietic progenitors in chronic myelogenous leukemia patients in complete cytogenetic remission following imatinib mesylate treatment. *Blood* **101**, 4701–4707 (2003).

58. Bao, S., Wu, Q., McLendon, R.E., Hao, Y., Shi, Q., Hjelmeland, A.B., Dewhirst, M.W., Bigner, D.D. and Rich, J.N. Glioma stem cells promote radioresistance by preferential activation of the DNA damage response. *Nature* **444**, 756–760 (2006).

59. Chen, J., Li, Y., Yu, T.S., McKay, R.M., Burns, D.K., Kernie, S.G. and Parada, L.F. A restricted cell population propagates glioblastoma growth after chemotherapy. *Nature* **488**, 522–526 (2012).

60. Kreso, A., O'Brien, C.A., Van Galen, P., Gan, O.I., Notta, F., Brown, A.M., Ng, K., Ma, J., Wienholds, E., Dunant, C. and Pollett, A. Variable clonal repopulation dynamics influence chemotherapy response in colorectal cancer. *Science* **339**, 543–548 (2013).

61. Shien, K., Toyooka, S., Yamamoto, H., Soh, J., Jida, M., Thu, K.L., Hashida, S., Maki, Y., Ichihara, E., Asano, H. and Tsukuda, K. Acquired resistance to EGFR inhibitors is associated with a manifestation of stem cell–like properties in cancer cells. *Cancer Res.* **73**, 3051–3061 (2013).

62. Creighton, C.J., Li, X., Landis, M., Dixon, J.M., Neumeister, V.M., Sjolund, A., Rimm, D.L., Wong, H., Rodriguez, A., Herschkowitz, J.I. and Fan, C. Residual breast cancers after conventional therapy display mesenchymal as well as tumor-initiating features. *Proc. Natl. Acad. Sci.* **106**, 13820–13825 (2009).

63. Sharma, P., Hu-Lieskovan, S., Wargo, J. A. and Ribas, A. Primary, adaptive, and acquired resistance to cancer immunotherapy. *Cell* **168**, 707–723 (2017).

64. Maccalli, C., Rasul, K. I., Elawad, M. and Ferrone, S. The role of cancer stem cells in the modulation of anti-tumor immune responses. *Sem. in Cancer Biol.* **53**, 189–200 (2018).

65. Hsu, J.M., Xia, W., Hsu, Y.H., Chan, L.C., Yu, W.H., Cha, J.H., Chen, C.T., Liao, H.W., Kuo, C.W., Khoo, K.H. and Hsu, J.L. STT3-dependent PD-L1 accumulation on cancer stem cells promotes immune evasion. *Nat. Commun.* **9**, 1-17 (2018).

66. Lee, Y., Shin, J.H., Longmire, M., Wang, H., Kohrt, H.E., Chang, H.Y. and Sunwoo, J.B. CD44+ cells in head and neck squamous cell carcinoma suppress T-cell-mediated immunity by selective constitutive and inducible expression of PD-L1. *Clin. Cancer Res.* **22**, 3571–3581 (2016).

67. Cioffi, M., Trabulo, S., Hidalgo, M., Costello, E., Greenhalf, W., Erkan, M., Kleeff, J., Sainz, B. and Heeschen, C. Inhibition of CD47 effectively targets pancreatic cancer stem cells via dual mechanisms. *Clin. Cancer Res.* **21,** 2325-2337 (2015).

68. Spranger, S., Bao, R. and Gajewski, T. F. Melanoma-intrinsic β-catenin signalling prevents anti-tumour immunity. *Nature* **523**, 231–235 (2015).

69. Miao, Y., Yang, H., Levorse, J., Yuan, S., Polak, L., Sribour, M., Singh, B., Rosenblum, M.D. and Fuchs, E. Adaptive immune resistance emerges from tumor-initiating stem cells. *Cell* **177**, 1172-1186 (2019).

70. Chaffer, C. L. & Weinberg, R. A. A Perspective on Cancer Cell Metastasis. *Science* **331,** 1559-1564 (2011).

71. Polyak, K. & Weinberg, R. A. Transitions between epithelial and mesenchymal states: acquisition of malignant and stem cell traits. *Nat. Rev. Cancer* **9**, 265–273 (2009).

72. Grillet, F., Bayet, E., Villeronce, O., Zappia, L., Lagerqvist, E.L., Lunke, S., Charafe-Jauffret, E., Pham, K., Molck, C., Rolland, N. and Bourgaux, J.F. Circulating tumour cells from patients with colorectal cancer have cancer stem cell hallmarks in ex vivo culture. *Gut* **66**, 1802–1810 (2017).

73. Balic, M., Lin, H., Young, L., Hawes, D., Giuliano, A., McNamara, G., Datar, R.H. and Cote, R.J. Most early disseminated cancer cells detected in bone marrow of breast cancer patients have a putative breast cancer stem cell phenotype. *Clin. Cancer Res.* **12**, 5615–5621 (2006).

74. Dieter, S.M., Ball, C.R., Hoffmann, C.M., Nowrouzi, A., Herbst, F., Zavidij, O., Abel, U., Arens, A., Weichert, W., Brand, K. and Koch, M. Distinct types of tumor-initiating cells form human colon cancer tumors and metastases. *Cell Stem Cell* **9**, 357–365 (2011).

75. Pang, R., Law, W.L., Chu, A.C., Poon, J.T., Lam, C.S., Chow, A.K., Ng, L., Cheung, L.W., Lan, X.R., Lan, H.Y. and Tan, V.P. A subpopulation of CD26+ cancer stem cells with metastatic capacity in human colorectal cancer. *Cell Stem Cell* **6**, 603–615 (2010).

76. Malanchi, I., Santamaria-Martínez, A., Susanto, E., Peng, H., Lehr, H.A., Delaloye, J.F. and Huelsken, J. Interactions between cancer stem cells and their niche govern metastatic colonization. *Nature* **481**, 85–91 (2012).

77. Baccelli, I., Schneeweiss, A., Riethdorf, S., Stenzinger, A., Schillert, A., Vogel, V., Klein, C., Saini, M., Bäuerle, T., Wallwiener, M. and Holland-Letz, T. Identification of a population of blood circulating tumor cells from breast cancer patients that initiates metastasis in a xenograft assay. *Nat. Biotechnol.* **31**, 539–544 (2013).

78. Ginestier, C., Hur, M.H., Charafe-Jauffret, E., Monville, F., Dutcher, J., Brown, M., Jacquemier, J., Viens, P., Kleer, C.G., Liu, S. and Schott, A. ALDH1 is a marker of normal and malignant human mammary stem cells and a predictor of poor clinical outcome. *Cell Stem Cell* **1**, 555–567 (2007).

79. Charafe-Jauffret, E., Ginestier, C., Iovino, F., Tarpin, C., Diebel, M., Esterni, B., Houvenaeghel, G., Extra, J.M., Bertucci, F., Jacquemier, J. and Xerri, L. Aldehyde dehydrogenase 1–positive cancer stem cells mediate metastasis and poor clinical outcome in inflammatory breast cancer. *Clin. Cancer Res.* **16**, 45–55 (2010).

80. Merlos-Suárez, A., Barriga, F.M., Jung, P., Iglesias, M., Céspedes, M.V., Rossell, D., Sevillano, M., Hernando-Momblona, X., da Silva-Diz, V., Muñoz, P. and Clevers, H. The intestinal stem cell signature identifies colorectal cancer stem cells and predicts disease relapse. *Cell Stem Cell* **8**, 511–524 (2011).

81. Pece, S., Tosoni, D., Confalonieri, S., Mazzarol, G., Vecchi, M., Ronzoni, S., Bernard, L., Viale, G., Pelicci, P.G. and Di Fiore, P.P. Biological and molecular heterogeneity of breast cancers correlates with their cancer stem cell content. *Cell* **140**, 62–73 (2010).

82. Nakanishi, Y., Seno, H., Fukuoka, A., Ueo, T., Yamaga, Y., Maruno, T., Nakanishi, N., Kanda, K., Komekado, H., Kawada, M. and Isomura, A. Dclk1 distinguishes between tumor and normal stem cells in the intestine. *Nat. Genet.* **45**, 98–103 (2012).

83. Boumahdi, S., Driessens, G., Lapouge, G., Rorive, S., Nassar, D., Le Mercier, M., Delatte, B., Caauwe, A., Lenglez, S., Nkusi, E. and Brohee, S. SOX2 controls tumour initiation and cancer stem-cell functions in squamous-cell carcinoma. *Nature* **511**, 246–250 (2014).

84. Clara, J. A., Monge, C., Yang, Y. and Takebe, N. Targeting signalling pathways and the immune microenvironment of cancer stem cells — a clinical update. *Nat. Rev. Clin. Oncol.* **17**, 204–232 (2020).

85. Yang, L., Shi, P., Zhao, G., Xu, J., Peng, W., Zhang, J., Zhang, G., Wang, X., Dong, Z., Chen, F. and Cui, H. Targeting cancer stem cell pathways for cancer therapy. *Signal Transduct. Target. Ther.* **5**, 1–35 (2020).

86. Basset-Séguin, N., Hauschild, A., Kunstfeld, R., Grob, J., Dréno, B., Mortier, L., Ascierto, P.A., Licitra, L., Dutriaux, C., Thomas, L. and Meyer, N. Vismodegib in patients with advanced basal cell carcinoma: Primary analysis of STEVIE, an international, open-label trial. *Eur. J. Cancer* **86**, 334–348 (2017).

87. Lear, J.T., Migden, M.R., Lewis, K.D., Chang, A.L.S., Guminski, A., Gutzmer, R., Dirix, L., Combemale, P., Stratigos, A., Plummer, R. and Castro, H. Long-term efficacy and safety of sonidegib in patients with locally advanced and metastatic basal cell carcinoma: 30-month analysis of the randomized phase 2 BOLT study. *J. Eur. Acad. Dermatology Venereol.* **32**, 372–381 (2018).

88. Cortes, J.E., Douglas Smith, B., Wang, E.S., Merchant, A., Oehler, V.G., Arellano, M., DeAngelo, D.J., Pollyea, D.A., Sekeres, M.A., Robak, T. and Ma, W.W. Glasdegib in combination with cytarabine and daunorubicin in patients with AML or high-risk MDS: Phase 2 study results. *Am. J. Hematol.* **93**, 1301–1310 (2018).

89. Sancho, P., Barneda, D. and Heeschen, C. Hallmarks of cancer stem cell metabolism. *Br. J. Cancer* **114**, 1305–1312 (2016).

90. Lanfranca, M.P., Thompson, J.K., Bednar, F., Halbrook, C., Lyssiotis, C., Levi, B. and Frankel, T.L. Metabolism and epigenetics of pancreatic cancer stem cells. *Semin. Cancer Biol.* **57**, 19–26 (2019).

91. Jagust, P., De Luxán-Delgado, B., Parejo-Alonso, B. and Sancho, P. Metabolism-based therapeutic strategies targeting cancer stem cells. *Front. Pharmacol.* **10**, 203 (2019).

92. Folmes, C. D. L., Dzeja, P. P., Nelson, T. J. and Terzic, A. Metabolic plasticity in stem cell homeostasis and differentiation. *Cell Stem Cell* **11**, 596–606 (2012).

93. Chae, Y. C. & Kim, J. H. Cancer stem cell metabolism: Target for cancer therapy. *BMB Reports* **51**, 319–326 (2018).

94. Shen, Y.A., Wang, C.Y., Hsieh, Y.T., Chen, Y.J. and Wei, Y.H. Metabolic reprogramming orchestrates cancer stem cell properties in nasopharyngeal carcinoma. *Cell cycle* **14,** 86-98 (2015).

95. Dong, C., Yuan, T., Wu, Y., Wang, Y., Fan, T.W., Miriyala, S., Lin, Y., Yao, J., Shi, J., Kang, T. and Lorkiewicz, P. Loss of FBP1 by Snail-mediated repression provides metabolic advantages in basal-like breast cancer. *Cancer Cell* **23**, 316–331 (2013).

96. Chen, C.L., Kumar, D.B.U., Punj, V., Xu, J., Sher, L., Tahara, S.M., Hess, S. and Machida, K. NANOG metabolically reprograms tumor-initiating stem-like cells through tumorigenic changes in oxidative phosphorylation and fatty acid metabolism. *Cell Metab.* **23**, 206–219 (2016).

97. Ye, X.Q., Li, Q., Wang, G.H., Sun, F.F., Huang, G.J., Bian, X.W., Yu, S.C. and Qian, G.S. Mitochondrial and energy metabolism-related properties as novel indicators of lung cancer stem cells. *Int. J. cancer* **129**, 820–831 (2011).

98. Sancho, P., Burgos-Ramos, E., Tavera, A., Kheir, T.B., Jagust, P., Schoenhals, M., Barneda, D., Sellers, K., Campos-Olivas, R., Graña, O. and Viera, C.R. MYC/PGC-1α balance determines the metabolic phenotype and plasticity of pancreatic cancer stem cells. *Cell Metab.* **22**, 590–605 (2015).

99. Janiszewska, M., Suvà, M.L., Riggi, N., Houtkooper, R.H., Auwerx, J., Clément-Schatlo, V., Radovanovic, I., Rheinbay, E., Provero, P. and Stamenkovic, I. Imp2 controls oxidative phosphorylation and is crucial for preserving glioblastoma cancer stem cells. *Genes Dev.* **26**, 1926–1944 (2012).

100. Chae, Y.K., Arya, A., Malecek, M.K., Shin, D.S., Carneiro, B., Chandra, S., Kaplan, J., Kalyan, A., Altman, J.K., Platanias, L. and Giles, F. Repurposing metformin for cancer treatment: current clinical studies. *Oncotarget* **7**, 40767–40780 (2016).

101. Chun, S.G., Liao, Z., Jeter, M.D., Chang, J.Y., Lin, S.H., Komaki, R.U., Guerrero, T.M., Mayo, R.C., Korah, B.M., Koshy, S.M. and Heymach, J.V. Metabolic responses to metformin in inoperable early-stage non-small cell lung cancer treated with stereotactic radiotherapy: results of a randomized phase II clinical trial. *Am. J. Clin.*

Oncol. **43**, 231–235 (2020).

102. Brown, J.R., Chan, D.K., Shank, J.J., Griffith, K.A., Fan, H., Szulawski, R., Yang, K., Reynolds, R.K., Johnston, C., McLean, K. and Uppal, S. Phase II clinical trial of metformin as a cancer stem cell-targeting agent in ovarian cancer. *JCI Insight* **5**, (2020).

103. Pimentel, I., Lohmann, A.E., Ennis, M., Dowling, R.J., Cescon, D., Elser, C., Potvin, K.R., Haq, R., Hamm, C., Chang, M.C. and Stambolic, V. A phase II randomized clinical trial of the effect of metformin versus placebo on progression-free survival in women with metastatic breast cancer receiving standard chemotherapy. *The Breast* **48**, 17–23 (2019).

104. Song, W., Tang, Z., Lei, T., Wen, X., Wang, G., Zhang, D., Deng, M., Tang, X. and Chen, X. Stable loading and delivery of disulfiram with mPEG-PLGA/PCL mixed nanoparticles for tumor therapy. *Nanomed. Nanotechnol. Biol. Med.* **12**, 377–386 (2016).

105. Huang, J., Chaudhary, R., Cohen, A.L., Fink, K., Goldlust, S., Boockvar, J., Chinnaiyan, P., Wan, L., Marcus, S. and Campian, J.L. A multicenter phase II study of temozolomide plus disulfiram and copper for recurrent temozolomide-resistant glioblastoma. *J. Neurooncol.* **142**, 537–544 (2019).

106. Nechushtan, H., Yousef Hamamreh, S.N., Gotfried, M., Baron, A., Shalev, Y.I., Nisman, B., Peretz, T. and Peylan-Ramu, N. A phase IIb trial assessing the addition of disulfiram to chemotherapy for the treatment of metastatic non-small cell lung cancer. *Oncologist* **20**, 366–367 (2015).

107. Halatsch, M.E., Kast, R.E., Karpel-Massler, G., Mayer, B., Zolk, O., Schmitz, B., Scheuerle, A., Maier, L., Bullinger, L., Mayer-Steinacker, R. and Schmidt, C. A phase Ib/IIa trial of 9 repurposed drugs combined with temozolomide for the treatment of recurrent glioblastoma: CUSP9v3. *Neuro-oncology Adv.* **3**, (2021).

108. Li, J., Condello, S., Thomes-Pepin, J., Ma, X., Xia, Y., Hurley, T.D., Matei, D. and Cheng, J.X. Lipid desaturation is a metabolic marker and therapeutic target of ovarian cancer stem cells. *Cell Stem Cell* **20**, 303-314 (2017).

109. Yi, M., Li, J., Chen, S., Cai, J., Ban, Y., Peng, Q., Zhou, Y., Zeng, Z., Peng, S., Li, X. and Xiong, W. Emerging role of lipid metabolism alterations in Cancer stem cells. *J. Exp. Clin. Cancer Res.* **37**, 1–18 (2018).

110. Carracedo, A., Cantley, L. C. and Pandolfi, P. P. Cancer metabolism: Fatty acid oxidation in the limelight. *Nat. Rev. Cancer* **13**, 227–232 (2013).

111. Wang, V.M.Y., Ferreira, R.M., Almagro, J., Evan, T., Legrave, N., Thin, M.Z., Frith, D., Carvalho, J., Barry, D.J., Snijders, A.P. and Herbert, E. CD9 identifies pancreatic cancer stem cells and modulates glutamine metabolism to fuel tumour growth. *Nat. Cell Biol.* **21**, 1425–1435 (2019).

112. Falchook, G., Infante, J., Arkenau, H.T., Patel, M.R., Dean, E., Borazanci, E., Brenner,

A., Cook, N., Lopez, J., Pant, S. and Frankel, A. First-in-human study of the safety, pharmacokinetics, and pharmacodynamics of first-in-class fatty acid synthase inhibitor TVB-2640 alone and with a taxane in advanced tumors. *EClinicalMedicine* **34**, (2021).

113. Keyvani-Ghamsari, S., Khorsandi, K., Rasul, A. and Zaman, M. K. Current understanding of epigenetics mechanism as a novel target in reducing cancer stem cells resistance. *Clin. Epigenetics* **13**, 1–31 (2021).

114. Waddington, C. H. The strategy of the genes. A discussion of some aspects of theoretical biology. With an appendix by H. Kacser. (1957).

115. Li, E. Chromatin modification and epigenetic reprogramming in mammalian development. *Nat. Rev. Genet.* **3**, 662–673 (2002).

116. Perino, M. & Veenstra, G. J. C. Chromatin control of developmental dynamics and plasticity. *Dev. Cell* **38**, 610–620 (2016).

117. Wu, H. & Yi, E.S. Epigenetic regulation of stem cell differentiation. *Pediatr. Res.* **59**, 21–25 (2006).

118. Khavari, D. A., Sen, G. L. and Rinn, J. L. DNA methylation and epigenetic control of cellular differentiation. *Cell Cycle* **9**, 3880–3883 (2010).

119. Sen, G. L., Reuter, J. A., Webster, D. E., Zhu, L. and Khavari, P. A. DNMT1 maintains progenitor function in self-renewing somatic tissue. *Nature* **463**, 563–567 (2010).

120. Pathania, R., Ramachandran, S., Elangovan, S., Padia, R., Yang, P., Cinghu, S., Veeranan-Karmegam, R., Arjunan, P., Gnana-Prakasam, J.P., Sadanand, F. and Pei, L. DNMT1 is essential for mammary and cancer stem cell maintenance and tumorigenesis. *Nat. Commun.* **6**, 1–11 (2015).

121. Tsai, C.C., Su, P.F., Huang, Y.F., Yew, T.L. and Hung, S.C. Oct4 and Nanog directly regulate Dnmt1 to maintain self-renewal and undifferentiated state in mesenchymal stem cells. *Mol. Cell* **47**, 169–182 (2012).

122. Bröske, A.M., Vockentanz, L., Kharazi, S., Huska, M.R., Mancini, E., Scheller, M., Kuhl, C., Enns, A., Prinz, M., Jaenisch, R. and Nerlov, C. DNA methylation protects hematopoietic stem cell multipotency from myeloerythroid restriction. *Nat. Genet.* **41**, 1207–1215 (2009).

123. Feinberg, A. P. Phenotypic plasticity and the epigenetics of human disease. *Nature* **447**, 433–440 (2007).

124. Shah, M. & Allegrucci, C. Stem cell plasticity in development and cancer: Epigenetic origin of cancer stem cells. *Subcell. Biochem.* **61**, 545–565 (2013).

125. Sharma, S.V., Lee, D.Y., Li, B., Quinlan, M.P., Takahashi, F., Maheswaran, S., McDermott, U., Azizian, N., Zou, L., Fischbach, M.A. and Wong, K.K. A chromatin-mediated reversible drug-tolerant state in cancer cell subpopulations. *Cell* **141**, 69–80 (2010).

126. Chaffer, C.L., Marjanovic, N.D., Lee, T., Bell, G., Kleer, C.G., Reinhardt, F., D'Alessio, A.C., Young, R.A. and Weinberg, R.A. Poised chromatin at the ZEB1 promoter enables breast cancer cell plasticity and enhances tumorigenicity. *Cell* **154**, 61 (2013).

127. French, R. & Pauklin, S. Epigenetic regulation of cancer stem cell formation and maintenance. *Int. J. Cancer* **148**, 2884–2897 (2021).

128. Toh, T. B., Lim, J. J. and Chow, E. K.-H. Epigenetics in cancer stem cells. *Mol. Cancer* **16**, 1–20 (2017).

129. Zagorac, S., Alcala, S., Bayon, G.F., Kheir, T.B., Schoenhals, M., González-Neira, A., Fraga, M.F., Aicher, A., Heeschen, C. and Sainz, B. DNMT1 inhibition reprograms pancreatic cancer stem cells via upregulation of the miR-17-92 cluster. *Cancer Res.* **76**, 4546–4558 (2016).

130. Trowbridge, J.J., Sinha, A.U., Zhu, N., Li, M., Armstrong, S.A. and Orkin, S.H. Haploinsufficiency of Dnmt1 impairs leukemia stem cell function through derepression of bivalent chromatin domains. *Genes Dev.* **26**, 344–349 (2012).

131. Banelli, B., Carra, E., Barbieri, F., Würth, R., Parodi, F., Pattarozzi, A., Carosio, R., Forlani, A., Allemanni, G., Marubbi, D. and Florio, T. The histone demethylase KDM5A is a key factor for the resistance to temozolomide in glioblastoma. *Cell Cycle* **14**, 3418 (2015).

132. Metzger, E., Stepputtis, S.S., Strietz, J., Preca, B.T., Urban, S., Willmann, D., Allen, A., Zenk, F., Iovino, N., Bronsert, P. and Proske, A. KDM4 inhibition targets breast cancer stem–like cells. *Cancer Res.* **77**, 5900–5912 (2017).

133. Witt, A.E., Lee, C.W., Lee, T.I., Azzam, D.J., Wang, B., Caslini, C., Petrocca, F., Grosso, J., Jones, M., Cohick, E.B. and Gropper, A.B. Identification of a cancer stem cell-specific function for the histone deacetylases, HDAC1 and HDAC7, in breast and ovarian cancer. *Oncogene* **36**, 1707–1720 (2016).

134. Kleer, C.G., Cao, Q., Varambally, S., Shen, R., Ota, I., Tomlins, S.A., Ghosh, D., Sewalt, R.G., Otte, A.P., Hayes, D.F. and Sabel, M.S. EZH2 is a marker of aggressive breast cancer and promotes neoplastic transformation of breast epithelial cells. *Proc. Natl. Acad. Sci.* **100**, 11606–11611 (2003).

135. van Vlerken, L.E., Kiefer, C.M., Morehouse, C., Li, Y., Groves, C., Wilson, S.D., Yao, Y., Hollingsworth, R.E. and Hurt, E.M. EZH2 is required for breast and pancreatic cancer stem cell maintenance and can be used as a functional cancer stem cell reporter. *Stem Cells Transl. Med.* **2**, 43–52 (2013).

136. Nepali, K. & Liou, J. P. Recent developments in epigenetic cancer therapeutics: clinical advancement and emerging trends. *J. Biomed. Sci.* **28**, 1–58 (2021).

137. Akar, R.O., Selvi, S., Ulukaya, E. and Aztopal, N. Key actors in cancer therapy: epigenetic modifiers. *Turkish J. Biol.* **43**, 155 (2019).

138. Mitchem, J.B., Brennan, D.J., Knolhoff, B.L., Belt, B.A., Zhu, Y., Sanford, D.E., Belaygorod, L., Carpenter, D., Collins, L., Piwnica-Worms, D. and Hewitt, S. Targeting tumor-infiltrating macrophages decreases tumor-initiating cells, relieves immunosuppression, and improves chemotherapeutic responses. *Cancer Res.* **73**, 1128–1141 (2013).

139. Su, S., Chen, J., Yao, H., Liu, J., Yu, S., Lao, L., Wang, M., Luo, M., Xing, Y., Chen, F. and Huang, D. CD10 + GPR77 + Cancer-Associated Fibroblasts Promote Cancer Formation and Chemoresistance by Sustaining Cancer Stemness. *Cell* **172**, 841-856 (2018).

140. Kleeff, J., Korc, M., Apte, M., La Vecchia, C., Johnson, C.D., Biankin, A.V., Neale, R.E., Tempero, M., Tuveson, D.A., Hruban, R.H. and Neoptolemos, J.P. Pancreatic cancer. *Nat. Rev. Dis. Prim. 2016 21* **2**, 1–22 (2016).

141. Rahib, L., Wehner, M.R., Matrisian, L.M. and Nead, K.T. Estimated projection of US Cancer incidence and death to 2040. *JAMA Netw. Open* **4**, e214708 (2021).

142. Siegel, R. L., Miller, K. D., Fuchs, H. E. and Jemal, A. Cancer Statistics, 2021. *CA. Cancer J. Clin.* **71**, 7–33 (2021).

143. Hruban, R. H., Goggins, M., Parsons, J. and Kern, S. E. Progression model for pancreatic cancer. *Clin. Cancer Res.* **6**, 2969–2972 (2000).

144. Hezel, A. F., Kimmelman, A. C., Stanger, B. Z., Bardeesy, N. and DePinho, R. A. Genetics and biology of pancreatic ductal adenocarcinoma. *Genes Dev.* **20**, 1218–1249 (2006).

145. Maitra, A., Adsay, N.V., Argani, P., Iacobuzio-Donahue, C., De Marzo, A., Cameron, J.L., Yeo, C.J. and Hruban, R.H. Multicomponent analysis of the pancreatic adenocarcinoma progression model using a pancreatic intraepithelial neoplasia tissue microarray. *Mod. Pathol.* **16**, 902–912 (2003).

146. Yachida, S. & Iacobuzio-Donahue, C. A. The pathology and genetics of metastatic pancreatic cancer. *Arch. Path. Lab.* **133**, 413–422 (2009).

147. Rhim, A.D., Mirek, E.T., Aiello, N.M., Maitra, A., Bailey, J.M., McAllister, F., Reichert, M., Beatty, G.L., Rustgi, A.K., Vonderheide, R.H. and Leach, S.D. EMT and dissemination precede pancreatic tumor formation. *Cell* **148**, 349–361 (2012).

148. Peixoto, R.D.A., Speers, C., McGahan, C.E., Renouf, D.J., Schaeffer, D.F. and Kennecke, H.F. Prognostic factors and sites of metastasis in unresectable locally advanced pancreatic cancer. *Cancer Med.* **4**, 1171–1177 (2015).

149. Lopez, N.E., Prendergast, C. and Lowy, A.M. Borderline resectable pancreatic cancer: definitions and management. *World J. Gastroenterol.* **20**, 10740–10751 (2014).

150. Von Hoff, D.D., Ervin, T., Arena, F.P., Chiorean, E.G., Infante, J., Moore, M., Seay, T., Tjulandin, S.A., Ma, W.W., Saleh, M.N. and Harris, M. Increased survival in pancreatic cancer with nab-paclitaxel plus gemcitabine. *N. Engl. J. Med.* **369**, 1691–1703 (2013).

151. Conroy, T., Hammel, P., Hebbar, M., Ben Abdelghani, M., Wei, A.C., Raoul, J.L., Choné, L., Francois, E., Artru, P., Biagi, J.J. and Lecomte, T. FOLFIRINOX or gemcitabine as adjuvant therapy for pancreatic cancer. *N. Engl. J. Med.* **379**, 2395–2406 (2018).

152. Paulson, A. S., Tran Cao, H. S., Tempero, M. A. and Lowy, A. M. Therapeutic advances in pancreatic cancer. *Gastroenterology* **144**, 1316–1326 (2013).

153. Lai, E., Puzzoni, M., Ziranu, P., Pretta, A., Impera, V., Mariani, S., Liscia, N., Soro, P., Musio, F., Persano, M. and Donisi, C. New therapeutic targets in pancreatic cancer. *Cancer Treat. Rev.* **81**, 101926 (2019).

154. Hayashi, A., Hong, J. and Iacobuzio-Donahue, C. A. The pancreatic cancer genome revisited. *Nat. Rev. Gastroenterol. Hepatol. 2021 187* **18**, 469–481 (2021).

155. Waddell, N., Pajic, M., Patch, A.M., Chang, D.K., Kassahn, K.S., Bailey, P., Johns, A.L., Miller, D., Nones, K., Quek, K. and Quinn, M.C. Whole genomes redefine the mutational landscape of pancreatic cancer. *Nature* **518**, 495–501 (2015).

156. Witkiewicz, A.K., McMillan, E.A., Balaji, U., Baek, G., Lin, W.C., Mansour, J., Mollaee, M., Wagner, K.U., Koduru, P., Yopp, A. and Choti, M.A. Whole-exome sequencing of pancreatic cancer defines genetic diversity and therapeutic targets. *Nat. Commun.* **6**, 1–11 (2015).

157. Dreyer, S. B., Chang, D. K., Bailey, P. and Biankin, A. V. Pancreatic cancer genomes: implications for clinical management and therapeutic development. *Clin. Cancer Res.* **23**, 1638–1646 (2017).

158. Bailey, P., Chang, D.K., Nones, K., Johns, A.L., Patch, A.M., Gingras, M.C., Miller, D.K., Christ, A.N., Bruxner, T.J., Quinn, M.C. and Nourse, C. Genomic analyses identify molecular subtypes of pancreatic cancer. *Nature* **531**, 47–52 (2016).

159. Collisson, E. A., Bailey, P., Chang, D. K. and Biankin, A. V. Molecular subtypes of pancreatic cancer. *Nat. Rev. Gastroenterol. Hepatol.* **16**, 207–220 (2019).

160. Moffitt, R. Virtual microdissection identifies distinct tumor- and stroma-specific subtypes of pancreatic ductal adenocarcinoma. *Nat. Genet.* **47**, 1168–1178 (2015).

161. Collisson, E. A., Sadanandam, A., Olson, P., Gibb W. J., Truitt, M., Gu, S., Cooc, J., Weinkle, J., Kim, G. E., Jakkula, L., Feiler, H. S., Ko, A. H., Olshen, A. B., Danenber, K. L., Tempero, M. A., Spellman, P. T., Hanahan, D., and Gray, J. W. Subtypes of pancreatic ductal adenocarcinoma and their differing responses to therapy. *Nat. Med.* **17**, 500–503 (2011).

162. Bailey, P., Chang, D.K., Nones, K., Johns, A.L., Patch, A.M., Gingras, M.C., Miller, D.K., Christ, A.N., Bruxner, T.J., Quinn, M.C. and Nourse, C. Genomic analyses identify molecular subtypes of pancreatic cancer. *Nature* **531**, 47–52 (2016).

163. Diaferia, G.R., Balestrieri, C., Prosperini, E., Nicoli, P., Spaggiari, P., Zerbi, A. and Natoli, G. Dissection of transcriptional and cis -regulatory control of differentiation in

human pancreatic cancer. *EMBO J.* **35**, 595–617 (2016).

164. Lomberk, G., Blum, Y., Nicolle, R., Nair, A., Gaonkar, K.S., Marisa, L., Mathison, A., Sun, Z., Yan, H., Elarouci, N. and Armenoult, L. Distinct epigenetic landscapes underlie the pathobiology of pancreatic cancer subtypes. *Nat. Commun.* **9**, 1–10 (2018).

165. Aung, K.L., Fischer, S.E., Denroche, R.E., Jang, G.H., Dodd, A., Creighton, S., Southwood, B., Liang, S.B., Chadwick, D., Zhang, A. and O'Kane, G.M. Genomics-driven precision medicine for advanced pancreatic cancer: early results from the COMPASS trial. *Clin Cancer Res* **24**, 1344-1354 (2018).

166. Morris, J. P., IV, Wang, S. C. and Hebrok, M. KRAS, Hedgehog, Wnt and the twisted developmental biology of pancreatic ductal adenocarcinoma. *Nat. Rev. Cancer* **10**, 683 (2010).

167. Lomberk, G., Dusetti, N., Iovanna, J. & Urrutia, R. Emerging epigenomic landscapes of pancreatic cancer in the era of precision medicine. *Nat. Commun. 2019 101* **10**, 1–10 (2019).

168. Hayashi, A., Fan, J., Chen, R., Ho, Y.J., Makohon-Moore, A.P., Lecomte, N., Zhong, Y., Hong, J., Huang, J., Sakamoto, H. and Attiyeh, M.A. A unifying paradigm for transcriptional heterogeneity and squamous features in pancreatic ductal adenocarcinoma. *Nat. Cancer* **1**, 59–74 (2020).

169. Zhu, Y.Y. & Yuan, Z. Pancreatic cancer stem cells. *Am. J. Cancer Res.* **5**, 894 (2015).

170. Kim, M.P., Fleming, J.B., Wang, H., Abbruzzese, J.L., Choi, W., Kopetz, S., McConkey, D.J., Evans, D.B. and Gallick, G.E. ALDH activity selectively defines an enhanced tumor-initiating cell population relative to CD133 expression in human pancreatic adenocarcinoma. *PLoS One* **6**, e20636 (2011).

171. Li, C., Wu, J.J., Hynes, M., Dosch, J., Sarkar, B., Welling, T.H., di Magliano, M.P. and Simeone, D.M. C-Met is a marker of pancreatic cancer stem cells and therapeutic target. *Gastroenterology* **141**, (2011).

172. Fox, R.G., Lytle, N.K., Jaquish, D.V., Park, F.D., Ito, T., Bajaj, J., Koechlein, C.S., Zimdahl, B., Yano, M., Kopp, J.L. and Kritzik, M. Image-based detection and targeting of therapy resistance in pancreatic adenocarcinoma. *Nature* **534**, 407–411 (2016).

173. Maeda, S., Shinchi, H., Kurahara, H., Mataki, Y., Maemura, K., Sato, M., Natsugoe, S., Aikou, T. and Takao, S. CD133 expression is correlated with lymph node metastasis and vascular endothelial growth factor-C expression in pancreatic cancer. *Br. J. Cancer* **98**, 1389 (2008).

174. Rasheed, Z.A., Yang, J., Wang, Q., Kowalski, J., Freed, I., Murter, C., Hong, S.M., Koorstra, J.B., Rajeshkumar, N.V., He, X. and Goggins, M. Prognostic significance of tumorigenic cells with mesenchymal features in pancreatic adenocarcinoma. *JNCI J. Natl. Cancer Inst.* **102**, 340–351 (2010).

175. Rasheed, Z. A. & Matsui, W. Biological and clinical relevance of stem cells in pancreatic adenocarcinoma. *J. Gastroenterol. Hepatol.* **27**, 15–18 (2012).

176. Ohara, Y., Oda, T., Sugano, M., Hashimoto, S., Enomoto, T., Yamada, K., Akashi, Y., Miyamoto, R., Kobayashi, A., Fukunaga, K. and Morishita, Y. Histological and prognostic importance of CD44+/CD24+/EpCAM+ expression in clinical pancreatic cancer. *Cancer Sci.* **104**, 1127–1134 (2013).

177. Ding, Q., Miyazaki, Y., Tsukasa, K., Matsubara, S., Yoshimitsu, M. and Takao, S. CD133 facilitates epithelial-mesenchymal transition through interaction with the ERK pathway in pancreatic cancer metastasis. *Mol. Cancer* **13**, 1–11 (2014).

178. Van den Broeck, A., Vankelecom, H., Van Delm, W., Gremeaux, L., Wouters, J., Allemeersch, J., Govaere, O., Roskams, T. and Topal, B. Human pancreatic cancer contains a side population expressing cancer stem cell-associated and prognostic genes. *PLoS One* **8**, e73968 (2013).

179. Feldmann, G., Fendrich, V., McGovern, K., Bedja, D., Bisht, S., Alvarez, H., Koorstra, J.B.M., Habbe, N., Karikari, C., Mullendore, M. and Gabrielson, K.L. An orally bioavailable small-molecule inhibitor of Hedgehog signaling inhibits tumor initiation and metastasis in pancreatic cancer. *Mol. Cancer Ther.* **7**, 2725–2735 (2008).

180. Ko, A.H., LoConte, N., Tempero, M.A., Walker, E.J., Kelley, R.K., Lewis, S., Chang, W.C., Kantoff, E., Vannier, M.W., Catenacci, D.V. and Venook, A.P. A phase I study of FOLFIRINOX plus IPI-926, a hedgehog pathway inhibitor, for advanced pancreatic adenocarcinoma. *Pancreas* **45**, 370 (2016).

181. Rhim, A.D., Oberstein, P.E., Thomas, D.H., Mirek, E.T., Palermo, C.F., Sastra, S.A., Dekleva, E.N., Saunders, T., Becerra, C.P., Tattersall, I.W. and Westphalen, C.B. Stromal elements act to restrain, rather than support, pancreatic ductal adenocarcinoma. *Cancer Cell* **25**, 735–747 (2014).

182. Sonbol, M.B., Ahn, D.H., Goldstein, D., Okusaka, T., Tabernero, J., Macarulla, T., Reni, M., Li, C.P., O'Neil, B., Van Cutsem, E. and Bekaii-Saab, T. CanStem111P trial: a Phase III study of napabucasin plus nab-paclitaxel with gemcitabine. *Future Oncol.* **15**, 1295–1302 (2019).

183. Tsai, K. K., Chan, T. S. and Shaked, Y. Next viable routes to targeting pancreatic cancer stemness: Learning from clinical setbacks. *J. Clin. Med.* **8**, 702 (2019).

Chapter 2. A multiscale map of the stem cell state in pancreatic adenocarcinoma

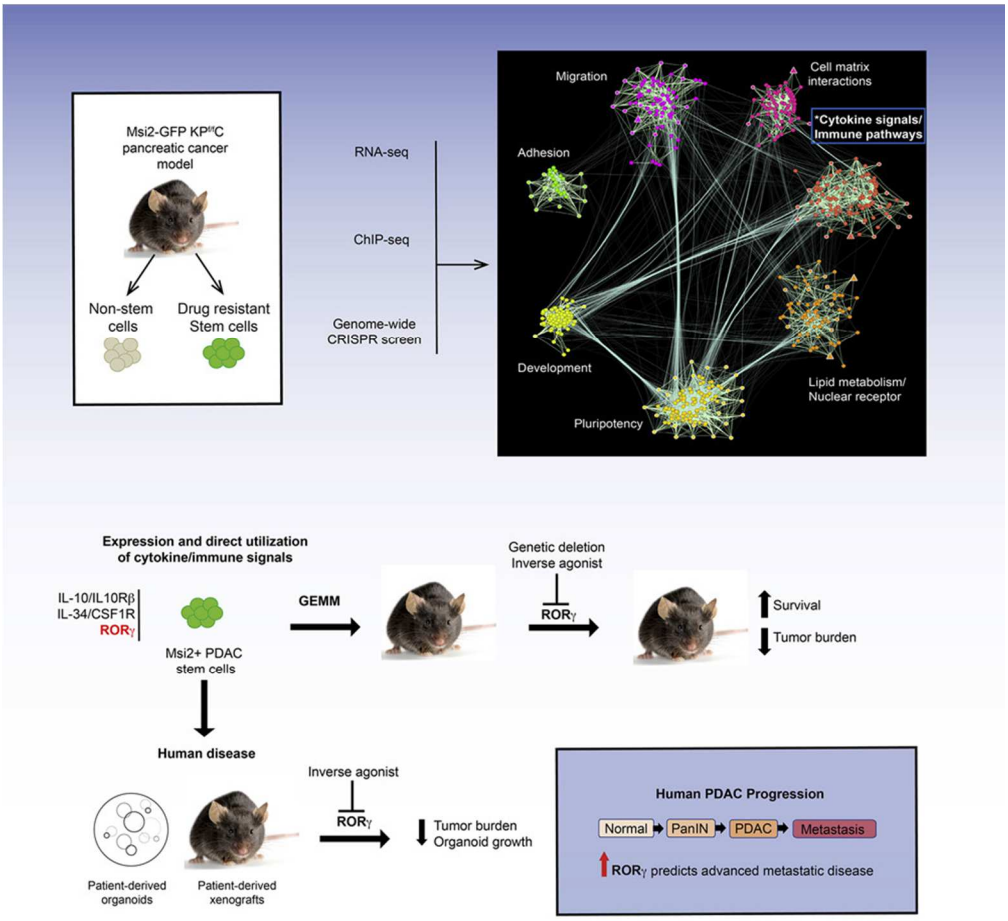

Figure 2.1. Graphical abstract.

2.1. Abstract

Drug resistance and relapse remain key challenges in pancreatic cancer. Here, we have used RNA sequencing (RNA-seq), chromatin immunoprecipitation (ChIP)-seq, and genome-wide CRISPR analysis to map the molecular dependencies of pancreatic cancer stem cells, highly therapy-resistant cells that preferentially drive tumorigenesis and progression. This integrated genomic approach revealed an unexpected utilization of immuno-regulatory signals by pancreatic cancer epithelial cells. In particular, the nuclear hormone receptor retinoic-acid-

receptor-related orphan receptor gamma (RORγ), known to drive inflammation and T cell differentiation, was upregulated during pancreatic cancer progression, and its genetic or pharmacologic inhibition led to a striking defect in pancreatic cancer growth and a marked improvement in survival. Further, a large-scale retrospective analysis in patients revealed that RORγ expression may predict pancreatic cancer aggressiveness, as it positively correlated with advanced disease and metastasis. Collectively, these data identify an orthogonal co-option of immuno-regulatory signals by pancreatic cancer stem cells, suggesting that autoimmune drugs should be evaluated as novel treatment strategies for pancreatic cancer patients.

2.2. Introduction

Although cytotoxic agents remain the standard of care for most cancers, their use is often associated with initial efficacy, followed by disease progression. This is particularly true for pancreatic cancer, a highly aggressive disease, where current multidrug chemotherapy regimens result in tumor regression in 30% of patients, quickly followed by disease progression in the vast majority of cases[1]. This progression is largely due to the inability of chemotherapy to successfully eradicate all tumor cells, leaving behind subpopulations that can trigger tumor re-growth. Thus, identifying the cells that are preferentially drug resistant, and understanding their vulnerabilities, is critical to improving patient outcome and response to current therapies.

In previous work, several groups have focused on identifying the most tumorigenic populations within pancreatic cancer. Through this, subpopulations of cells marked by expression of CD24+/CD44+/ESA+[2], cMet[3], CD133[4], nestin[5], ALDH[6], and more recently DCLK1[7] and Musashi[8] have been shown to harbor stem cell characteristics, in being enriched for the capacity to drive tumorigenesis, and recreate the heterogeneity of the original tumor[9]. Importantly, these tumor propagating cells or cancer stem cells have been shown to be highly

resistant to cytotoxic therapies, such as gemcitabine, consistent with the finding that cancer patients with a high cancer stem cell signature have poorer prognosis relative to those with a low stem cell signature[10]. Although pancreatic cancer stem cells are epithelial in origin, these cells frequently express epithelial-to-mesenchymal (EMT)-associated programs, which may in part explain their over-representation in circulation and propensity to seed metastatic sites[8,4]. Because these studies define stem cells as a population that presents a particularly high risk for disease progression, defining the molecular signals that sustain them remains an essential goal for achieving complete and durable responses.

Here, we have used a combination of RNA-sequencing (RNA-seq), chromatin immunoprecipitation (ChIP)-seq, and genome-wide CRISPR screening to define the molecular framework that sustains the aggressive nature of pancreatic cancer stem cells. These studies identified a network of key nodes regulating pancreatic cancer stem cells and revealed an unanticipated role for immuno-regulatory genes in their self-renewal and maintenance. Among these, the retinoic-acid-receptor-related orphan receptor gamma (RORγ), a nuclear hormone receptor known for its role in Th17 cell specification and regulation of inflammatory cytokine production[11], emerged as a key regulator of stem cells. RORγ expression increased with progression, and its blockade via genetic or pharmacologic approaches depleted the cancer stem cell pool and profoundly inhibited human and mouse tumor propagation, in part by suppressing a super-enhancer-associated oncogenic network. Finally, sustained treatment with a RORγ inhibitor led to a significant improvement in autochthonous models of pancreatic cancer. Together, our studies offer a unique comprehensive map of pancreatic cancer stem cells and identify critical vulnerabilities that may be exploited to improve therapeutic targeting of aggressive, drug-resistant pancreatic cancer cells.

2.3. Results

Transcriptomic and epigenetic map of pancreatic cancer cells reveals a unique stem cell state

In previous work, we used the *KP$^{f/f}$C* mouse model of pancreatic ductal adenocarcinoma (PDAC)[12,13] to show that a reporter mouse designed to mirror expression of the stem cell signal Musashi (Msi) could identify tumor cells that are preferentially drug resistant and can drive tumor re-growth[8]. Consistent with this, Msi2+ tumor cells were 209-fold enriched in the ability to give rise to organoids in limiting dilution assays[14] (Figures 2.2 A, and Figure 2.S2 A, B). Because Msi+ cells were enriched for tumor propagation and drug resistance- classically defined properties of cancer stem cells—we postulated that Msi reporters could be used as a tool to understand the molecular underpinnings of this aggressive subpopulation within pancreatic cancer.

To map the functional genomic landscape of the stem cell state, we utilized a combination of RNA-seq, ChIP-seq, and genome-wide CRISPR screening[15]. Pancreatic cancer cells were isolated from *Msi2-GFP* reporter (REM2) *KP$^{f/f}$C* mice based on GFP and EpCAM expression and analyzed by RNA-seq (Figure 2.2 B). Principal-component analysis showed that *KP$^{f/f}$C* reporter+ tumor cells were distinct from reporter− tumor cells at a global transcriptional level and were defined by a unique set of programs in turn driven by the differential expression of over a thousand genes (Figure 2.2 C,D). We focused on genes enriched in stem cells in order to understand the transcriptional programs that may functionally maintain the stem cell state. Gene set enrichment analysis (GSEA)[16] was used to compare this PDAC stem cell transcriptomic signature with other cell signatures (Table 2.1). This revealed that the transcriptional state of PDAC stem cells mapped closely with other developmental and stem cell states, indicating molecular features aligned with their observed functional traits (Figure 2.2 E,F). Additionally, the transcriptional signature of PDAC stem cells was inversely correlated with cell proliferation signatures (Figure 2.S2 C,D), consistent with

our finding that the stem cell pool is quiescent following chemotherapy (Figure 2.S2 E). Stem cells also harbored metabolic signatures associated with tumor aggressiveness, including increased sulfur amino acid metabolism[17] and enhanced glutathione synthesis, pathways that enable survival following radiation and chemotherapy[18] (Figure 2.2 G,H). Finally, the stem cell transcriptome bore similarities to signatures from relapsed cancers of the breast, liver, and colon (Figure 2.2 I,J); consistent with this, stem cells showed a significant overlap with mesenchymal cells in single-cell RNA-seq analysis of pancreatic tumors (Figure 2.2 K). These molecular properties may collectively underlie the ability of PDAC stem cells to survive chemotherapy and drive tumor recurrence.

Analysis of H3 lysine-27 acetylation (H3K27ac) (Figure 2.2 B and Figure 2.S2 F), a histone mark associated with active enhancers[19], revealed that the differential gene expression programs in stem cells and non-stem cells were driven by changes at the chromatin level. Thus, genomic regions enriched for H3K27ac coincided with regions where gene expression was increased in each cell type (Figure 2.S2 G-J; stem cells: $R^2 = 0.28$, $p = 7.1 \times 10^{-14}$; non-stem cells $R^2 = 0.46$, $p = 22 \times 10^{-16}$). Because super-enhancers have been proposed to be key drivers of cell identity[19,20], we mapped shared and unique super-enhancers in stem and non-stem cells (Figure 2.2 L-O). This analysis revealed that super-enhancer-associated H3K27ac marks were predominantly restricted to either stem cells or non-stem cells, with 65% of all super-enhancers being unique to each population (364 unique super-enhancers in stem cells/388 unique super-enhancers in non-stem cells). In contrast, almost all promoter and conventional enhancer-associated H3K27ac marks were shared between stem and non-stem cells, with less than 5% being unique. Further, although super-enhancers in the stem cell population were clearly demarcated by peaks with substantially greater relative enrichment than the same regions in non-stem cells (Figure 2.2 M), the super-enhancers found in non-stem cells showed a peak intensity that was only marginally greater than the

corresponding regions in stem cells (Figure 2.2 O). These data suggest that stem cells in pancreatic cancer have a more specialized super-enhancer landscape than non-stem cells and raise the possibility that super-enhancer linked genes and their regulators may serve to control stem cell identity in pancreatic cancer. In support of this, key transcription factors and programs that underlie developmental and stem cell states, such as *Tead4, Wnt7b*, and *Msi2* (Figure 2.2 L) and *Foxp*, *Klf7*, and *Hmga1* (Table 2.2), were associated with super-enhancers in *KP$^{f/f}$C* stem cells.

Genome-wide CRISPR screen identifies core functional programs in pancreatic cancer

To define which of the programs uncovered by the transcriptional and epigenetic analyses represented true functional dependencies of stem cells, we carried out a genome-wide CRISPR screen. Thus, primary cell cultures enriched for stem cells (Figure 2.S3 A) were derived from REM2 *KP$^{f/f}$C* mice and transduced with the mouse GeCKO CRISPRv2 single guide RNA (sgRNA) library[15] (Figure 2.3 A). The screen was multiplexed in order to identify genes required in conventional 2D cultures, as well as in 3D stem cell sphere cultures[21] that selectively allow stem cell growth[8] (Figure 2.3 A). The screens showed clear evidence of selection, with 807 genes depleted in 2D (Figure 2.3 B,C) and an additional 178 in 3D stem cell cultures (Figure 2.3 B,D). Importantly, the screens showed a loss of oncogenes and an enrichment of tumor suppressors in conventional cultures (Figure 2.3 C and Figure 2.S3 B) and a loss of stem cell signals and gain of negative regulators of stem signals in stem cell conditions (Figure 2.3 D, Figure 2.S3 C).

Figure 2.2. Transcriptomic and epigenetic map of pancreatic cancer cells reveals a unique stem cell state

(A) Tumor organoid formation from primary *Msi2*+ and *Msi2*− REM2-*KP$^{f/f}$C* tumor cells. Representative images, scale bars represent 100 μm.

(B) RNA-seq and ChIP-seq of EpCAM+GFP+ and Epcam+GFP− REM2-*KP$^{f/f}$C* tumor cells (n = 3 RNA-seq; n = 1 ChIP-seq).

(C) Principal-component analysis of *KP$^{f/f}$C* stem (purple) and non-stem (gray) cells.

(D) Transcripts enriched in stem (red and pink) and non-stem cells (dark blue and light blue). Pink, light blue, local false discovery rate (lfdr) < 0.3; red, dark blue, lfdr < 0.1.

(E–J) GSEA cell states and corresponding heatmaps associated with development (E and F), metabolism (G and H), and cancer relapse (I and J). (E, G, and I) Red denotes overlapping gene signatures; blue denotes non-overlapping gene signatures. (F, H, and J) Red, over-represented gene expression; blue, under-represented gene expression; shades denote fold change.

(K) Single-cell sequencing of *KP$^{R172H/+}$C* tumors (left) and map of *Msi2* expression in ETC and EMT clusters (right); CAF, cancer-associated fibroblasts (red); EMT, mesenchymal tumor cells (olive green); Endo, endothelial cells (green); ETC, epithelial tumor cells (blue); TAM, tumor-associated macrophages (magenta).

(L) Hockey stick plots of H3K27ac occupancy ranked by signal density. Stem cell super-enhancers (left) or shared super-enhancers (right) are demarcated by highest ranking and intensity signals.

(M–O) H3K27ac ChIP-seq reads across genes marked by stem cell super-enhancers (M), shared super-enhancers (N), or non-stem super-enhancers (O).

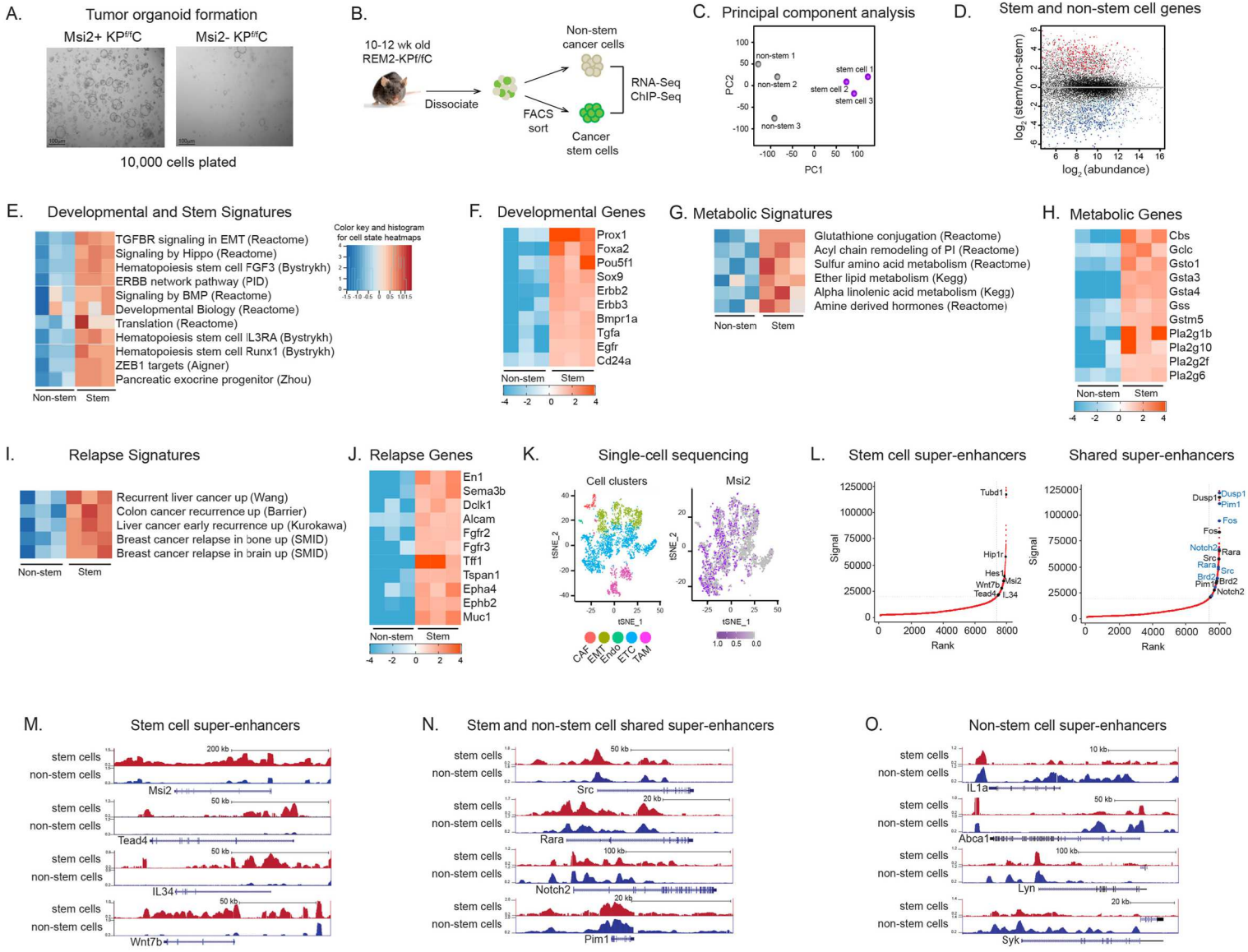
A.
Tumor organoid formation
Msi2+ KP^f/fC
Msi2- KP^f/fC
10,000 cells plated
B.
10-12 wk old
REM2-KPf/fC
Dissociate
Non-stem
cancer cells
FACS
sort
Cancer
stem cells
RNA-Seq
ChIP-Seq
C.
Principal component analysis
PC2
PC1
non-stem 1
non-stem 2
non-stem 3
stem cell 1
stem cell 2
stem cell 3
D.
Stem and non-stem cell genes
log2 (stem/non-stem)
log2 (abundance)
E.
Developmental and Stem Signatures
Color key and histogram
for cell state heatmaps
TGFBR signaling in EMT (Reactome)
Signaling by Hippo (Reactome)
Hematopoiesis stem cell FGF3 (Bystrykh)
ERBB network pathway (PID)
Signaling by BMP (Reactome)
Developmental Biology (Reactome)
Translation (Reactome)
Hematopoiesis stem cell IL3RA (Bystrykh)
Hematopoiesis stem cell Runx1 (Bystrykh)
ZEB1 targets (Aigner)
Pancreatic exocrine progenitor (Zhou)
Non-stem
Stem
F.
Developmental Genes
Prox1
Foxa2
Pou5f1
Sox9
Erbb2
Erbb3
Bmpr1a
Tgfa
Egfr
Cd24a
Non-stem
Stem
G.
Metabolic Signatures
Glutathione conjugation (Reactome)
Acyl chain remodeling of PI (Reactome)
Sulfur amino acid metabolism (Reactome)
Ether lipid metabolism (Kegg)
Alpha linolenic acid metabolism (Kegg)
Amine derived hormones (Reactome)
Non-stem
Stem
H.
Metabolic Genes
Cbs
Gclc
Gsto1
Gsta3
Gsta4
Gss
Gstm5
Pla2g1b
Pla2g10
Pla2g2f
Pla2g6
Non-stem
Stem
I.
Relapse Signatures
Recurrent liver cancer up (Wang)
Colon cancer recurrence up (Barrier)
Liver cancer early recurrence up (Kurokawa)
Breast cancer relapse in bone up (SMID)
Breast cancer relapse in brain up (SMID)
Non-stem
Stem
J.
Relapse Genes
En1
Sema3b
Dclk1
Alcam
Fgfr2
Fgfr3
Tff1
Tspan1
Epha4
Ephb2
Muc1
Non-stem
Stem
K.
Single-cell sequencing
Cell clusters
Msi2
tSNE_1
tSNE_2
CAF
EMT
EndO
ETC
TAM
L.
Stem cell super-enhancers
Shared super-enhancers
Signal
Rank
Tubd1
Hip1r
Hes1
Wnt7b
Tead4
Msi2
IL34
Dusp1
Pim1
Fos
Notch2
Rara
Src
Brd2
M.
Stem cell super-enhancers
stem cells
non-stem cells
Msi2
Tead4
IL34
Wnt7b
N.
Stem and non-stem cell shared super-enhancers
Src
Rara
Notch2
Pim1
O.
Non-stem cell super-enhancers
IL1a
Abca1
Lyn
Syk

Computational integration of the transcriptomic and CRISPR-based functional genomic data was carried out using a network propagation method similar to one developed previously[22]. First, the network was seeded with genes that were preferentially enriched in stem cells and also identified as essential for stem cell growth (Figure 2.3 E). The genes most proximal to the seeds were then determined using the mouse search tool for the retrieval of interacting genes/proteins (STRING) interactome[23] based on known and predicted protein-protein interactions using network propagation. Fold-change in RNA expression from the RNA-seq was overlaid onto the resulting subnetwork. The network was subsequently clustered into functional communities based on high interconnectivity between genes, and gene set over-representation analysis was performed on each community; this analysis identified seven subnetworks built around distinct biological pathways, thus providing a systems-level view of core programs that may be involved in driving pancreatic cancer growth. These programs identified stem and pluripotency pathways, developmental and proteasome signals, lipid metabolism and nuclear receptors, cell adhesion, cell-matrix, and cell migration, and immuno-regulatory signaling as pathways integral to the stem cell state (Figure 2.3 E and Figure 2.S3 D).

Figure 2.3. Genome-Scale CRISPR screen identifies core stem cell programs in pancreatic cancer.
(A) Schematic of CRISPR screen.
(B) Number of guides in each replicate following lentiviral infection (gray bars), puromycin selection (red bars), and sphere formation (blue bars).
(C and D) Volcano plots of guides depleted in 2D (C) and 3D (D). Genes indicated on plots, $p < 0.005$.
(E) Network propagation integrating transcriptomic, epigenetic, and functional analysis of stem cells. Stem-enriched genes by RNA-seq ($log_2FC > 2$) and depleted in 3D (false discovery rate [FDR]-adjusted $p < 0.5$) were used to seed the network (triangles) and then analyzed for protein-protein interactions. Each node represents a single gene; color denotes RNA-seq fold change; stem enriched, red; non-stem enriched, blue; not differentially expressed, gray. Labels shown are for genes enriched in stem cells or non-stem cells by RNA-seq (RNA log_2FC absolute value > 3.0) or by RNA-seq and ChIP-seq (RNA log_2FC absolute value > 2.0, ChIP-seq FDR < 0.01). Seven core programs were defined by gene groups with high connectivity; annotated by GO analysis (FDR < 0.05).

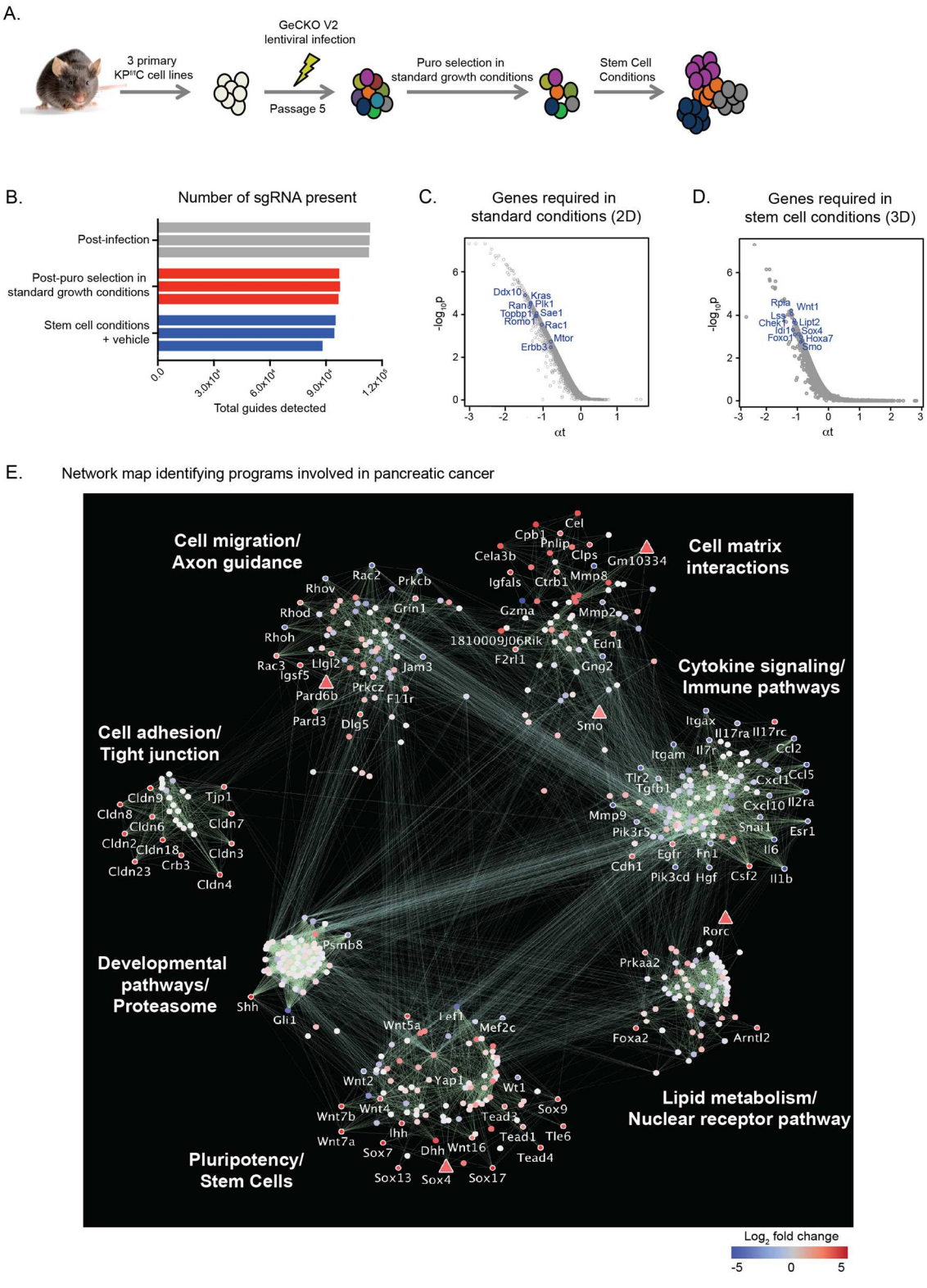
A.
3 primary KP^fl/fl C cell lines
GeCKO V2 lentiviral infection
Passage 5
Puro selection in standard growth conditions
Stem Cell Conditions
B.
Number of sgRNA present
Post-infection
Post-puro selection in standard growth conditions
Stem cell conditions + vehicle
0.0
3.0x10^5
6.0x10^5
9.0x10^5
1.2x10^6
Total guides detected
C.
Genes required in standard conditions (2D)
-log10p
αt
Ddx10
Kras
Ran
Plk1
Topbp1
Sae1
Romo1
Rac1
Mtor
Erbb3
D.
Genes required in stem cell conditions (3D)
Rpia
Wnt1
Lss
Chek1
Lipt2
Idi1
Sox4
Foxo1
Hoxa7
Smo
E.
Network map identifying programs involved in pancreatic cancer
Cell migration/ Axon guidance
Cell matrix interactions
Cytokine signaling/ Immune pathways
Cell adhesion/ Tight junction
Developmental pathways/ Proteasome
Lipid metabolism/ Nuclear receptor pathway
Pluripotency/ Stem Cells
Cel
Cpb1
Pnlip
Cela3b
Clps
Gm10334
Igfals
Ctrb1
Mmp8
Gzma
Mmp2
1810009J06Rik
Edn1
F2rl1
Gng2
Smo
Rac2
Prkcb
Rhov
Rhod
Grin1
Rhoh
Rac3
Llgl2
Jam3
Igsf5
Prkcz
Pard6b
F11r
Pard3
Dlg5
Itgax
Il17ra
Il17rc
Ccl2
Itgam
Il7r
Tlr2
Tgfb1
Ccl5
Cxcl1
Mmp9
Cxcl10
Il2ra
Pik3r5
Snai1
Esr1
Egfr
Fn1
Il6
Cdh1
Pik3cd
Hgf
Csf2
Il1b
Cldn9
Tjp1
Cldn8
Cldn6
Cldn7
Cldn2
Cldn18
Cldn3
Crb3
Cldn23
Cldn4
Rorc
Psmb8
Prkaa2
Shh
Gli1
Wnt5a
Lef1
Mef2c
Foxa2
Arntl2
Wnt2
Yap1
Wt1
Wnt4
Sox9
Wnt7b
Tead3
Ihh
Tead1
Tle6
Wnt7a
Sox7
Dhh
Wnt16
Tead4
Sox13
Sox4
Sox17
Log2 fold change
-5
0
5

Hijacked immuno-regulatory programs as direct regulators of pancreatic cancer cells

Ultimately, the power of such a map is the ability to identify and understand key new functional dependencies. Thus, we used the network map as a framework to select an integrated gene set based on the transcriptomic, epigenomic, and CRISPR analysis (Table 2.3). Selected genes were subsequently targeted via viral short hairpin RNA (shRNA) delivery into *KP$^{f/f}$C* cells and the impact on pancreatic cancer propagation assessed by sphere assays *in vitro* or tracking tumor growth *in vivo*. Although many genes within the pluripotency and development core program were known to be important in pancreatic cancer (e.g., Wnt, Hedgehog, and Hippo pathways), others, such as *Onecut3* and *Tudor3*, genes previously implicated in motor neuron development or in stress response, presented new opportunities for discovery and emerged as signals essential for pancreatic cancer stem cell growth (Figure 2.4 A and Figure 2.S4 A; Table 2.4). Further, novel metabolic factors, such as *Sptssb*, a key contributor to sphingolipid metabolism[24], and *Lpin2*, an enzyme involved in generation of pro-inflammatory very-low-density lipoproteins[25], were found to be critical stem cell dependencies, implicating lipid metabolism as a key point of control in pancreatic cancer (Figure 2.4 B; Table 2.4). This analysis also identified new gene families in pancreatic cancer: thus within the adhesion and cell matrix core program (Figure 2.4C-J and Figure 2.S4 B), several members of the multiple epidermal growth factor (EGF) repeat (MEGF) subfamily of orphan adhesion G-protein-coupled receptors (GPCRs) (8 of 12) were preferentially expressed in stem cells (Figure 2.4 E). Among this set, inhibition of *Celsr1*, *Celsr2* (Figure 2.S4.C,D), and *Pear1* or *Jedi* (Figure 2.S4 E) triggered apoptosis, depleted Msi+ stem cells, and potently blocked cancer propagation *in vitro* and *in vivo* (Figure 2.4 G-J and Figure 2.S4 F-J; Table 2.4). These pathways will likely be important to explore further, especially because GPCRs can frequently serve as effective drug targets.

An unexpected discovery from this map was the identification of immune pathways and

cytokine signaling as a core program. In line with this, retrospective analysis of the RNA-seq and ChIP-seq analysis revealed that multiple immuno-regulatory cytokine receptors and their ligands were expressed in stem and non-stem tumor epithelial cells (Figure 2.S4 K). This was of particular interest because many genes associated with this program, such as interleukin-10 (*Il10*), *Il34*, and *Csf1r*, have been previously studied in context of the tumor microenvironment but have not been reported to be expressed by, or to functionally impact, pancreatic epithelial cells directly. Single-cell RNA-seq analysis of $KP^{R172H/+}C$ tumor cells (Figure 2.1 K, Figure 2.4 K, and Figure 2.S4 L) confirmed the presence of *Il10rb*, *Il34*, and *Csf1r* in epithelial tumor cells (Figure 2.4 L), as well as in Msi2+ cancer stem cells (Figure 2.S4 M). Consistent with expression in stem cells, inhibition of *Il10rb* and *Csf1r* led to a marked loss of sphere-forming capacity and reduced stem cells (Figure 2.4 M,N and Figure 2.S4 N,O) *in vitro* and impaired tumor growth and propagation *in vivo* (Figure 2.4 O-Q and Figure 2.S4 P,Q). The activity of IL-10Rβ and CSF1R may, at least in part, be ligand dependent, as their ligands were both expressed in epithelial cells (Figure 2.4 R), and the impact of ligand and receptor inhibition mirrored each other (Figure 2.4 R). Collectively, these findings demonstrate an orthogonal co-option of inflammatory mediators by pancreatic cancer stem cells and suggest that agents that modulate cytokine networks may directly impact pancreatic cancer propagation.

Figure 2.4. Identification of novel pathway dependencies of pancreatic cancer stem cells.
(A–D) Genes from developmental processes (A), lipid metabolism (B), and cell adhesion, motility, and matrix components (C and D) were inhibited via shRNA in *KP$^{f/f}$C* cells and sphere or flank tumor growth assessed. Sphere, n = 3–6; flank transplant, n = 4.
(E–I) Relative RNA expression of MEGF family and related (*Celsr1) genes in KP$^{f/f}$C stem and non-stem cells (E). Red, over-represented; blue, under-represented; color denotes fold change from median values. Impact of inhibiting Celsr1, Celsr2, and Pear1 on KP$^{f/f}$C sphere formation (F) and flank transplants (G–I) is shown. Sphere, n = 3–6; flank transplant, n = 4.
Figure 2.4. Identification of novel pathway dependencies of pancreatic cancer stem cells, Continued.
(J) Impact of shRNA-mediated inhibition of Pear1 in human FG cells on colony formation (n = 3) and flank tumor propagation assessed (n = 4).
(K and L) Single-cell sequencing of *KP$^{R172H/+}$C* tumors (K) and tumor cells expressing IL-10Rβ, IL-34, and Csf1R (L). CAF (red); EMT (olive green); Endo (green); ETC (blue); TAM (magenta).
(M) Impact of shRNA-mediated inhibition of IL-10rβ and Csf1R on sphere formation of *KP$^{f/f}$C* cells, n = 3–6.
(N) Impact of shRNA-mediated inhibition of IL-10rβ and Csf1R on stem content (*Msi2-GFP*+) of *KP$^{f/f}$C* cells; assessed in 3D culture, n = 3.
(O and P) Impact of shRNA-mediated inhibition of IL-10rβ (O) and Csf1R (P) on *KP$^{f/f}$C* flank transplant growth, n = 4.
(**Q**) Impact of shRNA-mediated inhibition of IL-10Rβ in human FG cells on sphere formation, n = 3, or flank transplant, n = 4.
(**R**) Impact of shRNA-mediated inhibition of IL-10 and IL-34 on *KP$^{f/f}$C* sphere formation, n = 3. Data represented as mean ± SEM. *$p < 0.05$; **$p < 0.01$; ***$p < 0.001$ by Student's t test or one-way ANOVA

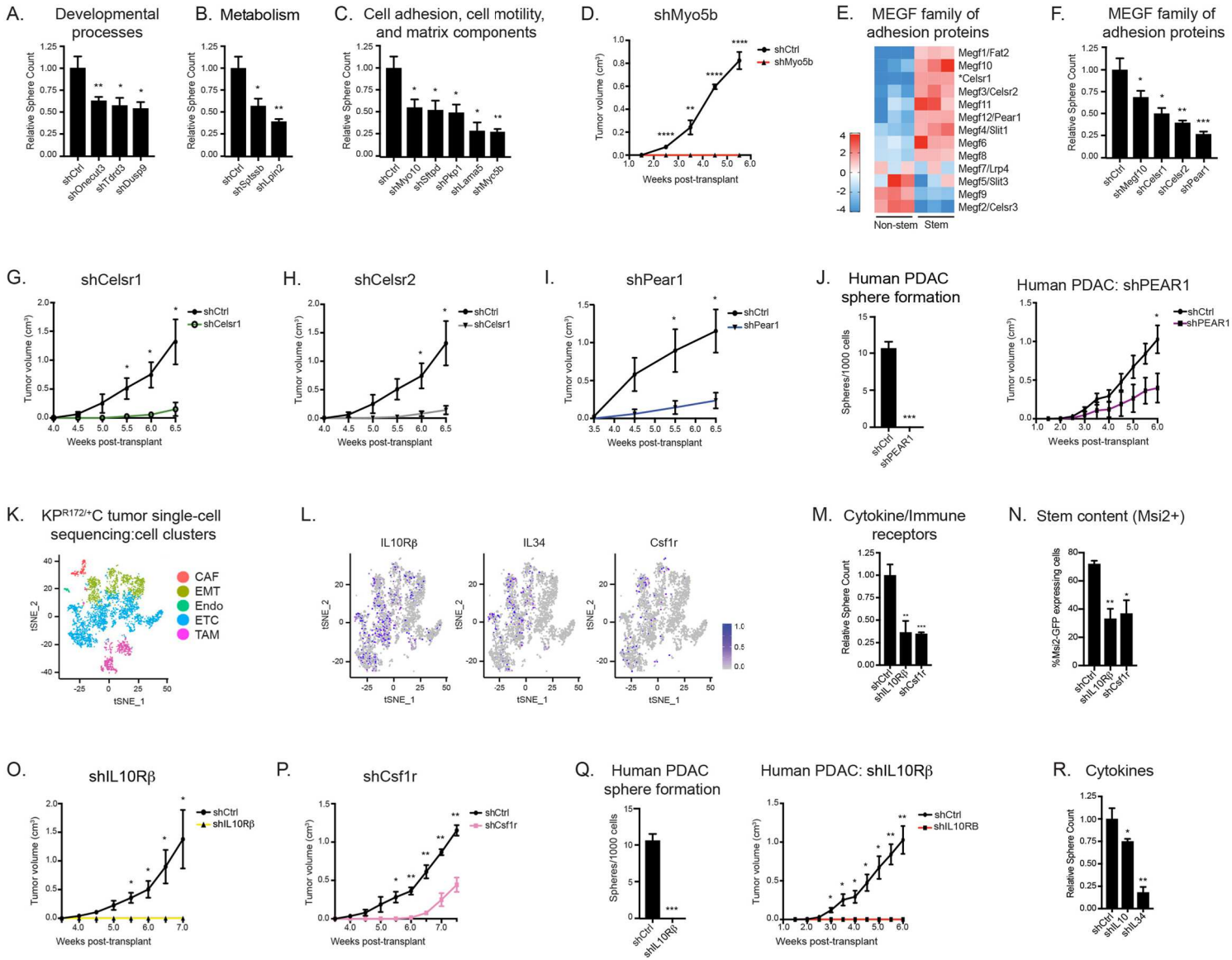
A. Developmental processes
Relative Sphere Count
shCtrl
shOnecut3
shTdrd3
shDusp9
B. Metabolism
shCtrl
shSptssb
shLpin2
C. Cell adhesion, cell motility, and matrix components
shCtrl
shMyo10
shSftpd
shPkp1
shLama5
shMyo5b
D. shMyo5b
Tumor volume (cm³)
Weeks post-transplant
shCtrl
shMyo5b
E. MEGF family of adhesion proteins
Megf1/Fat2
Megf10
*Celsr1
Megf3/Celsr2
Megf11
Megf12/Pear1
Megf4/Slit1
Megf6
Megf8
Megf7/Lrp4
Megf5/Slit3
Megf9
Megf2/Celsr3
Non-stem
Stem
F. MEGF family of adhesion proteins
shCtrl
shMegf10
shCelsr1
shCelsr2
shPear1
G. shCelsr1
shCtrl
shCelsr1
H. shCelsr2
I. shPear1
shPear1
J. Human PDAC sphere formation
Spheres/1000 cells
shPEAR1
Human PDAC: shPEAR1
shPEAR1
K. KP^R172/+C tumor single-cell sequencing:cell clusters
CAF
EMT
Endo
ETC
TAM
tSNE_1
tSNE_2
L.
IL10Rβ
IL34
Csf1r
M. Cytokine/Immune receptors
shIL10Rβ
shCsf1r
N. Stem content (Msi2+)
%Msi2-GFP expressing cells
O. shIL10Rβ
shIL10Rβ
P. shCsf1r
shCsf1r
Q. Human PDAC sphere formation
Human PDAC: shIL10Rβ
shIL10RB
R. Cytokines
shIL10
shIL34

RORγ, a mediator of T cell fate, is a critical dependency in pancreatic cancer

To understand how the gene networks defined above are controlled, we focused on transcription factors because of their broad role in initiating programs key to cell fate and identity[26]. Of the 53 transcription factors identified within the map, 12 were found to be enriched in stem cells by transcriptomic and epigenetic parameters (Figure 2.S5 A) and included several pro-tumorigenic pioneer factors, such as *Sox9*[27] and *Foxa2*[28]. Among transcription factors with no known role in pancreatic cancer (*Arntl2, Nr1d1,* and *Rorc*), only RORγ was actionable in the near term, with clinical-grade antagonists currently available (Table 2.5)[29]. Motif enrichment analysis identified RORγ sites as preferentially enriched in chromatin regions uniquely open in stem cells (Figure 2.S5 B) and in open chromatin regions that corresponded with enriched gene expression in stem cells (Figure 2.S5 B). These findings were consistent with RORγ having a preferential role in controlling gene expression programs important for defining the stem cell state in pancreatic cancer.

RORγ was an unanticipated dependency, as it is a nuclear hormone receptor that has been predominantly studied in Th17 cell differentiation[11] as well as in metabolism in context of the circadian rhythm[30]; consistent with this, it mapped to both the hijacked cytokine signaling and immune subnetwork and the nuclear receptor and metabolism subnetwork (Figure 2.3 E and Figure 2.S3 D). Although RORγ expression was low in normal murine pancreas (data not shown), it rose dramatically in $KP^{f/f}C$ tumors. Within epithelial tumor cells, RORγ expression was highly enriched in stem cells relative to non-stem cells (Figure 2.5 A, Figure 2.S5 C,D), mapping to individual EpCAM+Msi+ cells in single-cell RNA-seq analysis (Figure 2.S5E). RORγ was also expressed in $KP^{R172H/+}C$ tumor cells (not shown), suggesting it is active across models of pancreatic cancer. Importantly, RORγ expression in mouse models was predictive of expression in human pancreatic cancer: thus, although RORγ expression was low in the normal human pancreas and in pancreatitis, its expression increased significantly in epithelial

tumor cells with disease progression (Figure 2.4B,C and Figure 2.S5 F). Interestingly, RORγ levels decreased with inhibition of IL-1R signaling, suggesting that the upstream regulators of RORγ in pancreatic cancer and in Th17 cells may be shared (Figure 2.S5 G). Functionally, shRNA-mediated knockdown (Figure 2.S5 H) confirmed the role of RORγ identified by the genetic CRISPR-based screen, as it decreased stem cell sphere formation in both $KP^{R172H/+}C$ and $KP^{f/f}C$ cells (Figure 2.5 D,E). At a cellular level, RORγ inhibition led to increased cell death (Figure 2.S5 I), decreased proliferation (Figure 2.S5 I), and an ultimate depletion of Msi+ stem cells (Figure 2.5 F). Importantly, tumor cells lacking RORγ showed a striking defect in tumor initiation and propagation *in vivo*, with an 11-fold reduction in final tumor volume (Figure 2.5G and Figure 2.S5 J). Finally, analysis of $KP^{f/f}C$ mice crossed to either RORγ-null[11] or wild-type controls revealed that targeted genetic deletion of RORγ can trigger an overall decrease in tumor burden; this ranged from reduced tumor weight or cellularity to the presence of more normal and benign PanIN lesions and reduced areas of adenocarcinoma in the pancreata (Figure 2.5 H, I).

To define the transcriptional programs RORγ controls in pancreatic cancer cells, we used a combination of ChIP-seq and RNA-seq and found that RORγ knockdown led to extensive changes in transcriptional programs key to driving cancer growth: this included stem cell signals, such as Wnt, BMP, and Fox (Figure 2.5 J), and pro-tumorigenic signals, such as *Hmga2* (Figure 2.5 K). Further, 28% of stem cell super-enhancer-linked genes were downregulated in cells lacking RORγ (Figure 2.5 L). Consistent with this, ChIP-seq analysis of active chromatin regions identified RORγ binding sites as disproportionately present in stem cell super-enhancers compared to other transcription factors, such as CBFB, or even the pioneer factor SOX9 (Figure 2.5 M). Additional super-enhancer-linked stem cell genes regulated by RORγ included *Msi2*, *Klf7*, and *Ehf* (Figure 2.5 N,O), potent oncogenic signals that can control cell fate. Mechanistically, loss of RORγ did not markedly impact the stem cell

super-enhancer landscape in two independent *KP$^{f/f}$C*-derived lines (Figure 2.S5 K-M), suggesting that it may instead bind a pre-existing landscape to preferentially impact transcriptional changes. These data collectively suggest that RORγ is an upstream regulator of a powerful super-enhancer-linked oncogenic network in pancreatic cancer stem cells.

Figure 2.5. The immuno-regulatory gene RORγ Is a critical dependency of pancreatic cancer
(A) *Rorc* expression in stem and non-stem REM2-*KP$^{f/f}$C* tumor cells; representative of three biological replicates.
(B) Representative images of RORγ expression in normal adjacent human pancreas (left), PanINs (middle), and PDAC (right). RORγ (green), E-cadherin (red), DAPI (blue), scale bars represent 50 μm.
(C) Frequency of RORγ+ cells within E-cadherin+ epithelial fraction in patient samples quantified by immunofluorescence; Normal adjacent, n = 3; pancreatitis, n = 8; PanIN 1, n = 10; PanIN 2, n = 6; PDAC, n = 8.
(D and E) Impact of shRNA-mediated RORγ inhibition on 3D growth of *KP$^{R172H/+}$C* (D) and *KP$^{f/f}$C* (E) cells, n = 3 per shRNA.
(F) Impact of shRNA-mediated RORγ inhibition on *Msi2-GFP* stem cell content in *KP$^{f/f}$C* cells in 3D culture, n = 3.
(G) Impact of shRNA-mediated RORγ inhibition on flank tumor growth of *KP$^{f/f}$C* cells, n = 4.
(H and I) Reduced tumor burden in *Rorc$^{-/-}$KP$^{f/f}$C* mice. Age-matched wild-type (WT) *KP$^{f/f}$C* and *Rorc$^{-/-}$KP$^{f/f}$C* mice displayed reduced tumor cell number (H) and reduced adenocarcinoma content (I); low-grade PanIN indicated with red arrow, PDAC indicated with black arrow, scale bars represent 100 μm; n = 3 mice from 8–10 weeks of age; representative plots and images from matched mice are displayed.
(J and K) Relative RNA expression of stem cell programs (J) and pro-tumorigenic factors (K) in *KP$^{f/f}$C* cells transduced with shCtrl or shRorc. Red, over-represented; blue, under-represented; color denotes fold change.
(L) Venn diagram of genes downregulated with RORγ loss ($q < 0.05$, purple). Stem-specific super-enhancer-associated genes (green) and genes associated with H3K27ac peaks with RORγ consensus binding sites (orange) are shown.
(M) Number of RORγ, CBFB, and Sox9 binding sites found in stem cell super-enhancers relative to random genomic background of equivalent base-pair coverage ($p < 0.05$).
(N) Relative RNA expression of super-enhancer-associated oncogenes in *KP$^{f/f}$C* cells transduced with shCtrl or shRorc. Red, over-represented; blue, under-represented; color denotes fold change from median values.
(O) H3K27ac ChIP-seq reads for genes marked by stem cell super-enhancers and downregulated in RORγ-depleted *KP$^{f/f}$C* cells.
Data represented as mean ± SEM. $^{*}p < 0.05$; $^{**}p < 0.01$; $^{***}p < 0.001$ by Student's t test or one-way ANOVA.

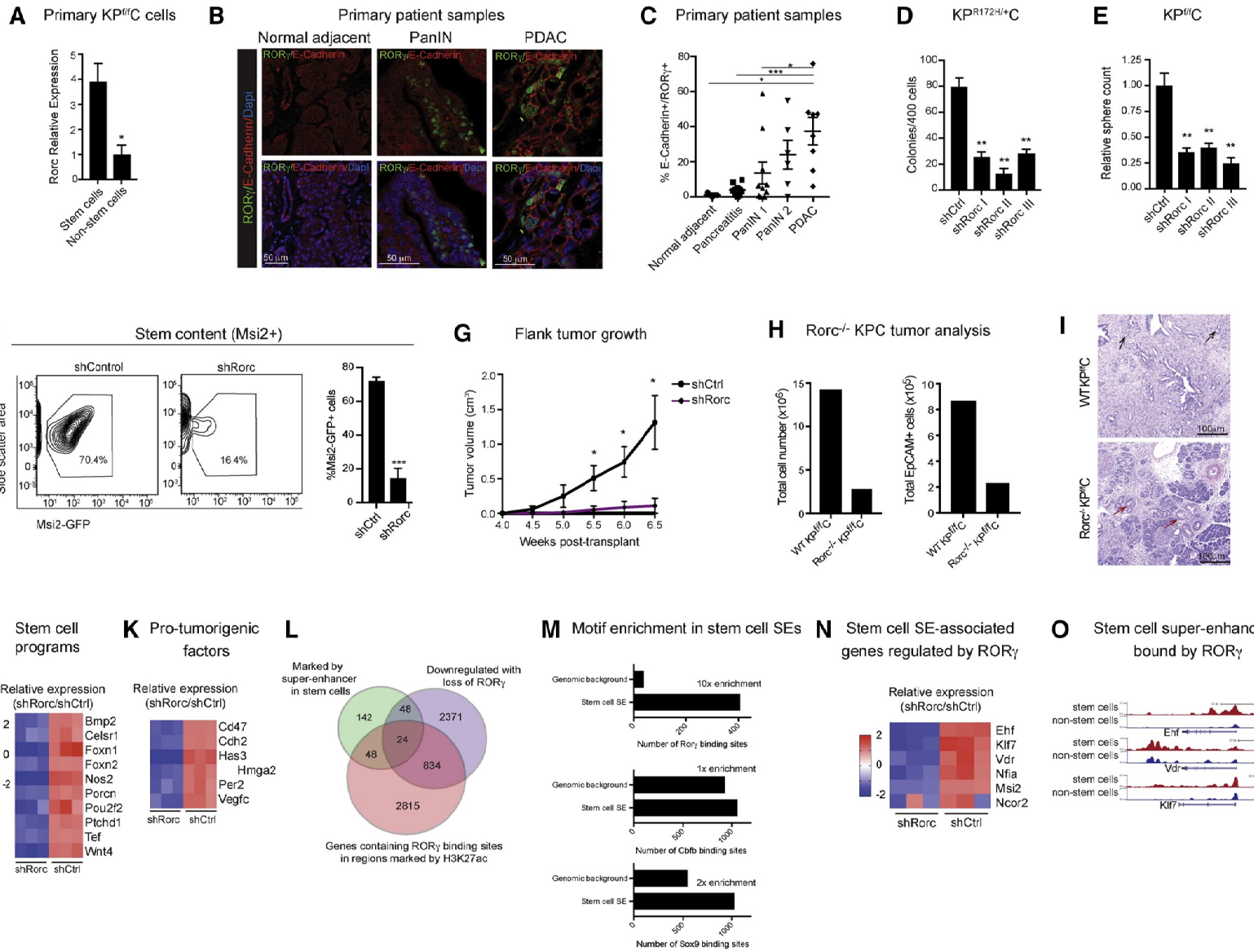
A
Primary KP^f/fC cells
Rorc Relative Expression
Stem cells
Non-stem cells
B
Primary patient samples
Normal adjacent
PanIN
PDAC
RORγ/E-Cadherin/Dapi
50 μm
C
Primary patient samples
% E-Cadherin+/RORγ+
Normal adjacent
Pancreatitis
PanIN 1
PanIN 2
PDAC
D
KP^R172H/+C
Colonies/400 cells
shCtrl
shRorc I
shRorc II
shRorc III
E
KP^f/fC
Relative sphere count
shCtrl
shRorc I
shRorc II
shRorc III
F
Stem content (Msi2+)
shControl
shRorc
Side scatter area
Msi2-GFP
70.4%
16.4%
%Msi2-GFP+ cells
shCtrl
shRorc
G
Flank tumor growth
Tumor volume (cm³)
Weeks post-transplant
shCtrl
shRorc
H
Rorc^-/- KPC tumor analysis
Total cell number (x10^6)
Total EpCAM+ cells (x10^6)
WT KP^f/fC
Rorc^-/- KP^f/fC
I
WT KP^f/fC
Rorc^-/- KP^f/fC
100μm
J
Stem cell programs
Relative expression (shRorc/shCtrl)
Bmp2
Celsr1
Foxn1
Foxn2
Nos2
Porcn
Pou2f2
Ptchd1
Tef
Wnt4
shRorc
shCtrl
K
Pro-tumorigenic factors
Relative expression (shRorc/shCtrl)
Cd47
Cdh2
Has3
Hmga2
Per2
Vegfc
shRorc
shCtrl
L
Marked by super-enhancer in stem cells
Downregulated with loss of RORγ
142
48
2371
24
48
834
2815
Genes containing RORγ binding sites in regions marked by H3K27ac
M
Motif enrichment in stem cell SEs
Genomic background
Stem cell SE
10x enrichment
Number of Rorγ binding sites
1x enrichment
Number of Cbfb binding sites
2x enrichment
Number of Sox9 binding sites
N
Stem cell SE-associated genes regulated by RORγ
Relative expression (shRorc/shCtrl)
Ehf
Klf7
Vdr
Nfia
Msi2
Ncor2
shRorc
shCtrl
O
Stem cell super-enhancers bound by RORγ
stem cells
non-stem cells
Ehf
Vdr
Klf7

The finding that RORγ is a key dependency in pancreatic cancer was particularly exciting, as multiple inhibitors have been developed to target this pathway in autoimmune disease[31]. Pharmacologic blockade of RORγ using the inverse agonist SR2211[32] decreased sphere and organoid formation in both *KP$^{f/f}$C* and *KP$^{R172H/+}$C* cells (Figure 2.6 A-D). To assess the impact of the inhibitor *in vivo*, SR2211 was delivered, either alone or in combination with gemcitabine, into immunocompetent *KP$^{f/f}$C*-derived, tumor-bearing mice (Figure 2.6 E and Figure 2.S6 A). SR2211 significantly reduced tumor growth as a single agent (Figure 2.6 F,G); further, although gemcitabine alone had no impact on the stem cell burden, SR2211 triggered a 3-fold depletion in CD133+ and Msi+ cells and an 11-fold depletion of CD133+ and 6-fold depletion of Msi2+ cells in combination with gemcitabine (Figure 2.6 H,I). This suggests the exciting possibility that SR2211 can eradicate chemotherapy-resistant cells (Figure 2.6 H,I). Finally, to assess any impact on survival, we delivered the RORγ inhibitor into autochthonous, tumor-bearing *KP$^{f/f}$C* mice; although none of the vehicle-treated mice were alive 25 days after the initiation of treatment, 75% of mice that received SR2211 were still alive at this point and 50% were alive even at 45 days after treatment initiation. SR2211 not only doubled median survival—18 days for vehicle-treated mice and 38.5 days for SR2211-treated mice—but also led to a 6-fold reduction in the risk of death (Figure 2.6 J; hazard ratio [HR] = 0.16). HMGA2, identified originally from the RNA-seq as a downstream target of RORγ, was downregulated in pancreatic epithelial cells following SR2211 delivery *in vivo*, suggesting effective target engagement at midpoint during treatment, although this was less apparent in end-stage tumors and may explain why treated mice ultimately succumbed to disease (Figure 2.S6 B,C). Collectively, these data show that pancreatic cancer stem cells are profoundly dependent on RORγ and suggest that its inhibition may lead to a significant improvement in disease control. Further, the fact that its impact on tumor burden was amplified several fold when combined with gemcitabine suggests that it may synergize with chemotherapy to more effectively target

tumors that remain refractory to therapy.

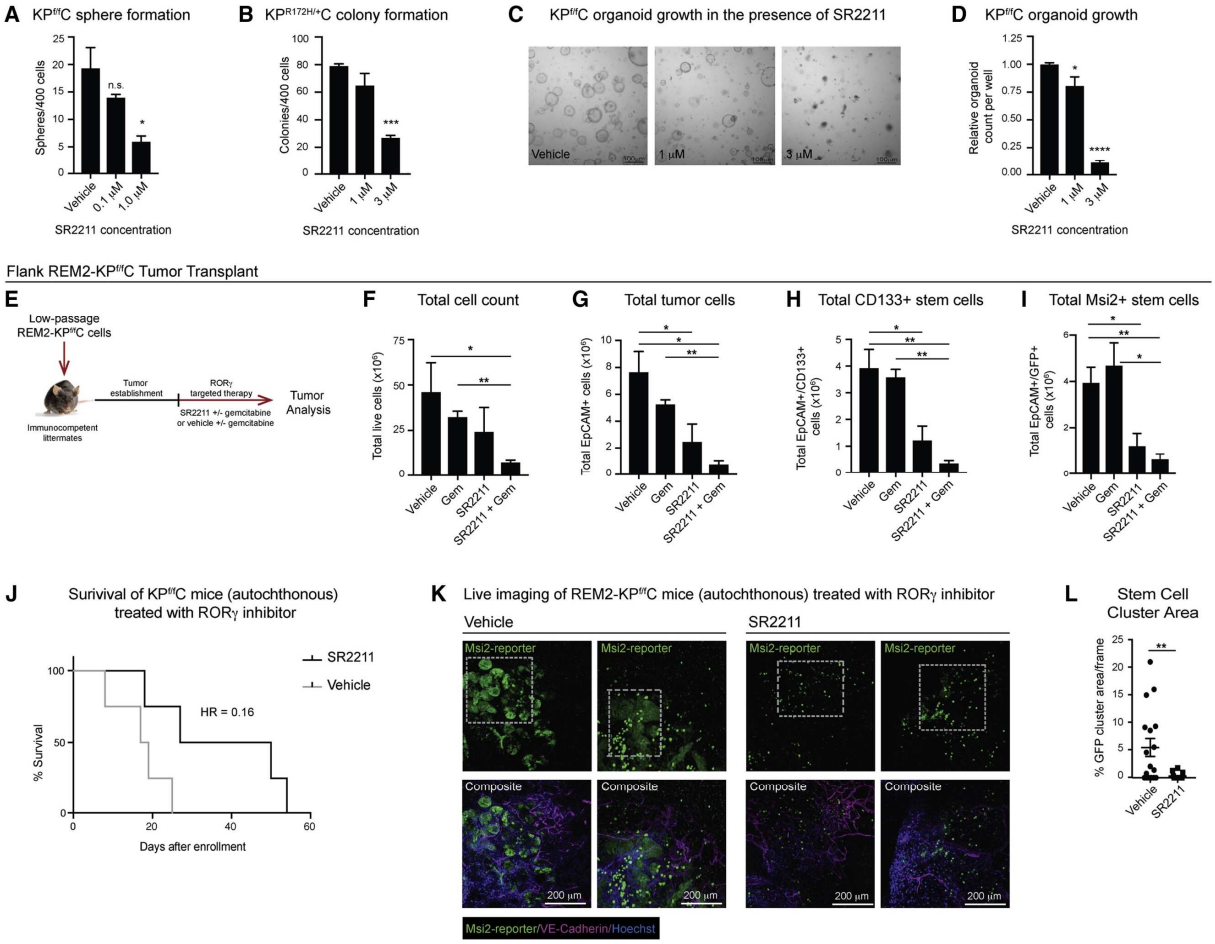

Figure 2.6. Pharmacologic targeting of RORγ impairs progression and improves survival in mouse models of pancreatic cancer.
(A and B) 3D growth of *KP$^{f/f}$C* cells (A) and *KP$^{R172H/+}$C* cells (B) in the presence of the SR2211 or vehicle (n = 3).
(C and D) *KP$^{f/f}$C* organoid formation in the presence of SR2211 or vehicle. Representative images I and quantification (D) are shown; scale bars represent 100 μm.
(E–I) Analysis of flank *KP$^{f/f}$C* tumor-bearing mice treated with SR2211 or vehicle for 3 weeks. Strategy I is shown. Total live cells (F), total EpCAM+ tumor cells (G), total EpCAM+/CD133+ stem cells (H), and total EpCAM+/Msi2+ stem cells (I) are shown (n = 4 vehicle; n = 2 vehicle + gemcitabine; n = 4 SR2211; n = 3 SR2211+gemcitabine).
(J) Survival of *KP$^{f/f}$C* mice treated daily with vehicle (gray) or SR2211 (black; p = 0.051; hazard ratio = 0.16; median survival: vehicle = 18 days, SR2211 = 38.5 days).
(K) Live imaging of REM2-*KP$^{f/f}$C* mice treated with vehicle or SR2211 for 8 days (n = 2). Msi2-reporter (green), VE-cadherin (magenta), and Hoechst (blue) are shown; Msi2-reporter+ stem cells, gray box; scale bars represent 200 μm.
(L) Quantification of stem cell clusters from REM2-*KP$^{f/f}$C* live imaging (n = 2; 6–10 frames analyzed per mouse).
Data represented as mean ± SEM. $^{*}p < 0.05$, $^{**}p < 0.01$, $^{***}p < 0.001$ by Student's t test or one-way ANOVA.

To visualize whether RORγ blockade impacts tumor progression by targeting stem cells, SR2211 was delivered in REM2-*KP$^{f/f}$C* mice with late-stage autochthonous tumors and responses tracked via live imaging. In vehicle-treated mice, large stem cell clusters could be readily identified throughout the tumor based on GFP expression driven by the Msi reporter (Figure 2.6 K,L). SR2211 led to a marked depletion of the majority of large stem cell clusters within 1 week of treatment (Figure 2.6 K,L), with no increased necrosis observed in surrounding tissues. This unique spatio-temporal analysis suggests that stem cell depletion is an early consequence of RORγ blockade and highlights the REM2-*KP$^{f/f}$C* model as an effective platform to assess the impact of new agents on therapy-resistant cells.

Because treatment with the inhibitor in immunocompetent mice or in patients *in vivo* could have an impact on both cancer cells and immune cells, we tested the effect of SR2211 in the context of an immunocompromised environment. SR2211 significantly impacted growth of *KP$^{f/f}$C* tumors in an immunodeficient background (Figure 2.7 A,B), suggesting that inflammatory T cells were not necessary for its effect. Further, in chimeric mice where wild-type tumors were transplanted into either wild-type or RORγ-null recipients, tumors grew equivalently (Figure 2.7 C,D), suggesting that loss of RORγ in only the immune cells (such as Th17) and microenvironment has no detectable impact on tumor growth. Finally, we delivered SR2211 into these chimeric mice to test whether RORγ antagonists may influence tumor growth via Th17 cells and found that the impact of SR2211 on tumor growth, cellularity, and stem cell content was equivalent in chimeric wild-type and RORγ-recipient mice (Figure 2.7 E-L). These data collectively suggest that most of the observed effect of RORγ inhibition is tumor cell specific and not indirect through an environmental and/or Th17 dependence on RORγ (Figure 2.7 E-L and Figure 2.S7 A,B). Consistent with a primarily epithelial cell impact, we did not detect any significant impact of SR2211 on non-neoplastic cells, such as CD45+, CD31+, myeloid derived suppressor cell (MDSC), macrophage, dendritic, or T cells within the

tumors at early time points (Figure 2.S7C-M). These data do not preclude the possibility that RORγ inhibitors may act on both tumor cells and immune cells in the human disease if more inflammatory T cells were present.

To further explore the functional relevance of RORγ to human pancreatic cancer, RORγ was inhibited through both genetic and through pharmacologic means in human PDAC cells. CRISPR-based disruption of RORγ led to an ~3- to 9-fold loss of colony formation in human fast growing (FG) PDAC cells (Figure 2.8 A). To test whether RORγ inhibition could block human tumor growth *in vivo*, we transplanted human PDAC cells into the flanks of immunocompromised mice and allowed tumors to become palpable before beginning treatment (Figure 2.8 B). Compared to vehicle treatment, SR2211 delivery was highly effective and tumor growth was essentially extinguished with a nearly 6-fold reduction in growth in mice receiving SR2211 (Figure 2.8 C). Primary patient tumor cells were also remarkably sensitive to RORγ blockade, with an ~300-fold reduction in total organoid volume following SR2211 treatment (Figure 2.8 D-F) and a severe reduction of *in vivo* tumor growth in primary patient-derived xenografts (Figure 2.8 G). Mechanistically, RNA-seq and gene ontology (GO) analysis of human FG and $KP^{f/f}C$ cells identified a set of cytokines and growth factors as key common RORγ-driven programs: thus, semaphorin 3c, its receptor neuropilin2, oncostatin M, and angiopoietin, all highly pro-tumorigenic factors harboring RORγ-binding motifs, were shared targets of RORγ in mouse and human pancreatic cancer (Figure 2.S8 A-D). The dependence of human pancreatic tumors on RORγ function are exciting in light of the fact that genomic amplification of RORC occurs in ~12% of pancreatic cancer patients (Figure 2.8 H). This raises the possibility that RORC status could serve as a biomarker for patients who may be particularly responsive to RORC inhibition.

Lastly, to determine whether expression of RORγ could serve as a prognostic for specific clinicopathologic features, we performed RORγ immunohistochemistry on tissue

microarrays from a clinically annotated retrospective cohort of 116 PDAC patients (Table 2.6). For 69 patients, matched pancreatic intraepithelial neoplasia (PanIN) lesions were available. RORγ protein was detectable (cytoplasmic expression only denoted as low or cytoplasmic and nuclear expression denoted as high; Figure 2.8 I) in 113 PDAC cases and 55 PanIN cases, respectively, and absent in 3 PDAC cases and 14 PanIN cases, respectively. Compared to cytoplasmic expression, nuclear RORγ expression in PDAC cases was significantly correlated with higher pathological tumor (pT) stages at diagnosis (Figure 2.8 J). In addition, RORγ expression in PanIN lesions was positively correlated with lymphatic vessel invasion (L1; Figure 2.8 K) and lymph node metastasis (pN1 and pN2; Figure 2.8 L) by the invasive carcinoma. These results indicate that RORγ expression in PanIN lesions and nuclear RORγ localization in invasive carcinoma could be useful markers to predict PDAC aggressiveness.

Figure 2.7. RORγ is a direct dependency of pancreatic tumor epithelial cells, Continued.
(A and B) Analysis of flank *KP$^{f/f}$C* tumor-bearing NOD scid gamma (NSG) mice treated with SR2211 or vehicle for 2 weeks. Strategy (A) is shown. Flank tumor growth following treatment with vehicle or SR2211 for 2 weeks (B) is shown. Fold change in tumor volume relative to volume at enrollment is shown (n = 4–6).
(C and D) Strategy I. Growth of *KP$^{f/f}$C* flank tumors in WT or *RORγ$^{-/-}$* recipient mice (D; n = 3–4).
(E–L) Strategy I. Flank tumor growth in WT recipients treated with vehicle or SR2211 for 2 weeks (F) is shown. Flank tumor growth in *RORγ$^{-/-}$* recipients treated with vehicle or SR2211 for 2 weeks (G) is shown. Tumor mass (H), total live cells (I), total EpCAM+ tumor cells (J), total EpCAM+/CD133+ stem cells (K), and total Th17 cells (L) in WT and RORγ$^{-/-}$ recipients are shown (n = 5–7).
Data represented as mean ± SEM. $^{*}p < 0.05$; $^{**}p < 0.01$; $^{***}p < 0.001$ by Student's t test or one-way ANOVA.

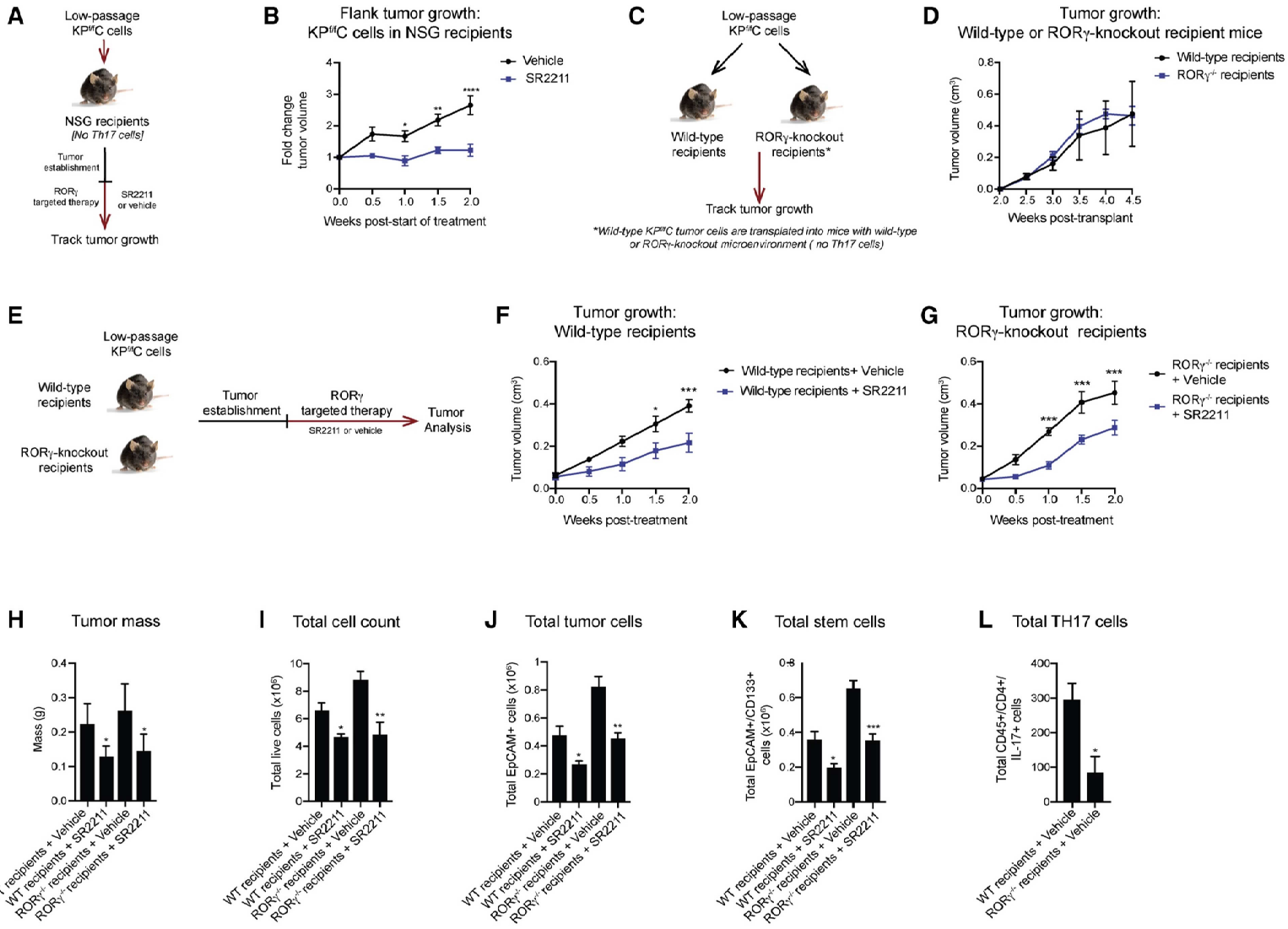
A
Low-passage KP^fl/fl C cells
NSG recipients
(No Th17 cells)
Tumor establishment
RORγ targeted therapy
SR2211 or vehicle
Track tumor growth
B
Flank tumor growth:
KP^fl/fl C cells in NSG recipients
Vehicle
SR2211
Fold change tumor volume
Weeks post-start of treatment
C
Low-passage KP^fl/fl C cells
Wild-type recipients
RORγ-knockout recipients*
Track tumor growth
*Wild-type KP^fl/fl C tumor cells are transplated into mice with wild-type or RORγ-knockout microenvironment (no Th17 cells)
D
Tumor growth:
Wild-type or RORγ-knockout recipient mice
Wild-type recipients
RORγ-/- recipients
Tumor volume (cm3)
Weeks post-transplant
E
Low-passage KP^fl/fl C cells
Wild-type recipients
RORγ-knockout recipients
Tumor establishment
RORγ targeted therapy
SR2211 or vehicle
Tumor Analysis
F
Tumor growth:
Wild-type recipients
Wild-type recipients+ Vehicle
Wild-type recipients + SR2211
Tumor volume (cm3)
Weeks post-treatment
G
Tumor growth:
RORγ-knockout recipients
RORγ-/- recipients + Vehicle
RORγ-/- recipients + SR2211
Tumor volume (cm3)
Weeks post-treatment
H
Tumor mass
Mass (g)
I
Total cell count
Total live cells (x10^6)
J
Total tumor cells
Total EpCAM+ cells (x10^6)
K
Total stem cells
Total EpCAM+/CD133+ cells (x10^6)
L
Total TH17 cells
Total CD45+/CD4+/ IL-17+ cells
WT recipients + Vehicle
WT recipients + SR2211
RORγ-/- recipients + Vehicle
RORγ-/- recipients + SR2211

Figure 2.8. RORγ is required for human pancreatic cancer growth and predicts advanced disease, Continued.
(A) Human FG colony formation after RORC CRISPR knockdown; n = 5.
(B) Representative images of RORγ expression in human FG tumors, RORγ (green), E-cadherin (red), and DAPI (blue). Scale bars represent 50 μm.
I Human FG tumor growth in mice treated with gemcitabine and either vehicle or SR2211 for 2.5 weeks. Tumor volume fold change is relative to volume at enrollment.
(D–F) Primary patient organoid growth in the presence of vehicle or SR2211. Representative images of organoids in Matrigel (D; scale bars represent 100 μm), following recovery from Matrigel (E; scale bars represent 50 μm), and quantification of organoid circumference (F, left) or volume (F, right) are shown.
(G) Growth of primary patient-derived xenografts treated with vehicle or SR2211 for 1.5 weeks; (n = 4).
(H) RORC amplification in tumors of patients diagnosed with various malignancies.
(I–L) Representative TMAs of PDAC and PanINs illustrating scoring for negative, cytoplasmic, and cytoplasmic + nuclear RORγ staining (I). Correlation between RORγ staining and tumor stage (J), lymphatic invasion (K), and lymph node status (L) is shown.
Data represented as mean ± SEM. $^{*}p < 0.05$; $^{**}p < 0.01$; $^{***}p < 0.001$ by Student's t test or one-way ANOVA.

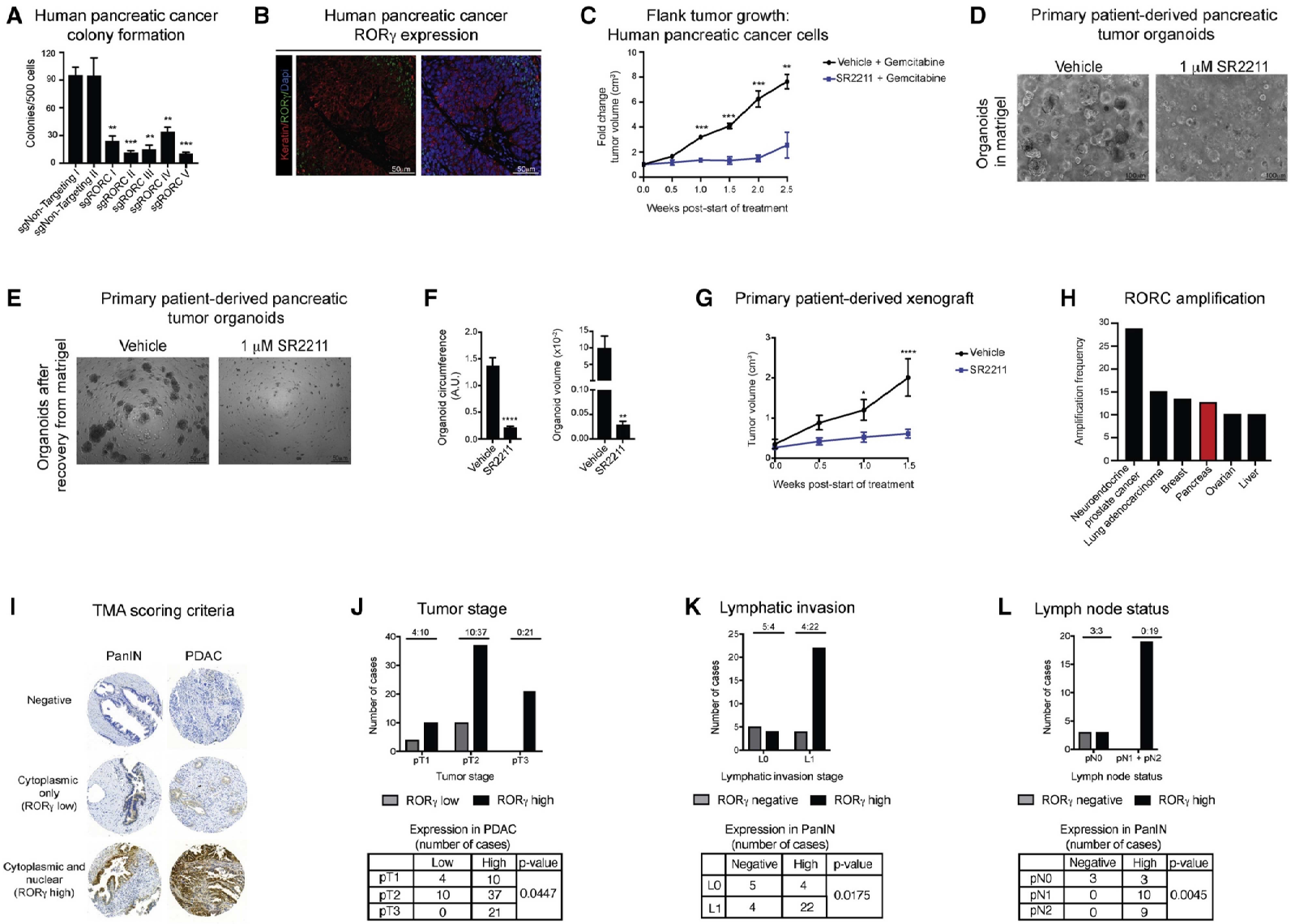

Expression in PDAC (number of cases)

	Low	High	p-value
pT1	4	10	0.0447
pT2	10	37	
pT3	0	21	

Expression in PanIN (number of cases)

	Negative	High	p-value
L0	5	4	0.0175
L1	4	22	

Expression in PanIN (number of cases)

	Negative	High	p-value
pN0	3	3	0.0045
pN1	0	10	
pN2	0	9	

2.4. Discussion

It is an unfortunate truth that the most common outcome for pancreatic cancer patients following a response to cytotoxic therapy is not cure but eventual disease progression and death driven by drug-resistant, stem-cell-enriched populations[8,34]. The work we report here has allowed us to develop a comprehensive molecular map of the core dependencies of pancreatic cancer stem cells by integrating their epigenetic, transcriptomic, and functional genomic landscape. This dataset thus provides a novel resource for understanding therapeutic resistance and relapse and for discovering new vulnerabilities in pancreatic cancer. As an example, the MEGF family of orphan receptors represents a potentially actionable family of adhesion GPCRs, as this class of signaling receptors has been considered druggable in cancer and other diseases[35]. Importantly, our epigenetic analyses revealed a significant relationship between super-enhancer-associated genes and functional dependencies in stem cell conditions; stem-cell-unique, super-enhancer-associated genes were more likely to drop out in the CRISPR screen in stem cell conditions compared to super-enhancer-associated genes in non-stem cells (Figure 2.S8 D). This provides additional evidence for the epigenetic and transcriptomic link to functional dependencies in cancer stem cells and further supports previous findings that super-enhancer-linked genes may be more important for maintaining cell identity and more sensitive to perturbation[20].

From the screens presented here, we identified an unexpected dependence of *KP$^{f/f}$C* stem cells on inflammatory and immune mediators, such as the CSF1R/IL-34 axis and IL-10R signaling. Although these have been previously thought to act primarily on immune cells in the microenvironment[36,37], our data suggest that stem cells may have evolved to co-opt this cytokine-rich milieu, allowing them to resist effective immune-based elimination. These findings also suggest that agents targeting CSF1R, which are under investigation for pancreatic cancer[38], may act not only on the tumor microenvironment but also directly on

pancreatic epithelial cells themselves. Our studies also raise the possibility that therapies designed to activate the immune system to attack tumors may have effects on tumor cells directly: just as we have learned chemotherapy can kill tumor cells but may also impair the immune system, therapies designed to activate the immune system, such as IL-10, may also promote the growth of tumor cells. This dichotomy of action will need to be considered in order to better optimize immunomodulatory treatment strategies.

A major new discovery driven by the development of the network map was the identification of RORγ as a key immuno-regulatory pathway hijacked in pancreatic cancer. This, together with prior work implicating RORγ in prostate cancer models[39], suggests that this pathway may not be restricted to pancreatic cancer but may be more broadly utilized in other epithelial cancers. Interestingly, although cytokines, such as IL-17, IL-21, IL-22, and CSF2, are known targets of RORγ in Th17 cells, none of these were downregulated in *Rorc*-deficient pancreatic tumor cells. The fact that RORγ regulated potent oncogenes marked by super-enhancers in stem cells suggests it may be critical for defining the stem cell state in pancreatic cancer. The basis of this intriguing epithelial-specific activity of RORγ will be an important area for future exploration. In addition, the network of genes impacted by RORγ inhibition included other immune modulators, such as CD47, raising the possibility that it may also mediate interaction with the surrounding niche and immune system cells. Finally, one particularly exciting aspect of this work is the identification of RORγ as a potential therapeutic target in pancreatic cancer. Given that inhibitors of RORγ are currently in phase II trials for autoimmune diseases[29], our findings suggest that repositioning these agents as pancreatic cancer therapies warrants further investigation.

2.5. Methods

Experimental model and subject details

Mice

REM2 (*Msi2*$^{eGFP/+}$) reporter mice were generated as previously described[8]; all of the reporter mice used in experiments were heterozygous for the *Msi2* allele. The LSL-KrasG12D (*Kras*$^{LSL/G12D}$) mouse, B6.129S4-Kras$^{tm4Tyj/J}$ (Stock No: 008179), the p53flox/flox mouse (*Trp53*$^{fl/fl}$) , B6.129P2- Trp53$^{tm1Brn/J}$ (Stock No: 008462), and the RORγ-knockout mouse (Stock No: 007571), were purchased from The Jackson Laboratory. Dr. Chris Wright provided Ptf1a-Cre mice as previously described[40]. LSL-R172H mutant p53 (*Trp53*^{R172H}) mice were provided by Dr. Tyler Jacks as previously described[41] (JAX Stock No: 008183). The mice listed above are immunocompetent, with the exception of RORγ-knockout mice which are known to lack Th17 T cells as described previously[11]; these mice were maintained on antibiotic water (sulfamethoxazole and trimethoprim) when enrolled in flank transplantation and drug studies as outlined below. Immune compromised NOD/SCID (NOD.CB17-Prkdc^{scid}/J, Stock No: 001303) and NSG (NOD.Cg-Prkdc^{scid}IL2rg^{tm1Wji}/SzJ, Stock No: 005557) mice purchased from The Jackson Laboratory. All mice were specific-pathogen free, and bred and maintained in the animal care facilities at the University of California San Diego. Animals had access to food and water *ad libitum*, and were housed in ventilated cages under controlled temperature and humidity with a 12 hour light-dark cycle. All animal experiments were performed according to protocols approved by the University of California San Diego Institutional Animal Care and Use Committee. No sexual dimorphism was noted in all mouse models. Therefore, males and females of each strain were equally used for experimental purposes and both sexes are represented in all datasets. All mice enrolled in experimental studies were treatment-naive and not previously enrolled in any other experimental study.

Both REM2 *KP*$^{f/f}$*C* and *WT-KP*$^{f/f}$*C* mice (*Msi2-GFP*; LSL-Kras$^{G12D/+}$; Trp53$^{f/f}$; Ptf1a-Cre

and LSL-Kras$^{G12D/+,}$; Trp53$^{f/f}$; Ptf1a-Cre respectively) were used for isolation of tumor cells, establishment of primary mouse tumor cell and organoid lines, and autochthonous drug studies as described below. REM2-*KP$^{f/f}$C* and *KP$^{f/f}$C* mice were enrolled in drug studies between 8 to 11 weeks of age, and were used for tumor cell sorting and establishment of cell lines when they reached end-stage disease between 10 and 12 weeks of age. REM2-*KP$^{f/f}$C* mice were used for *in vivo* imaging studies between 9.5-10.5 weeks of age. *KP^{R172H}C* (LSL-Kras$^{G12D/+,}$; Trp53$^{R172h/+}$; Ptf1a-Cre) mice were used for cell sorting and establishment of tumor cell lines when they reached end-stage disease between 16-20 weeks of age. In some studies, *KP$^{f/f}$C*-derived tumor cells were transplanted into the flanks of immunocompetent littermates between 5-8 weeks of age. Littermate recipients (WT or REM2-LSL-Kras$^{G12D/+,}$; Trp53$^{f/f}$ or Trp53$^{f/f}$ mice) do not develop disease or express Cre. NOD/SCID and NSG mice were enrolled in flank transplantation studies between 5 to 8 weeks of age; *KP$^{f/f}$C* derived cell lines and human FG cells were transplanted subcutaneously for tumor propagation studies in NOD/SCID recipients and patient-derived xenografts and *KP$^{f/f}$C* derived cell lines were transplanted subcutaneously in NSG recipients as described in detail below.

Human and mouse pancreatic cancer cell lines

Mouse primary pancreatic cancer cell lines and organoids were established from end-stage, treatment-naive *KP^{R172H}C* and WT- and REM2-*KP$^{f/f}$C* mice as follows: tumors from endpoint mice (10-12 weeks of age for *KP$^{f/f}$C* or 16-20 weeks of age for *KP^{R172H}C* mice) were isolated and dissociated into single cell suspension as described below. Cells were then either plated in 3D sphere or organoid culture conditions detailed below, or plated in 2D in 1x DMEM containing 10% FBS, 1x pen/strep, and 1x non-essential amino acids. At the first passage in 2D, cells were collected and resuspended in HBSS (GIBCO, Life Technologies) containing 2.5% FBS and 2 mM EDTA, then stained with FC block followed by 0.2 µg/10^6 cells anti-

EpCAM APC (eBioscience). EpCAM+ tumor cells were sorted then re-plated for at least one additional passage. To evaluate any cellular contamination and validate the epithelial nature of these lines, cells were analyzed by flow cytometry again at the second passage for markers of blood cells (CD45-PeCy7, eBioscience), endothelial cells (CD31-PE, eBioscience), and fibroblasts (PDGFR-PacBlue, Biolegend). Cell lines were derived from both female and male *KP^{R172H}C* and WT- and REM2-*KP$^{f/f}$C* mice equivalently; both sexes are equally represented in the cell-based studies outlined below. Functional studies were performed using cell lines between passage 2 and passage 6. Human FG cells were originally derived from a PDAC metastasis and have been previously validated and described[42]. Patient-derived xenograft cells and organoids were derived from originally-consented (now deceased) PDAC patients and use was approved by UCSD's IRB; cells were de-identified and therefore no further information on patient status, treatment or otherwise, is available. FG cell lines were cultured in 2D conditions in 1x DMEM (GIBCO, Life Technologies) containing 10% FBS, 1x pen/strep (GIBCO, Life Technologies), and 1x non-essential amino acids (GIBCO, Life Technologies). 3D *in vitro* culture conditions for all cells and organoids are detailed below.

Patient cohort for PDAC tissue microarray

The PDAC patient cohort and corresponding TMAs used for RORγ immunohistochemical staining and analysis have been reported previously[43]. Patient characteristics are detailed in Table 2.6. Briefly, a total of 4 TMAs with 0.6 mm core size was constructed: three TMAs for PDACs, with samples from the tumor center and invasive front (mean number of spots per patient: 10.5, range: 2-27) and one TMA for matching PanINs (mean number of spots per patient: 3.7, range: 1-6). Tumor samples from 116 patients (53 females and 63 males; mean age: 64.1 years, range: 34-84 years) with a diagnosis of PDAC were included. Matched PanIN samples were available for 69 patients. 99 of these patients

received some form of chemotherapy; 14 received radiotherapy. No sexual dimorphism was observed in any of the parameters assessed, including overall survival ($p = 0.227$), disease-free interval ($p = 0.3489$) or RORγ expression in PDAC ($p = 0.9284$) or PanINs ($p = 0.3579$). The creation and use of the TMAs were reviewed and approved by the Ethics Committee at the University of Athens, Greece, and the University of Bern, Switzerland, and included written informed consent from the patients or their living relatives.

Method Details

In vitro and *in vivo* experimental strategies

Tissue dissociation, cell isolation, and FACS analysis

Mouse pancreatic tumors were washed in MEM (GIBCO, Life Technologies) and cut into 1-2 mm pieces immediately following resection. Tumor pieces were collected into a 50 mL Falcon tube containing 10 mL Gey's balanced salt solution (Sigma), 5 mg Collagenase P (Roche), 2 mg Pronase (Roche), and 0.2 µg DNase I (Roche). Samples were incubated for 20 minutes at 37°C, then pipetted up and down 10 times and returned to 37°C. After 15 more minutes, samples were pipetted up and down 5 times, then passaged through a 100 µm nylon mesh (Corning). Red blood cells were lysed using RBC Lysis Buffer (eBioscience) and the remaining tumor cells were washed, then resuspended in HBSS (GIBCO, Life Technologies) containing 2.5% FBS and 2 mM EDTA for staining, FACS analysis, and cell sorting. Analysis and cell sorting were carried out on a FACSAria III machine (Becton Dickinson), and data were analyzed with FlowJo software (Tree Star). For analysis of cell surface markers by flow cytometry, $5x10^5$ cells were resuspended in HBSS containing 2.5% FBS and 2 mM EDTA, then stained with FC block followed by 0.5 µL of each antibody. For intracellular staining, cells were fixed and permeabilized using the BrdU flow cytometry kit (BD Biosciences); Annexin V apoptosis kit was used for analysis of apoptotic cells (eBioscience). The following rat

antibodies were used: anti-mouse EpCAM-APC (eBioscience), anti-mouse CD133-PE (eBioscience), anti-mouse CD45-PE and PE/Cy7 (eBioscience), anti-mouse CD31-PE (BD Bioscience), anti-mouse Gr-1-FITC (eBioscience), anti-mouse F4/80-PE (Invitrogen), anti-mouse CD11b-APC (Affymetrix), anti-mouse CD11c-BV421 (Biolegend), anti-mouse CD4-FITC (eBioscience) and CD4-Pacific blue (Bioglegend), anti-mouse CD8-PE (eBioscience), anti-mouse IL-17-APC (Biolegend), anti-mouse BrdU-APC (BD Biosciences), and anti-mouse Annexin-V-APC (eBioscience). Propidium-iodide (Life Technologies) was used to stain for dead cells.

In vitro growth assays

We describe below the distinct growth assays used for pancreatic cancer cells. Colony formation is an assay in Matrigel (thus adherent/semi-adherent conditions), while tumorsphere formation is an assay in non-adherent conditions. We have found that cell types from different sources grow better in different conditions. For example, the murine $KP^{R172H/+}C$ and the human FG cell lines grow much better in Matrigel, while $KP^{f/f}C$ cell lines often grow well in non-adherent, sphere conditions (though they can also grow in Matrigel).

Pancreatic tumorsphere formation assay

Pancreatic tumorsphere formation assays were performed and modified from Rovira et al.[21]. Briefly, low-passage (< 6 passages) WT or REM2-$KP^{f/f}C$ cell lines were infected with lentiviral particles containing shRNAs; positively infected (red) cells were sorted 72 hours after transduction. 100-300 infected cells were suspended in tumorsphere media: 100 µL DMEM F-12 (GIBCO, Life Technologies) containing 1x B-27 supplement (GIBCO, Life Technologies), 3% FBS, 100 µM B-mercaptoethanol (GIBCO, Life Technologies), 1x non-essential amino acids (GIBCO, Life Technologies), 1x N2 supplement (GIBCO, Life Technologies), 20 ng/ml

EGF (GIBCO, Life Technologies), 20 ng/ml $bFGF_2$ (GIBCO, Life Technologies), and 10 ng/ml ESGRO mLIF (Thermo Fisher). Cells in media were plated in 96-well ultra-low adhesion culture plates (Costar) and incubated at 37°C for 7 days. *KP$^{f/f}$C in vitro* tumorsphere formation studies were conducted at a minimum of n = 3 independent wells per cell line across two independent shRNA of n = 3 wells; however, the majority of these experiments were additionally completed in > 1 independently-derived cell lines n = 3, at n = 3 wells per shRNA. shRNA sequences and average knockdown efficiencies are available in Table 2.7.

Matrigel colony assay

For FG and *KP$^{R172H/+}$C* cells, 300-500 cells were resuspended in 50 µL tumorsphere media as described below, then mixed with Matrigel (BD Biosciences, 354230) at a 1:1 ratio and plated in 96-well ultra-low adhesion culture plates (Costar). After incubation at 37°C for 5 min, 50 µL tumorsphere media was placed over the Matrigel layer. Colonies were counted 7 days later. For RORγ inhibitor studies, SR2211 or vehicle was added to cells in tumorsphere media, then mixed 1:1 with Matrigel and plated. SR2211 or vehicle was also added to the media that was placed over the solidified Matrigel layer. For FG colony formation, n = 5 independent wells across 5 independent CRISPR sgRNA and two independent non-targeting gRNA. *KP$^{R172H/+}$C* cells were plated at n = 3 wells per shRNA from one cell line.

Organoid culture assays

Tumors from 10-12 week old end stage REM2-*KP$^{f/f}$C* mice were harvested and dissociated into a single cell suspension as described above. Tumor cells were stained with FC block then 0.2 µg/10^6 cells anti-EpCAM APC (eBioscience). Msi2+/EpCAM+ (stem) and Msi2-/EpCAM+ (non-stem) cells were sorted, resuspended in 20 µL Matrigel (BD Biosciences, 354230). For limiting dilution assay, single cells were resuspended in matrigel at the indicated

numbers from 20,000 to 10 cells/20uL and were plated as a dome in a pre-warmed 48 well plate. After incubation at 37°C for 5 min, domes were covered with 300 µL PancreaCult Organoid Growth Media (StemCell Technologies, Inc.). Organoids were imaged and quantified 6 days later. Limiting dilution analysis for stemness assessment was performed using web based- extreme limiting dilution analysis (ELDA) software[44]. Msi2+/EpCAM+ (stem) and Msi2-/EpCAM+ (non-stem) organoids were derived from n = 3 independent mice and plated at the indicated cell numbers.

Organoids from REM2-*KP$^{f/f}$C* were passaged at ~1:2 as previously described[14]. Briefly, organoids were isolated using Cell Recovery Solution (Corning 354253), then dissociated using Accumax Cell Dissociation Solution (Innovative Cell Technologies AM105), and plated in 20 µL matrigel (BD Biosciences, 354230) domes on a pre-warmed 48-well plate. After incubation at 37°C for 5 min, domes were covered with 300 µL PancreaCult Organoid Growth Media (StemCell Technologies, Inc.). SR2211 (Cayman Chemicals 11972) was resuspended in DMSO at 20 mg/ml, diluted 1:10 in 0.9% NaCl containing 0.2% acetic acid, and further diluted in PancreaCult Organoid Media (StemCell Technologies, Inc.) to the indicated dilutions. Organoids were grown in the presence of vehicle or SR2211 for 4 days, then imaged and quantified, n = 3 independent wells plated per dose per treatment group.

Primary patient organoids were established and provided by Dr. Andrew Lowy. Briefly, patient-derived xenografts were digested for 1 hour at 37°C in RPMI containing 2.5% FBS, 5mg/ml Collagenase II, and 1.25mg/ml Dispase II, then passaged through a 70 µM mesh filter. Cells were plated at a density of 1.5×10^5 cells per 50 µL Matrigel. After domes were solidified, growth medium was added as follows: RPMI containing 50% Wnt3a conditioned media, 10% R-Spondin1-conditioned media, 2.5% FBS, 50 ng/ml EGF, 5 mg/ml Insulin, 12.5 ng/ml hydrocortisone, and 14 µM Rho Kinase Inhibitor. After establishment, organoids were passaged and maintained as previously described[14]. Briefly, organoids were isolated using

Cell Recovery Solution (Corning 354253), then dissociated into single cell suspensions with TrypLE Express (ThermoFisher 12604) supplemented with 25 µg/ml DNase I (Roche) and 14 µM Rho Kinase Inhibitor (Y-27632, Sigma). Cells were split 1:2 into 20 µL domes plated on pre-warmed 48 well plates. Domes were incubated at 37°C for 5 min, then covered with human complete organoid feeding media[14] without Wnt3a-conditioned media. SR2211 was prepared as described above, added at the indicated doses, and refreshed every 3 days. Organoids were grown in the presence of vehicle or SR2211 for 7 days, then imaged and quantified, n = 3 independent wells plated per dose per treatment group. All images were acquired on a Zeiss Axiovert 40 CFL. Organoids were counted and measured using ImageJ 1.51 s software.

Flank tumor transplantation studies

For the flank transplantation studies outlined below, investigators blinded themselves when possible to the assigned treatment group of each tumor for analysis; mice were de-identified after completion of flow cytometry analysis. The number of tumors transplanted for each study is based on past experience with studies of this nature, where a group size of 10 is sufficient to determine if pancreatic cancer growth is significantly affected when a regulatory signal is perturbed (see Fox et al. 2016).

For shRNA-infected pancreatic tumor cell propagation *in vivo*, cells were infected with lentiviral particles containing shRNAs and positively infected (red) cells were sorted 72 hours after transduction. 1000 low passage, shRNA-infected $KP^{f/f}C$, or $2x10^5$ shRNA-infected FG cells were resuspended in 50 µL culture media, then mixed 1:1 with matrigel (BD Biosciences). Cells were injected subcutaneously into the left or right flank of 5-8 week-old NOD/SCID recipient mice. Subcutaneous tumor dimensions were measured with calipers 1-2x weekly for 6-8 weeks, and two independent transplant experiments were conducted for each shRNA at n = 4 independent tumors per group.

For drug-treated *KP$^{f/f}$C* flank tumors, 2x10^4 low passage REM2-*KP$^{f/f}$C* tumor cells were resuspended in 50 µL culture media, then mixed 1:1 with matrigel (BD Biosciences). Cells were injected subcutaneously into the left or right flank of 5-8 week-old non-tumor bearing, immunocompetent littermates or NSG mice. Tumor growth was monitored twice weekly; when tumors reached 0.1-0.3 cm^3, mice were randomly enrolled in treatment groups and were treated for 3 weeks as described below. After 3 weeks of therapy, tumors were removed, weighed, dissociated, and analyzed by flow cytometry. Tumor volume was calculated using the standard modified ellipsoid formula ½ (Length x Width^2); n = 2-4 tumors per treatment group in immunocompetent littermate recipients and n = 4-6 tumors per treatment group in NSG recipients.

For chimeric transplantation studies, 2x10^4 low passage REM2-*KP$^{f/f}$C* tumor cells were resuspended in 50 µL culture media, then mixed 1:1 with matrigel (BD Biosciences). Cells were injected subcutaneously into the left or right flank of 5-8 week-old RORγ-knockout or wild-type recipients; recipient mice were maintained on antibiotic water (sulfamethoxazole and trimethoprim). Tumor growth was monitored twice weekly; when tumors reached 0.1-0.3 cm^3, mice were randomly enrolled in treatment groups and were treated for 3 weeks as described below. After 3 weeks of therapy, tumors were removed, weighed, dissociated, and analyzed by flow cytometry. Tumor volume was calculated using the standard modified ellipsoid formula ½ (Length x Width^2); n = 5-7 tumors per treatment group.

For drug-treated human pancreatic tumors 2x10^4 human pancreatic FG cancer cells or 2x10^6 patient-derived xenograft cells were resuspended in 50 µL culture media, then mixed 1:1 with matrigel (BD Biosciences). Cells were injected subcutaneously into the left or right flank of 5-8 week-old NSG recipient mice. Mice were randomly enrolled in treatment groups and were treated for 3 weeks as described below. After 3 weeks of therapy, tumors were removed, weighed, and dissociated. Subcutaneous tumor dimensions were measured with

calipers 1-2x weekly. Tumor volume was calculated using the standard modified ellipsoid formula ½ (Length x Width^2); at minimum n = 4 tumors per treatment group.

In vivo and *in vitro* drug therapy

The RORγ inverse agonists SR2211 (Cayman Chemicals, 11972, or Tocris, 4869) was resuspended in DMSO at 20 mg/ml or 50 mg/ml, respectively, then mixed 1:20 in 8% Tween80-PBS prior to use. Gemcitabine (Sigma, G6423) was resuspended in H_2O at 20 mg/ml. For *in vitro* drug studies, low passage (< 6 passage) WT- or REM2-*KP$^{f/f}$C* cells, (< 10 passage) KP$^{R172H/+}$C cells, or FG cells were plated in non-adherent tumorsphere conditions or Matrigel colony conditions for 1 week in the presence of SR2211 or vehicle. For *KP$^{f/f}$C* littermate, NSG mice, and RORγ-knockout mice bearing *KP$^{f/f}$C*-derived flank tumors and for NSG mice bearing flank patient-derived xenograft tumors, mice were treated with either vehicle (PBS) or gemcitabine (25 mg/kg i.p., 1x weekly) alone or in combination with vehicle (5% DMSO, 8% Tween80-PBS) or SR2211 (10 mg/kg i.p., daily) for 3 weeks. RORγ-knockout mice and paired wild-type littermates were maintained on antibiotic water (sulfamethoxazole and trimethoprim). For NOD/SCID mice bearing flank FG tumors, mice were treated with either vehicle (5% DMSO in corn oil) or SR2211 (10 mg/kg i.p., daily) for 2.5 weeks. All flank tumors were measured 2x weekly and mice were sacrificed if tumors were > 2cm^3, in accordance with IACUC protocol. For *KP$^{f/f}$C* autochthonous survival studies, 8 week old tumor-bearing *KP$^{f/f}$C* mice were enrolled in either vehicle (10% DMSO, 0.9% NaCl with 0.2% acetic acid) or SR2211 (20 mg/kg i.p., daily) treatment groups, and treated until moribund, where n = 4 separate mice per treatment group. For all drug studies, tumor-bearing mice were randomly assigned into drug treatment groups; treatment group size was determined based on previous studies[8].

Immunofluorescence staining

Pancreatic cancer tissue from *KP$^{f/f}$C* mice was fixed in Z-fix (Anatech Ltd, Fisher Scientific) and paraffin embedded at the UCSD Histology and Immunohistochemistry Core at The Sanford Consortium for Regenerative Medicine according to standard protocols. 5 μm sections were obtained and deparaffinized in xylene. The human pancreas paraffin embedded tissue array was acquired from US Biomax, Inc (BIC14011a). For paraffin embedded mouse and human pancreas tissues, antigen retrieval was performed for 40 minutes in 95-100°C 1x Citrate Buffer, pH 6.0 (eBioscience). Sections were blocked in PBS containing 0.1% Triton X-100 (Sigma- Aldrich), 10% Goat Serum (Fisher Scientific), and 5% bovine serum albumin (Invitrogen).

KP$^{f/f}$C cells and human pancreatic cancer cell lines were suspended in DMEM (GIBCO, Life Technologies) supplemented with 50% FBS and adhered to slides by centrifugation at 500 rpm. 24 hours later, cells were fixed with Z-fix (Anatech Ltd, Fisher Scientific), washed in PBS, and blocked with PBS containing 0.1% Triton X-100 (Sigma-Aldrich), 10% Goat serum (Fisher Scientific), and 5% bovine serum albumin (Invitrogen). All incubations with primary antibodies were carried out overnight at 4°C. Incubation with Alexafluor-conjugated secondary antibodies (Molecular Probes) was performed for 1 hour at room temperature. DAPI (Molecular Probes) was used to detect DNA and images were obtained with a Confocal Leica TCS SP5 II (Leica Microsystems). The following primary antibodies were used: chicken anti-GFP (Abcam, ab13970) 1:500, rabbit anti-RORγ (Thermo Fisher, PA5-23148) 1:500, mouse anti-E-Cadherin (BD Biosciences, 610181) 1:500, anti-Keratin (Abcam, ab8068) 1:15, anti-HMGA2 (Abcam. Ab52039) 1:100, anti-CELSR1 (EMD Millipore abt119) 1:1000, anti-CELSR2 (BosterBio A06880) 1:250.

Tumor imaging

9.5-10.5 week old REM2-*KP$^{f/f}$C* mice were treated either vehicle or SR2211 (10 mg/kg

i.p., daily) for 8 days. For imaging, mice were anesthetized by intraperitoneal injection of ketamine and xylazine (100/20 mg/kg). In order to visualize blood vessels and nuclei, mice were injected retro-orbitally with AlexaFluor 647 anti-mouse CD144 (VE-cadherin) antibody and Hoechst 33342 immediately following anesthesia induction. After 25 minutes, pancreatic tumors were removed and placed in HBSS containing 5% FBS and 2mM EDTA. 80-150 µm images in 1024 × 1024 format were acquired with an HCX APO L20x objective on an upright Leica SP5 confocal system using Leica LAS AF 1.8.2 software. GFP cluster sizes were measure using ImageJ 1.51 s software. 2 mice per treatment group were analyzed in this study; 6-10 frames were analyzed per mouse.

Analysis of tissue microarrays

Immunohistochemistry (IHC) and staining analysis

TMAs were sectioned to 2.5 µm thickness. IHC staining was performed on a Leica BOND RX automated immunostainer using BOND primary antibody diluent and BOND Polymer Refine DAB Detection kit according to the manufacturer's instructions (Leica Biosystems). Pre-treatment was performed using citrate buffer at 100°C for 30 min, and tissue was stained using rabbit anti-human RORγ(t) (polyclonal, #PA5-23148, Thermo Fisher Scientific) at a dilution of 1:4000. Stained slides were scanned using a Pannoramic P250 digital slide scanner (3DHistech). RORγ(t) staining of individual TMA spots was analyzed in an independent and randomized manner by two board-certified surgical pathologists (C.M.S and M.W.) using Scorenado, a custom-made online digital TMA analysis tool. Interpretation of staining results was in accordance with the "reporting recommendations for tumor marker prognostic studies" (REMARK) guidelines. Equivocal and discordant cases were re-analyzed jointly to reach a consensus. RORγ(t) staining in tumor cells was classified microscopically as 0 (absence of any cytoplasmic or nuclear staining), 1+ (cytoplasmic staining only), and 2+

(cytoplasmic and nuclear staining). For patients in whom multiple different scores were reported, only the highest score was used for further analysis. Spots/patients with no interpretable tissue (less than 10 intact, unequivocally identifiable tumor cells) or other artifacts were excluded.

Statistical analysis of TMA data

Descriptive statistics were performed for patients' characteristics. Frequencies, means, and range values are given. Association of RORγ(t) expression with categorical variables was performed using the Chi-square or Fisher's Exact test, where appropriate, while correlation with continuous values was tested using the non-parametric Kruskal-Wallis or Wilcoxon test. Univariate survival time differences were analyzed using the Kaplan-Meier method and log-rank test. All p values were two-sided and considered significant if < 0.05.

shRNA lentiviral constructs and production

Short hairpin RNA (shRNA) constructs were designed and cloned into pLV-hU6-mPGK-red vector by Biosettia. The target sequences are listed in Table 2.7. Virus was produced in 293T cells transfected with 4 µg shRNA constructs along with 2 µg pRSV/REV, 2 µg pMDLg/pRRE, and 2 µg pHCMVG constructs[45,46]. Viral supernatants were collected for two days then concentrated by ultracentrifugation at 20,000 rpm for 2 hours at 4°C. Knockdown efficiency for the shRNA constructs used in this study varied from 45%–95% (Table 2.7).

RT-qPCR analysis

RNA was isolated using RNeasy Micro and Mini kits (QIAGEN) and converted to cDNA using Superscript III (Invitrogen). Quantitative real-time PCR was performed using an iCycler (BioRad) by mixing cDNAs, iQ SYBR Green Supermix (BioRad) and gene specific primers.

Primer sequences are available in Table 2.7. All real time data was normalized to B2M or Gapdh.

Genome-wide profiling and bioinformatic analysis

Primary Msi2+ and Msi2- *KP$^{f/f}$C* RNA-seq, data analysis, and visualization

Stem and non-stem tumor cell isolation followed by RNA-sequencing

Tumors from three independent 10-12 week old REM2-*KP$^{f/f}$C* mice were harvested and dissociated into a single cell suspension as described above. Tumor cells were stained with FC block then 0.2 µg/10^6 cells anti-EpCAM APC (eBioscience). 70,00-100,00 Msi2+/EpCAM+ (stem) and Msi2-/EpCAM+ (non-stem) cells were sorted and total RNA was isolated using RNeasy Micro kit (QIAGEN). Total RNA was assessed for quality using an Agilent Tapestation, and all samples had RIN ≥7.9. RNA libraries were generated from 65 ng of RNA using Illumina's TruSeq Stranded mRNA Sample Prep Kit following manufacturer's instructions, modifying the shear time to 5 minutes. RNA libraries were multiplexed and sequenced with 50 basepair (bp) single end reads (SR50) to a depth of approximately 30 million reads per sample on an Illumina HiSeq2500 using V4 sequencing chemistry.

RNA-seq analysis

RNA-seq fastq files were processed into transcript-level summaries using *kallisto*[47], an ultrafast pseudo-alignment algorithm with expectation maximization. Transcript-level summaries were processed into gene-level summaries by adding all transcript counts from the same gene. Gene counts were normalized across samples using *DESeq* normalization[48] and the gene list was filtered based on mean abundance, which left 13,787 genes for further analysis. Differential expression was assessed with an *R* package *limma*[49] applied to $\log_2$-transformed counts. Statistical significance of each test was expressed in terms of local false

discovery rate *lfdr*[50] using the *limma* function *eBayes*[51]. *lfdr*, also called posterior error probability, is the probability that a particular gene is not differentially expressed, given the data.

Cell state analysis

For cell state analysis, Genes Set Enrichment Analysis (GSEA)[16] was performed with the Bioconductor GSVA[52] and the Bioconductor GSVAdata c2BroadSets gene set collection, which is the C2 collection of canonical gene sets from MsigDB3.0[16]. Briefly, GSEA evaluates a ranked gene expression data-set against previously defined gene sets. GSEA was performed with the following parameters: mx.diff = TRUE, verbose = TRUE, parallel.sz = 1, min.sz = 5, max.sz = 500, rnaseq = F.

Primary Msi2+ and Msi2- *KP$^{f/f}$C* ChIP-seq for histone H3K27ac

Stem and non-stem tumor cell isolation followed by H3K27ac ChIP-sequencing

70,000 Msi2+/EpCAM+ (stem) and Msi2-/EpCAM+ (non-stem) cells were freshly isolated from a single mouse as described above. ChIP was performed as described previously[53]; cells were pelleted by centrifugation and crosslinked with 1% formalin in culture medium using the protocol described previously[53]. Fixed cells were then lysed in SDS buffer and sonicated on a Covaris S2 ultrasonicator. The following settings were used: Duty factor: 20%, Intensity: 4 and 200 Cycles/burst, Duration: 60 s for a total of 10 cycles to shear chromatin with an average fragment size of 200-400 bp. ChIP for H3K27Acetyl was performed using the antibody ab4729 (Abcam, Cambridge, UK) specific to the H3K27Ac modification. Library preparation of eluted chromatin immunoprecipitated DNA fragments was performed using the NEBNext Ultra II DNA library prep kit (E7645S and E7600S- NEB) for Illumina as per the manufacturer's protocol. Library prepped DNA was then subjected to single-end, 75-

nucleotide reads sequencing on the Illumina NexSeq500 sequencer at a sequencing depth of 20 million reads per sample.

H3K27ac signal quantification from ChIP-seq data

Pre-processed H3K27ac ChIP sequencing data was aligned to the UCSC mm10 mouse genome using the Bowtie2 aligner (version 2.1.0)[54], removing reads with quality scores of < 15. Non-unique and duplicate reads were removed using samtools (version 0.1.16)[55] and Picard tools (version 1.98), respectively. Replicates were then combined using BEDTools (version 2.17.0). Absolute H3K27ac occupancy in stem cells and non-stem cells was determined using the SICER-df algorithm without an input control (version 1.1[56], using a redundancy threshold of 1, a window size of 200bp, a fragment size of 150, an effective genome fraction of 0.75, a gap size of 200bp and an E-value of 1000. Relative H3K27ac occupancy in stem cells versus non-stem cells was determined as above, with the exception that the SICER-df-rb algorithm was used.

Determining the overlap between peaks and genomic features

Genomic coordinates for features such as coding genes in the mouse mm10 build were obtained from the Ensembl 84 build (Ensembl BioMart). The observed versus expected number of overlapping features and bases between the experimental peaks and these genomic features (datasets A and B) was then determined computationally using a custom python script, as described in Cole et al.[57]. Briefly, the number of base pairs within each region of A that overlapped with each region of B was computed. An expected background level of expected overlap was determined using permutation tests to randomly generate > 1000 sets of regions with equivalent lengths and chromosomal distributions to dataset B, ensuring that only sequenced genomic regions were considered. The overlaps between the random

datasets and experimental datasets were then determined, and p values and fold changes were estimated by comparing the overlap occurring by chance (expected) with that observed empirically (observed). This same process was used to determine the observed versus expected overlap of different experimental datasets.

RNA-Seq/ChIP-Seq correlation

Overlap between gene expression and H3K27ac modification

Genes that were up- or downregulated in stem cells were determined using the Cuffdiff algorithm, and H3K27ac peaks that were enriched or disfavored in stem cells were determined using the SICER-df-rb algorithm. The H3K27ac peaks were then annotated at the gene level using the 'ChippeakAnno'[58] and 'org.Mm.eg.db' packages in R, and genes with peaks that were either exclusively upregulated or exclusively downregulated (termed 'unique up' or 'unique down') were isolated. The correlation between upregulated gene expression and upregulated H3K27ac occupancy, or downregulated gene expression and downregulated H3K27ac occupancy, was then determined using the Spearman method in R.

Creation of composite plots

Composite plots showing RNA expression and H3K27ac signal across the length of the gene were created. Up- and downregulated RNA peaks were determined using the FPKM output values from Tophat2[59], and up- and downregulated H3K27ac peaks were determined using the SICER algorithm. Peaks were annotated with nearest gene information, and their location relative to the TSS was calculated. Data were then pooled into bins covering gene length intervals of 5%. Overlapping up/up and down/down sets, containing either up- or downregulated RNA and H3K27ac, respectively, were created, and the stem and non-stem peaks within these sets were plotted in Excel.

Super-enhancer identification

Enhancers in stem and non-stem cells were defined as regions with H3K27ac occupancy, as described in Hnisz et al., 2013. Peaks were obtained using the SICER-df algorithm before being indexed and converted to .gff format. H3K27ac Bowtie2 alignments for stem and non-stem cells were used to rank enhancers by signal density. Super-enhancers were then defined using the ROSE algorithm, with a stitching distance of 12.5kb and a TSS exclusion zone of 2.5kb. The resulting super-enhancers for stem or non-stem cells were then annotated at the gene level using the R packages 'ChippeakAnno'[58] and 'org.Mm.eg.db', and overlapping peaks between the two sets were determined using 'ChippeakAnno'. Super-enhancers that are unique to stem or non-stem cells were annotated to known biological pathways using the Gene Ontology (GO) over-representation analysis functionality of the tool WebGestalt[60].

Genome-wide CRISPR screen

CRISPR library amplification and viral preparation

The mouse GeCKO CRISPRv2 knockout pooled library[15] was acquired from Addgene (catalog# 1000000052) as two half-libraries (A and B). Each library was amplified according to the Zhang lab library amplification protocol[15] and plasmid DNA was purified using NucleoBond Xtra Maxi DNA purification kit (Macherey-Nagel). For lentiviral production, 24 x T225 flasks were plated with $21x10^6$ 293T each in 1x DMEM containing 10% FBS. 24 hours later, cells were transfected with pooled GeCKOv2 library and viral constructs. Briefly, media was removed and replaced with 12.5 mL warm OptiMEM (GIBCO). Per plate, 200 µL PLUS reagent (Life Technologies), 10 µg library A, and 10 µg library B was mixed in 4 mL OptiMEM along with 10 µg pRSV/REV (Addgene), 10 µg pMDLg/pRRE (Addgene), and 10 µg pHCMVG (Addgene) constructs. Separately, 200 µL Lipofectamine (Life Technologies) was mixed with

4 mL OptiMEM. After 5 minutes, the plasmid mix was combined with Lipofectamine and left to incubate at room temperature for 20 minutes, then added dropwise to each flask. Transfection media was removed 22 hours later and replaced with DMEM containing 10% FBS, 5 mM $MgCl_2$, 1 U/ml DNase (Thermo Scientific), and 20mM HEPES pH 7.4. Viral supernatants were collected at 24 and 48 hours, passaged through 0.45 μm filter (corning), and concentrated by ultracentrifugation at 20,000 rpm for 2 hours at 4°C. Viral particles were resuspended in DMEM containing 10% FBS, 5 mM $MgCl_2$, and 20 mM HEPES pH 7.4, and stored at −80°C.

CRISPR screen in primary *KP$^{f/f}$C* cells

3 independent primary REM2-*KP$^{f/f}$C* cell lines were established as described above and maintained in DMEM containing 10% FBS, 1x non-essential amino acids, and 1x pen/strep. At passage 3, each cell line was tested for puromycin sensitivity and GeCKOv2 lentiviral titer was determined. At passage 5, $1.6x10^8$ cells from each cell line were transduced with GeCKOv2 lentivirus at an MOI of 0.3. 48 hours after transduction, $1x10^8$ cells were harvested for sequencing ("T0") and $1.6x10^8$ were re-plated in the presence of puromycin according to previously tested puromycin sensitivity. Cells were passaged every 3-4 days for 3 weeks; at every passage, $5x10^7$ cells were re-plated to maintain library coverage. At 2 weeks post-transduction, cell lines were tested for sphere forming capacity. At 3 weeks, $3x10^7$ cells were harvested for sequencing ("2D; cell essential genes"), and $2.6x10^7$ cells were plated in sphere conditions as described above ("3D; stem cell essential genes"). After 1 week in sphere conditions, tumorspheres were harvested for sequencing.

Analysis of the 2D datasets revealed that while some genes were required for growth in 2D, other genes that were not (detectably) required for growth in 2D were still required for growth in 3D (for example, *Rorc Sox4, Foxo1*, *Wnt1* and *Robo3*). These findings suggested that growth in 3D is dependent on a distinct or additional set of pathways. Since only stem cells

give rise to 3D spheres, targets within the 3D datasets were prioritized for subsequent analyses. Of the genes that significantly dropped out in 3D, some also dropped out in 2D either significantly or as a trend.

DNA isolation, library preparation, and sequencing

Cells pellets were stored at −20°C until DNA isolation using QIAGEN Blood and Cell Culture DNA Midi Kit (13343). Briefly, per $1.5x10^7$ cells, cell pellets were resuspended in 2 mL cold PBS, then mixed with 2 mL cold buffer C1 and 6 mL cold H_2O, and incubated on ice for 10 minutes. Samples were pelleted 1300 x g for 15 minutes at 4°C, then resuspended in 1 mL cold buffer C1 with 3 mL cold H_2O, and centrifuged again. Pellets were then resuspended in 5 mL buffer G2 and treated with 100 µL RNase A (QIAGEN 1007885) for 2 minutes at room temperature followed by 95 µL Proteinase K for 1 hour at 50°C. DNA was extracted using Genomic-tip 100/G columns, eluted in 50°C buffer QF, and spooled into 300 µL TE buffer pH 8.0. Genomic DNA was stored at 4°C. For sequencing, gRNAs were first amplified from total genomic DNA isolated from each replicate at T0, 2D, and 3D (PCR1). Per 50 µL reaction, 4 µg gDNA was mixed with 25 µL KAPA HiFi HotStart ReadyMIX (KAPA Biosystems), 1 µM reverse primer1, and 1 µM forward primer1 mix (including staggers). Primer sequences are available upon request. After amplification (98°C 20 s, 66°C 20 s, 72°C 30 s, × 22 cycles), 50 µL of PCR1 products were cleaned up using QIAquick PCR Purification Kit (QIAGEN). The resulting ~200bp products were then barcoded with Illumina Adaptors by PCR2. 5 µL of each cleaned PCR1 product was mixed with 25 µL KAPA HiFi HotStart ReadyMIX (KAPA Biostystems), 10 µL H_2O, 1 µM reverse primer2, and 1 µM forward primer2. After amplification (98°C 20 s, 72°C 45 s, × 8 cycles), PCR2 products were gel purified, and eluted in 30 µL buffer EB. Final concentrations of the desired products were determined and equimolar amounts from each sample was pooled for Next Generation Sequencing.

Processing of the CRISPR screen data

Sequence read quality was assessed using fastqc (http://www.bioinformatics.babraham.ac.uk/projects/fastqc/). Prior to alignment, 5′ and 3′ adapters flanking the sgRNA sequences were trimmed off using cutadapt v1.11[61] with the 5′-adaptor TCTTGTGGAAAGGACGAAACACCG and the 3′ adaptor GTTTTAGAGCTAGAAATAGCAAGTT, which came from the cloning protocols of the respective libraries deposited on Addgene (https://www.addgene.org/pooled-library/). Error tolerance for adaptor identification was set to 0.25, and minimal required read length after trimming was set to 10 bp. Trimmed reads were aligned to the GeCKO mouse library using Bowtie2[54] in the–local mode with a seed length of 11, an allowed seed mismatch of 1 and the interval function set to 'S,1,0.75'. After completion, alignments were classified as either unique, failed, tolerated or ambiguous based on the primary ('AS') and secondary ('XS') alignment scores reported by Bowtie2. Reads with the primary alignment score not exceeding the secondary score by at least 5 points were discarded as ambiguous matches. Read counts were normalized by using the "size-factor" method as described in Li et al[62]. All of this was done using implementations in the PinAPL-Py webtool[63], with detailed code available at https://github.com/LewisLabUCSD/PinAPL-Py.

gRNA growth and decay analysis

We used a parametric method in which the cell population with damaged gene i grows as $N_i(t)=N_i(0)e^{(\alpha_0+\delta_i)t}$, where α_0 is the growth rate of unmodified cells and δ_i is the change of the growth rate due to the gene deletion. Since the aliquot extracted at each time point is roughly the same and represents only a fraction of the entire population, the observed sgRNA counts n_i do not correspond to N_i directly. The correspondence is only relative: if we define $c_i \equiv n_i/\sum_k n_k$ as the compositional fraction of sgRNA species i, the correspondence

is ci=Ni∑kNk. As a result, the exponential can only be determined up to a multiplicative constant, e−δit=A·ci(0)/ci(t). The constant is determined from the assumption that a gene deletion typically does not affect the growth rate. Mathematically, 1=Amed[ci(0)/ci(t)]. We define the statistic that measures the effect of gene deletion as xi≡e−δit and calculate it for every gene i fromxi=Aci(0)ci(t).Since we were interested in genes essential for growth, we performed a single-tailed test for xi. We collected the three values of xi, one from each biological replicate, into a vector xi. A statistically significant effect would have all three values large (> 1) and consistent. If xi were to denote position of a point in a three-dimensional space, we would be interested in points that lie close to the body diagonal and far away from the origin. A suitable statistic is s=(x·n)2−[x−(x·n)n]2, where n=(1,1,1)/3 is the unit vector in the direction of the body diagonal and · denotes scalar product. A q-value (false discovery rate) for each gene was estimated as the number of s-statistics not smaller than si expected in the null model divided by the observed number of s-statistics not smaller than si in the data. The null model was simulated numerically by permuting gene labels in xi for every experimental replicate, independently of each other, repeated 103 times.

STRING Interactome Network Analysis

The results from the CRISPR 3D experiment were integrated with the RNA-seq results using a network approach. We identified likely CRISPR-essential genes by filtering to include genes which had a false-discovery rate corrected p value of less than 0.5, resulting in 94 genes. We chose a relaxed filter here because the following filtering steps would help eliminate false positives, and our network analysis method would help to amplify weak signals. These genes were further filtered in two ways: first, we included only genes which were expressed in the RNA-seq data (this resulted in 57 genes), and second, we further restricted by genes which had enriched expression in stem cells by > 2 log fold change in the RNA-seq (this resulted in

10 genes). These results were used to seed the network neighborhood exploration. We used the STRING mouse interactome[23] as our background network, including only high confidence interactions (edge weight > 700). The STRING interactome contains known and predicted functional protein-protein interactions. The interactions are assembled from a variety of sources, including genomic context predictions, high throughput lab experiments, and co-expression databases. Interaction confidence is a weighted combination of all lines of evidence, with higher quality experiments contributing more. The high confidence STRING interactome contains 13,863 genes, and 411,296 edges. Because not all genes are found in the interactome, our seed gene sets were further filtered when integrated with the network. This resulted in 39 CRISPR-essential, RNA-expressed seed genes, and 5 CRISPR-essential, RNA differentially-expressed seed genes. After integrating the seed genes with the background interactome, we employed a network propagation algorithm to explore the network neighborhood around these seed genes. Network propagation is a powerful method for amplifying weak signals by taking advantage of the fact that genes related to the same phenotype tend to interact. We implemented the network propagation method developed in Vanunu et al.[22], which simulates how heat would diffuse, with loss, through the network by traversing the edges, starting from an initially hot set of 'seed' nodes. At each step, one unit of heat is added to the seed nodes, and is then spread to the neighbor nodes. A constant fraction of heat is then removed from each node, so that heat is conserved in the system. After a number of iterations, the heat on the nodes converges to a stable value. This final heat vector is a proxy for how close each node is to the seed set. For example, if a node was between two initially hot nodes, it would have an extremely high final heat value, and if a node was quite far from the initially hot seed nodes, it would have a very low final heat value. This process is described by the following as in Vanunu et al.[22]:$Ft=W'Ft-1+(1-\alpha)Y$ where Ft is the heat vector at time t, Y is the initial value of the heat vector, W' is the normalized adjacency matrix,

and $\alpha \in (0,1)$ represents the fraction of total heat which is dissipated at every timestep. We examined the results of the subnetwork composed of the 500 genes nearest to the seed genes after network propagation. This is referred to as the 'hot subnetwork'. In order to identify pathways and biological mechanisms related to the seed genes, we applied a clustering algorithm to the hot subnetwork, which partitioned the network into groups of genes which are highly interconnected within the group, and sparsely connected to genes in other groups. We used a modularity maximization algorithm for clustering[64] which has proven effective in detecting modules, or clusters, in protein-protein interaction networks[65]. These clusters were annotated to known biological pathways using the over-representation analysis functionality of the tool WebGestalt[60]. We used the 500 genes in the hot subnetwork as the background reference gene set. To display the networks, we used a spring-embedded layout, which is modified by cluster membership (along with some manual adjustment to ensure non-overlapping labels) (Figure 2.3 E). Genes belonging to each cluster were laid out radially along a circle, to emphasize the within cluster and between cluster connections. VisJS2jupyter[66] was used for network propagation and visualization. Node color is mapped to the RNA-seq log fold change, with downregulated genes displayed in blue, upregulated genes displayed in red, and genes with small fold changes displayed in gray. Labels are shown for genes which have a log fold change with absolute value greater than 3.0. Seed genes are shown as triangles with white outlines, while all other genes in the hot subnetwork are circles. The clusters have been annotated by selecting representative pathways from the enrichment analysis.

KP^{R172H}C single cell analysis

Freshly harvested tumors from two independent *KP^{R172h}C* mice were subjected to mechanical and enzymatic dissociation using a Miltenyi gentleMACS Tissue Dissociator to obtain single cells. The 10X Genomics Chromium Single Cell Solution was employed for

capture, amplification and labeling of mRNA from single cells and for scRNA-Seq library preparation. Sequencing of libraries was performed on a Illumina HiSeq 2500 system. Sequencing data was input into the Cell Ranger analysis pipeline to align reads and generate gene-cell expression matrices. Finally, Custom R packages were used to perform gene-expression analyses and cell clustering projected using the t-SNE (t-Distributed Stochastic Neighbor Embedding) clustering algorithm. scRNA-seq datasets from the two independent $KP^{R127h}C$ tumor tissues generated on 10xGenomics platform were merged and utilized to explore and validate the molecular signatures of the tumor cells under dynamic development. The tumor cells that were used to illustrate the signal of *Il10rb*, *Il34* and *Csf1r* etc. were characterized from the heterogeneous cellular constituents using SuperCT method developed by Dr. Wei Lin and confirmed by the Seurat FindClusters with the enriched signal of *Epcam*, *Krt19* and *Prom1* etc[67]. The tSNE layout of the tumor cells was calculated by Seurat pipeline using the single-cell digital expression profiles.

$KP^{f/f}C$ single cell analysis

Three age-matched *$KP^{f/f}C$* pancreatic tumors were collected and freshly dissociated, as described above. Tumor cells were stained with rat anti-mouse CD45-PE/Cy7 (eBioscience), rat anti-mouse CD31-PE (eBioscience), and rat anti-mouse PDGFRα-PacBlue (eBioscience) and tumor cells negative for these three markers were sorted for analysis. Individual cells were isolated, barcoded, and libraries were constructed using the 10x genomics platform using the Chromium Single Cell 3′ GEM library and gel bead kit v2 per manufacturer's protocol. Libraries were sequenced on an Illumina HiSeq4000. The Cell Ranger software was used for alignment, filtering and barcode and UMI counting. The Seurat R package was used for further secondary analysis using default settings for unsupervised clustering and cell type discovery.

shRorc versus shCtrl *KP$^{f/f}$C* RNA-seq

Primary WT-*KP$^{f/f}$C* cell lines were established as described above. WT-*KP$^{f/f}$C* cells derived from an individual low passage cell line (< 6 passage) were plated and transduced in triplicate with lentiviral particles containing shCtrl or shRorc. Positively infected (red) cells were sorted 5 days after transduction. Total RNA was isolated using the RNeasy Micro Plus kit (QIAGEN). RNA libraries were generated from 200 ng of RNA using Illumina's TruSeq Stranded mRNA Sample Prep Kit (Illumina) following manufacturer's instructions. Libraries were pooled and single end sequenced (1X75) on the Illumina NextSeq 500 using the High output V2 kit (Illumina Inc., San Diego CA).

Read data was processed in BaseSpace (https://basespace.illumina.com). Reads were aligned to *Mus musculus* genome (mm10) using STAR aligner (https://code.google.com/p/rna-star/) with default settings. Differential transcript expression was determined using the Cufflinks Cuffdiff package[68] (https://github.com/cole-trapnell-lab/cufflinks). Differential expression data was then filtered to represent only significantly differentially expressed genes (q value < 0.05). This list was used for pathway analysis and heatmaps of specific significantly differentially regulated pathways.

shRorc versus shCtrl *KP$^{f/f}$C* ChIP-seq for histone H3K27ac

Primary WT-*KP$^{f/f}$C* cell lines were established as described above. Low passage (< 6 passages) WT-*KP$^{f/f}$C* cells from two independent cell lines were plated and transduced in triplicate with lentiviral particles containing shCtrl or shRorc. Positively infected (red) cells were sorted 5 days after transduction. ChIP-seq for histone H3K27-ac, signal quantification, and determination of the overlap between peaks and genomic features was conducted as described above.

Super-enhancers in control and shRorc-treated *KP$^{f/f}$C* cell lines as well as Musashi stem

cells were determined from H3K27ac ChIP-seq data using the ROSE algorithm (http://younglab.wi.mit.edu/super_enhancer_code.html). The Musashi stem cell super-enhancer peaks were then further refined to include only those unique to the stem cell state (defined as present in stem cells but not non-stem cells) and/or those with RORγ binding sites within the peaks. Peak sequences were extracted using the 'getSeq' function from the 'BSGenome.MMusculus.UCSC.mm10' R package. RORγ binding sites were then mapped using the matrix RORG_MOUSE.H10MO.C.pcm (HOCOMOCO database) as a reference, along with the 'matchPWM' function in R at 90% stringency. Baseline peaks were then defined for each $KP^{f/f}C$ cell line as those overlapping each of the four Musashi stem cell peaklists with each KPC control super-enhancer list, giving eight in total. The R packages 'GenomicRanges' and 'ChIPpeakAnno' were used to assess peak overlap with a minimum overlap of 1bp used. To estimate the proportion of super-enhancers that are closed on RORC knockdown, divergence between each baseline condition and the corresponding $KP^{f/f}C$ shRorc super-enhancer list was assessed by quantifying the peak overlap and then expressing this as a proportion of the baseline list ('shared%'). The proportion of unique peaks in each condition was then calculated as 100%-shared% and plotted.

sgRORC versus sgNT human RNA-seq

Human FG cells were plated and transduced in triplicate with lentiviral particles containing Cas9 and non-targeting guide RNA or guide RNA against Rorc. Positively infected (green) cells were sorted 5 days after transduction. Total RNA was isolated using the RNeasy Micro Plus kit (QIAGEN). RNA libraries were generated from 200 ng of RNA using Illumina's TruSeq Stranded mRNA Sample Prep Kit (illumina) following manufacturer's instructions. Libraries were pooled and single end sequenced (1X75) on the Illumina NextSeq 500 using the High output V2 kit (Illumina Inc., San Diego CA).

Comparative RNA-seq and cell state analysis

RORC knockdown and control RNA-seq fastq files in mouse *KP$^{f/f}$C* and human FG cells were processed into transcript-level summaries using kallisto[47]. Transcript-level summaries were processed into gene-level summaries and differential gene expression was performed using sleuth with the Wald test[69]. GSEA was performed as detailed above[16]. Gene ontology analysis was performed using Metascape using a custom analysis with GO biological processes and default settings with genes with a FDR < 5% and a beta value > 0.5.

cBioportal

RORC genomic amplification data from cancer patients was collected from the Memorial Sloan Kettering Cancer Center cBioPortal for Cancer Genomics (http://www.cbioportal.org).

Quantification and Statistical Analysis

Statistical analyses were carried out using GraphPad Prism software version 7.0d (GraphPad Software Inc.). Sample sizes for *in vivo* drug studies were determined based on the variability of pancreatic tumor models used. For flank transplant and autochthonous drug studies, tumor bearing animals within each group were randomly assigned to treatment groups. Treatment sizes were determined based on previous studies[8]. Data are shown as the mean ± SEM. Two-tailed unpaired Student's t tests with Welch's correction or One-way analysis of variance (ANOVA) for multiple comparisons when appropriate were used to determine statistical significance ($^{*}p < 0.05$, $^{**}p < 0.01$, $^{***}p < 0.001$, $^{****}p < 0.0001$).

The level of replication for each *in vitro* and *in vivo* study is noted in the figure legends for each figure and described in detail in the section above. However to summarize briefly, *in vitro* tumorsphere or colony formation studies were conducted with n = 3

independent wells per cell line across two independent shRNA of n = 3 wells; however, the majority of these experiments were additionally completed in > 1 independently derived cell line, n = 3 wells per shRNA. For limiting dilution assays, organoids were derived from 3 independent mice; drug-treated mouse and human organoids were plated at n = 3 wells per dose per treatment condition. Flank shRNA studies were conducted twice independently, with n = 4 tumors per group in each experiment. Flank drug studies were conducted at n = 2-7 tumors per treatment group; autochthonous $KP^{f/f}C$ survival studies were conducted with a minimum of 4 mice enrolled in each treatment group. Live imaging studies were carried out with two mice per treatment group.

Statistical considerations and bioinformatic analysis of large data-sets generated are explained in great detail above. In brief, primary *$KP^{f/f}C$* RNA-seq was performed using Msi2+ and Msi2- cells sorted independently from three different end-stage *$KP^{f/f}C$* mice. Primary *$KP^{f/f}C$* ChIP-seq was performed using Msi2+ and Msi2- cells sorted from an individual end-stage *$KP^{f/f}C$* mouse. The genome-wide CRISPR screen was conducted using three biologically independent cell lines (derived from three different *$KP^{f/f}C$* tumors). Single-cell analysis of tumors represents merged data from ~10,000 cells across two $KP^{R172H}C$ and three *$KP^{f/f}C$* mice. RNA-seq for shRorc and shCtrl *$KP^{f/f}C$* cells was conducted in triplicate, while ChIP-seq was conducted in single replicates from two biologically independent *$KP^{f/f}C$* cell lines.

Data and Software Availability

The datasets generated during and/or analyzed during the current study are available from the corresponding author on reasonable request. Singe cell, Genome-wide CRISPR screen, H3K27ac ChIP, and RNA sequencing data have been deposited at NCBI GEO:

Primary Msi2+ and Msi2- *$KP^{f/f}C$* RNA-seq

https://www.ncbi.nlm.nih.gov/geo/query/acc.cgi?acc=GSE114906

Primary Msi2+ and Msi2- *KP$^{f/f}$C* ChIP-seq for histone H3K27ac

https://www.ncbi.nlm.nih.gov/geo/query/acc.cgi?acc=GSE113712

Genome-wide CRISPR screen

https://www.ncbi.nlm.nih.gov/geo/query/acc.cgi?acc=GSE114914

shRorc versus shControl *KP$^{f/f}$C* ChIP-seq for histone H3K27ac

https://www.ncbi.nlm.nih.gov/geo/query/acc.cgi?acc=GSE126536

shRorc versus shCtrl *KP$^{f/f}$C* RNA-seq

https://www.ncbi.nlm.nih.gov/geo/query/acc.cgi?acc=GSE126538

sgRORC versus sgNT human RNA-seq

https://www.ncbi.nlm.nih.gov/geo/query/acc.cgi?acc=GSE126537

KP$^{f/f}$C single cell analysis

https://www.ncbi.nlm.nih.gov/geo/query/acc.cgi?acc=GSE126539

KP^{R172H}C single cell analysis

https://www.ncbi.nlm.nih.gov/geo/query/acc.cgi?acc=GSE126388

Code availability

Custom code developed for CRISPR screen analysis and network propagation were deposited to github.com and can be accessed at:

https://github.com/ucsd-ccbb/crispr_network_analysis.

2.6. Acknowledgments

Chapter 2, is a reprint of the material as it appears in Cell, 2019. Lytle NK†, Ferguson LP†, Rajbhandari N, Gilroy K, Fox RG, Deshpande A, Schürch CM, Hamilton M, Robertson N, Lin W, Noel P, Wartenberg M, Zlobec I, Eichmann M, Galván JA, Karamitopoulou E, Gilderman

T, Esparza LA, Shima Y, Spahn P, French R, Lewis NE, Fisch KM, Sasik R, Rosenthal SB, Kritzik M, Von Hoff D, Han H, Ideker T, Deshpande AL, Lowy AM, Adams PD, and Reya T*. “A multiscale map of the stem cell state in pancreatic adenocarcinoma”. The dissertation author was co-first author and a primary contributor to this paper.

We are grateful to Olivier Harismendy, Prashant Mali, and Kristen Jepsen for help with the CRISPR screen design; Dan Littman for comments on the manuscript; Michael Karin and Ron Evans for scientific advice; Christopher Wright for providing the Ptf1a-Cre mice; and Armin Ahmadi and Kendall Chambers for technical support. N.K.L. received support from T32 GM007752 and a Ruth L. Kirschstein National Research Service Award F31 CA206416; L.P.F. received support from T32 GM007752; M.H. received support from T32 HL086344. The project was partially supported by the NIH grant UL1TR001442, as well as by CRUK program C10652-A16566 to P.D.A, CA169281 to H.H. and D.V.H., a grant from the National Foundation for Cancer Research to D.V.H., R35 GM119850 and NNF10CC1016517 to N.E.L., CA155620 to A.M.L., R35 CA197699 to T.R., and R01 CA186043 to A.M.L and T.R. This work was also supported by an SU2C–CRUK–Lustgarten Foundation Pancreatic Cancer Dream Team Research Grant (SU2C-AACR-DT-20-16) to D.V.H., H.H., A.M.L., and T.R. and an SU2C-Lustgarten Foundation pancreatic cancer collective grant (SU2C-AACR-PCC-05-18) to A.M.L. and T.R. The content is solely the responsibility of the authors and does not necessarily represent the official views of the NIH.

N.K.L. designed and performed the CRISPR screen and validation experiments, isolated tumor cells for ChIP-seq, prepared samples for RNA-seq, performed all functional experiments related to RORγ inhibition *in vitro* and *in vivo*, and performed histologic analysis and live imaging experiments. L.P.F. carried out CRISPR screen validation and related bioinformatic analysis, *in vivo* RORγ target analysis, protein expression, cytokine analysis, RNA-seq library preparation and helped with manuscript and figure preparation. N.

Rajbhandari analyzed Rorc$^{-/-}$ *KP$^{f/f}$C* mice and helped with *in vivo* drug studies and CRISPR screen validation; R.F., T.G., and L.A.E. provided experimental help; P.S., N.E.L., M.H., K.M.F., R.S., and S.B.R. performed bioinformatics analysis related to RNA-seq and CRISPR screen; P.N. and H.H. carried out the single-cell RNA-seq and W.L. and M.H. performed related computational analysis; A.D. and A.J.D. performed ChIP-seq; K.G., N. Robertson, and P.D.A. performed all ChIP-seq analysis; and for tissue microarray (TMA) analysis, C.M.S. and M.W. analyzed and interpreted TMA staining, C.M.S. created figures and wrote the report, I.Z. performed statistical analysis, M.E. created Scorenado and provided technical advice, J.A.G. performed TMA immunohistochemistry (IHC) staining, and E.K. created the TMAs and collected clinical data. T.I., D.V.H., A.M.L., and P.D.A. provided experimental and/or computational advice and comments on the manuscript. N.K.L., L.P.F., and M.K. helped write the paper. T.R. conceived of the project, planned and guided the research, and wrote the paper.

2.7. References

1. Conroy, T., Hammel, P., Hebbar, M., Ben Abdelghani, M., Wei, A.C., Raoul, J.L., Choné, L., Francois, E., Artru, P., Biagi, J.J. and Lecomte, T. FOLFIRINOX or gemcitabine as adjuvant therapy for pancreatic cancer. *N. Engl. J. Med.* **379**, 2395–2406 (2018).

2. Li, C., Heidt, D.G., Dalerba, P., Burant, C.F., Zhang, L., Adsay, V., Wicha, M., Clarke, M.F. and Simeone, D.M. Identification of pancreatic cancer stem cells. *Cancer Res.* **67**, 1030–1037 (2007).

3. Li, C., Wu, J.J., Hynes, M., Dosch, J., Sarkar, B., Welling, T.H., di Magliano, M.P. and Simeone, D.M. C-Met is a marker of pancreatic cancer stem cells and therapeutic target. *Gastroenterology* **141**, (2011).

4. Hermann, P.C., Huber, S.L., Herrler, T., Aicher, A., Ellwart, J.W., Guba, M., Bruns, C.J. and Heeschen, C. Distinct populations of cancer stem cells determine tumor growth and metastatic activity in human pancreatic cancer. *Cell Stem Cell* **1**, 313–323 (2007).

5. Kawamoto, M., Ishiwata, T., Cho, K., Uchida, E., Korc, M., Naito, Z. and Tajiri, T. Nestin expression correlates with nerve and retroperitoneal tissue invasion in

pancreatic cancer. *Hum. Pathol.* **40**, 189 (2009).

6. Rasheed, Z.A., Yang, J., Wang, Q., Kowalski, J., Freed, I., Murter, C., Hong, S.M., Koorstra, J.B., Rajeshkumar, N.V., He, X. and Goggins, M. Prognostic significance of tumorigenic cells with mesenchymal features in pancreatic adenocarcinoma. *JNCI J. Natl. Cancer Inst.* **102**, 340–351 (2010).

7. Bailey, J.M., Alsina, J., Rasheed, Z.A., McAllister, F.M., Fu, Y.Y., Plentz, R., Zhang, H., Pasricha, P.J., Bardeesy, N., Matsui, W. and Maitra, A. DCLK1 marks a morphologically distinct subpopulation of cells with stem cell properties in preinvasive pancreatic cancer. *Gastroenterology* **146**, 245–256 (2014).

8. Fox, R.G., Lytle, N.K., Jaquish, D.V., Park, F.D., Ito, T., Bajaj, J., Koechlein, C.S., Zimdahl, B., Yano, M., Kopp, J.L. and Kritzik, M. Image-based detection and targeting of therapy resistance in pancreatic adenocarcinoma. *Nature* **534**, 407–411 (2016).

9. Reya, T., Morrison, S. J., Clarke, M. F. & Weissman, I. L. Stem cells, cancer, and cancer stem cells. *Nature* **414**, 105–111 (2001).

10. Grosse-Wilde, A., Fouquier d'Hérouël, A., McIntosh, E., Ertaylan, G., Skupin, A., Kuestner, R.E., del Sol, A., Walters, K.A. and Huang, S. Stemness of the hybrid epithelial/mesenchymal state in breast cancer and its association with poor survival. *PLoS One* **10**, (2015).

11. Ivanov, I.I., McKenzie, B.S., Zhou, L., Tadokoro, C.E., Lepelley, A., Lafaille, J.J., Cua, D.J. and Littman, D.R. The orphan nuclear receptor RORgammat directs the differentiation program of proinflammatory IL-17+ T helper cells. *Cell* **126**, 1121–1133 (2006).

12. Hingorani, S.R., Petricoin III, E.F., Maitra, A., Rajapakse, V., King, C., Jacobetz, M.A., Ross, S., Conrads, T.P., Veenstra, T.D., Hitt, B.A. and Kawaguchi, Y. Preinvasive and invasive ductal pancreatic cancer and its early detection in the mouse. *Cancer Cell* **4**, 437–450 (2003).

13. Hingorani, S.R., Wang, L., Multani, A.S., Combs, C., Deramaudt, T.B., Hruban, R.H., Rustgi, A.K., Chang, S. and Tuveson, D.A. Trp53R172H and KrasG12D cooperate to promote chromosomal instability and widely metastatic pancreatic ductal adenocarcinoma in mice. *Cancer Cell* **7**, 469–483 (2005).

14. Boj, S.F., Hwang, C.I., Baker, L.A., Chio, I.I.C., Engle, D.D., Corbo, V., Jager, M., Ponz-Sarvise, M., Tiriac, H., Spector, M.S. and Gracanin, A. Organoid models of human and mouse ductal pancreatic cancer. *Cell* **160**, 324–338 (2015).

15. Sanjana, N. E., Shalem, O. and Zhang, F. Improved vectors and genome-wide libraries for CRISPR screening. *Nature Methods* **11**, 783–784 (2014).

16. Subramanian, A., Tamayo, P., Mootha, V.K., Mukherjee, S., Ebert, B.L., Gillette, M.A., Paulovich, A., Pomeroy, S.L., Golub, T.R., Lander, E.S. and Mesirov, J.P. Gene set enrichment analysis: A knowledge-based approach for interpreting genome-wide expression profiles. *Proc. Natl. Acad. Sci. U. S. A.* **102**, 15545–15550 (2005).

17. Ryu, C.S., Kwak, H.C., Lee, K.S., Kang, K.W., Oh, S.J., Lee, K.H., Kim, H.M., Ma, J.Y. and Kim, S.K. Sulfur amino acid metabolism in doxorubicin-resistant breast cancer cells. *Toxicol. Appl. Pharmacol.* **255**, 94–102 (2011).

18. Lu, H., Chen, I., Shimoda, L.A., Park, Y., Zhang, C., Tran, L., Zhang, H. and Semenza, G.L. Chemotherapy-Induced Ca2+ Release Stimulates Breast Cancer Stem Cell Enrichment. *Cell Rep.* **18**, 1946–1957 (2017).

19. Hnisz, D., Abraham, B.J., Lee, T.I., Lau, A., Saint-André, V., Sigova, A.A., Hoke, H.A. and Young, R.A. Super-enhancers in the control of cell identity and disease. *Cell* **155**, 934 (2013).

20. Whyte, W.A., Orlando, D.A., Hnisz, D., Abraham, B.J., Lin, C.Y., Kagey, M.H., Rahl, P.B., Lee, T.I. and Young, R.A. Master transcription factors and mediator establish super-enhancers at key cell identity genes. *Cell* **153**, 307–319 (2013).

21. Rovira, M., Scott, S.G., Liss, A.S., Jensen, J., Thayer, S.P. and Leach, S.D. Isolation and characterization of centroacinar/terminal ductal progenitor cells in adult mouse pancreas. *Proc. Natl. Acad. Sci. U. S. A.* **107**, 75–80 (2010).

22. Vanunu, O., Magger, O., Ruppin, E., Shlomi, T. and Sharan, R. Associating genes and protein complexes with disease via network propagation. *PLOS Comput. Biol.* **6**, e1000641 (2010).

23. Szklarczyk, D., Franceschini, A., Wyder, S., Forslund, K., Heller, D., Huerta-Cepas, J., Simonovic, M., Roth, A., Santos, A., Tsafou, K.P. and Kuhn, M. STRING v10: Protein-protein interaction networks, integrated over the tree of life. *Nucleic Acids Res.* **43**, D447–D452 (2015).

24. Zhao, L., Spassieva, S., Gable, K., Gupta, S.D., Shi, L.Y., Wang, J., Bielawski, J., Hicks, W.L., Krebs, M.P., Naggert, J. and Hannun, Y.A. Elevation of 20-carbon long chain bases due to a mutation in serine palmitoyltransferase small subunit b results in neurodegeneration. *Proc. Natl. Acad. Sci.* **112**, 12962–12967 (2015).

25. Dwyer, J.R., Donkor, J., Zhang, P., Csaki, L.S., Vergnes, L., Lee, J.M., Dewald, J., Brindley, D.N., Atti, E., Tetradis, S. and Yoshinaga, Y. Mouse lipin-1 and lipin-2 cooperate to maintain glycerolipid homeostasis in liver and aging cerebellum. *Proc. Natl. Acad. Sci.* **109**, E2486–E2495 (2012).

26. Neph, S., Stergachis, A.B., Reynolds, A., Sandstrom, R., Borenstein, E. and Stamatoyannopoulos, J.A. Circuitry and dynamics of human transcription factor regulatory networks. *Cell* **150**, 1274–1286 (2012).

27. Kopp, J.L., von Figura, G., Mayes, E., Liu, F.F., Dubois, C.L., Morris IV, J.P., Pan, F.C., Akiyama, H., Wright, C.V., Jensen, K. and Hebrok, M. Identification of Sox9-dependent acinar-to-ductal reprogramming as the principal mechanism for initiation of pancreatic ductal adenocarcinoma. *Cancer Cell* **22**, 737–750 (2012).

28. Bailey, P., Chang, D.K., Nones, K., Johns, A.L., Patch, A.M., Gingras, M.C., Miller,

D.K., Christ, A.N., Bruxner, T.J., Quinn, M.C. and Nourse, C. Genomic analyses identify molecular subtypes of pancreatic cancer. *Nature* **531**, 47–52 (2016).

29. Gege, C. Retinoid-related orphan receptor gamma t (RORγt) inhibitors from Vitae Pharmaceuticals (WO2015116904) and structure proposal for their Phase I candidate VTP-43742. *Expert Opin. Ther. Pat.* **26**, 737–744 (2016).

30. Cook, D. N., Kang, H. S. and Jetten, A. M. Retinoic acid-related orphan receptors (RORs): regulatory functions in immunity, development, circadian rhythm, and metabolism. *Nucl. Recept. Res.* **2**, (2015).

31. Huh, J. R. & Littman, D. R. Small molecule inhibitors of RORγt: Targeting Th17 cells and other applications. *Eur. J. Immunol.* **42**, 2232–2237 (2012).

32. Kumar, N., Lyda, B., Chang, M.R., Lauer, J.L., Solt, L.A., Burris, T.P., Kamenecka, T.M. and Griffin, P.R. Identification of SR2211: A potent synthetic RORγ-selective modulator. *ACS Chem. Biol.* **7**, 672–677 (2012).

33. Van den Broeck, A., Vankelecom, H., Van Delm, W., Gremeaux, L., Wouters, J., Allemeersch, J., Govaere, O., Roskams, T. and Topal, B. Human pancreatic cancer contains a side population expressing cancer stem cell-associated and prognostic genes. *PLoS One* **8**, e73968 (2013).

34. Lappano, R. & Maggiolini, M. G protein-coupled receptors: novel targets for drug discovery in cancer. *Nat. Rev. Drug Discov. 2011 101* **10**, 47–60 (2010).

35. Guillonneau, C., Bézie, S. and Anegon, I. Immunoregulatory properties of the cytokine IL-34. *Cell. Mol. Life Sci.* **74**, 2569–2586 (2017).

36. Wang, X., Wong, K., Ouyang, W. and Rutz, S. Targeting IL-10 family cytokines for the treatment of human diseases. *Cold Spring Harb. Perspect. Biol.* **11**, a028548 (2019).

37. Sankhala, K.K., Blay, J.Y., Ganjoo, K.N., Italiano, A., Hassan, A.B., Kim, T.M., Ravi, V., Cassier, P.A., Rutkowski, P., Sankar, N. and Qazi, I. A phase I/II dose escalation and expansion study of cabiralizumab (cabira; FPA-008), an anti-CSF1R antibody, in tenosynovial giant cell tumor (TGCT, diffuse pigmented villonodular synovitis D-PVNS). *J. Clin. Oncol.* **35**, 11078–11078 (2017).

38. Wang, J., Zou, J.X., Xue, X., Cai, D., Zhang, Y., Duan, Z., Xiang, Q., Yang, J.C., Louie, M.C., Borowsky, A.D. and Gao, A.C. ROR-γ drives androgen receptor expression and represents a therapeutic target in castration-resistant prostate cancer. *Nat. Med. 2016 225* **22**, 488–496 (2016).

39. Kawaguchi, Y., Cooper, B., Gannon, M., Ray, M., MacDonald, R.J. and Wright, C.V. The role of the transcriptional regulator Ptf1a in converting intestinal to pancreatic progenitors. *Nat. Genet.* **32**, 128–134 (2002).

40. Olive, K.P., Tuveson, D.A., Ruhe, Z.C., Yin, B., Willis, N.A., Bronson, R.T., Crowley, D. and Jacks, T. Mutant p53 gain of function in two mouse models of Li-Fraumeni syndrome. *Cell* **119**, 847–860 (2004).

41. Morgan R. T., Woods L. K., Moore G. E., Quinn L. A., McGavran L. and Gordon S. G. Human cell line (COLO 357) of metastasis pancreatic adenocarcinoma. *Int. J. Cancer* **25**, 591–598. (1980).

42. Wartenberg, M., Cibin, S., Zlobec, I., Vassella, E., Eppenberger-Castori, S., Terracciano, L., Eichmann, M.D., Worni, M., Gloor, B., Perren, A. and Karamitopoulou, E. Integrated genomic and immunophenotypic classification of pancreatic cancer reveals three distinct subtypes with prognostic/ predictive significance. *Clin. Cancer Res.* **24**, 4444–4454 (2018).

43. Hu, Y. & Smyth, G. K. ELDA: Extreme limiting dilution analysis for comparing depleted and enriched populations in stem cell and other assays. *J. Immunol. Methods* **347**, 70–78 (2009).

44. Dull, T., Zufferey, R., Kelly, M., Mandel, R.J., Nguyen, M., Trono, D. and Naldini, L. A third-generation lentivirus vector with a conditional packagingaSystem. *J. Virol.* **72**, 8463–8471 (1998).

45. Sena-Esteves, M., Tebbets, J. C., Steffens, S., Crombleholme, T. and Flake, A. W. Optimized large-scale production of high titer lentivirus vector pseudotypes. *J. Virol. Methods* **122**, 131–139 (2004).

46. Bray, N. L., Pimentel, H., Melsted, P. and Pachter, L. Near-optimal probabilistic RNA-seq quantification. *Nat. Biotechnol. 2016 345* **34**, 525–527 (2016).

47. Anders, S. & Huber, W. Differential expression analysis for sequence count data. *Nat. Preced.* (2010).

48. Ritchie, M.E., Phipson, B., Wu, D.I., Hu, Y., Law, C.W., Shi, W. and Smyth, G.K. limma powers differential expression analyses for RNA-sequencing and microarray studies. *Nucleic Acids Res.* **43**, e47–e47 (2015).

49. Efron, B. & Tibshirani, R. Empirical bayes methods and false discovery rates for microarrays. *Genet. Epidemiol.* **23**, 70–86 (2002).

50. Lönnstedt, I. & Speed, T. Replicated microarray data. *Stat. Sin.* **12**, 31-46 (2002).

51. Hänzelmann, S., Castelo, R. and Guinney, J. GSVA: gene set variation analysis for microarray and RNA-Seq data. *BMC Bioinforma.* **14**, 1–15 (2013).

52. Deshpande, A.J., Deshpande, A., Sinha, A.U., Chen, L., Chang, J., Cihan, A., Fazio, M., Chen, C.W., Zhu, N., Koche, R. and Dzhekieva, L. AF10 regulates progressive H3K79 methylation and HOX gene expression in diverse AML subtypes. *Cancer Cell* **26**, 896–908 (2014).

53. Langmead, B. & Salzberg, S. L. Fast gapped-read alignment with Bowtie 2. *Nat. Methods* **9**, 357–359 (2012).

54. Li, H., Handsaker, B., Wysoker, A., Fennell, T., Ruan, J., Homer, N., Marth, G.,

Abecasis, G. and Durbin, R. The sequence alignment/map format and SAMtools. *Bioinformatics* **25**, 2078–2079 (2009).

55. Zang, C., Schones, D.E., Zeng, C., Cui, K., Zhao, K. and Peng, W. A clustering approach for identification of enriched domains from histone modification ChIP-Seq data. *Bioinformatics* **25**, 1952–1958 (2009).

56. Cole, J. J., Robertson, N. A., Rather, M. I., Thomson, J. P., McBryan, T., Sproul, D., Wang, T., Brock, C., Clark, W., Ideker, T. and Meehan, R. R. Diverse interventions that extend mouse lifespan suppress shared age-associated epigenetic changes at critical gene regulatory regions. *Genome Biol.* **18**, 1–16 (2017).

57. Zhu, L.J., Gazin, C., Lawson, N.D., Pagès, H., Lin, S.M., Lapointe, D.S. and Green, M.R. ChIPpeakAnno: a Bioconductor package to annotate ChIP-seq and ChIP-chip data. *BMC Bioinforma.* **11**, 1–10 (2010).

58. Kim, D., Pertea, G., Trapnell, C., Pimentel, H., Kelley, R. and Salzberg, S.L. TopHat2: accurate alignment of transcriptomes in the presence of insertions, deletions and gene fusions. *Genome Biol.* **14**, 1–13 (2013).

59. Wang, J., Vasaikar, S., Shi, Z., Greer, M. and Zhang, B. WebGestalt 2017: a more comprehensive, powerful, flexible and interactive gene set enrichment analysis toolkit. *Nucleic Acids Res.* **45**, W130–W137 (2017).

60. Martin, M. Cutadapt removes adapter sequences from high-throughput sequencing reads. *EMBnet.journal* **17**, 10–12 (2011).

61. Li, W., Xu, H., Xiao, T., Cong, L., Love, M.I., Zhang, F., Irizarry, R.A., Liu, J.S., Brown, M. and Liu, X.S. MAGeCK enables robust identification of essential genes from genome-scale CRISPR/Cas9 knockout screens. *Genome Biol.* **15**, 1–12 (2014).

62. Spahn, P.N., Bath, T., Weiss, R.J., Kim, J., Esko, J.D., Lewis, N.E. and Harismendy, O. PinAPL-Py: A comprehensive web-application for the analysis of CRISPR/Cas9 screens. *Sci. Reports* **7**, 1–8 (2017).

63. Blondel, V.D., Guillaume, J.L., Lambiotte, R. and Lefebvre, E. Fast unfolding of communities in large networks. *J. Stat. Mech. Theory Exp.* P10008 (2008).

64. Laarhoven, T. van & Marchiori, E. Robust Community Detection Methods with Resolution Parameter for Complex Detection in Protein Protein Interaction Networks. *IAPR International Conference on Pattern Recognition in Bioinformatics* **7632 LNBI**, 1–13 (2012).

65. Rosenthal, S.B., Len, J., Webster, M., Gary, A., Birmingham, A. and Fisch, K.M. Interactive network visualization in Jupyter notebooks: visJS2jupyter. *Bioinformatics* **34**, 126–128 (2018).

66. Xie, P., Gao, M., Wang, C., Zhang, J., Noel, P., Yang, C., Von Hoff, D., Han, H., Zhang, M.Q. and Lin, W. SuperCT: A supervised-learning-framework to enhance the characterization of single-cell transcriptomic profiles. *Nucleic Acids Res* **47,** e48-e48

(2019).

67. Trapnell, C., Roberts, A., Goff, L., Pertea, G., Kim, D., Kelley, D.R., Pimentel, H., Salzberg, S.L., Rinn, J.L. and Pachter, L. Differential gene and transcript expression analysis of RNA-seq experiments with TopHat and Cufflinks. *Nat. Protoc.* **7**, 562–578 (2012).

68. Pimentel, H., Bray, N. L., Puente, S., Melsted, P. and Pachter, L. Differential analysis of RNA-seq incorporating quantification uncertainty. *Nat. Methods* **14**, 687–690 (2017).

2.8. Supplemental figures

Figure 2.S2. Overlap of transcriptional and epigenetic features in pancreatic cancer tumor-initiating cells (related to Figure 2.2).
(A) Tumor organoid formation from primary isolated Musashi2+ and Musashi2- *KP$^{f/f}$C* tumor cells. Number of cells plated is indicated above representative images, scale = 200um.
(B) Limiting dilution frequency (left) calculated for *Msi2*+ (black) and *Msi2*- (red) organoid formation. Table (right) indicates cell doses tested in biological replicates.
(C and D) Gene set enrichment analysis (GSEA) of stem and non-stem gene signatures. Cell states (C), and corresponding heat-maps (D) of selected genes related to cell cycle. (C) Red denotes overlapping gene signatures; blue denotes non-overlapping gene signatures. (D) Red, over-represented gene expression; blue, under-represented gene expression; shades denote fold change from median values.
(E) Frequency of proliferating (Ki67+) *Msi2*+ (left) and *Msi2*- (right) tumor cells in untreated 10-12 week old REM2-*KP$^{f/f}$C* mice (n = 3), or treated with gemcitabine for 72 hours (n = 1) or 6 days (n = 1) prior to analysis; 200 mg/kg gemcitabine i.p. was delivered every 72 hours.
(F) Overlap of H3K27ac peaks and genomic features. For each genomic feature, frequency of H3K27ac peaks in stem cells (blue) and non-stem cells (gray) are represented as ratio of observed peak distribution/expected random genomic distribution.
(G and H) Concordance of H3K27ac peaks with RNA expression in stem cells (G; $p = 7.1x10^{-14}$) and non-stem cells (H; $p < 22x10^{-16}$). (I and J) Ratio of observed/expected overlap in gene expression and H3K27ac enrichment comparing stem and non-stem cells. Down/Up, gene expression enriched in non-stem/H3K27ac enriched in stem; Up/Down, gene expression enriched in stem/H3K27ac enriched in non-stem; Down/Down, both gene expression and H3K27ac enriched in non-stem; Up/Up, both gene expression and H3K27ac enriched in stem.

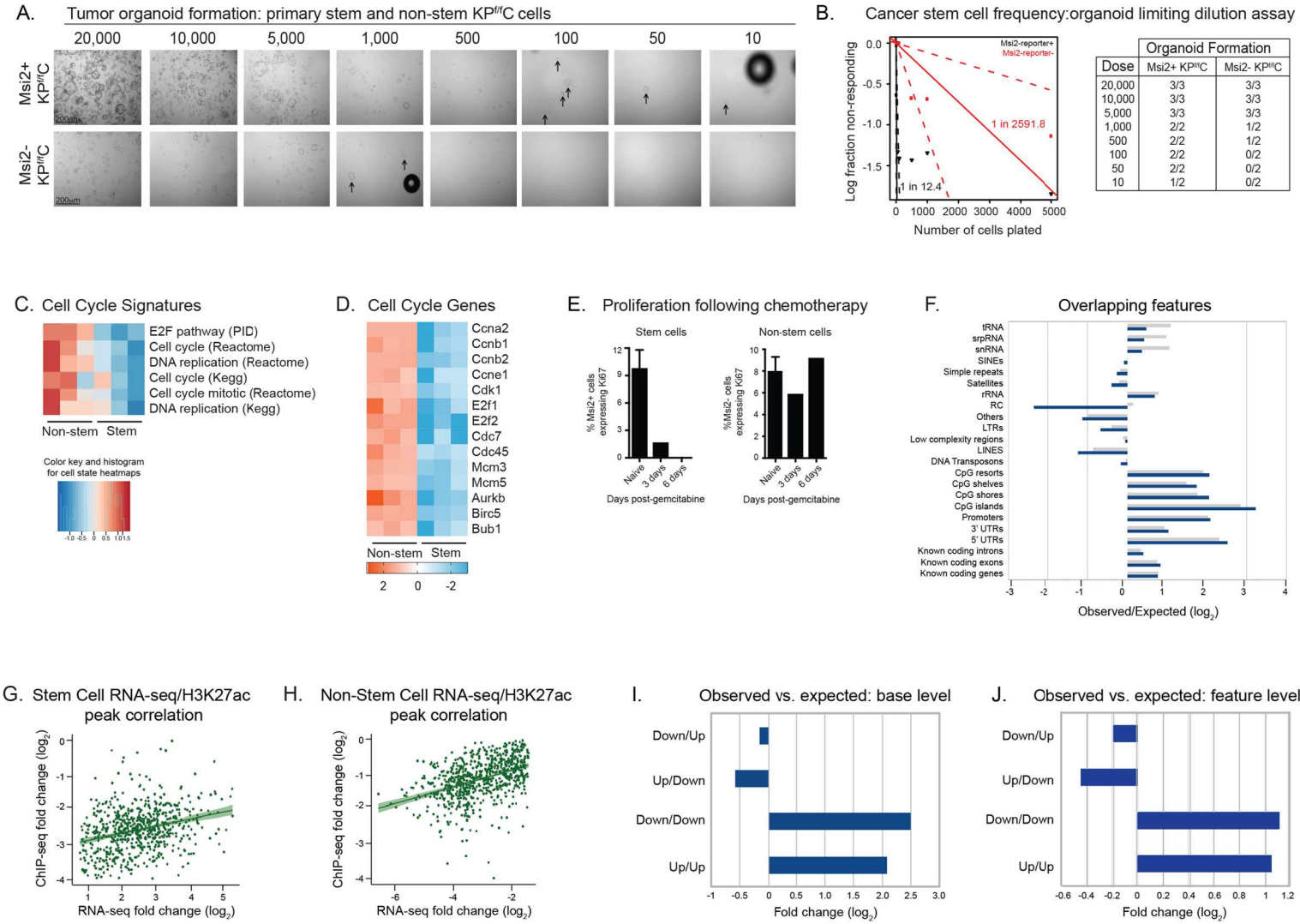
A.
Tumor organoid formation: primary stem and non-stem KP^f/fC cells
20,000
10,000
5,000
1,000
500
100
50
10
Msi2+ KP^f/fC
Msi2- KP^f/fC
200um
B.
Cancer stem cell frequency:organoid limiting dilution assay
Log fraction non-responding
Msi2-reporter+
Msi2-reporter-
1 in 2591.8
1 in 12.4
Number of cells plated
Organoid Formation
Dose | Msi2+ KP^f/fC | Msi2- KP^f/fC
20,000 | 3/3 | 3/3
10,000 | 3/3 | 3/3
5,000 | 3/3 | 3/3
1,000 | 2/2 | 1/2
500 | 2/2 | 1/2
100 | 2/2 | 0/2
50 | 2/2 | 0/2
10 | 1/2 | 0/2
C. Cell Cycle Signatures
E2F pathway (PID)
Cell cycle (Reactome)
DNA replication (Reactome)
Cell cycle (Kegg)
Cell cycle mitotic (Reactome)
DNA replication (Kegg)
Non-stem
Stem
Color key and histogram for cell state heatmaps
D. Cell Cycle Genes
Ccna2
Ccnb1
Ccnb2
Ccne1
Cdk1
E2f1
E2f2
Cdc7
Cdc45
Mcm3
Mcm5
Aurkb
Birc5
Bub1
Non-stem
Stem
E. Proliferation following chemotherapy
Stem cells
Non-stem cells
% Msi2+ cells expressing Ki67
%Msi2- cells expressing Ki67
Naive
3 days
6 days
Days post-gemcitabine
F. Overlapping features
tRNA
srpRNA
snRNA
SINEs
Simple repeats
Satellites
rRNA
RC
Others
LTRs
Low complexity regions
LINES
DNA Transposons
CpG resorts
CpG shelves
CpG shores
CpG islands
Promoters
3' UTRs
5' UTRs
Known coding introns
Known coding exons
Known coding genes
Observed/Expected (log2)
G. Stem Cell RNA-seq/H3K27ac peak correlation
ChIP-seq fold change (log2)
RNA-seq fold change (log2)
H. Non-Stem Cell RNA-seq/H3K27ac peak correlation
ChIP-seq fold change (log2)
RNA-seq fold change (log2)
I. Observed vs. expected: base level
Down/Up
Up/Down
Down/Down
Up/Up
Fold change (log2)
J. Observed vs. expected: feature level
Down/Up
Up/Down
Down/Down
Up/Up
Fold change (log2)

Figure 2.S3. Stem-specific map of core pancreatic cancer programs (related to Figure 2.3).
(A) Establishment of three independent REM2-*KP$^{f/f}$C* cell lines from end-stage REM2-*KP$^{f/f}$C* mice for genome-wide CRISPR-screen analysis. Stem cell content of freshly-dissociated REM2-*KP$^{f/f}$C* tumors (A, left), and after puromycin selection in standard growth conditions (A, right).
(B and C) Volcano plots of guides enriched in 2D (B, tumor suppressors) and 3D (C, negative regulators of stem cells). Genes indicated on plots, $p < 0.005$.
(D) Network propagation analysis integrating transcriptomic, epigenetic and functional analysis of stem cells. Genes enriched in stem cells by RNA-seq (ratio of stem to non-stem $\log_2$ fold-change > 2) and depleted in 3D stem cell growth conditions (FDR < 0.5) were used to seed the network (triangles), then analyzed for known and predicted protein-protein interactions and restricted to genes enriched in stem cells by RNA-seq (ratio of stem to non-stem $\log_2$ fold-change > 2). Each node represents a single gene; node color is mapped to the RNA-seq fold change; stem cell enriched genes in red. Labels shown for genes enriched in stem cells by RNA-seq (RNA $\log_2$FC absolute value > 3.0) or by RNA-seq and ChIP-seq (RNA Log_2FC absolute value > 2.0, ChIP-seq FDR < 0.01). Seven core programs were defined by groups of genes with high interconnectivity; each core program is annotated by Gene Ontology analysis (FDR < 0.05).

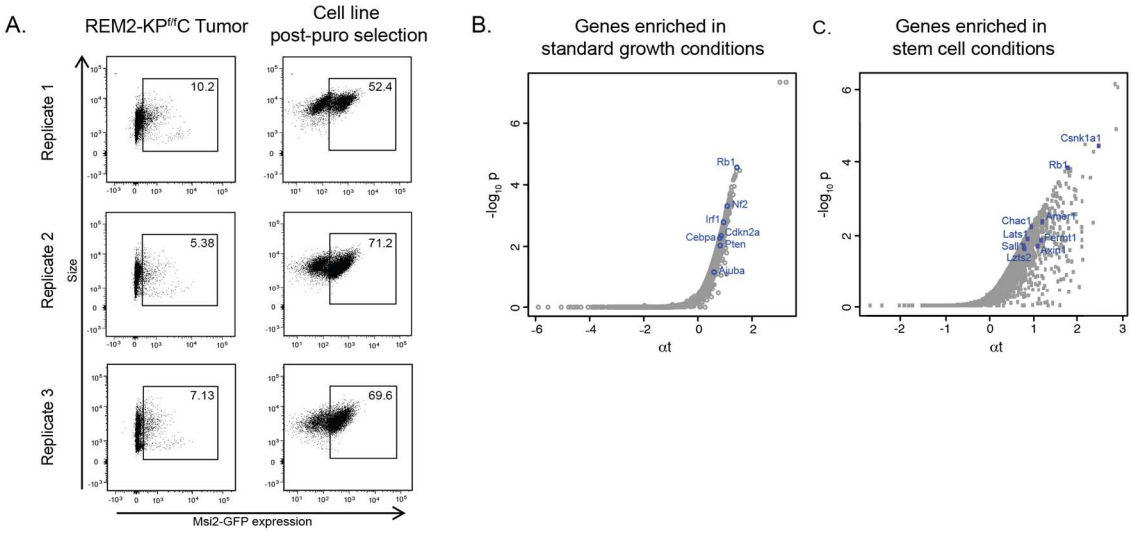

D. Network map restricted to genes enriched in stem cells

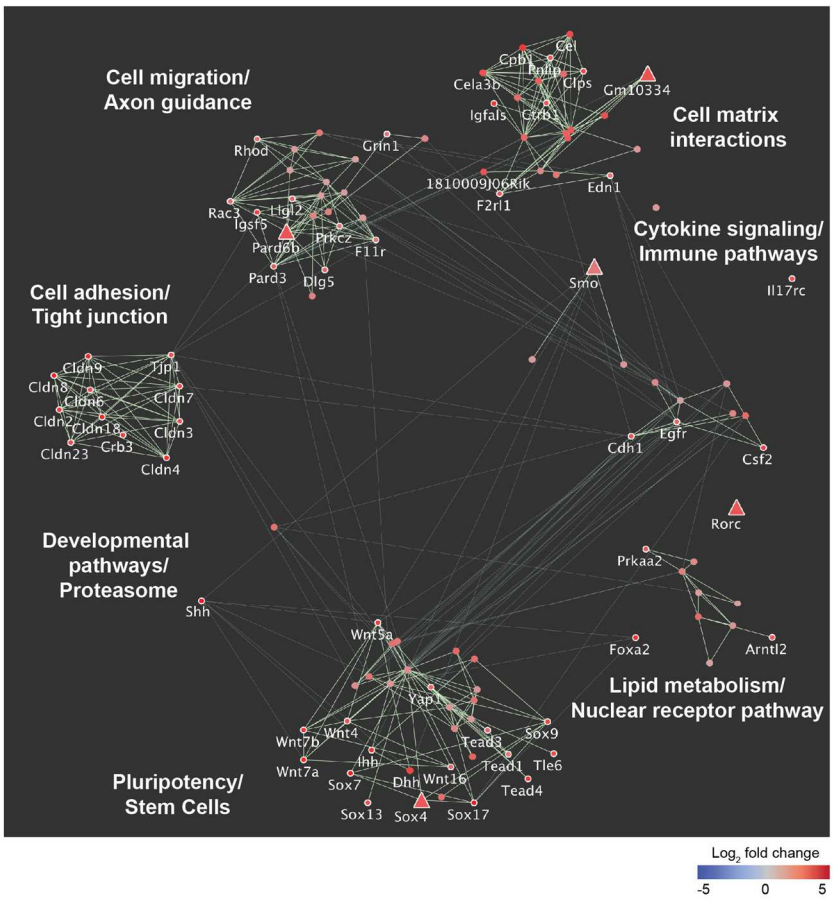

Figure 2.S4. Role of MEGF family and cytokine signals in pancreatic cancer (related to Figure 2.4)
(A and B) Sphere forming capacity of *KP$^{f/f}$C* cells following shRNA knockdown. Selected genes involved in stem and developmental processes (A) or cell adhesion, cell motility, and matrix components (B).
(C and D) Immunofluorescence analysis of Celsr1 (C) and Celsr2 (D) in EpCAM+ stem (CD133+) and non-stem (CD133-) primary tumor cells isolated from *KP$^{f/f}$C* mice. Three frames were analyzed per slide, and the frequency of Celsr1-high or Celsr2-high cells determined, scale = 25um.
(E) *KP$^{f/f}$C* cells were infected with shRNA against Pear1and protein knockdown efficiency determined five days post-transduction by western blot.
(F–H) Independent replicates for impact of shRNA inhibition of target genes on tumor growth *in vivo*. Celsr1 (F), Celsr2 (G), and Pear1 (H) were inhibited via shRNA delivery in *KP$^{f/f}$C* cells, and impact on tumor growth assessed by tracking flank transplants *in vivo*, n = 4 per condition.
(I) Pear1 was inhibited via shRNA in REM-KP$^{f/f}$C cells in sphere culture and impact on Msi+ stem cell content assessed by FACS, n = 3 per condition, p = 0.0629.
(J) Pear1 was inhibited via shRNA in *KP$^{f/f}$C* cells and impact on apoptosis in sphere culture as marked by Annexin-V assessed by FACS, n = 3 per condition.
(K) Heatmap of relative RNA expression of cytokines and related receptors in *KP$^{f/f}$C* stem and non-stem cells (left) and average RNA-seq TPM values in *Msi2*- and *Msi2*+ cells (right). Red, over-represented; blue, under-represented; color denotes fold change from median values.
(L) Single cell RNA Sequencing maps of *KP$^{R172H/+}$C* tumors. Tumor cells defined by expression of EpCAM (far left), Krt19 (left center), Cdh1 (right center), and Cdh2 (far right).
(**M)** Left, *KP$^{R172H/+}$C* tumor single-cell sequencing map of cells expressing Msi2 within the EpCAM+ tumor cell fraction. Right, *KP$^{R172H/+}$C* tumor single-cell sequencing map of cells expressing IL-10Rβ, IL-34, and CSF1R within the EpCAM+Msi2+ stem cell fraction.
(N) Cytokine receptors IL-10Rβ and CSF1R were inhibited by shRNA delivery in KP$^{f/f}$C cells and plated in sphere culture for one week. Increased apoptosis in *KP$^{f/f}$C* cells with shIL10Rb ($p < 0.05$) and shCSF1R (trend). Frequency of apoptotic cells determined by Annexin-V staining and FACS analysis, n = 3 per condition.
(O) Representative FACS plots for stem content analysis *in vitro*. IL-10rβ and Csf1R were inhibited via shRNA delivery in *KP$^{f/f}$C* cells, and impact on stem content (*Msi2-GFP*+ cells) in sphere culture assessed by FACS, n = 3 per condition.
(P and Q) Independent replicates for impact of shRNA inhibition of target genes on tumor growth *in vivo*. IL-10Rβ (P) and CSF1R (Q) were inhibited via shRNA delivery in KP$^{f/f}$C cells, and impact on tumor growth assessed by tracking flank transplants *in vivo*, n = 4 per condition.
(R) ELISA based quantification (Quantikine, R&D Systems) of IL-10, IL-34, and CSF-1 in media (left) and *KP$^{f/f}$C* cell lystate (right). Cytokines were quantified in fresh sphere culture media, *KP$^{f/f}$C* stem and non-stem cell conditioned media, and *KP$^{f/f}$C* epithelial cell lysate. Conditioned media was generated by culturing sorted CD133- or CD133+ *KP$^{f/f}$C* cells in sphere media for 48 hours; media was filtered and assayed immediately. Cell lysate was collected in RIPA buffer and assayed at 2 mg/mL for ELISA. n = 3 per condition.
Data represented as mean ± SEM. $^{*}p < 0.05$, $^{**}p < 0.01$ by Student's t test or One-way ANOVA.

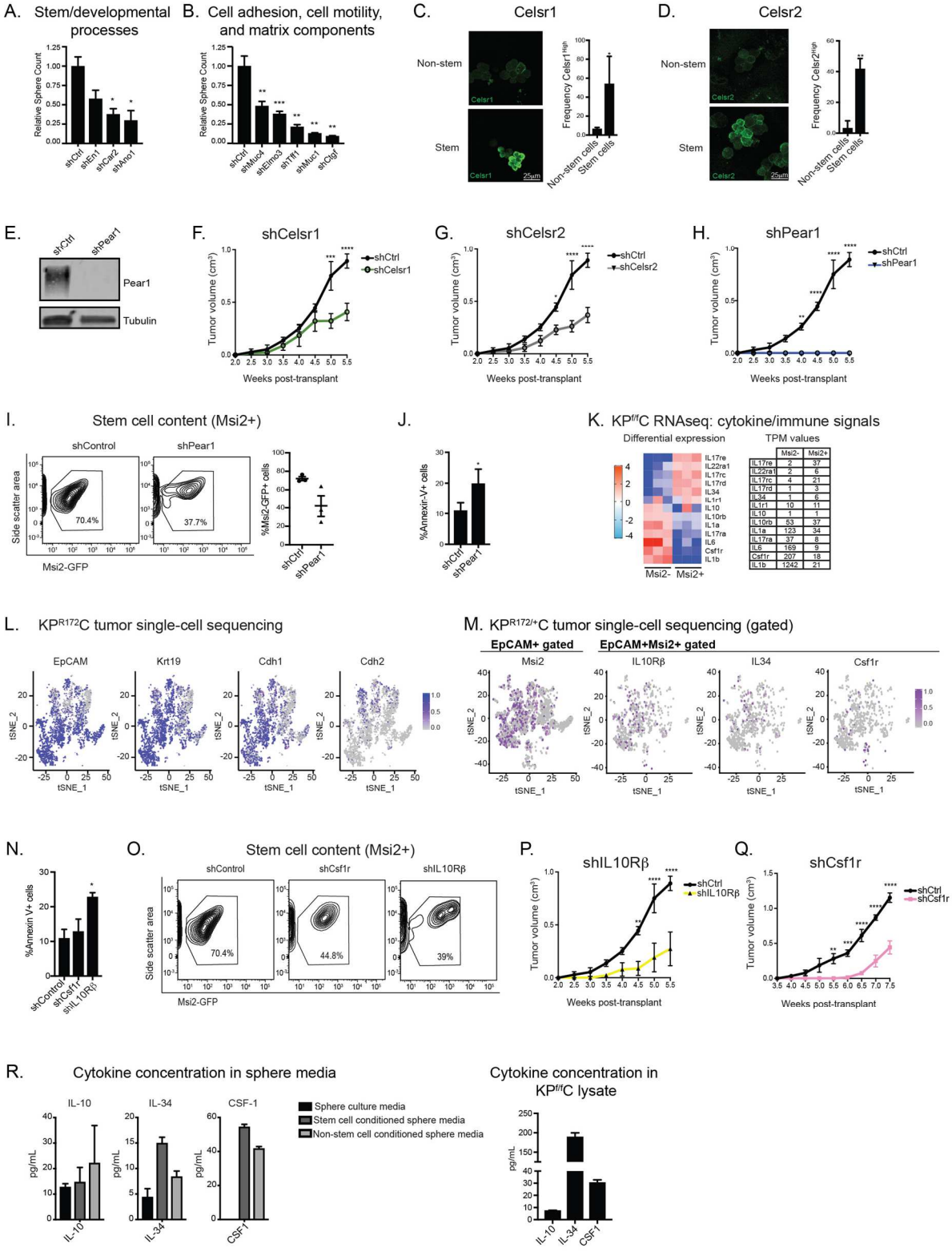
A. Stem/developmental processes
B. Cell adhesion, cell motility, and matrix components
C. Celsr1
D. Celsr2
E.
F. shCelsr1
G. shCelsr2
H. shPear1
I. Stem cell content (Msi2+)
J.
K. KP^f/fC RNAseq: cytokine/immune signals
L. KP^R172C tumor single-cell sequencing
M. KP^R172/+C tumor single-cell sequencing (gated)
N.
O. Stem cell content (Msi2+)
P. shIL10Rβ
Q. shCsf1r
R. Cytokine concentration in sphere media
Cytokine concentration in KP^f/fC lysate

Figure 2.S5. RORγ Is enriched in epithelial tumor stem cells and regulates tumor propagation in pancreatic cancer (related to Figure 2.5), Continued
(A) Heatmap of transcription factors in *KP$^{f/f}$C* stem and non-stem identified as possible pancreatic cancer stem cell dependencies within the network map (see Figure 2.3 E). Red, over-represented; blue, under-represented; color denotes fold change from median values.
(B) Distribution of RORγ consensus binding sites in genomic regions associated with H3K27ac. Down/Down, both gene expression and H3K27ac enriched in non-stem cells; Up/Up, both gene expression and H3K27ac enriched in stem cells.
(C) Biological replicates showing qPCR analysis of RORγ expression in primary *KP$^{f/f}$C* stem and non-stem tumor cells isolated from REM2-*KP$^{f/f}$C* mice.
(D) Immunofluorescence analysis of RORγ in primary *KP$^{f/f}$C* EpCAM+ CD133+ and CD133- tumor cells. Three frames were analyzed per slide, and the frequency of RORγ -high cells determined.
(E) *KP$^{f/f}$C* tumor single-cell sequencing map of cells expressing RORγ within the EpCAM+Msi2+ cell fraction (n = 3 mice represented).
(F) RORγ expression within E-Cadherin- stromal cells in patient samples.
(G) *Il1r1* was inhibited by CRISPR-mediated deletion in *KP$^{f/f}$C* cells, and impact on *Rorc* expression assessed by qPCR. Two distinct guide RNAs (sgIL1r1-1 and sgIL1r1-2) were used to knockout *Il1r*; expression was quantified by qPCR and is shown relative to control (non-targeting guide RNA), n = 3 per condition.
(H) Knockdown efficiency of RORγ in *KP$^{f/f}$C* cells infected with *Rorc* shRNA determined five days post-transduction. Relative expression in western blots quantified relative to tubulin loading control.
(I) Impact of shRNA-mediated RORγ inhibition on apoptosis and proliferation of in *KP$^{f/f}$C* cells in 3D culture n = 3.
(J) Independent replicate of shRNA *Rorc* impact on *KP$^{f/f}$C* tumor propagation as assessed by tracking flank transplants *in vivo*, n = 4 per condition.
(K–M) Super-enhancer analysis of shRorc *KP$^{f/f}$C* cells. *KP$^{f/f}$C* cells were infected with shRorc, and used for H3K27ac ChIP-seq and super-enhancer analysis, schematic (K). H3K27ac peaks were analyzed to assess super-enhancer overlap in shCtrl and shRorc samples (L). Super-enhancers lost in shRorc samples were crossed to stem-enriched and stem-unique super-enhancers identified in primary *Msi2-GFP+ KP$^{f/f}$C* tumors cells, and further restricted to super-enhancers containing RORγ binding motifs (M). Majority of super-enhancer landscape remained unchanged with RORγ loss, and landscape changes that did occur were not enriched in super-enhancers with RORγ binding sites. ChIP-seq analysis was conducted in two independent *KP$^{f/f}$C* cell lines.
Data represented as mean ± SEM. $^{*}p < 0.05$, $^{**}p < 0.01$, $^{***}p < 0.001$ by Student's t test or One-way ANOVA.

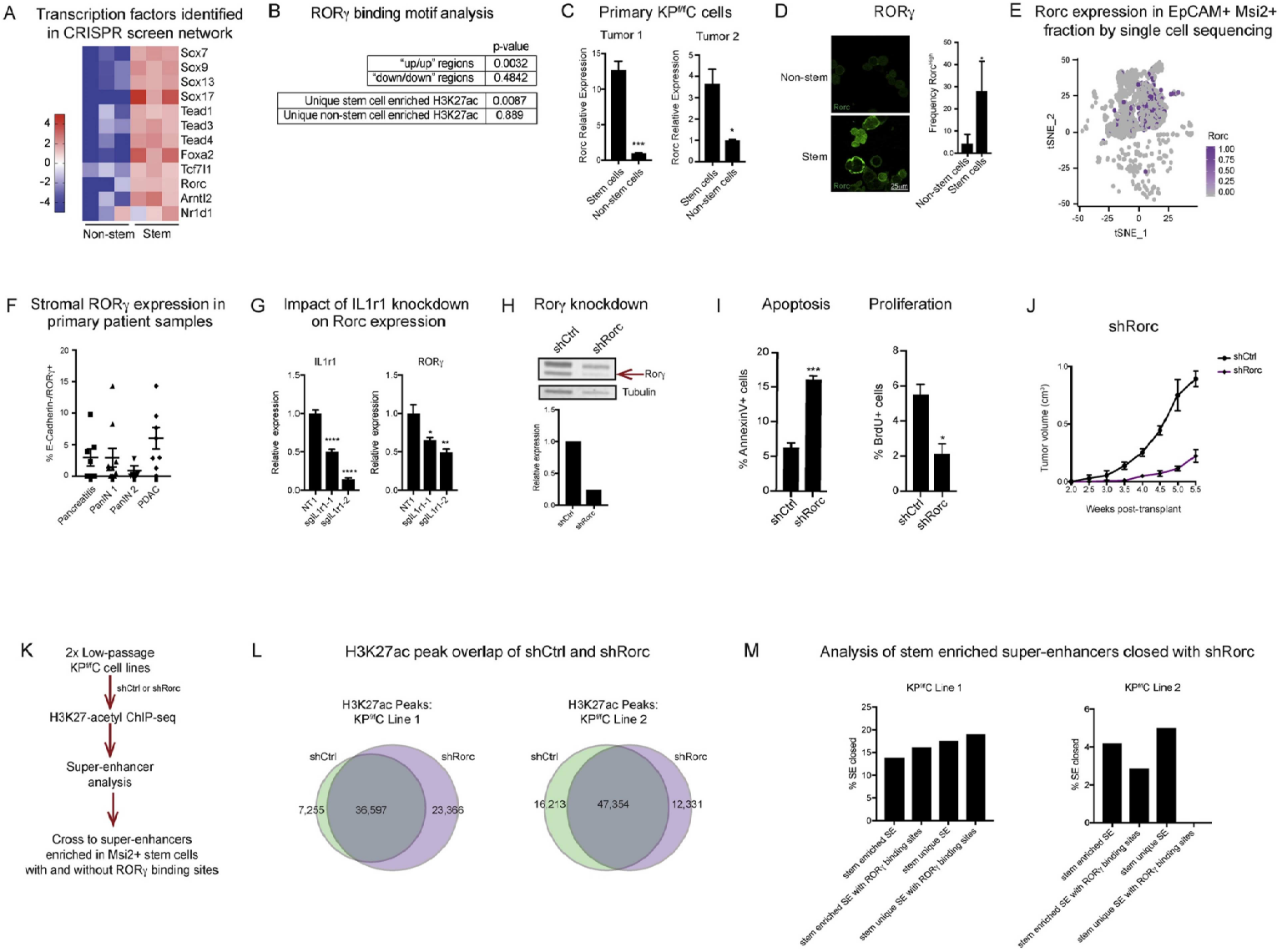
A
Transcription factors identified in CRISPR screen network
Sox7
Sox9
Sox13
Sox17
Tead1
Tead3
Tead4
Foxa2
Tcf7l1
Rorc
Arntl2
Nr1d1
Non-stem
Stem
B
RORγ binding motif analysis
p-value
"up/up" regions 0.0032
"down/down" regions 0.4842
Unique stem cell enriched H3K27ac 0.0087
Unique non-stem cell enriched H3K27ac 0.889
C
Primary KP^flC cells
Tumor 1
Tumor 2
Rorc Relative Expression
Stem cells
Non-stem cells
D
RORγ
Non-stem
Stem
Rorc
25um
Frequency Rorc^high
E
Rorc expression in EpCAM+ Msi2+ fraction by single cell sequencing
tSNE_1
tSNE_2
Rorc
F
Stromal RORγ expression in primary patient samples
% E-Cadherin-/RORγ+
Pancreatitis
PanIN 1
PanIN 2
PDAC
G
Impact of IL1r1 knockdown on Rorc expression
IL1r1
RORγ
Relative expression
NT1
sgIL1r1-1
sgIL1r1-2
H
Rorγ knockdown
shCtrl
shRorc
Rorγ
Tubulin
Relative expression
I
Apoptosis
% AnnexinV+ cells
Proliferation
% BrdU+ cells
J
shRorc
shCtrl
shRorc
Tumor volume (cm³)
Weeks post-transplant
K
2x Low-passage KP^flC cell lines
shCtrl or shRorc
H3K27-acetyl ChIP-seq
Super-enhancer analysis
Cross to super-enhancers enriched in Msi2+ stem cells with and without RORγ binding sites
L
H3K27ac peak overlap of shCtrl and shRorc
H3K27ac Peaks: KP^flC Line 1
shCtrl
shRorc
7,255
36,597
23,366
H3K27ac Peaks: KP^flC Line 2
16,213
47,354
12,331
M
Analysis of stem enriched super-enhancers closed with shRorc
KP^flC Line 1
KP^flC Line 2
% SE closed
stem enriched SE
stem enriched SE with RORγ binding sites
stem unique SE
stem unique SE with RORγ binding sites

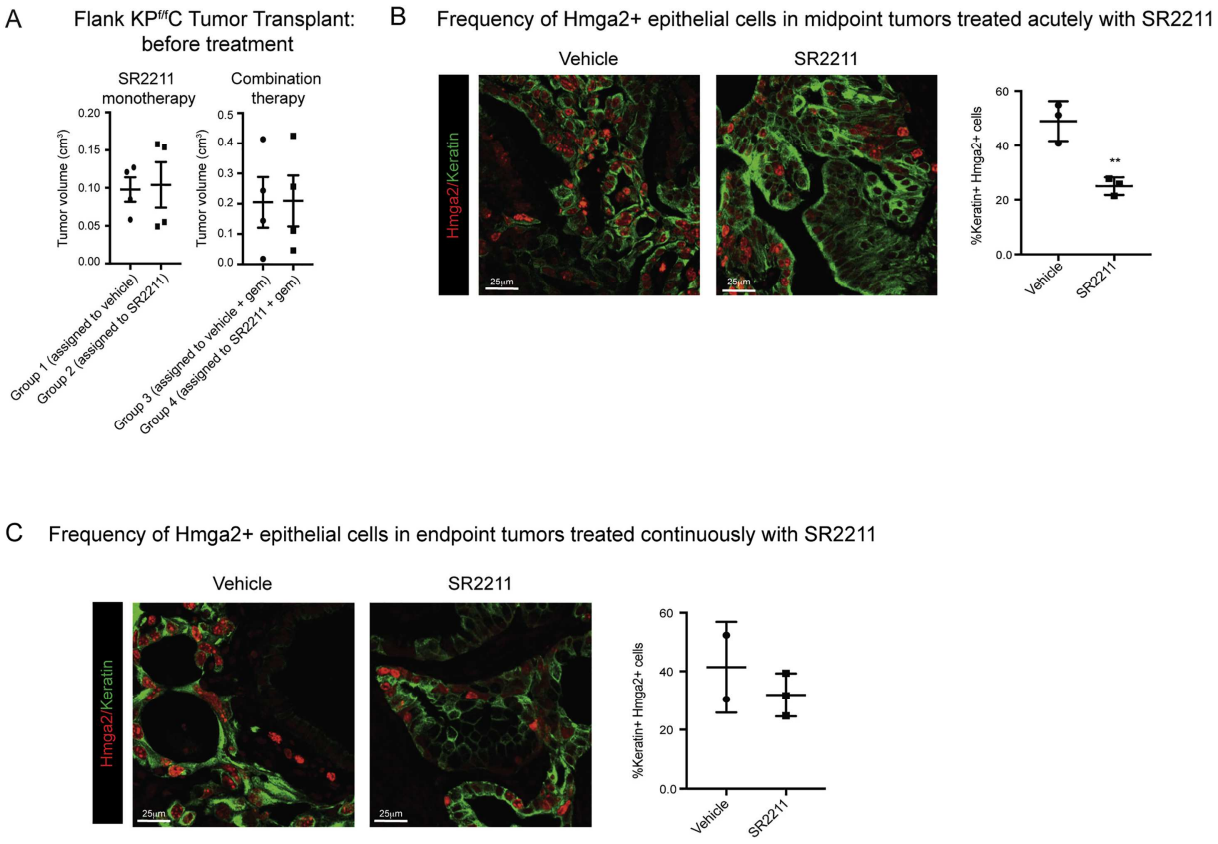

Figure 2.S6. RORγ target engagement *in vivo* (related to Figure 2.6).
(A) Size of flank KP$^{f/f}$C tumors in immunocompetent mice prior to enrollment into RORγ targeted therapy. Group 1, vehicle; group 2, SR2211; group 3, vehicle + gemcitabine; group 4, SR2211 + gemcitabine.
(B) Target engagement following acute RORγ inhibition *in vivo*. 9.5 week tumor-bearing *KP$^{f/f}$C* mice were treated with vehicle or SR2211 for two weeks (midpoint), after which tumors were isolated, fixed, and analyzed for target engagement of HMGA2 in epithelial cells by immunofluorescence. Representative images (left) and quantification (right) of HMGA2+ Keratin+ epithelial cells in vehicle or SR2211 treated tumors. Four frames were analyzed per mouse, n = 2-4 mice per condition, HMGA2 (red), Keratin (green), scale = 25um.
(C) Target engagement in endpoint tumors following continuous RORγ inhibition *in vivo*. 8 week tumor-bearing *KP$^{f/f}$C* mice were treated till endpoint with either vehicle or SR2211, after which tumors were isolated, fixed, and analyzed for target engagement of HMGA\2 in epithelial cells by immunofluorescence. Representative images (left) and quantification (right) of HMGA2+ Keratin+ epithelial cells in vehicle or SR2211 treated tumors. Four frames were analyzed per mouse, n = 2-4 mice per condition, HMGA2 (red), Keratin (green).
Data represented as mean ± SEM. $^{*}p < 0.05$, $^{**}p < 0.01$, $^{***}p < 0.001$ by Student's t test or One-way ANOVA. Grubb's test (p = 0.1) was used to remove an outlier from the midpoint SR2211 treated group, scale = 25um.

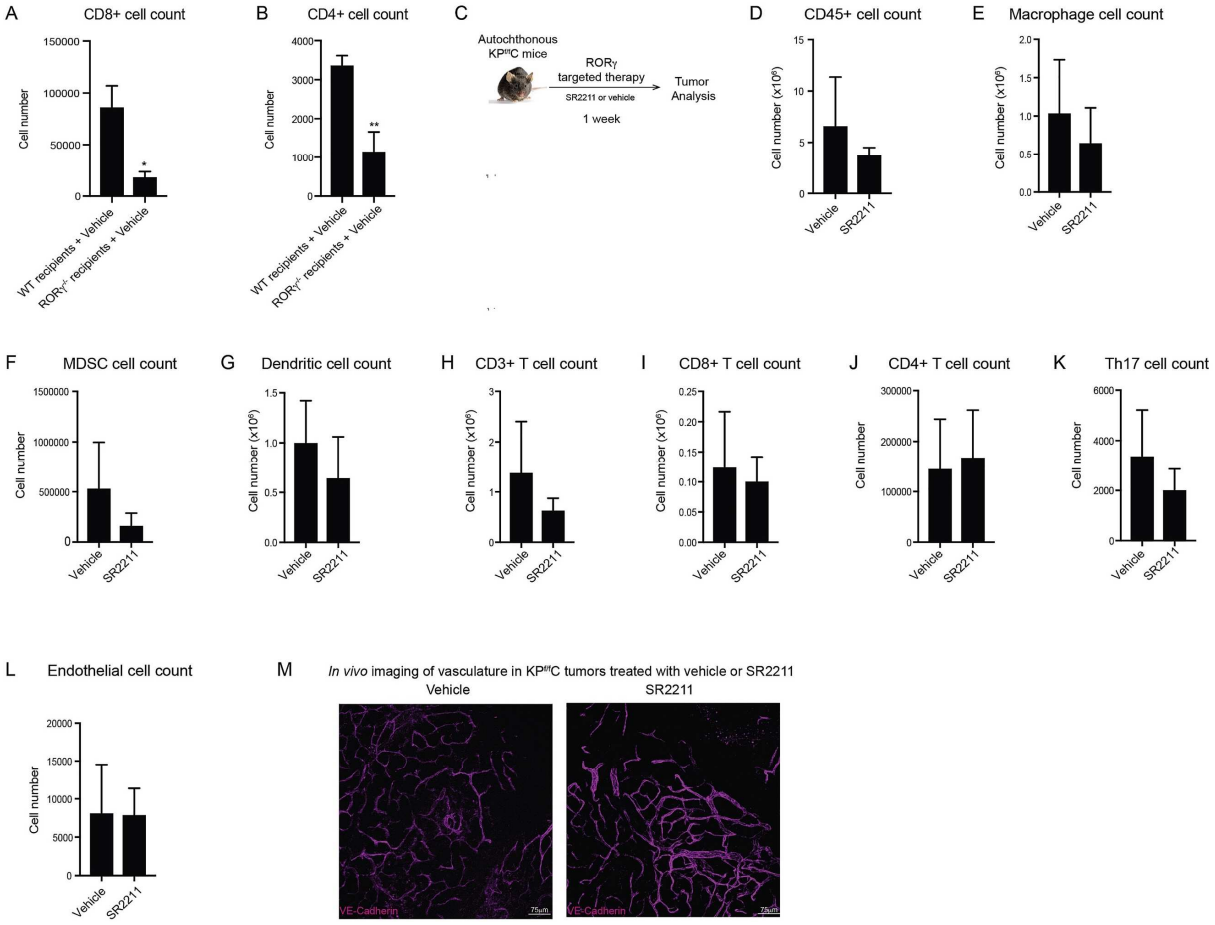

Figure 2.S7. Impact of RORγ inhibition on neoplastic cells (related to Figure 2.7)
(A and B) Analysis of T cell subsets in *KP$^{f/f}$C* tumors transplanted into wild-type or Rorc-knockout recipient mice (vehicle-treated groups shown). Absolute cell numbers of the following populations were evaluated: (A) CD45+/CD3+/CD8+ or CD8+ T cells, (B) CD45+/CD3+/CD4+ or CD4+ T cells.
(C–L) FACS analysis of non-neoplastic cell populations in autochthonous tumors from KP$^{f/f}$C mice treated with vehicle or SR2211 for 1 week. Schematic I. Absolute cell numbers of the following populations were evaluated: CD45+ cells (D), CD11b+/F480+ cells (macrophage) I, CD11b+/Gr-1+ cells (MDSC) (F), CD11c+ cells (dendritic) (G), CD45+/CD3+ T cells (H), CD3+/CD8+ T cells (I), CD3+/CD4+ T cells (J), CD4+/IL-17+ Th17 cells (K), CD31+ cells (endothelial) (L). (n = 3 per condition).
(M) *In vivo* imaging of tumor vasculature of *KP$^{f/f}$C* mice treated with vehicle or SR2211. Vasculature is marked by *in vivo* delivery of anti-VE-Cadherin (magenta), scale = 75um.
Data represented as mean ± SEM. *p < 0.05 by Student's t test or One-way ANOVA.

Figure 2.S8. Analysis of downstream targets of RORγ in murine and human pancreatic cancer cells identifies shared pro-tumorigenic cytokine pathways (related to Figure 2.8).
(A–D) Gene ontology and gene set enrichment analysis of RNA-seq in human and mouse pancreatic cancer cells to identify common genes and pathways regulated by RORγ. Gene ontology analysis of *KP$^{f/f}$C* RNA-seq showing genes downregulated with shRorc were enriched for cytokine-mediated signaling pathway GO term (A). Differentially expressed genes in KP$^{f/f}$C within cytokine-mediated signaling pathway (B) were crossed with differentially expressed genes identified by RNA-seq analysis of human pancreatic cancer cells (FG) where RORC was knocked out using CRISPR. Gene set enrichment analysis of mouse and human RNA-seq shows common cytokine gene sets regulated by Rorc across species (D).
(E) Analysis of CRISPR guide depletion in stem cell conditions for super-enhancer-associated genes expressed in stem or non-stem cells.
Data represented as mean ± SEM. $^{*}p < 0.05$, $^{**}p < 0.01$, $^{***}p < 0.001$ by Student's t test or One-way

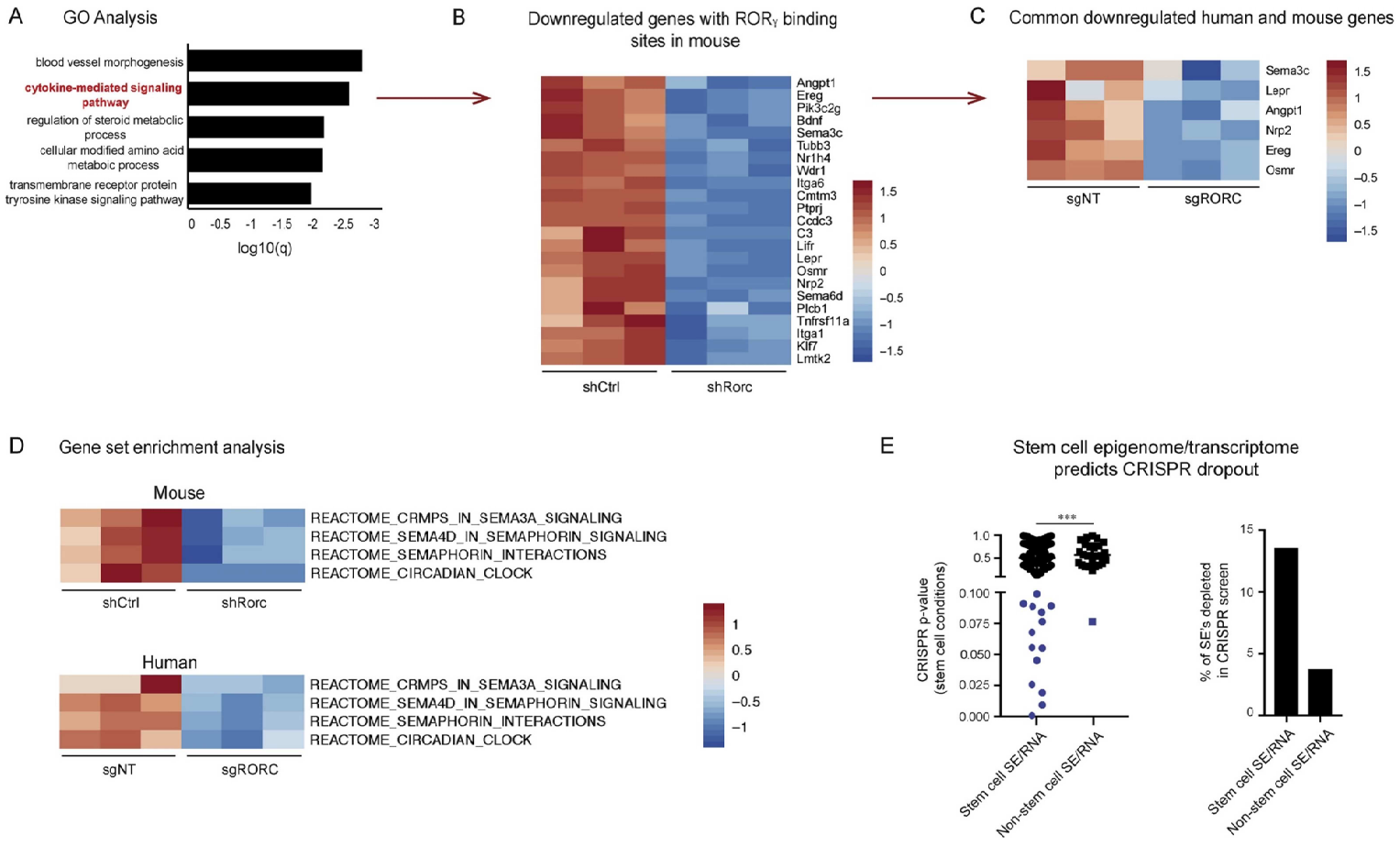
A
GO Analysis
blood vessel morphogenesis
cytokine-mediated signaling pathway
regulation of steroid metabolic process
cellular modified amino acid metabolic process
transmembrane receptor protein tyrosine kinase signaling pathway
0 -0.5 -1 -1.5 -2 -2.5 -3
log10(q)
B
Downregulated genes with RORγ binding sites in mouse
Angpt1
Ereg
Pik3c2g
Bdnf
Sema3c
Tubb3
Nr1h4
Vdr1
Itga6
Cmtm3
Ptprj
Ccdc3
C3
Lifr
Lepr
Osmr
Nrp2
Sema6d
Plcb1
Tnfrsf11a
Itga1
Klf7
Lmtk2
1.5
1
0.5
0
−0.5
−1
−1.5
shCtrl
shRorc
C
Common downregulated human and mouse genes
Sema3c
Lepr
Angpt1
Nrp2
Ereg
Osmr
1.5
1
0.5
0
−0.5
−1
−1.5
sgNT
sgRORC
D
Gene set enrichment analysis
Mouse
REACTOME_CRMPS_IN_SEMA3A_SIGNALING
REACTOME_SEMA4D_IN_SEMAPHORIN_SIGNALING
REACTOME_SEMAPHORIN_INTERACTIONS
REACTOME_CIRCADIAN_CLOCK
shCtrl
shRorc
Human
REACTOME_CRMPS_IN_SEMA3A_SIGNALING
REACTOME_SEMA4D_IN_SEMAPHORIN_SIGNALING
REACTOME_SEMAPHORIN_INTERACTIONS
REACTOME_CIRCADIAN_CLOCK
sgNT
sgRORC
1
0.5
0
−0.5
−1
E
Stem cell epigenome/transcriptome predicts CRISPR dropout
***
CRISPR p-value (stem cell conditions)
1.0
0.5
0.100
0.075
0.050
0.025
0.000
Stem cell SE/RNA
Non-stem cell SE/RNA
% of SE's depleted in CRISPR screen
15
10
5
0
Stem cell SE/RNA
Non-stem cell SE/RNA

2.9. Supplemental information

Table 2.1. Gene Set Enrichment Analysis of *KP$^{f/f}$C* stem and non-stem cell RNA-seq

Table 2.2. Super enhancer analysis of *KP$^{f/f}$C* H3K27ac ChIP-Seq

Table 2.3. Selected genes from stem cell networks (related to Figure 2.3)

Table 2.4. Selected novel genes in pancreatic cancer (related to Figure 2.4)

Gene	Known function/role	*In vitro* sphere formation	*In vivo* tumor growth
Cell Adhesion			
Celsr1 Celsr2/Megf3	G protein-coupled adhesion receptors; epithelial planar cell polarity, early embryogenesis	✓	✓
Pear1/JEDI/Megf12	Adhesion and signaling receptor; platelet aggregation	✓	✓
Megf10	Adhesion and signaling receptor; clearance of apoptotic cells, synapse remodeling, muscle differentiation	✓	ND
Metabolism			
Lpin2	Phosphatidic acid phosphatase; lipid biosynthesis	✓	ND
Developmental Pathways			
Onecut3	Transcription factor; neuronal development	✓	ND
Tdrd3	Transcriptional co-activator and auxiliary factor for topoisomerase IIIb; epigenetic regulation	✓	ND

✓: impact observed following shRNA-mediated inhibition
ND: not determined

Table 2.5. Clinical and tool compound antagonists (related to Figures 2.4 and 2.5).
Table includes select novel drug targets in pancreatic cancer, and indicates the impact of target inhibition by the indicated antagonist *in vitro* and *in vivo* pancreatic cancer cell growth. Check marks indicate the extent of growth suppression observed in the indicated assay; -, no detectable response; ND, not determined.

Target	Core program	Known function	Drug/Compound	*In vitro* sphere formation	*In vivo* tumor growth
RORg	Immune/cytokine signaling	Nuclear receptor	SR2211	✓✓✓✓	✓✓
IL-10	Immune/cytokine signaling	Cytokine	AS101	✓✓✓	-
Dusp	Developmental pathways	Phosphatase	BCI	✓✓	-
Wnk4	Developmental pathways	Serine/threonine kinase	Wnk463	✓✓	ND
Myo5	Cell motility/migration	Myosin	Pentabromopseudilin	✓✓	ND
IL-7	Immune/cytokine signaling	Cytokine	Anti-IL7	✓	-
CD83	Immune/cytokine signaling	Ig superfamily membrane protein	GC7	✓	ND
Cxcl2	Immune/cytokine signaling	Chemokine	Danirixin	-	ND
Drd2/3	Immune/cytokine signaling	Dopamine receptor	Eticlopride	-	-

✓✓✓✓: dose response observed; growth suppressed by 8-fold or more relative to control
✓✓✓: dose response observed; growth suppressed between 4-fold and 8-fold relative to control
✓✓: dose response observed; growth suppressed less than 4-fold relative to control
✓: response observed only at highest drug dose tested
- : no detectable response
ND: not determined

Table 2.6. PDAC patients' characteristics (n = 116) (related to Figure 2.8)

Table 2.7. Average knockdown efficiency for all target genes.

Gene name	shRNA-I	shRNA-II	shRNA-III
Mouse			
Onecut3	71.6%	68.9%	-
Tdrd3	73.9%	58.0%	-
Dusp9	43.8%	66.8%	68.0%
En1	78.9%	-	-
Car2	95.1%	73.2%	-
Ano1	47.7%	61.1%	-
Sptssb	76.3%	35.1%	79.4%
Lpin2	79.3%	80.0%	81.6%
Myo10	72.1%	-	-
Sftpd	84.9%	35.2%	97.2%
Pkp1	57.6%	-	-
Lama5	98.0%	94.3%	97.4%
Myo5b	72.0%	60.0%	-
Muc4	66.7%	96.5%	-
Elmo3	97.1%	75.3%	-
Tff1	73.1%	94.8%	98.1%
Muc1	56.1%	70.3%	-
Ctgf	60.7%	57.9%	-
Megf10	54.7%	37.7%	-
Celsr1	61.9%	87.4%	-
Celsr2	63.8%	64.9%	-
Pear1	52.2%	90.8%	-
Csf1r	60.7%	97.9%	-
IL10rb	96.6%	95.1%	-
IL10	54.2%	69.6%	-
IL34	93.4%	80.7%	-
Rorc	81.6%	93.8%	98.5%
Human			
IL10rb	99.5%	98.2%	-
Pear1	100.0%	-	-

Chapter 3. SMARCD3 is a key epigenetic dependency for pancreatic adenocarcinoma

3.1. Abstract

Pancreatic cancer is characterized by extensive resistance to conventional therapies, making clinical management a challenge. Here we have explored the epigenetic dependencies of cancer stem cells, the population of cells that preferentially evade therapy and drive progression, and identified SMARCD3, a member of the SWI/SNF complex, as a critical dependency. Although SWI/SNF subunits often act as tumor suppressors, we show that *SMARCD3* is in fact amplified in cancer, uniquely enriched in pancreatic cancer stem cells and upregulated in human pancreatic tumors. Diverse genetic mouse models of pancreatic cancer that enabled stage-specific *Smarcd3* deletion revealed that *Smarcd3* dependency is bimodal, with a preferential impact in established tumors, improving survival and chemosensitivity *in vivo.* Mechanistically, *Smarcd3* inhibition acted together with FOXA1 to shift the metabolic dependencies in cancer cells, impairing lipid and fatty acid metabolism programs, which are associated with therapy resistance and poor prognosis in cancer. Collectively, these data identify SMARCD3 as a critical epigenetic dependency responsible for establishing the metabolic landscape in aggressive pancreatic cancer cells and a potential target for new therapies.

3.2. Introduction

Pancreatic ductal adenocarcinoma (pancreatic cancer, PDAC) is a highly lethal disease with poor clinical outcomes. Currently the 3rd leading cause of cancer-related deaths, pancreatic cancer is predicted to become the 2nd leading cause in the United States by 2030 and has a five-year survival rate of only 10%[1,2]. Mortality is usually driven by characteristically late diagnosis, early metastasis, and resistance to conventional and targeted therapies[3,4,5,6,7].

Understanding the molecular programs that underpin the growth of therapy-resistant cells remains a crucial priority for developing new strategies for pancreatic cancer treatment[8]. Previous work has shown that therapy resistance is driven by differential responses to conventional agents fueled by the heterogeneity of tumor cells[9]; in particular, subpopulations that harbor stem cell characteristics are highly enriched for therapy resistance[10,11,12,13,14,15]. As in development, the undifferentiated state of these cells is driven in large part by epigenomic shifts rather than genetic changes[16,17,18]. But how these epigenetic changes are regulated, and how these regulatory programs shift as cancer cells become established during disease progression remains relatively unexplored. Given the reliance of these aggressive cells on epigenetic regulation, identifying chromatin-level drivers and the mechanisms by which they support the stem cell state in cancer is key to better understanding therapy resistance.

To define the epigenetic programs that may be leveraged by therapy-resistant pancreatic cancer stem cells to enforce their fate and function, we used a curated functional screen that led to the identification of SMARCD3 as a novel epigenetic dependency in PDAC. *Smarcd3* encodes the Baf60c subunit of SWI/SNF, a nucleosome remodeling complex that coordinates state-specific enhancers and is required for stem cell function in development[19,20,21]. This modular complex has many variable compositions, enabling the execution of cell state-specific programs by unique SWI/SNF assemblies[22]. Although a limited number of studies have identified cancer stem cell functions for SWI/SNF *in vivo*[23,24,25,26], we are only beginning to understand the SWI/SNF subunits preferentially required to support stem cell fate, and the mechanisms by which these chromatin remodelers control core functional programs in cancer. Further, as emerging research has revealed the highly context-specific roles of SWI/SNF subunits in cancer, determining how SWI/SNF dependencies vary across tissue and disease stage may enable the appropriate design of epigenetic therapies. As technology for targeting these proteins advances, identifying and targeting SWI/SNF subunits

with stem-specific functions in cancer could have far-reaching impacts on cancer therapy[27,28,29].

Here, we show that *Smarcd3* is uniquely upregulated in the stem cell fraction of mouse pancreatic tumors, and is further amplified and enriched in human pancreatic tumors[30]. Functionally, *Smarcd3* had a bimodal impact *in vivo*; we used diverse stage-specific conditional genetic models to show that *Smarcd3* deletion drives ductal-specific tumorigenesis at initiation, while conversely improving survival and synergizing with chemotherapy in tumors post-establishment, acting as a context-specific dependency in pancreatic cancer. Consistent with this, SMARCD3 was required for the propagation of patient-derived tumors *in vitro* and *in vivo*. Mechanistically, comprehensive ChIP-seq and RNA-seq analysis showed that *Smarcd3* inhibition drove global losses in SWI/SNF binding and histone acetylation at active enhancers co-bound by FOXA1, downregulating a network of genes implicated in lipid homeostasis. Functionally, loss of *Smarcd3* blunted fatty acid metabolism *in vivo,* positioning SMARCD3 as a new epigenetic regulator of fatty acid metabolism, which has been associated with stem cell signaling, therapy resistance, and poor prognosis in cancer[31,32,33]. Collectively these data identify SMARCD3 as a SWI/SNF subunit that is uniquely required for the growth of aggressive cancer stem cells and exerts its influence by regulating the metabolic landscape in pancreatic cancer.

3.3 Results

SMARCD3 is a functional epigenetic dependency of PDAC stem cells

To define epigenetic and transcriptional regulatory programs required for PDAC stem cell function, we used an RNA-sequencing (RNA-seq) dataset[16] to identify factors significantly enriched in the therapy-resistant Msi2+ stem cell fraction[14] of primary tumors from the *Kras$^{G12D/+}$; p53$^{f/f}$; Ptf1a-Cre* (*KP$^{f/f}$C*) model of pancreatic cancer (Figure 3.1 A)[34,35,36,37]. To assess their impact, we conducted a targeted functional screen using primary cancer stem

cells derived from *Msi2-GFP* reporter *KP$^{f/f}$C* tumors (Figure 3.1 B)[14], where cells were transduced with lentiviral shRNA or sgRNA, and growth was analyzed in sphere-forming conditions[38]. Master transcription factors and histone deacetylases such as *Klf4*[39], *Oct4*[40], *Sox9*[41], *Hdac11*[42] and *Hdac7*[43] were required for the growth of PDAC stem cells, serving as controls (Figure 3.1 C). Among genes not previously linked to pancreatic cancer, inhibition of *Smarcd3*, a SWI/SNF family member, reduced sphere formation of *KP$^{f/f}$C* stem cells by 50% (Figure 3.1 C). SMARCD3 was particularly interesting not only because it was the only significantly stem-enriched chromatin remodeling factor (FC>2, FDR<0.25), but because, unlike many other SWI/SNF subunits that are targeted for loss-of-function[44], *SMARCD3* was amplified in cancer (Figure 3.1 D and Figure 3.S1 A; cBioPortal[45,46]).

Consistent with a potential role in cancer, SMARCD3 was highly expressed in end-stage primary tumors from *KP$^{f/f}$C* mice, an aggressive model of pancreatic cancer driven by *p53* deletion[37] (Figure 3.1 E). SMARCD3 was also expressed in both primary and metastatic lesions from the *Kras$^{G12D/+}$; p53$^{R172H/+}$; Ptf1a-Cre* (*KP$^{R172H/+}$C*) model, which recapitulates the metastatic behavior of the human disease (Figure 3.1 E)[37]. Further, although the core SWI/SNF subunit SMARCA4 was expressed in almost all primary stem and non-stem tumor cells (Figure 3.S1 B), SMARCD3 expression was upregulated within primary CD133+ tumor cells, consistent with a role in the stem cell compartment (Figure 3.1 F and Figure 3.S1 C,D). While SMARCD3 was detected in the cytoplasm of non-stem cells, it was more frequently localized to the nucleus in CD133+ stem cells, suggesting a functional difference in SMARCD3 localization and SWI/SNF incorporation in pancreatic cancer stem cells[47,48].

Figure 3.1. SMARCD3 is a functional epigenetic dependency of PDAC stem cells, Continued
(A) Relative expression of stem cell-enriched epigenetic and transcriptional regulatory factors identified by RNA-seq. Relative expression of candidate transcription factors or epigenetic regulatory genes in primary stem (*Msi2-GFP+)* versus non-stem (*Msi2-GFP-*) EpCAM+ $KP^{f/f}C$ tumor cells by RNA-seq.
(B) Schematic of targeted functional screen for candidate regulatory factors *in vitro.* Primary *Msi2-GFP* reporter $KP^{f/f}C$ mouse pancreatic cancer cell lines were derived by dissociating endpoint *Msi2-GFP* $KP^{f/f}C$ tumors and sorting EpCAM+ cells by FACS. Early passage cell lines were transduced with RFP-tagged lentiviral shRNA or puromycin-selectable sgRNA; 72 hours post-transduction *Msi2-GFP*+ transduced cells were FACS sorted and plated in 3D sphere-forming conditions. Number of spheres was counted 1 week later.
(C) Functional screen *in vitro* identifies SMARCD3 as a novel regulator of PDAC stem cell growth. Relative sphere formation of *Msi2-GFP*+ $KP^{f/f}C$ cells was analyzed at 1 week; sphere formation is normalized to shControl or non-targeting gRNA (NT1) to enable comparison across experiments (n=3).
(D) Genetic amplifications have been detected in the *SMARCD3* locus in clinical cases of pancreatic cancer (cBioPortal).
(E) SMARCD3 is expressed in genetically engineered mouse models of PDAC. Representative images of immunofluorescent staining for SMARCD3 (red) in epithelial tumor cells (pan-keratin+, green) of a primary end-stage $KP^{f/f}C$ tumor, primary end-stage *KPC* tumor, and *KPC* lung and diaphragm metastases from the same mouse; nuclei stained with DAPI (blue), representative images from n=3-6 mice.
(F) The frequency of nuclear SMARCD3+ cells is significantly increased within the CD133+ stem cell fraction of primary $KP^{f/f}C$ tumors. Primary CD133- and CD133+ EpCAM+ tumor cells were FACS sorted from end-stage $KP^{f/f}C$ tumors and cytospins were analyzed for nuclear SMARCD3 expression by immunofluorescence for DAPI (blue) and SMARCD3 (red); cells with any positive staining for SMARCD3 in the nucleus were counted. Representative images from n=3 frames, n=2 biological replicates.
(G) Inhibition of *Smarcd3* using two independent shRNA blocks 3D growth of CD133+ *KPC* cells *in vitro* in matrigel; n=3, representative of n=3 biological replicates.
(H) Inhibition of *Smarcd3* using two independent shRNA blocks 3D sphere formation of CD133+ (Msi2+) $KP^{f/f}C$ cells *in vitro*; n=3, representative of n=10 biological replicates.
(I) Inhibition of *Smarcd3* using shRNA blocks proliferation of CD133+ $KP^{f/f}C$ cells *in vitro*, as determined by the frequency of cells positive for BrdU incorporation by FACS staining in 2D culture; one biological replicate (n=3).
(J) Inhibition of *Smarcd3* using shRNA blocks growth of $KP^{f/f}C$ stem cells *in vivo*. Inhibition of *Smarcd3* blocks growth of Msi2+ $KP^{f/f}C$ cells in the flank of NSG mice, reducing tumor growth rate (shControl slope= 43.8mm^3/day; shSmarcd3 slope= 10.08mm^3/day, p=<.0001), mass, cell count, and total number of Msi2+ EpCAM+ tumor cells at endpoint (n=3 for 3 biological replicates)
Data represented as mean ± SEM. $^{*}p < 0.05$; $^{**}p < 0.01$; $^{***}p < 0.001$ by Student's t test or one-way ANOVA.

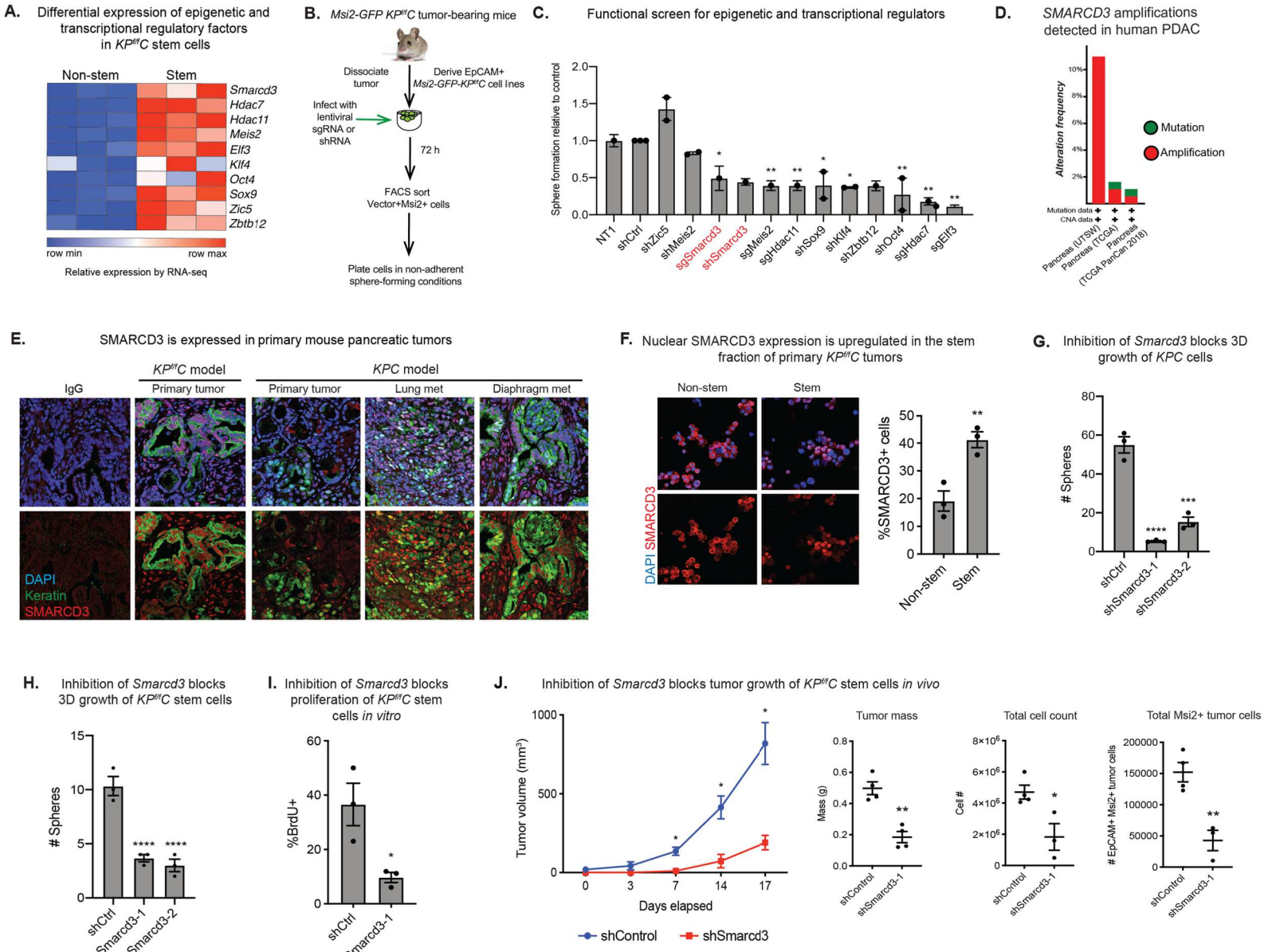
A.
Differential expression of epigenetic and transcriptional regulatory factors in KP^fl/fl C stem cells
Non-stem
Stem
Smarcd3
Hdac7
Hdac11
Meis2
Elf3
Klf4
Oct4
Sox9
Zic5
Zbtb12
row min
row max
Relative expression by RNA-seq
B.
Msi2-GFP KP^fl/fl C tumor-bearing mice
Dissociate tumor
Derive EpCAM+ Msi2-GFP-KP^fl/fl C cell lines
Infect with lentiviral sgRNA or shRNA
72 h
FACS sort Vector+Msi2+ cells
Plate cells in non-adherent sphere-forming conditions
C.
Functional screen for epigenetic and transcriptional regulators
Sphere formation relative to control
NT1
shCtrl
shZic5
shMeis2
sgSmarcd3
shSmarcd3
sgMeis2
sgHdac11
shSox9
shKlf4
shZbtb12
shOct4
sgHdac7
sgElf3
D.
SMARCD3 amplifications detected in human PDAC
Alteration frequency
Mutation
Amplification
Mutation data
CNA data
Pancreas (UTSW)
Pancreas (TCGA)
Pancreas (TCGA PanCan 2018)
E.
SMARCD3 is expressed in primary mouse pancreatic tumors
IgG
KP^fl/fl C model
Primary tumor
KPC model
Primary tumor
Lung met
Diaphragm met
DAPI
Keratin
SMARCD3
F.
Nuclear SMARCD3 expression is upregulated in the stem fraction of primary KP^fl/fl C tumors
Non-stem
Stem
DAPI SMARCD3
%SMARCD3+ cells
Non-stem
Stem
G.
Inhibition of Smarcd3 blocks 3D growth of KPC cells
Spheres
shCtrl
shSmarcd3-1
shSmarcd3-2
H.
Inhibition of Smarcd3 blocks 3D growth of KP^fl/fl C stem cells
Spheres
shCtrl
shSmarcd3-1
shSmarcd3-2
I.
Inhibition of Smarcd3 blocks proliferation of KP^fl/fl C stem cells in vitro
%BrdU+
shCtrl
shSmarcd3-1
J.
Inhibition of Smarcd3 blocks tumor growth of KP^fl/fl C stem cells in vivo
Tumor volume (mm^3)
Days elapsed
shControl
shSmarcd3
Tumor mass
Mass (g)
Total cell count
Cell #
Total Msi2+ tumor cells
EpCAM+ Msi2+ tumor cells

Inhibition of *Smarcd3* mediated by two independent shRNAs reduced 3D growth of *KP$^{R172H/+}$C* and *KP$^{f/f}$C* cells by over 50% (Figure 3.1 G,H and Figure 3.S1 E-G), inhibiting proliferation and increasing cell death *in vitro* (Figure 3.1 I, Figure 3.S1 H). Further, shRNA-mediated inhibition of *Smarcd3* in Msi2+ *KP$^{f/f}$C* cells almost completely blocked flank tumor growth in NOD-SCID mice *in vivo,* reducing growth rate by over 4-fold (Figure 3.1 J and Figure 3.S1 I,J), and total tumor cell and Msi2+ tumor stem cell counts by 2.5 and 3.5-fold (Figure 3.1 J). As a corollary, we found that overexpression of *SMARCD3* in *KP$^{f/f}$C* cells increased their 3D growth by 2-fold and sustained the CD133+ fraction *in vitro* (Figure 3.S1 K-N), supporting an oncogenic function aligned with amplifications in the *SMARCD3* locus in PDAC[30]. These data collectively indicate that *Smarcd3* represents a core dependency program for pancreatic cancer cells in transplant-based models.

Genetic inhibition of Smarcd3 impairs tumor growth

To better understand how *Smarcd3* contributes to the establishment and sustained propagation of cancer cells through the course of tumor progression *in vivo,* we used a diverse set of autochthonous genetic models to delete *Smarcd3* in a temporally restricted manner. To test how *Smarcd3* contributes to early pancreas cancer establishment in diverse contexts, we crossed a conditional *Smarcd3$^{f/f}$* line[49] to the *Kras$^{LSL/+}$*; Ptf1a-Cre (*KC*) model, where embryonic activation of KRAS in pancreatic precursors drives the formation of benign PanIN lesions[36], as well two KRAS-driven models where benign lesions are initiated in adult acinar or ductal cells: *Kras$^{LSL/+}$*; *Ptf1a-Cre^{ER}* (acinar) and *Kras$^{LSL/+}$*; *Sox9-Cre^{ER}* (ductal). While embryonic *Smarcd3* deletion concomitant with Ras activation increased the formation of fibrotic lesions arising from pancreatic progenitors (Figure 3.S2 A), *Smarcd3* deletion with Ras activation in adults had an impact that was cell type dependent; thus, *Smarcd3* deletion increased the formation of fibrotic nodules when Ras was activated in ductal cells, but reduced the frequency of lesions observed

when Ras was activated in acinar cells (Figure 3.S2 B). This indicated that in context of initiation, SMARCD3 acts bimodally in a cell type specific manner.

To assess the function of *Smarcd3* in fully advanced pancreatic tumors driven by both Ras activation and p53 loss, we crossed *Smarcd3*$^{f/f}$ mice into two independent autochthonous models that enabled temporally distinct deletion of *Smarcd3,* either embryonically or in adult mice. First, *Smarcd3*$^{f/f}$ mice were crossed into the *KP*$^{f/f}$*C* model (Figure 3.2 A), where *Smarcd3* is deleted synchronously with Ras activation/p53 deletion in pancreatic progenitors embryonically. Interestingly, despite the apparent tumor suppressor function of *Smarcd3* in the context of embryonic Ras activation at initiation, *Smarcd3*^{KO}*-KP*$^{f/f}$*C* tumors (Figure 3.2 B) showed a trend towards reduced EpCAM+ tumor cell content, and a 2.5-fold reduction in EpCAM+Msi2+ cancer stem cells at midpoint (7-8 weeks) (Figure 3.2 C and Figure 3.S2 C). *Smarcd3* deletion led to a greater 3-fold loss in EpCAM+ tumor cells (p=0.051), and a significant 3.5-fold reduction in EpCAM+Msi2+ tumor stem cells in secondary transplants (Figure 3.2 D,E), suggesting that *Smarcd3* inhibition reduces the self-renewal capability of established tumor cells. *Smarcd3* deletion also improved median survival of *KP*$^{f/f}$*C* mice (13% survival benefit; Figure 3.2 F), providing an even greater survival benefit in the presence of chemotherapy (gemcitabine, 28% survival benefit; Figure 3.2 F). These results indicate that *Smarcd3* is a functional dependency of cancer cells in established tumors *in vivo*, and demonstrate that depletion of cancer stem cells by *Smarcd3* deletion can sensitize to chemotherapy.

Figure 3.2. Genetic inhibition of *Smarcd3* impairs tumor growth
(A) Schematic shows strategy for conditional *Smarcd3* deletion in the *KP$^{f/f}$C* model. A *Smarcd3$^{f/f}$* line was crossed into the *Kras$^{G12D/+}$;Trp53$^{f/f}$; Ptf1a-Cre* or *KP$^{f/f}$C* model enabling pancreas-specific deletion of *Smarcd3* concomitant with *Kras* mutation and *p53* deletion.
(B) SMARCD3 is not expressed in *Smarcd3^{KO}-KP$^{f/f}$C* tumors; representative images of immunofluorescent staining for SMARCD3 (red) in epithelial tumor cells (pan-keratin+, green) of primary end-stage *Smarcd3^{WT}-KP$^{f/f}$C* (WT) and *Smarcd3^{KO}-KP$^{f/f}$C* (KO) tumors; nuclei stained with DAPI (blue).
(C) *Smarcd3* deletion reduces primary tumor burden and stem cell content in *KP$^{f/f}$C* tumors. Midpoint tumors were isolated from 7-8 week old *Smarcd3^{WT}-KP$^{f/f}$C* (WT) and *Smarcd3^{KO}-KP$^{f/f}$C* (KO) mice and analyzed for tumor mass* (p= 0.0979) and cell count* (p= 0.4874); EpCAM+ tumor cell number** (p= 0.0896) and EpCAM+CD133+** (p= 0.2477) and EpCAM+Msi2+ (p= 0.0345) tumor stem cell number by FACS (n=5-14 per genotype; *1 outlier was removed, **2 outliers were removed ROUT Q=1%).
(D) Schematic for secondary syngeneic transplants in the *KP$^{f/f}$C* model. Midpoint *Smarcd3^{WT}-KP$^{f/f}$C* (WT) and *Smarcd3^{KO}-KP$^{f/f}$C* (KO) tumor cells from the *KP$^{f/f}$C* model were isolated, dissociated, and EpCAM+ tumor cells were FACS sorted for secondary transplant into the flank of syngeneic immunocompetent littermate recipients; tumor burden was analyzed 5 weeks later.
(E) *Smarcd3* deletion impairs self-renewal in *KP$^{f/f}$C* tumor cells. Analysis 5 weeks post-transplant shows that tumor burden in secondary transplants was more significantly reduced than in the primary setting (Figure 3.2 C); *Smarcd3^{KO}-KP$^{f/f}$C* (KO) tumors have reductions in EpCAM+ tumor cell number* (p= 0.0510), and EpCAM+CD133+* (p= 0.1984) and EpCAM+Msi2+ (p= 0.0021) tumor stem cell number (n=3-4 biological replicates, n=2-4 technical transplant replicates each; *1 outlier was removed ROUT Q=1%).
(F) *Smarcd3* deletion improves survival and synergizes with chemotherapy in the *KP$^{f/f}$C* model. Survival is significantly improved in *Smarcd3^{KO}-KP$^{f/f}$C* (KO) mice; median survival for *Smarcd3^{WT}-KP$^{f/f}$C* (WT) mice was 65 days vs. 73.5 days for *Smarcd3^{KO}-KP$^{f/f}$C* mice (8.5 day survival benefit; p= 0.0268). Median survival was improved more significantly in the context of low-dose chemotherapy; median survival for mice treated once weekly with 25mg/kg gemcitabine (gem) was 68 days for *Smarcd3^{WT}-KP$^{f/f}$C* and 87 days for *Smarcd3^{KO}-KP$^{f/f}$C* mice (19 day survival benefit; p= 0.0113). *Smarcd3* deletion synergized with chemotherapy; *Smarcd3^{WT}-KP$^{f/f}$C* median survival improved 8.5 days with *Smarcd3* deletion and 3 days with gemcitabine treatment while the survival benefit of both *Smarcd3* deletion and gemcitabine treatment was 22 days (greater than the sum of either effect).
(G) Schematic for inducible deletion of *Smarcd3* in the *KPF* model. To delete *Smarcd3* specifically in established tumors, *Smarcd3$^{f/f}$* mice were crossed to a dual-recombinase model (*FSF-Kras$^{G12D/+}$,p53$^{FRT/FRT}$,Pdx-Flp; KPF*) driven by *Kras* mutation/*p53* deletion by a pancreas-specific flippase. These mice were crossed to the global *R26-CreER^{T2}* line, enabling inducible global *Smarcd3* deletion upon tamoxifen delivery. *Smarcd3$^{f/f}$-KPF-R26-CreER^{T2}* tumors were isolated, dissociated, and EpCAM+ tumor cells were transplanted in the flanks of NSG recipients; when tumors became palpable (~4mm) they were measured and randomized into treatment with tamoxifen (100mg/kg) or vehicle (100uL corn oil) for 5 days. Tumor burden was analyzed 3 weeks later.
(H) Tamoxifen delivery drives *Smarcd3* deletion in the *KPF* model *in vivo.* Representative images of immunofluorescent staining for SMARCD3 (red) in epithelial tumor cells (pan-keratin+, green) of *Smarcd3$^{f/f}$-KPF-R26-CreER^{T2}* flank transplants treated with tamoxifen/vehicle; DAPI (blue).
(I) Inducible *Smarcd3* deletion blocks growth of established *KPF* tumors. Vehicle and tamoxifen treated *Smarcd3$^{f/f}$-KPF-R26-CreER^{T2}* flank transplants were isolated and analyzed 3 weeks after enrollment; tumor mass was measured and total tumor area and tumor cell number of representative sections were analyzed using QuPath software. Tumors were cut in half along their longest diameter for collection and histological analysis; sections were cut from this plane and H&E stained for QuPath analysis of total viable tumor area, or stained with hematoxylin and analyzed for total tumor cell number in QuPath. Total tumor cell number was determined by training an object classifier in QuPath to classify tumor, necrosis, and stroma, and then count nuclei within classified regions of the entire tissue section area (representative data from 1 biological replicate; n=2 biological replicates, n=3-4 technical transplant replicates, n=2 sections/tumor for histological analysis).
Data represented as mean ± SEM. $^{*}p < 0.05$; $^{**}p < 0.01$; $^{***}p < 0.001$ by Student's t test or one-way ANOVA

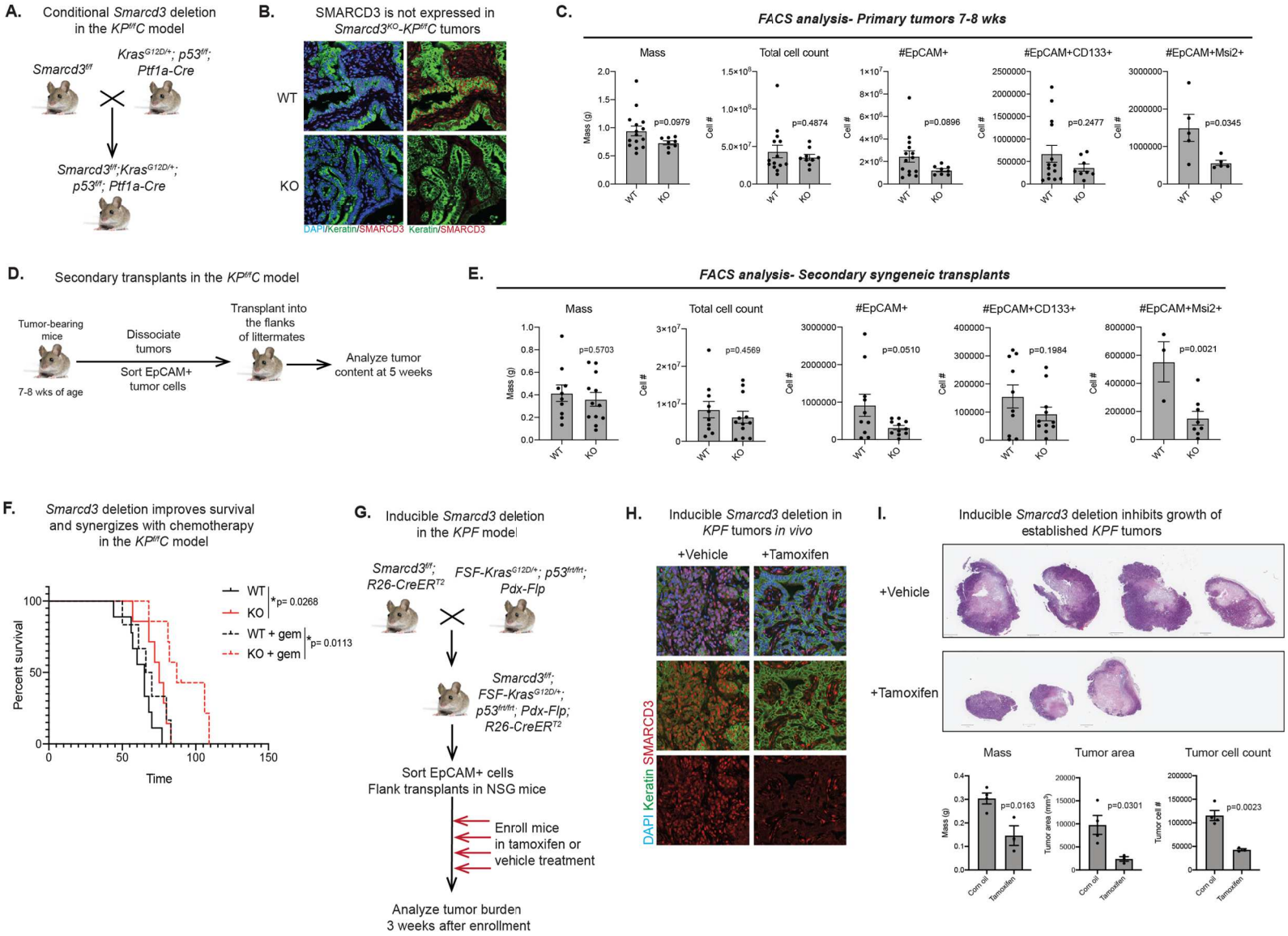
A.
Conditional Smarcd3 deletion in the KPf/fC model
Smarcd3f/f
KrasG12D/+; p53f/+; Ptf1a-Cre
Smarcd3f/f;KrasG12D/+; p53f/+; Ptf1a-Cre
B.
SMARCD3 is not expressed in Smarcd3KO-KPf/fC tumors
WT
KO
DAPI/Keratin/SMARCD3
Keratin/SMARCD3
C.
FACS analysis- Primary tumors 7-8 wks
Mass
Total cell count
#EpCAM+
#EpCAM+CD133+
#EpCAM+Msi2+
Mass (g)
Cell #
p=0.0979
p=0.4874
p=0.0896
p=0.2477
p=0.0345
WT
KO
D.
Secondary transplants in the KPf/fC model
Tumor-bearing mice
7-8 wks of age
Dissociate tumors
Sort EpCAM+ tumor cells
Transplant into the flanks of littermates
Analyze tumor content at 5 weeks
E.
FACS analysis- Secondary syngeneic transplants
Mass
Total cell count
#EpCAM+
#EpCAM+CD133+
#EpCAM+Msi2+
Mass (g)
Cell #
p=0.5703
p=0.4569
p=0.0510
p=0.1984
p=0.0021
WT
KO
F.
Smarcd3 deletion improves survival and synergizes with chemotherapy in the KPf/fC model
Percent survival
Time
WT
KO
WT + gem
KO + gem
*p= 0.0268
*p= 0.0113
G.
Inducible Smarcd3 deletion in the KPF model
Smarcd3f/f; R26-CreERT2
FSF-KrasG12D/+; p53frt/frt; Pdx-Flp
Smarcd3f/f; FSF-KrasG12D/+; p53frt/frt; Pdx-Flp; R26-CreERT2
Sort EpCAM+ cells
Flank transplants in NSG mice
Enroll mice in tamoxifen or vehicle treatment
Analyze tumor burden 3 weeks after enrollment
H.
Inducible Smarcd3 deletion in KPF tumors in vivo
+Vehicle
+Tamoxifen
DAPI Keratin SMARCD3
I.
Inducible Smarcd3 deletion inhibits growth of established KPF tumors
+Vehicle
+Tamoxifen
Mass
Tumor area
Tumor cell count
Mass (g)
Tumor area (mm2)
Tumor cell #
p=0.0163
p=0.0301
p=0.0023
Corn oil
Tamoxifen

To directly test the function of *Smarcd3* in context of established tumors in adult mice (uncoupled from deletion at initiation) we utilized a model that allowed for genetic deletion post-tumor establishment by crossing *Smarcd3*$^{f/f}$ mice into the *FSF-Kras*$^{G12D/+}$*; p53*$^{frt/frt}$*; Pdx-Flp* (*KPF*) dual-recombinase model of pancreatic cancer. In this model, *Kras* mutation and *p53* deletion are driven by a pancreas-specific *Pdx-Flp* recombinase, allowing independent spatiotemporal control over *Smarcd3* deletion with Cre[50]. *Smarcd3* deletion was induced *in vitro* by adenoviral Cre (adCre) and *in vivo* via tamoxifen treatment. Viral Cre-mediated deletion reduced sphere formation of *Smarcd3*$^{f/f}$*-KPF* tumor cells by 70%, depleted CD133+ stem cells *in vitro* (Figure 3.S2 D-G) and impaired *Smarcd3*$^{f/f}$*-KPF* tumor transplant growth *in vivo* by over 3-fold (Figure 3.S2 H). To induce deletion post-establishment *in vivo*, *Smarcd3*$^{f/f}$*-KPF* mice were crossed to a globally expressed tamoxifen-inducible *R26-CreER*^{T2} Cre (Figure 3.2 G)[51]. End-stage *Smarcd3*$^{f/f}$*-KPF-R26-CreER*^{T2} tumor cells were transplanted subcutaneously and recipient mice were treated with tamoxifen or vehicle once tumors were established; tumor burden was then analyzed 3 weeks later. *Smarcd3* deletion (Figure 3.2 H and Figure 3.S2 I) led to a striking 4-fold reduction in total tumor area[52] and 2-fold reduction in tumor mass and cell number in tamoxifen-treated mice (Figure 3.2 I), even though one of three tamoxifen-treated tumors showed escaper SMARCD3 re-expression (Figure 3.S2 J). These data show that pancreatic cancer cells have a deeper *Smarcd3* addiction post-establishment and reflect a context-dependent function of *Smarcd3*.

SMARCD3 inhibition blocks tumor growth in human models of PDAC

Although genetically engineered mouse models (GEMMs) are useful models that are representative of human disease, PDAC patient tumors are diverse and exhibit more complex mutational landscapes. While SMARCD3 was rarely expressed in benign inflamed tissue (pancreatitis), the frequency of nuclear SMARCD3+ epithelial cells rose in PanIN and, to a

greater degree, in PDAC in a human tissue microarray (Figure 3.3 A). In addition, the frequency of *SMARCD3* expression was enriched within CD133+ and Msi2+ tumor cells (1.5-fold and 3-fold respectively) in primary human PDAC tumors in a published single-cell RNA-seq dataset[53] (Figure 3.3 B and Figure 3.S3 A), supporting the data from genetic models (Figure 3.1 A,F and Figure 3.S1 C,D).

To test whether SMARCD3 is a functional dependency in human pancreatic tumors, we inhibited *SMARCD3* in the human FG PDAC cell line (Figure 3.S3 B). shRNA-mediated *SMARCD3* inhibition markedly inhibited the 3D growth of FG cells (Figure 3.3 C), reducing proliferation by 5-fold (Figure 3.3 D). Inhibition of *SMARCD3* also reduced the 3D growth of two independent patient-derived organoid lines *in vitro* by greater than 3-fold (Figure 3.3 E-H). To extend these findings *in vivo*, we inhibited *SMARCD3* in three independent SMARCD3+ patient-derived xenograft (PDX) tumors (Figure 3.3 I,J). PDX tumors were infected with GFP-tagged lentiviral shRNA *in vitro*, and then re-transplanted subcutaneously in NSG mice (Figure 3.3 J). While each PDX sample was transduced equivalently at t=0 (Figure 3.3 K and Figure 3.S3 C), the relative frequency and total number of GFP+ EpCAM+ tumor cells were reduced by 2 to 50-fold in shSmarcd3 tumors at endpoint (Figure 3.3 L and Figure 3.S3 D). Further, the total number of CD133+ stem cells within the GFP+ EpCAM+ tumor fraction was reduced by up to 100-fold in shSmarcd3-treated tumors relative to shControl (Figure 3.3 L, right). These data indicate a strong dependence of patient-derived PDAC tumor cells in general, and the most therapy-resistant CD133+ stem cells in particular, on SMARCD3 for *in vivo* growth and propagation.

Figure 3.3. SMARCD3 inhibition blocks tumor growth in human models of PDAC, Continued
(A) SMARCD3 is upregulated from PanIN to PDAC in human cancer. The frequency of nuclear (DAPI, blue) SMARCD3+ (red) cells within the epithelial compartment (pan-keratin+, green) in cases of pancreatitis (benign inflammation), PanIN, and PDAC were analyzed by immunofluorescence using a commercially available TMA; (representative images; n=1-3 representative frames per case, n=8-15 cases/condition; each data point represents the mean of all frames per case); frequency of nuclear SMARCD3+ epithelial cells per frame were counted in ImageJ.
(B) The frequency of *SMARCD3*+ cells is increased in the stem cell fraction of primary human PDAC tumors in a published single-cell RNA-seq study (Peng et al., 2019). The fraction of cells positive for *SMARCD3* RNA were quantified within Msi2+ and CD133+ EpCAM+ tumor stem cells relative to bulk EpCAM+ tumor cells.
(C) Inhibition of *SMARCD3* using shRNA blocks 3D growth of human FG PDAC cells *in vitro* in Matrigel (representative of n=4 biological replicates, n=3 each)
(D) Inhibition of *SMARCD3* using shRNA blocks proliferation of human FG PDAC cells *in vitro* as determined by the frequency of BrdU+ cells incorporation by FACS in 2D culture; one biological replicate (n=3).
(E) Schematic for *in vitro* transduction of patient-derived organoids with lentiviral shRNA; organoid lines were derived from 2 independent PDX tumors that were propagated in NSG mice. Tumors were dissociated and plated in 3D organoid culture and passaged to select for tumor cells. Organoids were dissociated, spinfected with lentiviral GFP-tagged shRNA, replated for 72 hours, and re-dissociated, FACS sorted, and plated in 3D organoid conditions in Matrigel. Organoids were imaged and counted 2 weeks later.
(F-H) Inhibition of *SMARCD3* using shRNA blocks growth of patient-derived PDAC organoids *in vitro*. Image of representative well from organoid line #1 (F) (n= 1 biological replicate per organoid line at n=3-4 technical replicates). Number of organoids is reduced in shSmarcd3 treated PDX cells *in vitro* in organoid line #1(G) and #2 (H) (n= 1 biological replicate per line at n=3 technical replicates).
(I) Patient-derived xenograft (PDX) PDAC tumors express nuclear SMARCD3. Three independent PDX tumors subsequently used for functional studies *in vivo* were stained for SMARCD3 (red) within the epithelium (pan-keratin, green) by immunofluorescence; nuclei stained with DAPI (blue).
(J) Schematic for transduction and transplant of PDX tumor cells. PDX tumors were dissociated and transduced with GFP-tagged lentiviral shRNA overnight. Bulk cells were then transplanted subcutaneously into immunodeficient NSG mice, and infection frequency at the time of transplant (t=0) was analyzed by FACS 48 hours after transduction using a small aliquot of cells kept *in vitro*. After 3 months, endpoint tumors were dissociated and the frequency and number of GFP+ EpCAM+ and CD133+ tumor cells were analyzed by FACS.
(K) PDX tumors are transduced equivalently with shControl and shSmarcd3 lentivirus at t=0. The frequency of transduced (GFP+) EpCAM+ PDX tumor cells was analyzed by FACS 48 hours post-transduction (t=0). Frequency is normalized to shControl to allow comparison across 3 independent PDX samples/5 total technical replicates where infection frequency was variable across samples.
(L) Inhibition of *SMARCD3* using shRNA blocks *in vivo* growth of patient-derived xenograft PDAC tumors. At endpoint, xenograft tumors were isolated and dissociated; the total number of tumor cells was counted and tumors were analyzed by FACS for GFP (shRNA vector), EpCAM, and CD133 expression. The frequency of GFP+ EpCAM+ tumor cells (left), total number of GFP+ EpCAM+ tumor cells (middle), and total number of GFP+ CD133+ EpCAM+ tumor cells (right) were significantly reduced by inhibition of *SMARCD3*. Endpoint analyses are all normalized to shControl to allow comparison across 3 independent PDX samples/5 total replicates where cell number and infection frequency were variable across samples.
Data represented as mean ± SEM. $^{*}p < 0.05$, $^{**}p < 0.01$, $^{***}p < 0.001$ by Student's t test or One-way ANOVA.

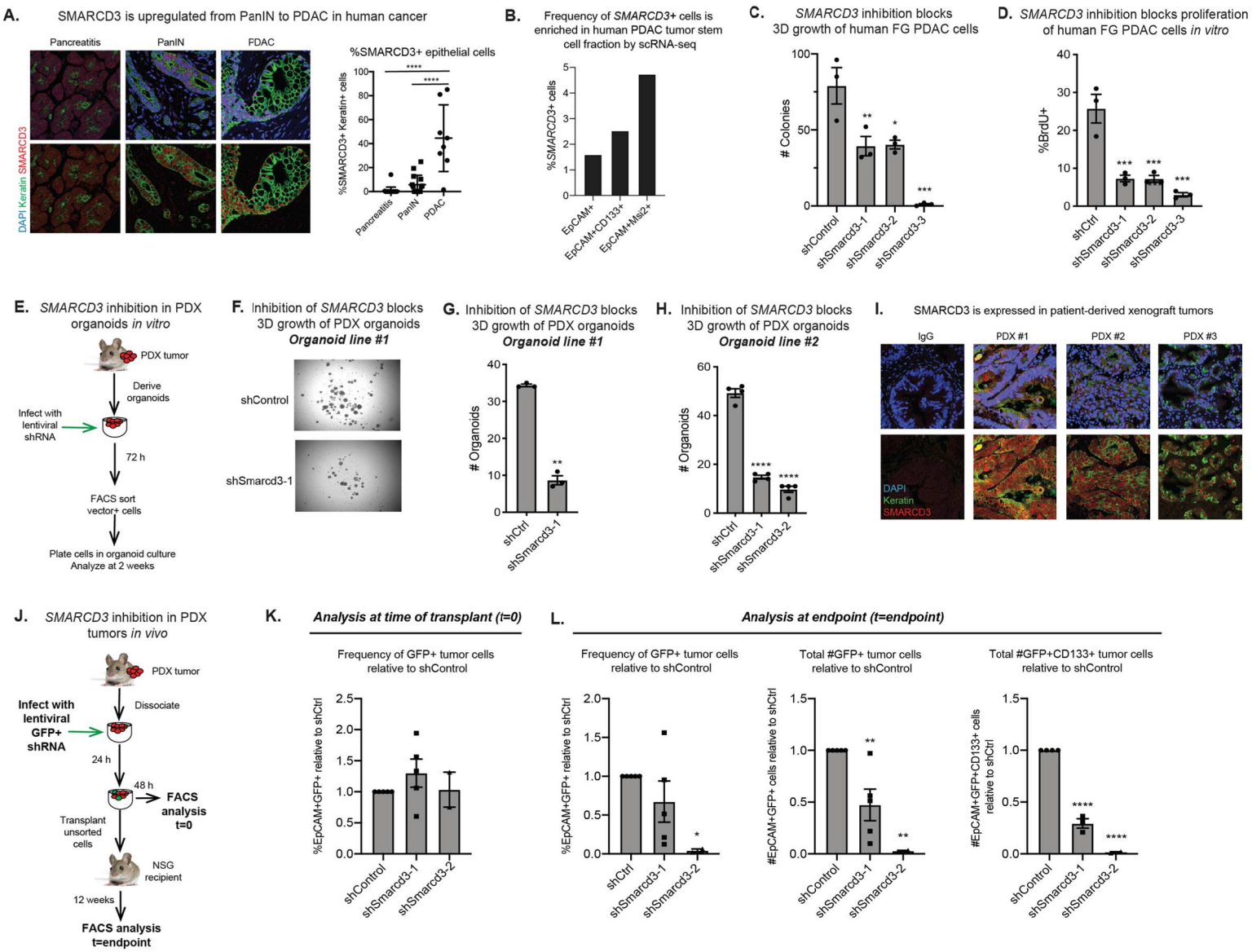
A.
SMARCD3 is upregulated from PanIN to PDAC in human cancer
Pancreatitis
PanIN
PDAC
DAPI Keratin SMARCD3
%SMARCD3+ epithelial cells
%SMARCD3+ Keratin+ cells
Pancreatitis
PanIN
PDAC
B.
Frequency of SMARCD3+ cells is enriched in human PDAC tumor stem cell fraction by scRNA-seq
%SMARCD3+ cells
EpCAM+
EpCAM+CD133+
EpCAM+Msi2+
C.
SMARCD3 inhibition blocks 3D growth of human FG PDAC cells
Colonies
shControl
shSmarcd3-1
shSmarcd3-2
shSmarcd3-3
D.
SMARCD3 inhibition blocks proliferation of human FG PDAC cells in vitro
%BrdU+
shCtrl
shSmarcd3-1
shSmarcd3-2
shSmarcd3-3
E.
SMARCD3 inhibition in PDX organoids in vitro
PDX tumor
Derive organoids
Infect with lentiviral shRNA
72 h
FACS sort vector+ cells
Plate cells in organoid culture
Analyze at 2 weeks
F.
Inhibition of SMARCD3 blocks 3D growth of PDX organoids
Organoid line #1
shControl
shSmarcd3-1
G.
Inhibition of SMARCD3 blocks 3D growth of PDX organoids
Organoid line #1
Organoids
shCtrl
shSmarcd3-1
H.
Inhibition of SMARCD3 blocks 3D growth of PDX organoids
Organoid line #2
Organoids
shCtrl
shSmarcd3-1
shSmarcd3-2
I.
SMARCD3 is expressed in patient-derived xenograft tumors
IgG
PDX #1
PDX #2
PDX #3
DAPI
Keratin
SMARCD3
J.
SMARCD3 inhibition in PDX tumors in vivo
PDX tumor
Dissociate
Infect with lentiviral GFP+ shRNA
24 h
48 h
FACS analysis t=0
Transplant unsorted cells
NSG recipient
12 weeks
FACS analysis t=endpoint
K.
Analysis at time of transplant (t=0)
Frequency of GFP+ tumor cells relative to shControl
%EpCAM+GFP+ relative to shCtrl
shControl
shSmarcd3-1
shSmarcd3-2
L.
Analysis at endpoint (t=endpoint)
Frequency of GFP+ tumor cells relative to shControl
%EpCAM+GFP+ relative to shCtrl
shCtrl
shSmarcd3-1
shSmarcd3-2
Total #GFP+ tumor cells relative to shControl
#EpCAM+GFP+ cells relative to shCtrl
shControl
shSmarcd3-1
shSmarcd3-2
Total #GFP+CD133+ tumor cells relative to shControl
#EpCAM+GFP+CD133+ cells relative to shCtrl
shControl
shSmarcd3-1
shSmarcd3-2

SMARCD3 regulates the epigenetic landscape and BAF complex binding at FOXA1 binding sites in mouse pancreatic cancer cells

As a subunit of a chromatin modifying complex, SMARCD3 may control tumor cell function by regulating SWI/SNF binding and the epigenetic landscape. SWI/SNF complexes exist as three variants (BAF, PBAF, ncBAF)[54,55,56,57]; of these, SMARCD3 was predominantly incorporated into the more abundant BAF complex and to some extent PBAF in *KP$^{f/f}$C* cells (Figure 3.S4 A,B). Thus, we focused on defining SMARCD3-dependent changes in BAF complex binding using ChIP-seq with antibodies against the core ATP-ase SMARCA4 and BAF-specific ARID1A (Figure 3.4 A). *Smarcd3* loss reduced SMARCA4 and ARID1A binding at 1,628 common sites (Fold change 1.5, Poisson p=0.05). Motif enrichment on these SMARCD3-dependent BAF binding sites revealed a significant enrichment for KLF5 and FOXA1 motifs, as well as AP-1 which served as a control[58] (Figure 3.4 B). Analysis of published ChIP-seq data in *KP$^{R172H/+}$C* cells[59] confirmed that FOXA1 and KLF5 were co-bound with SMARCA4 and ARID1A at 31% and 30% of sites respectively, suggesting an association between these factors and SMARCD3-containing BAF (Figure 3.4 C).

SWI/SNF complexes typically regulate cell fate by binding to cis-regulatory elements of the genome, including promoters and enhancers. Using ChIP-seq for H3K4me, H3K4me3, and H3K27ac histone modifications that can be used to distinguish cis-regulatory elements (Figure 3.4 A)[60,61,62], we found that SMARCA4 and ARID1A co-bound sites, and downregulated co-bound sites in particular, were preferentially enriched at active enhancers (Figure 3.4 D), suggesting SMARCD3 loss differentially impacted BAF complex binding at enhancers relative to promoters. While KLF5 binding was most enriched at promoters, FOXA1 binding was enriched at active enhancers, suggesting that FOXA1 may be the more relevant partner for SMARCD3 activity. Consistent with this, proximity ligation showed FOXA1 interacting with both SMARCD3 and SMARCA4 in *KP$^{f/f}$C* tumors (Figure 3.4 E and Figure 3.S4 C); this interaction was enriched in primary *KP$^{f/f}$C* stem cells (Figure 3.4 F). Further, FOXA1 was co-bound at 47%

of common SMARCD3-dependent BAF binding sites (Figure 3.4 G); these results support a collaboration between the SMARCD3-containing BAF complex and FOXA1 in pancreatic cancer cells. Supporting a role for SMARCD3 and FOXA1 in cancer stem cells, SMARCD3/FOXA1 interactions were enriched within the nuclei of primary CD133+ mouse cells. Further *Smarcd3* inhibition led to reduced H3K27ac at sites that lost SMARCA4/ARID1A binding (Figure 3.4 G,H) predicting reduced transcriptional activity at these conserved SMARCD3-dependent BAF complex binding sites.

Figure 3.4. SMARCD3 regulates the epigenetic landscape and BAF complex binding at FOXA1 binding sites in mouse pancreatic cancer cells

(A) Schematic for ChIP-seq analysis in *KP$^{f/f}$C* cells. Early passage primary CD133^{High} *KP$^{f/f}$C* cells were transduced with RFP-tagged shRNA against *Smarcd3* or control. 72 hours post-transduction, RFP+ transduced cells were sorted by FACS and plated in 2D culture; 1 week post-transduction cells were collected for ChIP-seq and downstream analysis as follows. ChIP-seq for SMARCA4 and ARID1A was used to assess the impact of *Smarcd3* inhibition on BAF complex binding and motif analysis on downregulated BAF complex binding sites was used to predict SMARCD3-BAF associated transcription factors. Publicly available ChIP-seq data for KLF5 and FOXA1, factors predicted to associate with SMARCD3-BAF, was overlaid with SMARCA4 and ARID1A ChIP-seq to determine if these factors were co-bound at SMARCD3-dependent BAF complex binding sites (see Fig. 4c). ChIP-seq for H3K27ac, H3K4me, and H3K4me3 was used to map SMARCD3-dependent BAF and transcription factor binding at promoters and enhancer classes (see Fig. 4d). Finally, we assessed the impact of *Smarcd3* inhibition on H3K27ac levels at altered BAF or transcription factor binding sites to predict downstream impacts on transcription.

(B) Motif enrichment on common sites that lose SMARCA4 and ARID1A binding when *Smarcd3* is inhibited. Motif enrichment analysis on 1,628 commonly down-regulated SMARCA4 and ARID1A binding sites by ChIP-seq shows that these commonly lost sites are enriched for ATF3 (AP-1), KLF5, and FOX (FOXA1) motifs.

(C) FOXA1 and KLF5 binding sites overlap with SMARCA4 and ARID1A binding sites in *KP$^{f/f}$C* cells. Publicly available FOXA1 and KLF5 ChIP-seq data in pancreatic cancer cells was overlaid with our SMARCA4 and ARID1A ChIP-seq to identify overlapping binding sites in *KP$^{f/f}$C* cells.

(D) SMARCA4, ARID1A, and FOXA1 binding is enriched at active enhancers. Using ChIP-seq for H3K27ac, H3K4me, and H3K4me3 we mapped SMARCA4/ARID1A, KLF5, and FOXA1 binding at genomic elements (poised, active, and super enhancers as well as promoters). SMARCA4/ARID1A co-bound sites and FOXA1 are most enriched at active enhancers while KLF5 is enriched at promoters. Common sites that lose SMARCA4/ARID1A binding when *Smarcd3* is inhibited are also significantly enriched at active enhancers.

(E) FOXA1 interacts with SMARCD3 and SMARCA4. Using proximity ligation assay with antibodies against FOXA1, SMARCD3, and SMARCA4, we found positive PLA signals (red) in the nuclei (DAPI, blue) of *KP$^{f/f}$C* tumor cells (E-Cadherin, green) *in vivo*, representing associations between both FOXA1 and SMARCD3, and FOXA1 and the core SMARCA4 ATP-ase subunit of SWI/SNF in mouse pancreatic tumor tissue (representative images from n=2 mice, n=5 frames/tumor)

(F) FOXA1/SMARCD3 interactions are enriched in primary *KP$^{f/f}$C* stem cells by proximity ligation assay. Using proximity ligation assay with antibodies against FOXA1 and SMARCD3 we found positive PLA signals were enriched in CD133+ stem cells relative to CD133- non-stem cells isolated from *KP$^{f/f}$C* tumors. End-stage *KP$^{f/f}$C* tumors were dissociated and stained for CD133 and EpCAM to isolate stem and non-stem fractions of EpCAM+ tumor cells for cytospin and subsequent analysis by immunofluorescence (n=1 mice, n=5 frames/tumor).

(G) FOXA1 is co-bound and H3K27-acetylation is reduced at sites that lose SMARCA4/ARID1A binding upon *Smarcd3* inhibition. SMARCA4 and ARID1A ChIP-seq density at commonly lost sites when *Smarcd3* is inhibited overlap with FOXA1 binding sites (left); H3K27-acetylation is reduced at sites that commonly lose BAF binding when *Smarcd3* is inhibited (right).

(H) H3K27-acetylation is reduced at sites that lose SMARCA4/ARID1A binding upon *Smarcd3* inhibition. At sites were SMARCA4 and ARID1A binding is lost (left, middle) H3K27-acetylation is also reduced (right).

Data represented as mean ± SEM. $^{*}p < 0.05$, $^{**}p < 0.01$, $^{***}p < 0.001$ by Student's t test or One-way ANOVA.

A. Schematic for ChIP-seq analysis in *KP^{fl}C* cells

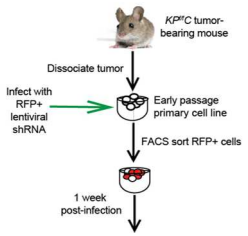

Collect cells for analysis:

+ ChIP-seq for ARID1A, SMARCA4 (BAF complex)

Predict SMARCD3-BAF associated transcription factors by running motif enrichment on SMARCD3-dependent BAF complex binding sites

+ Overlay transcription factor ChIP-seq

Determine if enriched transcription factors co-bind at SMARCD3-dependent BAF binding sites

+ ChIP-seq for H3K4me, H3K4me3, H3K27ac

Map SMARCD3-dependent BAF and transcription factor binding at promoters and enhancer classes

+ Analyze H3K27ac levels

Assess the impact of Smarcd3 inhibition on H3K27ac levels at altered BAF or transcription factor binding sites

B. Motif enrichment analysis of common sites that lose SMARCA4 and ARID1A in shSmarcd3/shControl (n = 1,628)

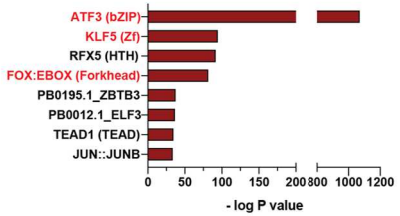

C. Overlap of ChIP-seq peaks

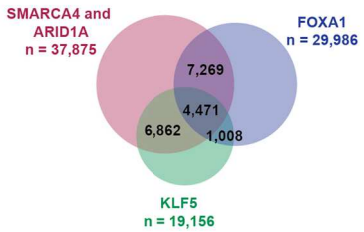

D. Genomic localization of ChIP-seq peaks

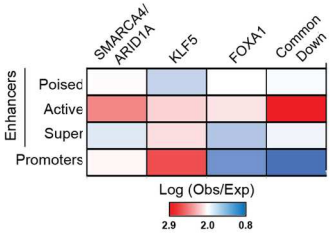

E. FOXA1 interacts with SMARCD3 and SMARCA4 in *KP^{fl}C* tumors by proximity ligation assay

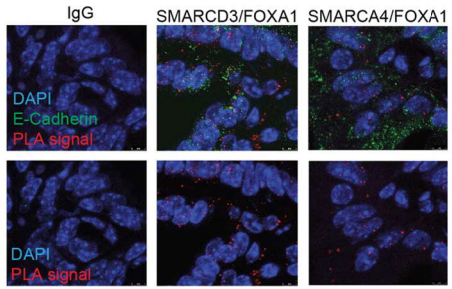

F. FOXA1/SMARCD3 interactions are enriched in primary *KP^{fl}C* tumor stem cells by proximity ligation assay

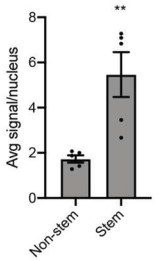

G. FOXA1 is co-bound and H3K27-acetylation is reduced at sites that lose SMARCA4/ARID1A binding when *Smarcd3* is inhibited

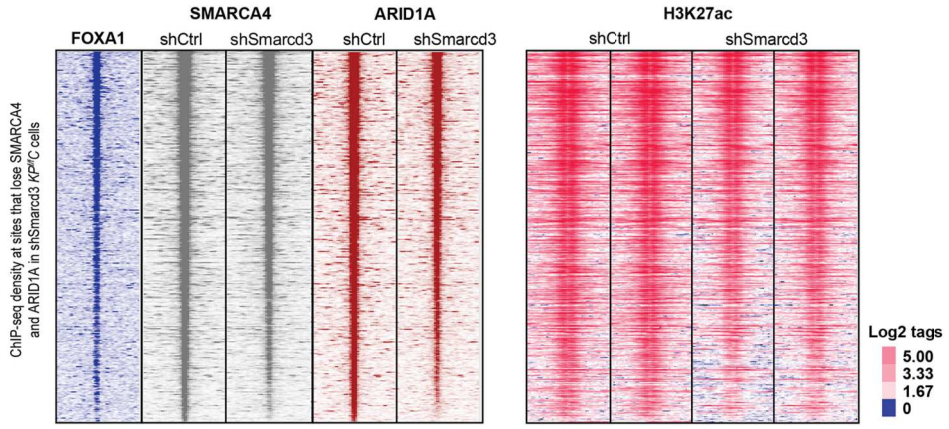

H. H3K27-acetylation is reduced at sites that lose SMARCA4/ARID1A binding upon *Smarcd3* inhibition

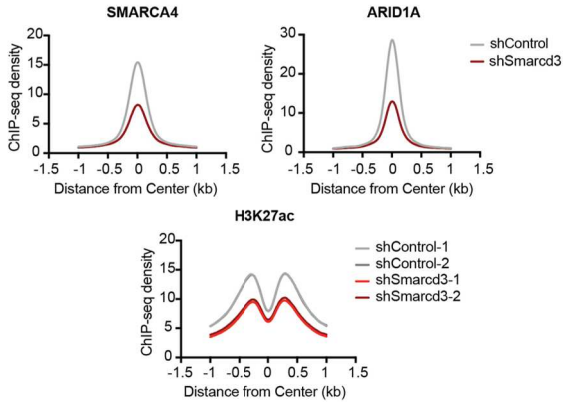

SMARCD3 regulates transcriptional networks implicated in lipid metabolism.

We analyzed the functional consequence of these epigenetic changes on gene expression using RNA-seq analysis of *Smarcd3*-inhibited *KP$^{f/f}$C* cells (Figure 3.5 A). *Smarcd3* inhibition drove the differential expression of over a thousand genes (Figure 3.5 B) with these changes overlapping significantly with FOXA1-regulated gene sets[59], supporting a co-regulatory function for FOXA1 and SMARCD3 (Figure 3.5 C and Figure 3.S5 A). A high-confidence STRING network of down-regulated genes (Figure 3.5 D; nodes colored by cluster, node size scaled to logFC), identified 12 SMARCD3-regulated transcriptional hubs enriched for diverse functions including glycosylation, extracellular matrix organization and immune signaling (Figure 3.5 D, and Table 3.1). Strikingly, four of these hubs converged on lipid metabolism annotations (Figure 3.5 D in yellow, Figure 3.5 E), encompassing functions in arachidonic acid metabolism, fatty acid metabolism, cholesterol biosynthesis, and metabolic regulation. As lipid metabolism has emerged as an important feature of aggressive cancer stem cell populations[32,33], we further focused on this functional program.

Within lipid-associated network hubs (Figure 3.5 E), SMARCD3-regulated genes were involved at almost every level of lipid homeostasis. *Smarcd3* loss downregulated lipid transport and storage genes, as well as major transcriptional regulators of lipid metabolism (Table 3.1). Further, *Smarcd3* inhibition drove down the expression of core enzymes involved in the metabolism of lipid families with known functions in cancer: cholesterol, prostaglandins, and fatty acids (Table 3.1). Both cholesterol and fatty acid metabolism are enriched in cancer stem cells and have been associated with stem cell signaling and therapy resistance in many cancers[63,64,31,65,66,67,68,69,70,71,72,73,74], indicating that SMARCD3 may regulate stem cell-enriched metabolic pathways. Several core genes within the lipid subnetwork such as *Pparg, Scd1, Hmgcr, Ptgs1*, and *Vldlr*; were directly bound by SMARCD3-BAF and FOXA1, highlighting a direct coordinated role for SMARCD3-BAF and FOXA1 in the regulation of lipid homeostasis.

We next used a curated metabolic screen to test whether transcriptional changes in lipid pathways reflected functional shifts and found that while *Smarcd3^{KO}-KPF* cells retained dependence on cholesterol metabolism (Lovastatin[65]) and prostaglandin synthesis or COX (Celexcoxib[75]), they had lost sensitivity to inhibitors of fatty acid synthesis (TOFA[76], CAY10566[77], Fatostatin[78]) and beta oxidation (Etomoxir[79]) *in vitro* (Figure 3.5 F). Further, tamoxifen-mediated *Smarcd3* deletion led to a ~3-fold drop in total free fatty acid content in EpCAM+ *Smarcd3$^{f/f}$-KPF-R26-CreER^{T2}* tumor cells *in vivo,* as determined by gas chromatography-mass spectrometry (GC-MS) (Figure 3.S5 B). Of all downregulated fatty acid species (Figure 3.S5 C), the most significant were the monounsaturated fatty acids oleic acid (C18:1) and eicosenoic acid (C20:1), and the long chain saturated fatty acids tricosylic (C23:0) and lignoceric acid (C24:0) (Figure 3.5 G), which can contribute to the synthesis of complex lipids and play a role in signaling and survival in cancer cells[80,81]. Collectively, these results demonstrate that SMARCD3-BAF, in concert with FOXA1, is a key regulator of fatty acid metabolism, and draw a new link between SWI/SNF and stem cell-enriched metabolic programs in pancreatic cancer.

Figure 3.5. SMARCD3 regulates transcriptional networks implicated in lipid metabolism, Continued.
(A) Schematic for RNA-seq analysis in *KP$^{f/f}$C* cells. Early passage primary CD133^{High} *KP$^{f/f}$C* cells were transduced with RFP-tagged shRNA against *Smarcd3* or control. 72 hours post-transduction, RFP+ transduced cells were sorted by FACS and plated in triplicate in 2D culture; 1 week post-transduction cells were collected for RNA-seq analysis.
(B) *Smarcd3* inhibition leads to significant transcriptional changes in *KP$^{f/f}$C* cells. PCA plot (top) demonstrates clustering of shControl (red) and shSmarcd3 (blue) replicates by RNA-seq (plots generated in clustviz). MA plot (bottom) of differential gene expression by RNA-seq (generated in Galaxy); normalized counts per gene are plotted against log fold change in expression, with differentially expressed genes shown in red.
(C) Genes down-regulated by *Smarcd3* inhibition are enriched within FOXA1-regulated gene sets. Gene set enrichment analysis (GSEA) on our RNA-seq dataset revealed a significant enrichment for two FOXA1-regulated gene sets within genes down-regulated by *Smarcd3* inhibition.
(D) STRING network of genes down-regulated by *Smarcd3* inhibition demonstrates global regulation of programs involved in cell cycle, immune processes, and extracellular matrix organization, and lipid metabolism. Significantly down-regulated genes by RNA-seq (padj<0.05, log(fold change)<-0.35) were used to map a SMARCD3-dependent network within the high confidence (0.8) mouse STRING interactome (node size scaled to log(fold change) expression by RNA-seq). A community clustering algorithm was applied to the network to generate 12 closely related programmatic hubs (nodes are colored by cluster); STRING functional enrichment analysis was used to identify significantly enriched functional annotations for each hub (network hubs with lipid-related functional annotations are denoted with a yellow label).
(E) SMARCD3-BAF and FOXA1 directly regulate genes within lipid metabolism network hub. All four lipid-associated network hubs (yellow labels in Fig. 5d) were merged (nodes colored by cluster as in Fig. 5d, node size scaled to logFC expression by RNA-seq) and nodes with specific lipid-metabolic functions were labeled. Within those nodes with known functions in lipid metabolism, we identified potential direct targets of SMARCD3-BAF and FOXA1; these are genes that are both bound by FOXA1 by ChIP-seq and lose BAF complex binding (genes where both SMARCA4 and ARID1A binding was reduced) by ChIP-seq when *Smarcd3* is inhibited (SMARCD3-BAF/FOXA1 target genes labeled in yellow, denoted with yellow diamond shaped node, connected to SMARCD3-BAF/FOXA1 node by dashed yellow edges).
(F) *Smarcd3^{KO}-KPF* cells are no longer dependent on fatty acid synthesis or beta oxidation. A curated screen of metabolic inhibitors was conducted *in vitro* in *Smarcd3^{WT}* and *Smarcd3^{KO}-KPF* cells. Primary tumor cell lines were derived from end-stage *Smarcd3$^{f/f}$-KPF* tumors (not expressing *Rosa-Cre^{ERT2}*) and *Smarcd3* deletion was driven by the delivery of adenoviral Cre or GFP. GFP-transduced *Smarcd3^{WT}-KPF* (WT) and Cre-transduced *Smarcd3^{KO}-KPF* (KO) cells were plated in 3D sphere-forming conditions in a 96-well plate and treated with inhibitors for 72 hours; viability was then assessed using a 3D CellTiterGlo viability assay. Celecoxib is a COX inhibitor, targeting prostaglandin synthesis. Lovastatin is an inhibitor of cholesterol synthesis. Etomoxir is an inhibitor of fatty acid beta oxidation. TOFA (fatty acid synthesis, FAS, inhibitor), CAY10566 (SCD1 inhibitor), and Fatostatin (SREBP inhibitor) all target fatty acid synthesis.
(G) Free fatty acids are reduced in *Smarcd3$^{f/f}$-KPF-R26-CreER^{T2}* tumors treated with tamoxifen. *Smarcd3$^{f/f}$-KPF-R26-CreER^{T2}* tumors treated with vehicle or tamoxifen were dissociated and EpCAM+ tumor cells were sorted by FACS and flash frozen for free fatty acid analysis by GC-MS (n=3 tumors per group, data are represented as mean ± SEM). The most significantly down-regulated fatty acid species in tamoxifen-treated tumor cells are shown here.
Data represented as mean ± SEM. $^{*}p < 0.05$, $^{**}p < 0.01$, $^{***}p < 0.001$ by Student's t test or One-way ANOVA.

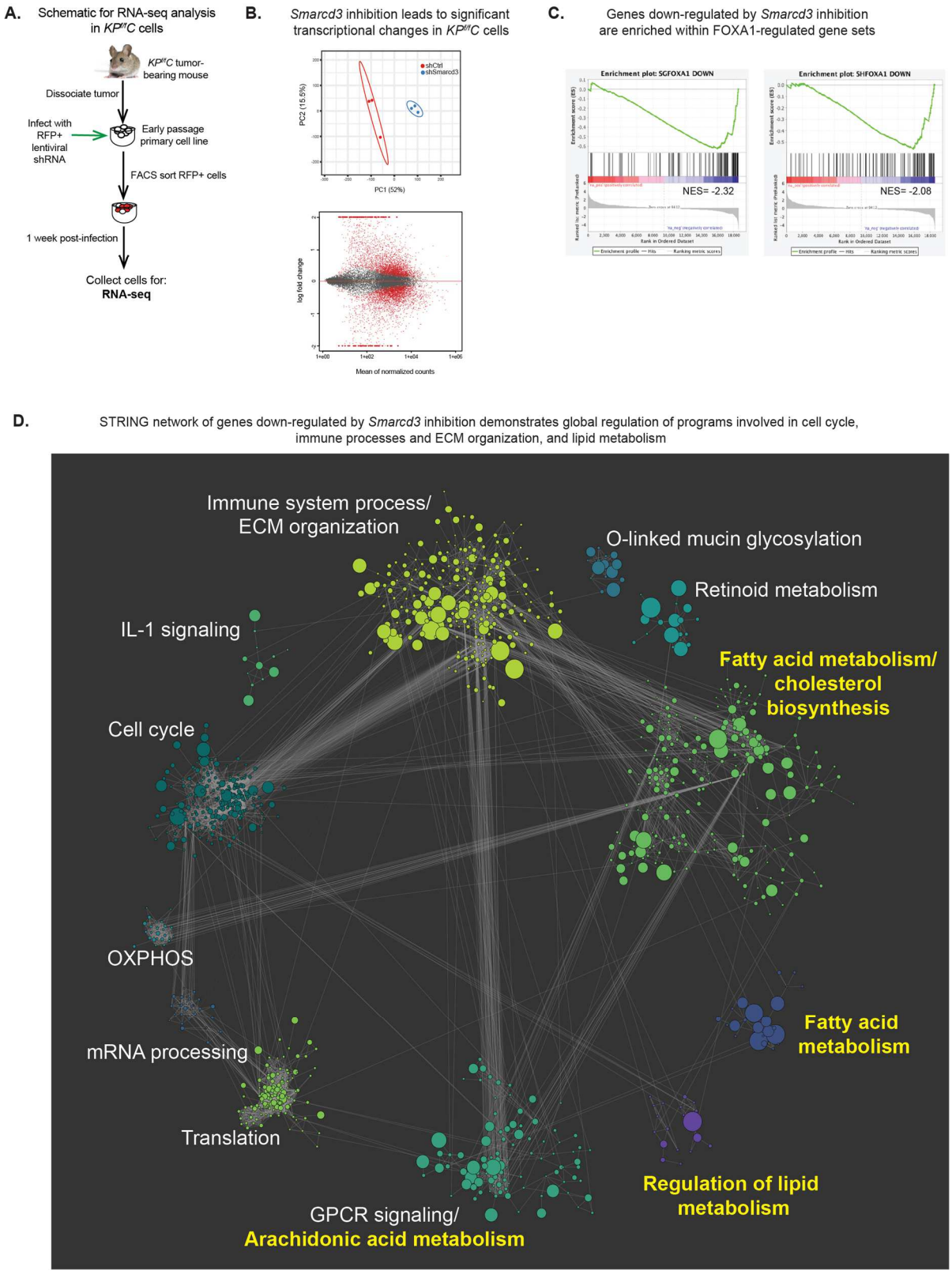
A.
Schematic for RNA-seq analysis in KPflC cells
KPflC tumor-bearing mouse
Dissociate tumor
Infect with RFP+ lentiviral shRNA
Early passage primary cell line
FACS sort RFP+ cells
1 week post-infection
Collect cells for: RNA-seq
B.
Smarcd3 inhibition leads to significant transcriptional changes in KPflC cells
shCtrl
shSmarcd3
PC2 (15.6%)
PC1 (52%)
log fold change
Mean of normalized counts
C.
Genes down-regulated by Smarcd3 inhibition are enriched within FOXA1-regulated gene sets
Enrichment plot: SGFOXA1 DOWN
NES= -2.32
Enrichment plot: SHFOXA1 DOWN
NES= -2.08
D.
STRING network of genes down-regulated by Smarcd3 inhibition demonstrates global regulation of programs involved in cell cycle, immune processes and ECM organization, and lipid metabolism
Immune system process/ ECM organization
O-linked mucin glycosylation
Retinoid metabolism
IL-1 signaling
Fatty acid metabolism/ cholesterol biosynthesis
Cell cycle
OXPHOS
Fatty acid metabolism
mRNA processing
Translation
Regulation of lipid metabolism
GPCR signaling/ Arachidonic acid metabolism

E. SMARCD3-BAF and FOXA1 directly regulate genes within lipid metabolism network hub

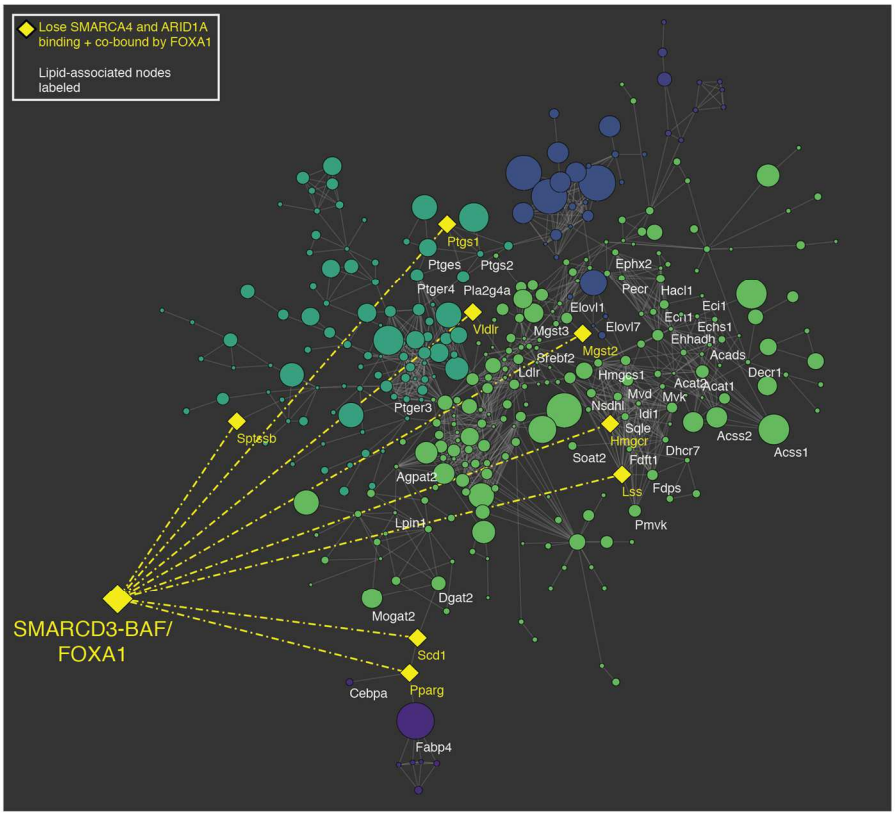

F. *Smarcd3^{KO}-KPF* cells are no longer dependent on fatty acid synthesis or beta oxidation

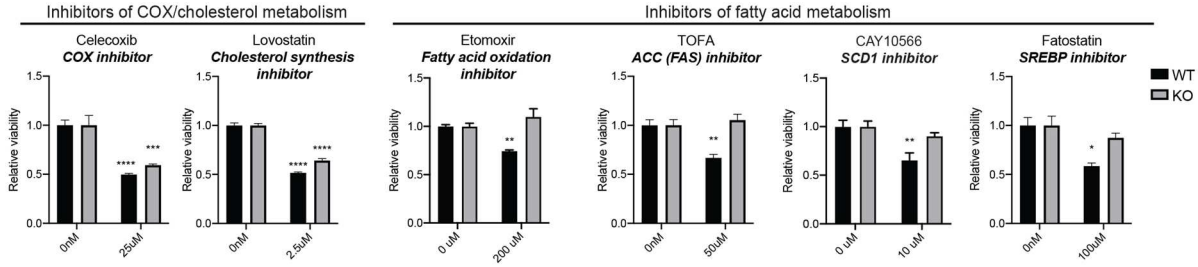

G. Free fatty acids are reduced in tamoxifen-treated *Smarcd3^{KO}-KPF-R26-CreER^{T2t}* tumor cells *in vivo*

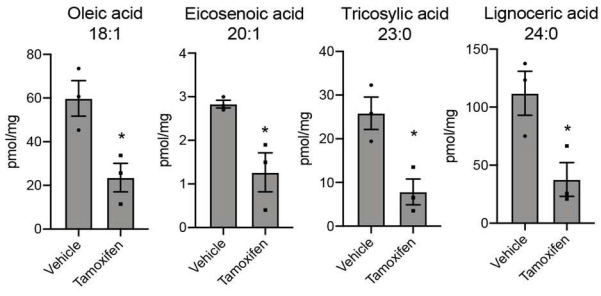

Figure 3.5. SMARCD3 regulates transcriptional networks implicated in lipid metabolism, Continued

3.4. Discussion

Despite clinical advances in many cancers, pancreatic cancer mortality remains high, driven by early metastasis and therapy resistance[3,4,5,6,7] which can be attributed in part to cancer stem cells, subpopulations with the tumor bulk enriched for developmental signals and self-renewal[10,11,12,13,14,15]. These therapy-resistant cells are epigenetically unique[16], suggesting that they may exploit developmental epigenetic mechanisms to maintain a stem cell state and drive relapse. Our work here has led to the identification of SMARCD3 as a new stem cell-enriched functional dependency in PDAC. SMARCD3 is a subunit of SWI/SNF, a nucleosome remodeling complex with core functions in development and cancer[27,29,44]. Given the potential for SWI/SNF to coordinate a broad range of cell-type specific functions, targeting cancer-specific SWI/SNF activity is an appealing therapeutic paradigm[27,28,29]. To this end, several studies have shown that SWI/SNF-mutant cancers can be successfully treated by inhibiting residual synthetic-lethal complex subunits[29]. However, although over 20% of cancers are SWI/SNF-mutant[44], the mechanisms by which dysregulated SWI/SNF activity contributes to tumor heterogeneity and disease progression in the remaining 80% of cancers remains relatively unexplored, and could have far-reaching impacts on therapy[27,28,29]. The role of SWI/SNF in establishment and propagation of therapy-resistant cancer stem cells remains largely understudied, and our work provides an important complement to emerging studies showing that the SWI/SNF ATP-ase SMARCA4 supports stem function in glioma[23,24] and in leukemia[26].

Here, we show that SMARCD3 is uniquely enriched in the stem cell fraction of pancreatic tumors, and a critical functional dependency of established cancer stem cells *in vivo.* Using a diverse set of conditional genetic models, we identified stage and cell-type specific roles for *Smarcd3* in pancreas cancer. Similar to deletion of *Smarca4*, *Smarcd3* deletion in context of *Kras* mutation alone increased benign lesions if they originated

embryonically or in adult ductal cells, but inhibited development of similar lesions if they originated from adult acinar cells[82,83]. Although similar in impact, the expression of SMARCA4 and SMARCD3 are very distinct in normal mouse pancreatic tissue; SMARCA4 is ubiquitous and SMARCD3 is restricted to ducts (Figurte 3.S5 D). Many stem cell signals are similarly restricted to the ducts in the normal pancreas[38,84,85,86]. It is thus tempting to speculate that SMARCD3 may actually enable cell-type specific functions of SMARCA4 to enforce cell fate in normal duct cells. Similarly, the fact that SMARCD3 is elevated from PanIN to PDAC suggests that it may be required to support ductal fate later in disease progression, and serve as an important enabler of SMARCA4 function in cancer.

Because loss-of-function alterations in *SMARCD3* have not been identified in cancer, it is unlikely that its deletion significantly drives tumorigenesis in the human disease. Instead, amplifications in *SMARCD3* have been detected[30] and we found that SMARCD3 expression increased most robustly from PanIN to PDAC in human tissues, supporting a more dominant role for SMARCD3 in cancer progression. In support of this, we found that genetic *Smarcd3* deletion in the *KP$^{f/f}$C* model blocked growth of secondary transplants, synergized with chemotherapy and improved survival. Further, using the dual-recombinase *KPF* model, we directly demonstrated that *Smarcd3* deletion impaired established tumor growth. Consistent with this, SMARCD3 was required for the propagation of patient-derived xenografts *in vivo,* providing strong evidence that *Smarcd3* is required for advanced cancer growth. This aligns with a pro-tumorigenic function for SMARCD3 identified in breast cancer[87] and stands in contrast to *Smarcb1*[88] or *Arid1a*[89,90], which serve as tumor suppressors in established tumors. Our work shows that SWI/SNF function is highly dependent on cellular context, highlighting the importance of testing genetic SWI/SNF deletion in the appropriate context in GEMMs and demonstrating the utility of dual-recombinase models for investigating chromatin remodeler function in cancer. Although *Smarcd3* was the only significantly stem-enriched SWI/SNF

subunit in *KP$^{f/f}$C* tumors (FC>2, FDR<0.25), the expression of many chromatin remodeling-associated genes did vary between stem and non-stem tumor cells (Figure 3.S5 E). The functional relevance of these subunits, and the composition of SWI/SNF in heterogeneous cancer cell populations would be an important avenue of future research.

As a SWI/SNF subunit, SMARCD3 can exert broad regulatory control over epigenetic and transcriptional programs, likely by scaffolding transcription factors. Integrating RNA-seq and ChIP-seq via network analysis we found that *Smarcd3* inhibition drove losses in BAF complex binding and H3K27-acetylation at active enhancers co-bound by FOXA1. FOXA1 was directly associated with both SMARCD3 and SMARCA4 *in vivo*, suggesting that SMARCD3 coordinates FOXA1/BAF activity, controlling downstream transcriptional programs with diverse functions including extracellular matrix organization, glycosylation, and immune signaling (Table 3.1). The regulation of these programs suggests a putative role for SMARCD3 in orchestrating interactions between pancreatic cancer cells and the microenvironment. The regulation of prostaglandin synthesis by SMARCD3 could also impact inflammation in the tumor microenvironment. Strikingly, human SMARCD3+ PDAC tumors were enriched for tertiary lymphoid structures (Figure 3.S5 F), raising the possibility of an association between SMARCD3 and the immune environment in patients. SWI/SNF mutational status can determine immunotherapy response in some cancers[91], so connections between SMARCD3 and the tumor microenvironment may be an clinically relevant avenue for future study.

A central finding of importance in our work, is the discovery that SMARCD3 controls the landscape of lipid metabolism in pancreatic cancer cells. While genes involved in cholesterol, prostaglandin, and fatty acid synthesis and beta oxidation were all downregulated by *Smarcd3* inhibition, *Smarcd3^{KO}* cells specifically lost dependence on fatty acid pathways and exhibited reduced fatty acid content *in vivo*. These results link SMARCD3 and fatty acid metabolism, which has been associated with therapy-resistance in cancer[31,32,33]. Though

SWI/SNF is known to regulate metabolism[92,93,94], to our knowledge this is the first study to connect SWI/SNF and the regulation of cancer lipid metabolism through the SMARCD3 subunit in association with FOXA1. Given the emerging role for fatty acid metabolism in therapy-resistant cancer cells[31,32,33], these results position SMARCD3 as a key regulator of stem cell-enriched metabolic programs. The role of SMARCD3 in metabolic regulation is also particularly interesting given its nutrient-sensing function in normal tissues[95,96]; it is possible that SMARCD3 may similarly act as a metabolic sensor in cancer. In support of this, we found that *Smarcd3* expression was sensitive to glucose *in vitro* (Figure 3.S5 G), suggesting that SMARCD3 may have the potential to integrate SWI/SNF and transcription factor activity to enable epigenetic adaptation to the metabolic environment. The mechanism by which SMARCD3 may sense metabolic status could provide critical insight into the role of SWI/SNF in regulating metabolic plasticity in cancer. Collectively, our results position SMARCD3 as an oncogenic SWI/SNF subunit that could drive important metabolic functions in aggressive cancer cells and serve as an effective target for new therapies.

3.5. Methods

Data availability

The *KP$^{f/f}$C* RNA-seq and H3K27-acetyl, H3K4me, H3K4me3, ARID1A, and SMARCA4 ChIP-seq datasets generated during this study will be available at GEO under accession code GSE168490. (https://www.ncbi.nlm.nih.gov/geo/query/acc.cgi?&acc=GSE168490). Please use the reviewer token: anqruiogprufpkb. The published FOXA1 ChIP-seq data[59] used in this paper is available at GEO (GSE99311).

Experimental models

Mice

The *LSL-Kras G12D* (*Kras*$^{G12D/+}$) mouse, B6.129S4-Kras$^{tm4Tyj/J}$ (Stock No: 008179), *p53*$^{flox/flox}$ (*p53*$^{f/f}$) mouse, B6.129P2- Trp53$^{tm1Brn/J}$ (Stock No: 008462), *R26-CreER*^{T2} mouse, B6.129-*Gt(ROSA)26Sor*$^{tm1(cre/ERT2)Tyj}$/J (Stock No: 008463), *Ptf1a*$^{CRE-ERTM}$, Ptf1a$^{tm2(cre/ESR1)Cvw}$/J (Stock No: 019378), and the *Sox9-CreER*^{T2}, Tg(Sox9-cre/ERT2)1Msan/J (Stock No: 018829) were purchased from The Jackson Laboratory. *Msi2*$^{eGFP/+}$ (Msi2-GFP) reporter mice were generated as previously described(); all of the reporter mice used in experiments were heterozygous for the Msi2 allele. Dr. Chris Wright provided *p48-Cre* (*Ptf1a-Cre*) mice as previously described[34]. *LSL-R172H* mutant *p53* (p53$^{R172H/+}$), Trp53^{R172H} mice were provided by Dr. Tyler Jacks as previously described[99] (JAX Stock No: 008183). Dr. Benoit Bruneau generated *Smarcd3*$^{f/f}$ mice as previously described[49]; mice were provided by Dr. Lorenzo Puri. Dr. Dieter Saur provided *Pdx-FlpO*^{KI} (*Pdx-Flp*), *p53*$^{frt/frt}$, and *FSF-Kras*$^{G12D/+}$ mice as previously described[50]. Immune compromised NOD/SCID (NOD.CB17-Prkdc^{scid}/J, Stock No: 001303) and NSG (NOD.Cg-Prkdc^{scid}IL2rg^{tm1Wji}/SzJ, Stock No: 005557) mice were purchased from The Jackson Laboratory.

All animal experiments were performed according to protocols approved by the University of California San Diego Institutional Animal Care and Use Committee. All mice were specific pathogen-free, and bred and maintained in the animal care facilities at the University of California San Diego; all animals were maintained as mixed background. Animals had access to food and water *ad libitum* and were group-housed in ventilated cages under controlled temperature and humidity with a 12-hour light-dark cycle. No sexual dimorphism was noted in all mouse models. Therefore, males and females of each strain were equally used for experimental purposes and both sexes are represented in all data sets; littermates of the same sex were randomized into experimental groups when applicable or possible based on available mice. All mice enrolled in experimental studies were treatment-naïve and not previously enrolled in any other experimental study.

Mouse and human pancreatic cancer cell lines

Mouse primary pancreatic cancer cell lines were established from end-stage wild-type *KP$^{f/f}$C* and *Msi2-GFP-KP$^{f/f}$C* (9-12 weeks of age), *KP$^{R172H/+}$C* (16-20 weeks of age), *Smarcd3$^{f/f}$-KPF* (10-15 weeks of age) mice as follows: tumors were isolated and dissociated into single cell suspension as described below, then plated in 1x DMEM containing 10% FBS, 1x pen/strep, and 1x non-essential amino acids. At the first passage, cells were collected and resuspended in HBSS (Gibco, Life Technologies) containing 2.5% FBS and 2 mM EDTA, then stained with FC block followed by 0.2 ug/10^6 cells anti-EpCAM APC (eBioscience, #17-5791-82). EpCAM-APC+ tumor cells were sorted and re-plated for at least one additional passage. Functional studies were performed using cell lines between passage 2 and passage 9. Cell lines were cultured in 1x DMEM (Gibco, Life Technologies) containing 10% FBS, 1x pen/strep (Gibco, Life Technologies), and 1x non-essential amino acids (Gibco, Life Technologies). To evaluate any cellular contamination and validate the epithelial nature of these lines, cells were analyzed by flow cytometry again at the second passage for markers of blood cells (CD45-PeCy7, eBioscience, #25-0451-82), endothelial cells (CD31-PE, eBioscience, #12-0311-82), and fibroblasts (PDGFR-PacBlue, BD Bioscience, 566293). Cell lines were derived from both female and male mice equivalently; both sexes are equally represented in the cell-based studies outlined below.

FG human pancreatic cancer cell lines (also known as COLO-357) were provided by Dr. Andrew Lowy; these cells were originally derived from a PDAC metastasis and have been previously validated and described[98]. FG cells were maintained in 2D culture in 1x DMEM containing 10% FBS, 1x pen/strep, and 1x non-essential amino acids. Cells were tested for the presence of mycoplasma and verified to be negative.

Patient-derived xenograft tumors and organoids

Patient-derived xenograft (PDX) tumors and organoids were derived from originally consented PDAC patients in accordance with the Declaration of Helsinki and use was approved by UCSD's IRB; samples were de-identified and therefore no further information on patient status, treatment or otherwise, is available. PDX tumors were maintained and passaged in NSG mice; end-stage tumors were isolated, sectioned, and 2mm tumor pieces were transplanted subcutaneously in NSG recipients. PDX tumors used for functional studies were below passage 7 *in vivo.*

Organoid lines were derived by isolating end-stage PDX tumors and dissociating to single cell as follows; tumors were washed in MEM (Gibco, Life Technologies) and cut into 1–2 mm pieces immediately following resection. Tumor pieces were collected into a 50 ml Falcon tube containing 10 ml Gey's balanced salt solution (Sigma), 5 mg Collagenase P (Roche), 0.2 µg DNAse I (Roche), and 10.5uM Rho Kinase inhibitor (SelleckChem Y-27632). Samples were incubated for 10 minutes at 37°C, then pipetted up and down 10 times and returned to 37°C. After 10 more minutes, samples were pipetted up and down 5 times, then passed through a 100 µm nylon mesh (Corning). Red blood cells were lysed using RBC Lysis Buffer (eBioscience) and the remaining tumor cells were washed, then resuspended in Matrigel and plated in pre-warmed 24-well plate in 25uL Matrigel domes. After 15 minutes, domes were covered in human organoid growth media, and passaged and maintained as previously described[99].

Patient cohort for PDAC tissue microarray

The PDAC patient cohort and corresponding TMAs used for SMARCD3 immunohistochemical staining and analysis have been reported previously[100]. Briefly, a total of 3 TMAs with 0.6 mm core size was constructed: three TMAs for PDACs, with samples from

the tumor center and invasive front (mean number of spots per patient: 10.5, range: 2–27). Tumor samples from 116 patients (53 females and 63 males; mean age: 64.1 years, range: 34–84 years) with a diagnosis of PDAC were included. 99 of these patients received some form of chemotherapy; 14 received radiotherapy. The creation and use of the TMAs were reviewed and approved by the Ethics Committee at the University of Athens, Greece, and the University of Bern, Switzerland, and included written informed consent from the patients or their living relatives.

Method details

In vitro growth assays

We describe below the distinct growth assays used for pancreatic cancer cells. Colony formation is an assay in Matrigel (adherent/semi-adherent conditions), while sphere formation is an assay in non-adherent conditions. We have found that cell types from different sources grow better in different conditions. For example, the murine $KP^{R172H/+}C$ and the human FG cell lines grow much better in Matrigel, while *KPF* and $KP^{f/f}C$ cell lines grow well in non-adherent, sphere conditions (though they can also grow in Matrigel). Patient-derived organoids are always grown or plated in Matrigel domes in organoid growth conditions (these cells require a defined media as previously described[99,101,102].

Pancreatic sphere formation assay

Pancreatic sphere formation assays were modified from Rovira et al. 2010[38]. Briefly, low passage (<6 passages) $KP^{f/f}C$ cell lines were infected with lentiviral particles containing RFP-tagged shRNAs; positively infected RFP+ stem cells (Msi2-GFP+ or CD133-APC+) cells were sorted 72 h after transduction. Similarly, *KPF* cell lines were infected with adenoviral GFP (adGFP) or GFP-tagged Cre (adCre) virus particles; transduced GFP+ cells were sorted 72 h

after transduction. Per well, 350 infected cells were suspended in sphere media: 100 µl DMEM F-12 (Gibco, Life Technologies) containing 1x B-27 supplement (Gibco, Life Technologies), 3% FBS, 100 µM B-mercaptoethanol (Gibco, Life Technologies), 1x non-essential amino acids (Gibco, Life Technologies), 1x N2 supplement (Gibco, Life Technologies), 20 ng/ml EGF (Gibco, Life Technologies), and 20 ng/ml bFGF2 (Gibco, Life Technologies). Cells in media were plated in 96-well ultra-low adhesion culture plates (Costar) and incubated at 37°C for 7 days. *KP$^{f/f}$C in vitro* sphere formation studies were conducted at a minimum of n=3 independent wells per cell line across two independent shRNA; however, the majority of these experiments were additionally completed in >2 independently derived cell lines n=3. For imaging of spheres, 10,000 cells were plated in 500uL sphere media in a 24-well ultra-low attachment plate for one week. All images were acquired on a Zeiss Axiovert 40 CFL.

For metabolic inhibitor studies, *KPF* cells were plated in sphere media as described above at 350 cells/well in 90uL media. The day after plating, 10uL inhibitor or vehicle (DMSO) was added to cells in 90uL sphere media. 72 h later, viability in sphere culture was assessed using the 3D CellTiterGlo assay (Promega) per manufacturers protocol. Inhibitors tested included celecoxib, lovastatin, etomoxir, TOFA, CAY10566, and Fatostatin (Selleckchem).

Matrigel colony assay

KP$^{R127H/+}$C cells were transduced and sorted as above. FG cells were infected with GFP-tagged shRNAs and transduced cells GFP+ were sorted 72 h after transduction. 500 *KP$^{R172H/+}$C* or FG cells were resuspended in 50 µl sphere media as described below, then mixed with 50uL Matrigel (BD Biosciences, 354230) at a 1:1 ratio and plated in 96-well culture plates (Costar). After incubation at 37°C for 5 min, 50 µl sphere media was placed over the Matrigel layer. Colonies were counted 7 days later. Colony assay were completed at n=3

biological replicates, n=3 wells/experiment for *KP*$^{R172H/+}$*C* cells and n=4 biological replicates at n=3 wells for FG cells.

Organoid culture assays

Organoid lines were derived by isolating end-stage PDX tumors and dissociating to single cell by adapting from Tuveson lab organoid protocols as follows[99,101,102]; tumors were washed in MEM (Gibco, Life Technologies) and cut into 1–2 mm pieces immediately following resection. Tumor pieces were collected into a 50 ml Falcon tube containing 10 ml Gey's balanced salt solution (Sigma), 5 mg Collagenase P (Roche), 0.2 µg DNAse I (Roche), and 10.5uM Rho Kinase inhibitor (SelleckChem, Y-27632). Samples were incubated for 10 minutes at 37°C, then pipetted up and down 10 times and returned to 37°C. After 10 more minutes, samples were pipetted up and down 5 times, then passed through a 100 µm nylon mesh (Corning). Red blood cells were lysed using RBC Lysis Buffer (eBioscience) and the remaining tumor cells were washed, then resuspended in Matrigel and plated in pre-warmed 24-well plate in 25uL Matrigel domes. After 15 minutes, domes were covered in human organoid growth media containing: Advanced DMEM/F12, 10mM HEPES (pH 7.2-7.5), 1X GlutaMAX, 100 ug/mL primocin, 50% Wnt3a conditioned media, 10% R-Spondin1-conditioned media, 1X-B27 supplement, 10mM nicotinamide, 1.25 mM N-acetyl cysteine, 100 ng/mL murine noggin, 50 ng/mL human-EGF, 100 ng/mL human-FGF, 10 nM human gastrin, 500 nM A-83-01, and 10.5 uM Rho Kinase inhibitor (SelleckChem, Y-27632). Organoids were passaged and maintained as previously described[99,101,102].

For shRNA studies, organoids were isolated from Matrigel using Cell Recovery Solution on ice (Corning 354253), then dissociated into single cell suspensions with TrypLE Express (ThermoFisher 12604) supplemented with 25 µg/ml DNase I (Roche) and 14 µM Rho Kinase inhibitor (SelleckChem, Y-27632). The single cell suspension was split into ~0.5x10^6 cells per

well in a 24-well plate in 500uL of organoid growth media and 500uL lentivirus and 8 ug/mL polybrene. Cells were spinfected at 600 RCF for 1 h at room temperature and left to rest in the incubator at 37C for 1-6 h. Cells were then collected, spun down, and washed in growth media before being replated in a pre-warmed 24-well plate in 35uL domes/well. 15 minutes after plating the domes, they were covered in 1mL organoid growth media. Three days after spinfection and plating, organoids were isolated and dissociated to single cell suspension again as described above. Transduced GFP+ organoid cells were sorted by FACS and re-plated for functional studies as follows. Cells were plated at 1,000 cells per well in 50uL organoid growth media plus 50uL Matrigel in a 96-well cell culture plate. 20 minutes after plating, 100uL organoid growth media was added to each well. 2 weeks after plating, the total number of organoids were counted in each well (all planes). These functional studies were conducted at 1 biological replicate across 2 independent organoid lines; each experiment was completed in n=3-4 technical replicates (wells) per condition. To image organoids, each well was collected in Cell Recovery Solution for 30 minutes. Each well was then spun down and resuspended in growth media in a 96-well u-bottom plate to facilitate the imaging of all organoids in each well. All images were acquired on a Zeiss Axiovert 40 CFL. Images were just used to allow us to visualize organoids; manual counts from the entire well were used to interpret functional impact to avoid any error from organoid or cell loss during isolation from Matrigel.

Proliferation and cell death analysis by FACS

To analyze proliferation (BrdU) or cell death (Annexin V) by FACS, *KP$^{f/f}$C* or FG were infected with shRNA and sorted 72 h later; 50,000 transduced cells were plated in a 24-well plate in 10% DMEM. For BrdU analysis, 24 h after plating, media was refreshed with media containing BrdU (BD Biosciences) as per manufacturers instructions; after an 18 h pulse in

BrdU-containing media, cells were trypsinized, fixed, permeabilized, and stained with anti-BrdU-APC using the BrdU flow cytometry kit (BD Biosciences). For Annexin V analysis, cells were trypsinized and analyzed with the Annexin V apoptosis kit (eBioscience) 48 h after plating.

Tumor growth studies *in vivo*

shRNA or adCRE transplants in *KP$^{f/f}$C* or *KPF* cells

KP$^{f/f}$C cells were infected with lentiviral particles containing RFP-tagged shRNAs against *Smarcd3* or control. 72 h post-transduction, positively infected stem cells (RFP+ Msi2-GFP+ or CD133-APC+, CD133-APC, eBioscience, #17-1331-81) were sorted for transplants. Sorted cells were resuspended at 1,000 cells in 50 uL Matrigel plus 50 uL 10% DMEM media; 100uL of the tumor cell mixture was injected subcutaneously into the left or right flank of NOD/SCID recipient mice (6-8 weeks old). Flank tumors were measured weekly or bi-weekly using calipers for 3 weeks. Similarly, *KPF* cells were infected with adenoviral GFP (adGFP) or GFP-tagged Cre (adCre) virus particles; 72 h post-transduction, positively infected GFP+ cells were sorted and transplanted as described above at 2,000 cells in 50:50 uL Matrigel:10% DMEM media. 3 weeks post-transplant, *KPF* flank tumors were isolated and dissociated for FACS analysis as described below. *KP$^{f/f}$C* flank transplants were replicated in three independent cell lines at n=3-6 tumor transplants/condition per experiment. *KPF* flank transplants were replicated twice in one cell line at n=3-6 tumor transplants/condition per experiment.

Secondary syngeneic transplant of *KP$^{f/f}$C* cells

The secondary syngeneic transplant of *Smarcd3^{WT}-KP$^{f/f}$C* and *Smarcd3^{KO}-KP$^{f/f}$C* tumor cells was performed as follows. Mid-point *Smarcd3^{WT}-KP$^{f/f}$C* and *Smarcd3^{KO}-KP$^{f/f}$C* tumors (7-8 weeks of age) were isolated, dissociated, and stained for FACS as described below. EpCAM-

APC+ tumor cells were resuspended at 20,000 cells in 50 uL Matrigel plus 50 uL 10% DMEM media; 100uL of the tumor cell mixture was injected subcutaneously into the left flank of immune competent littermate recipients (8 weeks of age). Male and female littermate recipients were used equivalently when possible; littermate recipients did not express Cre. 5 weeks post-transplant flank tumors were isolated, dissociated, and analyzed by FACS as described below. Secondary syngeneic transplants were conducted from n=3-4 independent primary tumors per genotype, each transplanted into n=2-4 littermate recipients.

Inducible deletion of *Smarcd3* in *KPF-R26-CreER^{T2}* transplants

The transplant of *Smarcd3$^{f/f}$-KPF-R26-CreER^{T2}* tumor cells was performed as follows. Tumors from end-stage *Smarcd3$^{f/f}$-KPF-R26-CreER^{T2}* mice (10-15 weeks of age) were isolated, dissociated, and stained for FACS as described below. EpCAM-APC+ tumor cells were resuspended at 5,000 cells in 50 uL Matrigel plus 50 uL 10% DMEM media and 100uL of the tumor cell mixture was injected subcutaneously into the left flank of NSG recipient mice (6-8 weeks old). After transplant, mice were monitored bi-weekly for tumor development. When tumors >3mm were detected, they were measured by caliper, and mice were randomized into IP treatment with tamoxifen (100mg/kg, 5 consecutive days) or vehicle (100uL corn oil, 5 consecutive days). Three weeks after the first dose of tamoxifen or vehicle, tumors were isolated and analyzed by FACS as described below. *Smarcd3$^{f/f}$-KPF-R26-CreER^{T2}* transplants were performed from two independent primary *Smarcd3$^{f/f}$-KPF-R26-CreER^{T2}* tumors, each transplanted at n=3-4 flank tumors per treatment group.

Patient-derived xenograft transplants

Patient-derived xenograft (PDX) tumors were maintained as described above. For functional studies, PDX tumors were isolated and dissociated to a single cell suspension as

described below. 500,000 tumor cells were plated in a 24-well ultra-low attachment cell culture plate in 500 uL human organoid growth media (described in detail above) and 250-500uL GFP-tagged shRNA (MOI=25) against *SMARCD3* or control with 8ug/mL polybrene. The next day, each well was collected, and resuspended in 50uL organoid media. 15uL resuspended cells in media were set aside and replated in 100uL organoid growth media in a 96-well ultra-low attachment plate; these cells were cultured for an additional 24 h (total 48 h post-transduction) and then stained with EpCAM-PE and analyzed by FACS to assess the efficiency of transduction (GFP+ EpCAM-PE+ tumor cells) at t=0. Meanwhile, the remaining 35uL cell suspension was mixed with 35uL Matrigel; the 70uL mixture was transplanted directly into the left flank of NSG recipient mice. 12 weeks after transplant, tumors were isolated and dissociated for FACS analysis at endpoint as described below. PDX shRNA studies *in vivo* were conducted using three independent PDX samples; one PDX sample was run singly while the other two samples were run in duplicate across 2 independent shRNA.

Tumor initiation studies

To assess tumor initiation, pancreatic tissues were isolated from *Smarcd3*$^{f/f}$*; Kras*$^{G12D/+}$*; Ptf1a-Cre* (*Smarcd3*$^{f/f}$*-KC*) mice between 9 and 10 weeks of age. Pancreas tissue was examined for any gross morphological cysts or tumors and then collected for histological analysis and H&E staining (conducted at the UCSD Tissue Technology Shared Resource according to standard protocols). The frequency of PDAC and PanIN present in tissues from *Smarcd3*^{WT}*-KC* and *Smarcd3*^{KO}*-KC* mice were determined from gross morphological presentation of the pancreas; PDAC was counted by the presence of any overt, fibrotic tumor nodules and presence of PanINs was confirmed by H&E (n=7-9 mice per genotype). To induce recombination and tumor initiation in ductal or acinar-specific lines, 8 week old *Smarcd3*$^{f/f}$*-Kras*$^{G12D/+}$*-Ptf1a*$^{CRE-ERTM}$ or *Smarcd3*$^{f/f}$*-Kras*$^{G12D/+}$*-Sox9-CreER*^{T2} mice were treated with 3 doses

or 1 dose respectively of 150mg/kg tamoxifen (in corn oil), IP. 90 days after the first tamoxifen dose, pancreatic tissue was isolated and assessed as above for gross morphological presentation of PDAC (n=7-8 *Ptf1a*$^{CRE\text{-}ERTM}$ mice/genotype, n=3-4 *Sox9-CreER*^{T2} mice/genotype).

Gemcitabine treatment *in vivo*

At 6 weeks of age, *Smarcd3*^{WT}*-KP*$^{f/f}$*C* and *Smarcd3*^{KO}*-KP*$^{f/f}$*C* mice were weighed and enrolled into treatment with 25mg/kg gemcitabine in PBS; mice were re-weighed and treated once weekly until humane endpoint for analysis of overall survival (n=6-7 mice per genotype).

Tissue dissociation, cell isolation, and FACS analysis

Mouse pancreatic tumors from mid-point *KP*$^{f/f}$*C* mice, syngeneic secondary *KP*$^{f/f}$*C* transplants, *KPF* and *KPF-R26-CreER*^{T2} transplants were dissociated and analyzed by FACS as follows. Mouse pancreatic tumors were washed in MEM (Gibco, Life Technologies) and cut into 1–2 mm pieces immediately following resection. Tumor pieces were collected into a 50 ml Falcon tube containing 10 ml Gey's balanced salt solution (Sigma), 5 mg Collagenase P (Roche), 2 mg Pronase (Roche), and 0.2 µg DNAse I (Roche). Samples were incubated for 15 minutes at 37°C, then pipetted up and down 10 times and returned to 37°C. After 15 more minutes, samples were pipetted up and down 5 times, then passed through a 100 µm nylon mesh (Corning). Red blood cells were lysed using RBC Lysis Buffer (eBioscience) and the remaining tumor cells were washed, then resuspended in HBSS (Gibco, Life Technologies) containing 2.5% FBS and 2 mM EDTA for staining, FACS analysis, and cell sorting. Analysis and cell sorting were carried out on a FACSAria III machine (Becton Dickinson), and data were analyzed with FlowJo software v.10.5.3 (Tree Star). The following rat antibodies were used: anti-mouse EpCAM-APC (eBioscience, #17-5791-82), anti-mouse CD133-PE (eBioscience,

#12-1331-82), anti-mouse CD45-PE/Cy7 (eBioscience, #25-0451-82), anti-mouse CD31-PE (BD Bioscience, #12-0311-82), anti-mouse PDGFR-BV421 (BD Bioscience, 566293), anti-mouse BrdU-APC (BD Biosciences, 552598), and anti-mouse Annexin-V-APC (eBioscience, #88-8007-72). Propidium-iodide (Life Technologies) was used to stain for dead cells. Msi2 expression was assessed by GFP expression in *Msi2-GFP-KP$^{f/f}$C* mice.

Patient-derived xenograft tumors were washed in MEM (Gibco, Life Technologies) and cut into 1–2 mm pieces immediately following resection. Tumor pieces were collected into a 50 ml Falcon tube containing 10 ml Gey's balanced salt solution (Sigma), 5 mg Collagenase P (Roche), 0.2 µg DNAse I (Roche), and 10.5uM Rho Kinase inhibitor (SelleckChem, Y-27632). Samples were incubated for 10 minutes at 37°C, then pipetted up and down 10 times and returned to 37°C. After 10 more minutes, samples were pipetted up and down 5 times, then passed through a 100 µm nylon mesh (Corning). Red blood cells were lysed using RBC Lysis Buffer (eBioscience) and the remaining tumor cells were washed, then resuspended in HBSS (Gibco, Life Technologies) containing 2.5% FBS and 2 mM EDTA for staining as described above. Human tissues were stained with rat antibodies against anti-human EpCAM-PE (ThermoFisher #12-9326-42) and CD133-BV421 (BD Biosciences, #566598) or CD133-APC (Miltenyi #130-113-746).

Analysis of free fatty acids by GC-MS

Smarcd3$^{f/f}$-KPF-R26-ER^{T2} flank tumor cell transplants were treated with tamoxifen or vehicle (corn oil); 3 weeks after treatment, tumors were dissociated and ~100,000 EpCAM-APC+ tumor cells were sorted, washed in PBS, and flash frozen for analysis of free fatty acids by gas chromatography-mass spectrometry (GC-MS) at the UCSD Lipidomics Core according to standard protocols. Free fatty acid concentration was normalized to protein concentration for each sample.

Western blot

Western blot analysis was used to assess the protein knockdown of SMARCD3 in *KP$^{f/f}$C* and FG cells, as well as SMARCD1 and SMARCD2 in *KP$^{f/f}$C* cells. Cells transduced with shRNA were sorted and plated in 2D culture for 72 h; cells were then collected and lysed in RIPA buffer. Protein was quantified by Bradford assay; 30ug was denatured at 95C for 5 min in 4x Laemmli sample buffer (Biorad) and loaded per well in a 4-15% precast Mini-PROTEAN TGX gel (Biorad). Gels were run at 100V for 1 h and transferred to PVDF at 90V/250mA for 1 h. Blots were blocked in Odyssey buffer (Li-cor) for 1 h at room temperature and then incubated in primary antibodies diluted in Odyssey buffer plus 0.1% Tween20 overnight. Blots were washed and incubated in secondary antibodies (1:10,000, Li-cor) the next day at room temperature for 1 h before images were collected (Li-cor scanner). Primary antibodies used for blots were α-tubulin (Abcam, ab7291) 1:10,000, SMARCD2 (Abcam, ab221168), SMARCD1 (BD Biosciences, 611728), SMARCD3 (Abcam, ab204745).

IP-Western and IP-Mass Spectrometry analysis of BAF complex

Primary *Smarcd3^{WT}* and *Smarcd3^{KO}-KP$^{f/f}$C* cell lines were derived from end-stage tumors as described above. *Smarcd3^{WT}-KP$^{f/f}$C* and *Smarcd3^{KO}-KP$^{f/f}$C* cells were collected for lysis and downstream analysis of BAF complex composition using immunoprecipitation (IP) followed by western blot or mass spectrometry (MS).

Nuclear lysates were collected following a revised Dignam protocol[103]. After cellular swelling in Buffer A (10 mM HEPES pH 7.9, 1.5 mM MgCl2, 10 mM KCl) supplemented with 1 mM DTT, 1 mM PMSF, 1 mM pepstatin, 10 mM leupeptin and 10 mM chymostatin, cells were lysed by homogenization using a 21-gauge needle with six to eight strokes. If lysis remained incomplete, cells were treated with 0.1% Igepal-630 for ten minutes on ice prior to nuclei collection. Nuclei were spun down at 1,300 x g for five minutes then resuspended in Buffer C

(20 mM HEPES pH 7.9, 20% glycerol. 420 mM NaCl, 1.5 mM MgCl2, 0.2 mM EDTA) supplemented with 1 mM DTT, 1 mM PMSF, 1 mM pepstatin, 10 mM leupeptin and 10 mM chymostatin. After thirty minutes of end-to-end rotation at 4°C, the samples were clarified at 21,000 x g for ten minutes. Supernatant was collected, flash frozen in liquid nitrogen and stored in the -80°C until use.

For IP-Western analysis, anti-IgG (Cell Signaling, 2729S), anti-SMARCA4 (Abcam, ab110641), anti-BRD9 (Active Motif, 61537), anti-ARID1A (Santa Cruz, sc-32761), anti-SMARCD1 (Santa Cruz, sc-135843), and anti-SMARCD3 (Cell Signaling, 62265) were used to immunoprecipitate BAF complex subunits from 200 mg of nuclear lysate per IP. Bound proteins from each IP were bound to 50:50 Protein A:Protein G Dynabeads (Invitrogen) for one to 2 h and washed extensively with IP wash buffer (50 mM Tris pH 8, 150 mM NaCl, 0.2 mM EDTA, 0.1% Igepal-630, 1 mM MgCl2). Proteins were eluted in SDS-PAGE loading solution with boiling for five minutes and analyzed by western blotting to determine the association of SMARCD3 with the BAF and PBAF complexes.

For IP-MS analysis, anti-IgG (Cell Signaling, 2729S) or anti-SMARCA4 antibody (Abcam, ab110641) was used for immunoprecipitation from *Smarcd3^{WT}-KP$^{f/f}$C* and *Smarcd3^{KO}-KP$^{f/f}$C* lysates. Antibodes were crosslinked to Protein A:Protein G Dynabeads (Invitrogen) using bis(sulfosuccinimidyl) suberate (BS3). Briefly, dynabeads were blocked by incubating with 10 **m**g/**m**L sheared salmon-sperm DNA in wash buffer (WB, 0.1 M NaPO4 pH 8.2, 0.1% Tween-20) then incubated with antibody at room temperature for fifteen minutes. After two washes with conjugation buffer (20 mM NaPO4 pH 8.2, 150 mM NaCl), the antibody-beads complexes were incubated with 5 mM BS3 for thirty minutes at room temperature. Cross-linking was quenched with Tris-HCl pH 7.4, and the complexes were washed with conjugation buffer and equilibrated with IP buffer (50 mM Tris pH 8, 150 mM NaCl, 0.1% Igepal-630). IP was performed as described above, but washed with RIPA buffer (50 mM Tris pH 8,

150 mM NaCl, 1% Igepal-630, 0.5% sodium deoxycholate, 0.1% SDS). Proteins were eluted in 20 mM Tris pH 8, 150 mM NaCl, 1x SDS-PAGE loading dye, 10 mM DTT with boiling. Samples were precipitated by methanol/chloroform. Dried pellets were dissolved in 8 M Urea/100 mM TEAB pH 8.5. Proteins were reduced with 5 mM tris(2-carboxyethyl)phosphine hydrochloride and alkylated with 10 mM chloroacetamide. Proteins were digested overnight at 37C in 2 M Urea/100 mM TEAB pH 8.5 with trypsin. Digestion was quenched with formic acid, 5% final concentration. The digested samples were analyzed on a Fusion Orbitrap tribrid mass spectrometer (Thermo) in a data-dependent mode.

Immunofluorescence staining

Pancreatic cancer tissue from *KP$^{f/f}$C*, *KP$^{R172H/+}$C*, *KPF*, *KPF-R26-ER^{T2}*, *KC,* or PDX tumors was fixed in 10% neutral buffered formalin (Millipore Sigma, HT501128-4L) and paraffin embedded at the UCSD Tissue Technology Shared Resource according to standard protocols. 5 µm sections were obtained and deparaffinized in xylene. The human pancreas paraffin embedded tissue array was acquired from US Biomax, Inc (BIC14011a). For paraffin embedded mouse and human pancreas tissues, antigen retrieval was performed for 45 minutes in 95–100°C 1x Citrate Buffer, pH 6.0 (eBioscience). Red blood cells were lysed by incubating slides for 10 minutes in ammonium chloride. Sections were blocked for 1 h in PBS containing 0.1% Triton X100 (Sigma- Aldrich), 10% Goat Serum (Fisher Scientific), and 5% bovine serum albumin (Invitrogen).

Primary *KP$^{f/f}$C* cells were suspended in DMEM (Gibco, Life Technologies) supplemented with 50% FBS and adhered to slides by centrifugation at 500 rpm. After drying for 15 minutes, cells were fixed with 4% paraformaldehyde (Fisher Scientific, AAJ19943K2), washed in PBS, and blocked for 1 h with PBS containing 0.1% Triton X-100 (Sigma-Aldrich), 10% Goat serum (Fisher Scientific), and 5% bovine serum albumin (Invitrogen).

All incubations with primary antibodies were carried out overnight at 4°C. Incubation with AlexaFluor-conjugated secondary antibodies (Molecular Probes) was performed for 45 minutes at room temperature. DAPI (Molecular Probes) was used to detect DNA and images were obtained with a Confocal Leica TCS SP5 II (Leica Microsystems). Signal amplification was used to boost SMARCD3 staining signal of mouse or human pancreatic tissue; overnight primary antibody staining was followed by incubation with anti-rabbit biotin antibody (Millipore Sigma AP187B, 1:200) for 1 h. Slides were then incubated with AlexaFluor streptavidin 568, DAPI, and Alexa-Fluor-conjugated secondary antibodies (Molecular Probes) against any co-stains for 45 minutes at room temperature. The following primary antibodies were used: rabbit anti-SMARCD3 (for mouse tissues, Abcam ab204745; for human tissues, Aviva Systems Biology, ARP35652_P050, QC20007-43594) 1:100, mouse anti-Keratin (Abcam, ab8068) 1:15, DAPI 1:750. All secondary antibodies were used at 1:500.

For proximity ligation assays, tissue processing was performed as described above and the promixity ligation assay was performed in accordance with manufacturers protocol (DuoLink PLA detection, red, Millipore Sigma). The blocking and antibody diluent were used as provided and the amplification step was conducted for 2 hours. The following primary antibodies were used: rabbit anti-SMARCD3 (Abcam ab204745) 1:100, goat anti-FOXA1 (Thermo Fisher, PA5-18168) 1:100, goat anti-SMARCA4 (Thermo Fisher, A303-877A) 1:500. DuoLink rabbit probes (MINUS) and goat probes (PLUS) were used. When appropriate, images were analyzed using ImageJ software version 1.50i[104].

Immunohistochemical analysis of tumors

Total area of H&E-stained tumor sections was analyzed using QuPath software[105]. Briefly, tumors were isolated and cut evenly in half along their longest diameter; tissue was fixed in 10% neutral buffered formalin and paraffin embedded, sectioned, H&E-stained, and

scanned at the UCSD Tissue Technology Shared Resource according to standard protocols. H&E sections cut from the largest, middle plane were used for QuPath analysis of tumor area. Briefly, thresholding was used to detect whole tissue and live H&E-stained tumor tissue; parameters were saved as a classifier and applied to each section for tissue and live tumor tissue detection as well as tumor area measurements. To analyze tumor cell number, serial sections were stained with hematoxylin to identify nuclei and used to train an object classifier in QuPath to detect tumor and stromal cells and regions of necrosis. This object classifier was applied to all stained sections and used to detect and count total tumor cell number within the entire tissue slice region.

Analysis of clinically annotated TMA

TMAs were sectioned to 2.5 μm thickness. IHC staining was performed on a Leica BOND RX automated immunostainer using BOND primary antibody diluent and BOND Polymer Refine DAB Detection kit according to the manufacturer's instructions (Leica Biosystems). Pre-treatment was performed using citrate buffer at 100°C for 30 min, and tissue was stained using rabbit anti-human Smarcd3 antibody (Aviva Systems Biology, ARP35652_P050, QC20007-43594). at a dilution of 1:400. Stained slides were scanned using a Pannoramic P250 digital slide scanner (3DHistech). Smarcd3 staining of individual TMA spots was analyzed in an independent and randomized manner by two board-certified surgical pathologists (C.M.S and M.W.) using Scorenado, a custom-made online digital TMA analysis tool. Interpretation of staining results was in accordance with the "reporting recommendations for tumor marker prognostic studies" (REMARK) guidelines. Equivocal and discordant cases were reviewed by a third board-certified surgical pathologist (E.K.) to reach a consensus. Smarcd3 staining in tumor cells was classified microscopically as negative (absence of any staining), vs. positive (any positive staining in tumor cells). Spots/patients with no interpretable

tissue (less than 10 intact, unequivocally identifiable tumor cells) or other artifacts were excluded.

RT-qPCR

RNA was isolated using RNeasy Micro and Mini kits (Qiagen) and converted to cDNA using Superscript III (Invitrogen). Quantitative real-time PCR was performed using an iCycler (BioRad) by mixing cDNAs, iQ SYBR Green Supermix (BioRad) and gene specific primers. All real time data was normalized to B2M.

Viral constructs and production

Short hairpin RNA (shRNA) constructs against mouse genes were designed using the Broad RNAi consortium and cloned into the lentiviral pLV-hU6-mPGK-red vector by Biosettia. shRNA against human genes were designed using the Broad RNAi consortium and cloned into the lentiviral FG12 vector[106]. Single guide RNA (sgRNA) constructs were designed using Benchling and cloned into the GeCKO lentiv2 vector; lentiCRISPR v2 was a gift from Feng Zhang (Addgene plasmid #52961)[107]. GFP-tagged lentiviral human *SMARCD3* overexpression vector and IRES-GFP control were provided by Dr. Pier Lorenzo Puri[108.109]. Virus was produced in 293T cells transfected with 4 µg shRNA constructs along with 2 µg pRSV/REV, 2 µg pMDLg/pRRE, and 2 µg pHCMVG constructs[110],[111]. Viral supernatants were collected for two days then concentrated by ultracentrifugation at 20,000 rpm for 2 h at 4°C. Adenoviral GFP and Cre high-titer viral particles were purchased from the viral vector core at the University of Iowa.

Genome-wide sequencing and analysis

Analysis of SMARCD3+ cells within human PDAC scRNA-seq

Human PDAC single-cell RNA sequencing obtained from[53] was aligned to the 10X Genomics pre-built hg38 reference, and feature-barcode matrices were generated using Cell Ranger v3[112]. Secondary analysis was performed using the Seurat v3.1 R package[113]. Cells were filtered for a minimum of 500 features, a maximum of 2,500 features and a mitochondrial percentage less than 10% per cell. Read counts were normalized using log normalization and 2,000 variable features were identified using a vst selection method. PCA dimensionality reduction was performed, and elbow plots were used to determine dimensionality. Cluster resolutions were adjusted between 0.3-0.6 accordingly to obtain discrete gene signatures among the clusters. Uniform Manifold Approximation (UMAP) was used to render final single cell composition plots. Cells were gated on *EPCAM*+ and *SMARCD3*+ cells were quantified within *EPCAM*+ cells, *EpCAM*+*PROM1*+ (CD133+) cells, and *EPCAM*+*MSI2*+ cells.

RNA-sequencing

Low-passage primary CD133^{High} *KP$^{f/f}$C* tumor cells were derived as outline above. 1x10^6 cells were infected with RFP-tagged shRNA against *Smarcd3* or control in triplicate; transduced RFP+ cells were sorted 72 h post-transduction and plated in a 10cm cell culture plate in 10% DMEM growth media. 5 days after plating, cells were collected for parallel analysis by RNA-seq and ChIP-seq. >300,00 cells per replicate were collected for RNA-seq; total RNA was isolated using Quick-RNA Miniprep Kit (Zymo Research). Total RNA was assessed for quality using an Agilent Tapestation, and all samples had RIN >7. RNA libraries were generated from 100ng RNA using Illumina's TruSeq Stranded mRNA Sample Prep Kit following manufacturer's instructions for subsequent sequencing.

ChIP-sequencing

KP$^{f/f}$C cells were transduced and plated as above for both RNA-seq and ChIP-seq analysis. For SWI/SNF subunit ChIP-seq, 6-7e^6 cells were collected per condition and cross-

linked first in 3mM disuccinimidyl glutarate (DSG) then in 1% formaldehyde. For histone modification ChIP-seq, $2e^6$ cells were collected per condition and cross-linked with 1% formaldehyde. After quenching the excess formaldehyde with 125 mM glycine, the fixed cells were washed, pelleted and flash-frozen. Upon thawing, the cells were resuspended in lysis solution (50 mM HEPES-KOH pH 8, 140 mM NaCl, 1 mM EDTA, 10% glycerol, 0.5% NP40, 0.25% Triton X-100 and incubated on ice for ten minutes. The isolated nuclei were washed with wash solution (10 mM Tris-HCl pH 8, 1 mM EDTA, 0.5 mM EGTA, 200 mM NaCl) and shearing buffer (0.1% SDS, 1 mM EDTA, 10 mM Tris-HCl pH 8) then sheared in a Covaris E229 sonicator for 10 minutes to generate DNA fragments between ~ 200-1000 bp. After clarification of insoluble material by centrifugation, the chromatin was immunoprecipitated overnight at 4°C with antibodies against SMARCA4 (Abcam, ab110641), ARID1A (Cell Signaling Technology, CST 12354), H3K4me (Abcam ab8895), H3K4me3 (Millipore 05-745) and H3K27ac (Abcam ab4729) then bound to Protein A+G Dynabeads (Invitrogen) in ChIP buffer (50 mM HEPES-KOH pH 7.5, 300 mM NaCl, 1 mM EDTA, 1% Triton X-100, 0.1% DOC, 0.1% SDS). Antibody bound DNA were washed and treated with Proteinase K and RNase A and the purified ChIP DNA was used for library generation (NuGen Ovation Ultralow Library System V2) for subsequent sequencing.

Analysis of RNA-seq and ChIP-seq data

Reads were aligned to the mouse genome (mm10) using STAR alignment tool (v2.5) for RNA-seq and ChIP-seq. In all cases, only reads that mapped to a unique genomic location (MAPQ>10) were used for downstream analysis. HOMER[114] (v4.8, http://homer.salk.edu/homer/) was used to process alignment files to generate ChIP-seq bed files. ChIP-seq peaks for SMARCA4 and ARID1A were found by using the findPeaks program in HOMER with the parameter “-style factor” versus the appropriate ChIP input experiments as

background. ChIP-seq peaks for H3K4me, H3K4me3, and H3K27ac were called using the parameter "-style histone". SMARCA4 and ARID1A peaks were called when enriched >four-fold over input and over local tag counts, with FDR 0.001 (Benjamin-Hochberg). For histone ChIP-seq, peaks within a 1000 bp range were stitched together to form regions. Differential ChIP-seq peaks were found by merging peaks from shControl and shSmarcd3 groups and called using getDifferentialPeaks with fold change 1.5, Poisson p value < 0.0001. For motif enrichment analysis, sequences within 200 bp of peak centers were compared to motifs in the HOMER database using the findMotifsGenome.pl command using default fragment size and motif length parameters. Random GC content-matched genomic regions were used as background. Enriched motifs are statistically significant motifs in input over background by a p-value of less than 0.05. P-values were calculated using cumulative binomial distribution.

For RNA-seq, RNA expression was quantified as raw integer counts using analyzeRepeats.pl in HOMER using the following parameters: -strand both -count exons -condenseGenes -noadj. To identify differentially expressed genes, we performed getDiffExpression.pl in HOMER, which uses the DESeq2 R package to calculate the biological variation within replicates. Cut-offs were set at log2 FC = 0.585 and FDR at 0.05.

GSEA analysis

Gene Set Enrichment Analysis (GSEA)[115] was performed with the Bioconductor GSVA data C2, C6, and C7 BroadSets gene set collections; these are the C2 collection of curated gene sets, the C6 collection of oncogenic signature gene sets, and the C7 collection of immunologic signatures gene sets from MsigDB3.0[115]. Additionally, we used a collection of curated gene sets we derived from published data in the context of shFoxa1 or sgFoxa1 knockdown[59], sgKlf5 knockdown[116], and a gene signature enriched within primary *Msi2*+ *KP$^{f/f}$C*

stem cells and *Msi2-KP$^{f/f}$C* non-stem cells[16]. Briefly, GSEA evaluates a ranked gene expression data-set against previously defined gene sets.

Network analysis

We used a network approach to map the results from the *KP$^{f/f}$C* RNA-seq experiment. Briefly, genes significantly down-regulated by Smarcd3 inhibition (padj<0.05, logFC<-0.35) were used to construct a SMARCD3-regulated network using high confidence (>0.8) interactions within the STRING mouse interactome[117] in Cytoscape[118]. The STRING interactome contains known and predicted functional protein-protein interactions. The interactions are assembled from a variety of sources, including genomic context predictions, high throughput lab experiments, and co-expression databases. Interaction confidence is a weighted combination of all lines of evidence, with higher quality experiments contributing more. The SMARCD3-regulated STRING network contained 1,030 nodes connected by 7,860 edges; node size was scaled to logFC by RNA-seq to allow visualization of gene expression data (larger nodes = large -logFC). To interrogate how interacting proteins within the network may be segregated into different functional programs, we applied a community clustering algorithm (GLay) to the network using clusterMaker[119]. This generated 12 network hubs of clustered interacting proteins; we then used STRING functional enrichment to identify functionally enriched annotations for each hub (hubs are colored by cluster number). Finding 4 hubs implicated in lipid metabolism, we pulled all genes from these 4 hubs into a “lipid subnetwork” regulated by SMARCD3. We labelled specific nodes with known functions in lipid metabolism, and further overlaid our ChIP-seq data on this network to identify nodes that were directly regulated by SMARCD3-BAF and FOXA1. Node genes that were both co-bound by FOXA1 by ChIP-seq and lost SMARCA4/ARID1A (BAF) binding by ChIP-seq were considered putative direct targets of SMARCD3-BAF/FOXA1; direct targets with known lipid functions

were highlighted in our network with a yellow node label, yellow diamond-shaped node, and manually inserted yellow edges indicating direct regulation of this subnetwork by SMARCD3-BAF/FOXA1.

Quantification and statistical analysis

Statistical analyses were carried out using GraphPad Prism software version 8.2.0 (GraphPad Software Inc.). Sample sizes for *in vivo* drug studies were determined based on the variability of pancreatic tumor models used. For flank transplant and autochthonous drug studies, tumor bearing animals within each group were randomly assigned to treatment groups. Experimental group sizes were determined based on previous studies[14,16]. Data are shown as the mean ± SEM. Two-tailed unpaired Student's t-tests with Welch's correction or One-way analysis of variance (ANOVA) for multiple comparisons when appropriate were used to determine statistical significance (*P<0.05, **P<0.01, ***P<0.001, ****P<0.0001); p values were adjusted for multiple comparisons in the case of analysis by ANOVA.

. The level of replication for each *in vitro* and *in vivo* study is noted in the figure legends for each figure and described in detail in the Method Details section above. However, to summarize briefly, *in vitro* sphere or colony formation studies were conducted with n=3 independent wells per cell line across two independent shRNA of n=3 wells; the majority of these experiments were additionally completed in >2 independently derived cell line, n=3 wells per shRNA. Because material was limited, PDX organoids treated with shRNA were plated in n=3-4 wells per experiment, for one experiment each using two independent PDX organoid lines. Flank shRNA studies were conducted three times using independent cell lines, with n=3-4 tumors per group in each experiment. Analysis of midpoint (7-8 weeks old) $KP^{f/f}C$ tumors was conducted with n=5-16 mice per group. Secondary syngeneic transplants were conducted with n=3-4 independent tumors per group, transplanted into n=2-4 littermate recipients each.

Survival studies in *KP$^{f/f}$C* mice plus and minus gemcitabine treatment were conducted with n=6-10 mice per group. Flank *KPF* + adCre and *KPF-R26-CreER^{T2}* tamoxifen treated transplants were conducted in 2 biological replicates at n=3-5 tumors per group. Tumor initiation studies in the autochthonous *KC* model were conducted with n=3-9 mice for all Cre systems used. 3 independent PDX tumors were used for shRNA studies *in vivo*, one PDX sample was used for one experiment while the other two were completed in duplicate for a total of n=4-5 per shRNA for 2 independent shRNA. RNA-seq in *KP$^{f/f}$C* cells was run in triplicate, H3K27-acetyl ChIP-seq was run in duplicate, and one ChIP each was run for H3K4me, H3K4me3, SMARCA4, and ARID1A ChIP-seq.

3.6. Acknowledgements

Chapter 3 has been submitted as it may appear in Nature Communications, 2022. Ferguson LP†, Gatchalian J, Chambers K, McDermott ML, Rajbhandari N, Lytle NK, Rosenthal SB, Schürch CM, Hamilton M, Albini S, Wartenberg M, Zlobec I, Galván JA, Karamitopoulou E, Puri PL, Bruneau BG, Lowy AM, Hargreaves DC*, and Reya T*. “SMARCD3 is a key epigenetic dependency for pancreatic adenocarcinoma”**.** The dissertation author was the primary investigator and author of this paper.

We are grateful to Christopher Wright for providing the *Ptf1a-Cre* mice, Dieter Saur for providing *FSF-Kras$^{G12D/+}$; p53$^{frt/frt}$; Pdx-Flp* mice, the UCSD Lipidomics Core for GC-MS analysis of free fatty acids and the UCSD Tissue Technology Shared Resource for processing of tissues for histological analysis. L.P.F. received support from T32 GM007752 and a Ruth L. Kirschstein National Research Service Award F31 CA247489. M.L.M received support from T32 GM007752. N.R. received support from the Tobacco Related Disease Research Program T29FT0280. M.H. received support from T32 HL086344. J.G. received support from T32 T32CA009370 and a Ruth L. Kirschstein National Research Service Award F32

GM128377. D.C.H. received support from the American Cancer Society Scholar Award and the Pew-Stewart Scholars Program for Cancer Research.This work was also supported by R01 CA186043 to A.M.L and T.R, R35 CA197699 to T.R. and an SU2C–CRUK–Lustgarten Foundation Pancreatic Cancer Dream Team Research Grant (SU2C-AACR-DT-20-16) to A.M.L. and T.R

L.P.F conducted the curated screen *in vitro*, performed all qPCR, western blot, and functional studies in mouse and human pancreatic cancer cells *in vitro,* derived patient-derived organoid lines, conducted mouse and patient-derived xenograft transplant experiments, performed immunofluorescence, histological analysis, proximity ligation assay, stained and analyzed commercial human PDAC TMA, treated mice with gemcitabine or tamoxifen, performed FACS analysis on primary and transplanted mouse and human pancreatic tumors, sorted tumor cells for RNA-seq, ChIP-seq, and GC-MS, prepped RNA-seq libraries, and performed GSEA analysis. J.G performed and analyzed ChIP-seq for H3K27ac, H3K4me, H3K4me3, ARID1A, and SMARCA4, performed motif analysis, analyzed published KLF5 and FOXA1 ChIP-seq data and overlaid with BAF ChIP-seq data, analyzed RNA-seq data, conducted IP-Western blot for SWI/SNF subunits, and performed and analyzed IP-Mass spectrometry for SMARCA4 in mouse pancreatic cancer cells with assistance from D.C.H. K.C assisted with culture and expansion of patient-derived organoid lines. M.L.M assisted with functional validation of shRNA experiments *in vitro* and dosing of mice with gemcitabine and tamoxifen for *in vivo* studies. N.R. assisted with *in vivo* studies. N.K.L. advised on initial curated screen and *in vivo* studies. M.H. analyzed the published sc-RNAseq dataset for *SMARCD3* enrichment within CD133+ and Msi2+ tumor fractions. S.B.R assisted with generation and visualization of RNA-seq network. S.A and P.L.P provided the SMARCD3 overexpression vector and shared *Smarcd3*$^{f/f}$ mice. B.G.B provided *Smarcd3*$^{f/f}$ mice. J.A.G performed immunohistochemical staining for SMARCD3 in an independent clinically annotated TMA; E.K.

created the TMA and collected clinical data. M.W. and C.M.S analyze and interpreted TMA staining and I.Z. performed statistical analysis. A.M.L. and C.M.S provided advice and comments on the manuscript. L.P.F. and J.G. helped write the paper. D.C.H. guided the epigenetic analysis and mechanistic studies and helped write the paper. T.R. conceived of the project, planned and guided the research, and wrote the paper.

3.7. References

1. Rahib, L., Wehner, M. R., Matrisian, L. M. and Nead, K. T. Estimated Projection of US Cancer Incidence and Death to 2040. *JAMA Netw. Open* **4**, e214708 (2021).

2. Siegel, R. L., Miller, K. D., Fuchs, H. E. and Jemal, A. Cancer Statistics, 2021. *CA. Cancer J. Clin.* **71**, 7–33 (2021).

3. Hruban, R. H., Goggins, M., Parsons, J. and Kern, S. E. Progression model for pancreatic cancer. *Clinical Cancer Research* **6**, 2969–2972 (2000).

4. Maitra, A., Adsay, N.V., Argani, P., Iacobuzio-Donahue, C., De Marzo, A., Cameron, J.L., Yeo, C.J. and Hruban, R.H. Multicomponent analysis of the pancreatic adenocarcinoma progression model using a pancreatic intraepithelial neoplasia tissue microarray. *Mod. Pathol.* **16**, 902–912 (2003).

5. Hezel, A. F., Kimmelman, A. C., Stanger, B. Z., Bardeesy, N. and DePinho, R. A. Genetics and biology of pancreatic ductal adenocarcinoma. *Genes Dev.* **20**, 1218–1249 (2006).

6. Yachida, S. & Iacobuzio-Donahue, C. A. The pathology and genetics of metastatic pancreatic cancer. *Arch. Path. Lab.* **133**, 413–422 (2009).

7. Rhim, A.D., Mirek, E.T., Aiello, N.M., Maitra, A., Bailey, J.M., McAllister, F., Reichert, M., Beatty, G.L., Rustgi, A.K., Vonderheide, R.H. and Leach, S.D. EMT and dissemination precede pancreatic tumor formation. *Cell* **148**, 349–361 (2012).

8. Batlle, E. & Clevers, H. Cancer stem cells revisited. *Nat. Med.* **23**, 1124–1134 (2017).

9. Black, J. R. M. & McGranahan, N. Genetic and non-genetic clonal diversity in cancer evolution. *Nat. Rev. Cancer* **21,** 1–14 (2021).

10. Reya, T., Morrison, S. J., Clarke, M. F. and Weissman, I. L. Stem cells, cancer, and cancer stem cells. *Nature* **414**, 105–111 (2001).

11. Hermann, P.C., Huber, S.L., Herrler, T., Aicher, A., Ellwart, J.W., Guba, M., Bruns, C.J. and Heeschen, C. Distinct populations of cancer stem cells determine tumor

growth and metastatic activity in human pancreatic cancer. *Cell Stem Cell* **1**, 313–323 (2007).

12. García-Silva, S., Frias-Aldeguer, J. and Heeschen, C. Stem cells & pancreatic cancer. in *Pancreatology* **13**, 110–113 (2013).

13. Zhan, H.X., Xu, J.W., Wu, D., Zhang, T.P. and Hu, S.Y. Pancreatic cancer stem cells: New insight into a stubborn disease. *Cancer Lett.* **357**, 429–437 (2015).

14. Fox, R.G., Lytle, N.K., Jaquish, D.V., Park, F.D., Ito, T., Bajaj, J., Koechlein, C.S., Zimdahl, B., Yano, M., Kopp, J.L. and Kritzik, M. Image-based detection and targeting of therapy resistance in pancreatic adenocarcinoma. *Nature* **534**, 407–411 (2016).

15. Hermann, P. C. & Sainz, B. Pancreatic cancer stem cells: A state or an entity? *Semin. Cancer Biol.* **53**, 223–231 (2018).

16. Lytle, N.K., Ferguson, L.P., Rajbhandari, N., Gilroy, K., Fox, R.G., Deshpande, A., Schürch, C.M., Hamilton, M., Robertson, N., Lin, W., Noel, P. A., Wartenberg, M., Zlobec, I., Eichmann, M., Galván, J. A., Karamitopolous, E., Gilderman, T., Esparza, L. A., Shima, Y., Spahn, P., French, R., Lewis, N. E., Fisch, K. M., Sasik, R., Rosenthal S. B., Kritzik, M., Von Hoff, D., Han, H., Ideker, T., Desphande A. J., Lowy, A. M., Adams, P. D., and Reya T. A multiscale map of the stem cell state in pancreatic adenocarcinoma. *Cell* **177**, 572-586 (2019).

17. Wainwright, E. N. & Scaffidi, P. Epigenetics and cancer stem cells: Unleashing, hijacking, and restricting cellular plasticity. *Trends in Cancer* **3**, 372–386 (2017).

18. Lanfranca, M.P., Thompson, J.K., Bednar, F., Halbrook, C., Lyssiotis, C., Levi, B. and Frankel, T.L. Metabolism and epigenetics of pancreatic cancer stem cells. *Semin. in Cancer Biol.* **57**, 19–26 (2019).

19. Numata, M., Morinaga, S., Watanabe, T., Tamagawa, H., Yamamoto, N., Shiozawa, M., Nakamura, Y., Kameda, Y., Okawa, S., Rino, Y. and Akaike, M. The clinical significance of SWI/SNF complex in pancreatic cancer. *Int. J. Oncol.* **42**, 403–410 (2013).

20. Alver, B.H., Kim, K.H., Lu, P., Wang, X., Manchester, H.E., Wang, W., Haswell, J.R., Park, P.J. and Roberts, C.W. The SWI/SNF chromatin remodelling complex is required for maintenance of lineage specific enhancers. *Nat. Commun.* **8**, (2017).

21. Barisic, D., Stadler, M. B., Iurlaro, M. and Schübeler, D. Mammalian ISWI and SWI/SNF selectively mediate binding of distinct transcription factors. *Nature* **569**, 136–140 (2019).

22. Wu, J. I., Lessard, J. & Crabtree, G. R. Understanding the words of chromatin regulation. *Cell* **136**, 200–206 (2009).

23. Hiramatsu, H., Kobayashi, K., Kobayashi, K., Haraguchi, T., Ino, Y., Todo, T. and Iba, H. The role of the SWI/SNF chromatin remodeling complex in maintaining the stemness of glioma initiating cells. *Sci. Rep.* **7**, 1–13 (2017).

24. Ganguly, D., Sims, M., Cai, C., Fan, M. and Pfeffer, L. M. Chromatin remodeling factor BRG1 regulates stemness and chemosensitivity of glioma initiating sells. *Stem Cells* **36**, 1804–1815 (2018).

25. Saladi, S.V., Ross, K., Karaayvaz, M., Tata, P.R., Mou, H., Rajagopal, J., Ramaswamy, S. and Ellisen, L.W. ACTL6A is co-amplified with p63 in squamous cell carcinoma to drive YAP activation, regenerative proliferation, and poor prognosis. *Cancer Cell* **31**, 35–49 (2017).

26. Buscarlet, M., Krasteva, V., Ho, L., Simon, C., Hébert, J., Wilhelm, B., Crabtree, G.R., Sauvageau, G., Thibault, P. and Lessard, J.A. Essential role of BRG, the ATPase subunit of BAF chromatin remodeling complexes, in leukemia maintenance. *Blood* **123**, 1720–1728 (2014).

27. Mittal, P. & Roberts, C. W. M. The SWI/SNF complex in cancer — biology, biomarkers and therapy. *Nat. Rev. Clin. Oncol.* **17**, 435–448 (2020).

28. Arnaud, O., Le Loarer, F. and Tirode, F. BAFfling pathologies: Alterations of BAF complexes in cancer. *Cancer Lett.* **419**, 266–279 (2018).

29. Centore, R. C., Sandoval, G. J., Soares, L. M. M., Kadoch, C. and Chan, H. M. Mammalian SWI/SNF chromatin remodeling complexes: Emerging mechanisms and therapeutic strategies. *Trends Genet.* **36**, 936–950 (2020).

30. Hasan, N. & Ahuja, N. The emerging roles of ATP-dependent chromatin remodeling complexes in pancreatic cancer. *Cancers (Basel)* **11**, 1859 (2019).

31. Röhrig, F. & Schulze, A. The multifaceted roles of fatty acid synthesis in cancer. *Nat. Rev. Cancer* **16**, 732–749 (2016).

32. Kuo, C. Y. & Ann, D. K. When fats commit crimes: Fatty acid metabolism, cancer stemness and therapeutic resistance. *Cancer Commun.* **38**, (2018).

33. Jagust, P., De Luxán-Delgado, B., Parejo-Alonso, B. & Sancho, P. Metabolism-based therapeutic strategies targeting cancer stem cells. *Front. Pharmacol.* **10**, 203 (2019).

34. Kawaguchi, Y., Cooper, B., Gannon, M., Ray, M., MacDonald, R.J. and Wright, C.V. The role of the transcriptional regulator Ptf1a in converting intestinal to pancreatic progenitors. *Nat. Genet.* **32**, 128–134 (2002).

35. Aguirre, A.J., Bardeesy, N., Sinha, M., Lopez, L., Tuveson, D.A., Horner, J., Redston, M.S. and DePinho, R.A. Activated Kras and Ink4a/Arf deficiency cooperate to produce metastatic pancreatic ductal adenocarcinoma. *Genes Dev.* **17**, 3112–3126 (2003).

36. Hingorani, S.R., Petricoin III, E.F., Maitra, A., Rajapakse, V., King, C., Jacobetz, M.A., Ross, S., Conrads, T.P., Veenstra, T.D., Hitt, B.A. and Kawaguchi, Y. Preinvasive and invasive ductal pancreatic cancer and its early detection in the mouse. *Cancer Cell* **4**, 437–450 (2003).

37. Bardeesy, N., Aguirre, A.J., Chu, G.C., Cheng, K.H., Lopez, L.V., Hezel, A.F., Feng, B., Brennan, C., Weissleder, R., Mahmood, U. and Hanahan, D. Both p16Ink4a and the p19Arf-p53 pathway constrain progression of pancreatic adenocarcinoma in the mouse. *Proc. Natl. Acad. Sci. U. S. A.* **103**, 5947–5952 (2006).

38. Rovira, M., Scott, S.G., Liss, A.S., Jensen, J., Thayer, S.P. and Leach, S.D. Isolation and characterization of centroacinar/terminal ductal progenitor cells in adult mouse pancreas. *Proc. Natl. Acad. Sci. U. S. A.* **107**, 75–80 (2010).

39. Yang, L., Shi, P., Zhao, G., Xu, J., Peng, W., Zhang, J., Zhang, G., Wang, X., Dong, Z., Chen, F. and Cui, H. Targeting cancer stem cell pathways for cancer therapy. *Signal Transduct. Target. Ther.* **5**, 1–35 (2020).

40. Lu, Y., Zhu, H., Shan, H., Lu, J., Chang, X., Li, X., Lu, J., Fan, X., Zhu, S., Wang, Y. and Guo, Q. Knockdown of Oct4 and Nanog expression inhibits the stemness of pancreatic cancer cells. *Cancer Lett.* **340**, 113–123 (2013).

41. Seymour, P. A. Sox9: A master regulator of the pancreatic program. *Rev. Diabet. Stud.* **11**, 51–83 (2014).

42. Shouksmith, A.E., Shah, F., Grimard, M.L., Gawel, J.M., Raouf, Y.S., Geletu, M., Berger-Becvar, A., De Araujo, E.D., Luchman, H.A., Heaton, W.L. and Bakhshinyan, D. Identification and characterization of AES-135, a hydroxamic acid-based HDAC inhibitor that prolongs survival in an orthotopic mouse model of pancreatic cancer. *J. Med. Chem.* **62**, 2651–2665 (2019).

43. Cai, M.H., Xu, X.G., Yan, S.L., Sun, Z., Ying, Y., Wang, B.K. and Tu, Y.X. Depletion of HDAC1, 7 and 8 by histone deacetylase inhibition confers elimination of pancreatic cancer stem cells in combination with gemcitabine. *Sci. Rep.* **8**, (2018).

44. Shain, A.H., Giacomini, C.P., Matsukuma, K., Karikari, C.A., Bashyam, M.D., Hidalgo, M., Maitra, A. and Pollack, J.R. Convergent structural alterations define SWItch/Sucrose NonFermentable (SWI/SNF) chromatin remodeler as a central tumor suppressive complex in pancreatic cancer. *Proc. Natl. Acad. Sci. U. S. A.* **109**, (2012).

45. Cerami, E., Gao, J., Dogrusoz, U., Gross, B.E., Sumer, S.O., Aksoy, B.A., Jacobsen, A., Byrne, C.J., Heuer, M.L., Larsson, E. and Antipin, Y. The cBio Cancer Genomics Portal: An open platform for exploring multidimensional cancer genomics data. *Cancer Discov.* **2**, 401–404 (2012).

46. Gao, J., Aksoy, B.A., Dogrusoz, U., Dresdner, G., Gross, B., Sumer, S.O., Sun, Y., Jacobsen, A., Sinha, R., Larsson, E. and Cerami, E. Integrative analysis of complex cancer genomics and clinical profiles using the cBioPortal. *Sci. Signal.* **6**, (2013).

47. Forcales, S.V., Albini, S., Giordani, L., Malecova, B., Cignolo, L., Chernov, A., Coutinho, P., Saccone, V., Consalvi, S., Williams, R. and Wang, K. Signal-dependent incorporation of MyoD-BAF60c into Brg1-based SWI/SNF chromatin-remodelling complex. *EMBO J.* **31**, 301–316 (2012).

48. Wang, Y., Wong, R.H., Tang, T., Hudak, C.S., Yang, D., Duncan, R.E. and Sul, H.S.

Phosphorylation and recruitment of BAF60c in chromatin remodeling for lipogenesis in response to insulin. *Mol. Cell* **49**, 283–297 (2013).

49. Sun, X., Hota, S.K., Zhou, Y.Q., Novak, S., Miguel-Perez, D., Christodoulou, D., Seidman, C.E., Seidman, J.G., Gregorio, C.C., Henkelman, R.M. and Rossant, J. Cardiac-enriched BAF chromatin-remodeling complex subunit Baf60c regulates gene expression programs essential for heart development and function. *Biol. Open* **7**, (2018).

50. Schönhuber, N., Seidler, B., Schuck, K., Veltkamp, C., Schachtler, C., Zukowska, M., Eser, S., Feyerabend, T.B., Paul, M.C., Eser, P. and Klein, S. A next-generation dual-recombinase system for time- and host-specific targeting of pancreatic cancer. *Nat. Med.* **20**, 1340–1347 (2014).

51. Ventura, A., Kirsch, D.G., McLaughlin, M.E., Tuveson, D.A., Grimm, J., Lintault, L., Newman, J., Reczek, E.E., Weissleder, R. and Jacks, T. Restoration of p53 function leads to tumour regression in vivo. *Nature* **445**, 661–665 (2007).

52. Andricovich, J., Perkail, S., Kai, Y., Casasanta, N., Peng, W. and Tzatsos, A. Loss of KDM6A activates super-enhancers to induce gender-specific squamous-like pancreatic cancer and confers sensitivity to BET inhibitors. *Cancer Cell* **33**, 512-526.e8 (2018).

53. Peng, J., Sun, B.F., Chen, C.Y., Zhou, J.Y., Chen, Y.S., Chen, H., Liu, L., Huang, D., Jiang, J., Cui, G.S. and Yang, Y. Single-cell RNA-seq highlights intra-tumoral heterogeneity and malignant progression in pancreatic ductal adenocarcinoma. *Cell Res.* **29**, 725–738 (2019).

54. Alpsoy, A. & Dykhuizen, E. C. Glioma tumor suppressor candidate region gene 1 (GLTSCR1) and its paralog GLTSCR1-like form SWI/SNF chromatin remodeling subcomplexes. *J. Biol. Chem.* **293**, 3892–3903 (2018).

55. Gatchalian, J., Malik, S., Ho, J., Lee, D.S., Kelso, T.W., Shokhirev, M.N., Dixon, J.R. and Hargreaves, D.C. A non-canonical BRD9-containing BAF chromatin remodeling complex regulates naive pluripotency in mouse embryonic stem cells. *Nat. Commun.* **9**, 1–16 (2018).

56. Mashtalir, N., D'Avino, A.R., Michel, B.C., Luo, J., Pan, J., Otto, J.E., Zullow, H.J., McKenzie, Z.M., Kubiak, R.L., Pierre, R.S. and Valencia, A.M. Modular organization and assembly of SWI/SNF family chromatin remodeling complexes. *Cell* **175**, 1272-1288.e20 (2018).

57. Michel, B.C., D'Avino, A.R., Cassel, S.H., Mashtalir, N., McKenzie, Z.M., McBride, M.J., Valencia, A.M., Zhou, Q., Bocker, M., Soares, L.M. and Pan, J. A non-canonical SWI/SNF complex is a synthetic lethal target in cancers driven by BAF complex perturbation. *Nat. Cell Biol.* **20**, 1410–1420 (2018).

58. Vierbuchen, T., Ling, E., Cowley, C.J., Couch, C.H., Wang, X., Harmin, D.A., Roberts, C.W. and Greenberg, M.E. AP-1 transcription factors and the BAF complex mediate signal-dependent enhancer selection. *Mol. Cell* **68**, 1067-1082.e12 (2017).

59. Roe, J.S., Hwang, C.I., Somerville, T.D., Milazzo, J.P., Lee, E.J., Da Silva, B., Maiorino, L., Tiriac, H., Young, C.M., Miyabayashi, K. and Filippini, D. Enhancer reprogramming promotes pancreatic cancer metastasis. *Cell* **170**, 875-888.e20 (2017).

60. Creyghton, M.P., Cheng, A.W., Welstead, G.G., Kooistra, T., Carey, B.W., Steine, E.J., Hanna, J., Lodato, M.A., Frampton, G.M., Sharp, P.A. and Boyer, L.A. Histone H3K27ac separates active from poised enhancers and predicts developmental state. *Proc. Natl. Acad. Sci. U. S. A.* **107**, 21931–21936 (2010).

61. Hnisz, D., Abraham, B.J., Lee, T.I., Lau, A., Saint-André, V., Sigova, A.A., Hoke, H.A. and Young, R.A. Super-enhancers in the control of cell identity and disease. *Cell* **155**, 934 (2013).

62. Whyte, W.A., Orlando, D.A., Hnisz, D., Abraham, B.J., Lin, C.Y., Kagey, M.H., Rahl, P.B., Lee, T.I. and Young, R.A. Master transcription factors and mediator establish super-enhancers at key cell identity genes. *Cell* **153**, 307–319 (2013).

63. Carracedo, A., Cantley, L. C. and Pandolfi, P. P. Cancer metabolism: Fatty acid oxidation in the limelight. *Nat. Rev. Cancer* **13**, 227–232 (2013).

64. Sancho, P., Barneda, D. and Heeschen, C. Hallmarks of cancer stem cell metabolism. *Br. J. Cancer* **114**, 1305–1312 (2016).

65. Brandi, J., Dando, I., Dalla Pozza, E., Biondani, G., Jenkins, R., Elliott, V., Park, K., Fanelli, G., Zolla, L., Costello, E. and Scarpa, A. Proteomic analysis of pancreatic cancer stem cells: Functional role of fatty acid synthesis and mevalonate pathways. *J. Proteomics* **150**, 310–322 (2017).

66. Biancur, D. E. & Kimmelman, A. C. The plasticity of pancreatic cancer metabolism in tumor progression and therapeutic resistance. *Biochim. Biophys. Acta Rev. Cancer* **1870**, 67–75 (2018).

67. Sunami, Y., Rebelo, A. and Kleeff, J. Lipid metabolism and lipid droplets in pancreatic cancer and stellate cells. *Cancers* **10**, (2018).

68. Yin, Y., Liu, L., Zhao, Z., Yin, L., Bauer, N., Nwaeburu, C.C., Gladkich, J., Gross, W., Hackert, T., Sticht, C. and Gretz, N. Simvastatin inhibits sonic hedgehog signaling and stemness features of pancreatic cancer. *Cancer Lett.* **426**, 14–24 (2018).

69. Gupta, V.K., Sharma, N.S., Kesh, K., Dauer, P., Nomura, A., Giri, B., Dudeja, V., Banerjee, S., Bhattacharya, S., Saluja, A. and Banerjee, S. Metastasis and chemoresistance in CD133 expressing pancreatic cancer cells are dependent on their lipid raft integrity. *Cancer Lett.* **439**, 101–112 (2018).

70. Zhang, J., Li, Q., Wu, Y., Wang, D., Xu, L., Zhang, Y., Wang, S., Wang, T., Liu, F., Zaky, M.Y. and Hou, S. Cholesterol content in cell membrane maintains surface levels of ErbB2 and confers a therapeutic vulnerability in ErbB2-positive breast cancer. *Cell Commun. Signal.* **17**, (2019).

71. Deshpande, I., Liang, J., Hedeen, D., Roberts, K.J., Zhang, Y., Ha, B., Latorraca, N.R., Faust, B., Dror, R.O., Beachy, P.A. and Myers, B.R. Smoothened stimulation by membrane sterols drives Hedgehog pathway activity. *Nature* **571**, 284–288 (2019).

72. Espiau-Romera, P., Courtois, S., Parejo-Alonso, B. and Sancho, P. Molecular and metabolic subtypes correspondence for pancreatic ductal adenocarcinoma classification. *J. Clin. Med.* **9**, 4128 (2020).

73. Kubo, M., Gotoh, K., Eguchi, H., Kobayashi, S., Iwagami, Y., Tomimaru, Y., Akita, H., Asaoka, T., Noda, T., Takeda, Y. and Tanemura, M. Impact of CD36 on chemoresistance in pancreatic ductal adenocarcinoma. *Ann. Surg. Oncol.* **27**, 610–619 (2020).

74. Bian, Y., Yu, Y., Wang, S. and Li, L. Up-regulation of fatty acid synthase induced by EGFR/ERK activation promotes tumor growth in pancreatic cancer. *Biochem. Biophys. Res. Commun.* **463**, 612–617 (2015).

75. Ding, N., Cui, X.X., Gao, Z., Huang, H., Wei, X., Du, Z., Lin, Y., Shih, W.J., Rabson, A.B., Conney, A.H. and Hu, C. A triple combination of atorvastatin, celecoxib and tipifarnib strongly inhibits pancreatic cancer cells and xenograft pancreatic tumors. *Int. J. Oncol.* **45**, 2139–2145 (2014).

76. Nishi, K., Suzuki, M., Yamamoto, N., Matsumoto, A., Iwase, Y., Yamasaki, K., Otagiri, M. and Yumita, N. Glutamine deprivation enhances Acetyl-CoA carboxylase inhibitor-induced death of human pancreatic cancer cells. *Anticancer Res.* **38**, 6683–6689 (2018).

77. Ye, Z., Zhuo, Q., Hu, Q., Xu, X., Zhang, Z., Xu, W., Liu, W., Fan, G., Qin, Y., Yu, X. and Ji, S. FBW7-NRA41-SCD1 axis synchronously regulates apoptosis and ferroptosis in pancreatic cancer cells. *Redox Biol.* **38**, 101807 (2021).

78. Sekar, S., Gopalakrishnan, V. and Taghibiglou, C. Sterol regulatory element-binding protein 1 inhibitors decrease pancreatic cancer cell viability and proliferation. *Biochem. Biophys. Res. Commun.* **488**, 136–140 (2017).

79. Biancur, D.E., Paulo, J.A., Małachowska, B., Del Rey, M.Q., Sousa, C.M., Wang, X., Sohn, A.S., Chu, G.C., Gygi, S.P., Harper, J.W. and Fendler, W. Compensatory metabolic networks in pancreatic cancers upon perturbation of glutamine metabolism. *Nat. Commun.* **8**, 1–15 (2017).

80. Koundouros, N. & Poulogiannis, G. Reprogramming of fatty acid metabolism in cancer. *Br. J. Cancer* **122**, 4–22 (2020).

81. Nagarajan, S. R., Butler, L. M. and Hoy, A. J. The diversity and breadth of cancer cell fatty acid metabolism. *Cancer Metab.* **9**, 2 (2021).

82. Von Figura, G., Fukuda, A., Roy, N., Liku, M.E., Morris Iv, J.P., Kim, G.E., Russ, H.A., Firpo, M.A., Mulvihill, S.J., Dawson, D.W. and Ferrer, J. The chromatin regulator Brg1 suppresses formation of intraductal papillary mucinous neoplasm and pancreatic ductal adenocarcinoma. *Nat. Cell Biol.* **16**, 255–267 (2014).

83. Roy, N., Malik, S., Villanueva, K.E., Urano, A., Lu, X., Von Figura, G., Seeley, E.S., Dawson, D.W., Collisson, E.A. and Hebrok, M. Brg1 promotes both tumor-suppressive and oncogenic activities at distinct stages of pancreatic cancer formation. *Genes Dev.* **29**, 658–671 (2015).

84. Immervoll, H., Hoem, D., Sakariassen, P., Steffensen, O. J. and Molven, A. Expression of the 'stem cell marker' CD133 in pancreas and pancreatic ductal adenocarcinomas. *BMC Cancer* **8**, 48 (2008).

85. Burke, Z. D., Thowfeequ, S., Peran, M. and Tosh, D. Stem cells in the adult pancreas and liver. *Biochem. J.* **404**, 169 (2007).

86. Grün, D., Muraro, M.J., Boisset, J.C., Wiebrands, K., Lyubimova, A., Dharmadhikari, G., van den Born, M., Van Es, J., Jansen, E., Clevers, H. and de Koning, E.J. De novo prediction of stem cell identity using single-cell transcriptome data. *Cell Stem Cell* **19**, 266–277 (2016).

87. Jordan, N.V., Prat, A., Abell, A.N., Zawistowski, J.S., Sciaky, N., Karginova, O.A., Zhou, B., Golitz, B.T., Perou, C.M. and Johnson, G.L. SWI/SNF chromatin-remodeling factor Smarcd3/Baf60c controls epithelial-mesenchymal transition by inducing Wnt5a signaling. *Mol. Cell. Biol.* **33**, 3011–3025 (2013).

88. Genovese, G., Carugo, A., Tepper, J., Robinson, F.S., Li, L., Svelto, M., Nezi, L., Corti, D., Minelli, R., Pettazzoni, P. and Gutschner, T. Synthetic vulnerabilities of mesenchymal subpopulations in pancreatic cancer. *Nature* **542**, 362–366 (2017).

89. Wang, W., Friedland, S.C., Guo, B., O'Dell, M.R., Alexander, W.B., Whitney-Miller, C.L., Agostini-Vulaj, D., Huber, A.R., Myers, J.R., Ashton, J.M. and Dunne, R.F. ARID1A, a SWI/SNF subunit, is critical to acinar cell homeostasis and regeneration and is a barrier to transformation and epithelial-mesenchymal transition in the pancreas. *Gut* **68**, 1245–1258 (2019).

90. Wang, S.C., Nassour, I., Xiao, S., Zhang, S., Luo, X., Lee, J., Li, L., Sun, X., Nguyen, L.H., Chuang, J.C. and Peng, L. SWI/SNF component ARID1A restrains pancreatic neoplasia formation. *Gut* **68**, 1259–1270 (2019).

91. Miao, D., Margolis, C.A., Gao, W., Voss, M.H., Li, W., Martini, D.J., Norton, C., Bossé, D., Wankowicz, S.M., Cullen, D. and Horak, C. Genomic correlates of response to immune checkpoint therapies in clear cell renal cell carcinoma. *Science* **359**, 801–806 (2018).

92. Nickerson, J. A., Wu, Q. and Imbalzano, A. N. Mammalian SWI/SNF enzymes and the epigenetics of tumor cell metabolic reprogramming. *Front. Oncol.* **7**, 49 (2017).

93. Wang, R.R., Pan, R., Zhang, W., Fu, J., Lin, J.D. and Meng, Z.X. The SWI/SNF chromatin-remodeling factors BAF60a, b, and c in nutrient signaling and metabolic control. *Protein and Cell* **9**, 207–215 (2018).

94. Morrison, A. J. Chromatin-remodeling links metabolic signaling to gene expression.

Mol. Metab. **38**, 100973 (2020).

95. Meng, Z.X., Li, S., Wang, L., Ko, H.J., Lee, Y., Jung, D.Y., Okutsu, M., Yan, Z., Kim, J.K. and Lin, J.D. Baf60c drives glycolytic metabolism in the muscle and improves systemic glucose homeostasis through Deptor-mediated Akt activation. *Nat. Med.* **19**, 640–645 (2013).

96. Meng, Z.X., Gong, J., Chen, Z., Sun, J., Xiao, Y., Wang, L., Li, Y., Liu, J., Xu, X.S. and Lin, J.D. Glucose sensing by skeletal myocytes couples nutrient signaling to systemic homeostasis. *Mol. Cell* **66**, 332-344.e4 (2017).

97. Olive, K.P., Tuveson, D.A., Ruhe, Z.C., Yin, B., Willis, N.A., Bronson, R.T., Crowley, D. and Jacks, T. Mutant p53 gain of function in two mouse models of Li-Fraumeni syndrome. *Cell* **119**, 847–860 (2004).

98. Morgan R. T., Woods L. K., Moore G. E., Quinn L. A., McGavran L. and Gordon S. G. Human cell line (COLO 357) of metastasis pancreatic adenocarcinoma. *Int. J. Cancer* **25**, 591–598. (1980).

99. Boj, S.F., Hwang, C.I., Baker, L.A., Chio, I.I.C., Engle, D.D., Corbo, V., Jager, M., Ponz-Sarvise, M., Tiriac, H., Spector, M.S. and Gracanin, A. Organoid models of human and mouse ductal pancreatic cancer. *Cell* **160**, 324–338 (2015).

100. Wartenberg, M., Cibin, S., Zlobec, I., Vassella, E., Eppenberger-Castori, S., Terracciano, L., Eichmann, M.D., Worni, M., Gloor, B., Perren, A. and Karamitopoulou, E. Integrated genomic and immunophenotypic classification of pancreatic cancer reveals three distinct subtypes with prognostic/ predictive significance. *Clin. Cancer Res.* **24**, 4444–4454 (2018).

101. Baker, L., Tiriac, H., Corbo, V. and Young, C. M. *Tuveson Laboratory Murine and Human Organoid Protocols*. (2017).

102. Huch, M., Bonfanti, P., Boj, S.F., Sato, T., Loomans, C.J., Van De Wetering, M., Sojoodi, M., Li, V.S., Schuijers, J., Gracanin, A. and Ringnalda, F. Unlimited in vitro expansion of adult bi-potent pancreas progenitors through the Lgr5/R-spondin axis. *EMBO J.* **32**, 2708–2721 (2013).

103. Andrews, N. C. & Faller, D. V. A rapid micrqpreparation technique for extraction of DNA-binding proteins from limiting numbers of mammalian cells. *Nucleic Acids Res.* **19**, 2499 (1991).

104. Schneider, C. A., Rasband, W. S. and Eliceiri, K. W. NIH Image to ImageJ: 25 years of image analysis. *Nat. Methods* **9**, 671–675 (2012).

105. Bankhead, P., Loughrey, M.B., Fernández, J.A., Dombrowski, Y., McArt, D.G., Dunne, P.D., McQuaid, S., Gray, R.T., Murray, L.J., Coleman, H.G. and James, J.A. QuPath: Open source software for digital pathology image analysis. *Sci. Rep.* **7**, 1–7 (2017).

106. Qin, X. F., An, D. S., Chen, I. S. Y. and Baltimore, D. Inhibiting HIV-1 infection in human T cells by lentiviral-mediated delivery of small interfering RNA against CCR5.

Proc. Natl. Acad. Sci. U. S. A. **100**, 183–188 (2003).

107. Sanjana, N. E., Shalem, O. and Zhang, F. Improved vectors and genome-wide libraries for CRISPR screening. *Nat. Methods* **11**, 783–784 (2014).

108. Albini, S. & Puri, P. L. Generation of myospheres from hESCs by epigenetic reprogramming. *J. Vis. Exp.* **88**, 51243 (2014).

109. Albini, S., Coutinho, P., Malecova, B., Giordani, L., Savchenko, A., Forcales, S.V. and Puri, P.L. Epigenetic reprogramming of human embryonic stem cells into skeletal muscle cells and generation of contractile myospheres. *Cell Rep.* **3**, 661–670 (2013).

110. Dull, T., Zufferey, R., Kelly, M., Mandel, R.J., Nguyen, M., Trono, D. and Naldini, L. A third-generation lentivirus vector with a conditional packagingaSystem. *J. Virol.* **72**, 8463–8471 (1998).

111. Sena-Esteves, M., Tebbets, J. C., Steffens, S., Crombleholme, T. and Flake, A. W. Optimized large-scale production of high titer lentivirus vector pseudotypes. *J. Virol. Methods* **122**, 131–139 (2004).

112. Zheng, G.X., Terry, J.M., Belgrader, P., Ryvkin, P., Bent, Z.W., Wilson, R., Ziraldo, S.B., Wheeler, T.D., McDermott, G.P., Zhu, J. and Gregory, M.T. Massively parallel digital transcriptional profiling of single cells. *Nat. Commun.* **8**, 1–12 (2017).

113. Satija, R., Farrell, J. A., Gennert, D., Schier, A. F. and Regev, A. Spatial reconstruction of single-cell gene expression data. *Nat. Biotechnol.* **33**, 495–502 (2015).

114. Heinz, S., Benner, C., Spann, N., Bertolino, E., Lin, Y.C., Laslo, P., Cheng, J.X., Murre, C., Singh, H. and Glass, C.K. Simple combinations of lineage-determining transcription factors prime cis-regulatory elements required for macrophage and B cell identities. *Mol. Cell* **38**, 576–589 (2010).

115. Subramanian, A., Tamayo, P., Mootha, V.K., Mukherjee, S., Ebert, B.L., Gillette, M.A., Paulovich, A., Pomeroy, S.L., Golub, T.R., Lander, E.S. and Mesirov, J.P. Gene set enrichment analysis: A knowledge-based approach for interpreting genome-wide expression profiles. *Proc. Natl. Acad. Sci. U. S. A.* **102**, 15545–15550 (2005).

116. Diaferia, G.R., Balestrieri, C., Prosperini, E., Nicoli, P., Spaggiari, P., Zerbi, A. and Natoli, G. Dissection of transcriptional and cis -regulatory control of differentiation in human pancreatic cancer. *EMBO J.* **35**, 595–617 (2016).

117. Szklarczyk, D., Franceschini, A., Wyder, S., Forslund, K., Heller, D., Huerta-Cepas, J., Simonovic, M., Roth, A., Santos, A., Tsafou, K.P. and Kuhn, M. STRING v10: Protein-protein interaction networks, integrated over the tree of life. *Nucleic Acids Res.* **43**, D447–D452 (2015).

118. Shannon, P., Markiel, A., Ozier, O., Baliga, N.S., Wang, J.T., Ramage, D., Amin, N., Schwikowski, B. and Ideker, T. Cytoscape: A software Environment for integrated models of biomolecular interaction networks. *Genome Res.* **13**, 2498–2504 (2003).

119. Morris, J.H., Apeltsin, L., Newman, A.M., Baumbach, J., Wittkop, T., Su, G., Bader, G.D. and Ferrin, T.E. ClusterMaker: A multi-algorithm clustering plugin for Cytoscape. *BMC Bioinformatics* **12**, (2011).

3.8. Supplemental figures

Figure 3.S1. SMARCD3 is a functional epigenetic dependency of PDAC stem cells (related to Figure 3.1)
(A) *SMARCD3* is targeted for amplifications in cancer. Genetic amplifications have been detected in the *SMARCD3* locus in cases of diverse cancers (top 10 studies with the highest frequency of *SMARCD3* alteration shown, cBioPortal).
(B) Nuclear SMARCA4 is expression cells is equivalently expressed in stem and non-stem primary *KP$^{f/f}$C* tumor cells. CD133- (non-stem) and CD133+ (stem) EpCAM+ tumor cells were FACS sorted from endpoint *KP$^{f/f}$C* tumors and cytospins were analyzed for nuclear SMARCA4 expression by immunofluorescence; cells with any positive staining for SMARCA4 in the nucleus were counted. Representative images from n=3 frames, n=1 biological replicate.
(C) *Smarcd3* RNA expression is upregulated within the CD133+ stem cell fraction of a primary *KP$^{f/f}$C* tumor; CD133- and CD133+ EpCAM+ *KP$^{f/f}$C* tumor cells were sorted and *Smarcd3* expression was analyzed by qPCR; one biological replicate (n=2).
(D) Nuclear SMARCD3 expression cells is upregulated within the CD133+ stem cell fraction of primary *KP$^{f/f}$C* tumors. CD133- and CD133+ EpCAM+ tumor cells were FACS sorted from endpoint *KP$^{f/f}$C* tumors and cytospins were analyzed for nuclear SMARCD3 expression by immunofluorescence for DAPI (blue) and SMARCD3 (red); cells with any positive staining for SMARCD3 in the nucleus were counted. Representative images from n=3 frames, n=2 biological replicates.
(E) shRNA knockdown of *Smarcd3* in *KP$^{f/f}$C* cell lines assessed by qPCR *in vitro*. *KP$^{f/f}$C* cell lines were transduced with lentiviral RFP-tagged shRNA and sorted 72 hrs post-transduction by FACS; cells were plated in 2D and collected for qPCR analysis 72hrs after plating; n=4-7 independent biological replicates at technical replicate n=3 each.
(F) shRNA knockdown of *Smarcd3* in *KP$^{f/f}$C* cell lines assessed by western blot *in vitro*. *KP$^{f/f}$C* cell lines were transduced with lentiviral RFP-tagged shRNA and sorted 72 hrs post-transduction by FACS; cells were plated in 2D and collected for western blot analysis 72hrs after plating (α-tubulin used as loading control).
(G) *Smarcd3* shRNA are specific and do not significantly reduce *Smarcd1* or *Smarcd2* expression by western blot. *KP$^{f/f}$C* cell lines were transduced with lentiviral RFP-tagged shRNA and sorted 72 hours post-transduction by FACS; cells were plated in 2D and collected for western blot analysis 72 hours after plating (α-tubulin used as loading control).
(H) Inhibition of *Smarcd3* using shRNA increases apoptosis of CD133+ *KP$^{f/f}$C* cells *in vitro*, as determined by the frequency of cells positive for Annexin V by FACS staining in 2D culture; one biological replicate (n=3).
(I and J) Inhibition of *Smarcd3* using shRNA blocks growth of *KP$^{f/f}$C* stem cells *in vivo.* Biological replicate #2 (I) and #3 (J). Inhibition of *Smarcd3* blocks growth of CD133+ or Msi2+ *KP$^{f/f}$C* cells in the flank of NSG mice (n=3, data are represented as mean ± SEM; n=3 biological replicates).
(K) Overexpression of *SMARCD3* in *KP$^{f/f}$C* cells *in vitro*. *KP$^{f/f}$C* cell lines were transduced with lentiviral GFP-tagged *SMARCD3* overexpression vector or empty GFP control and sorted 72 hours post-transduction by FACS; cells were plated in 2D and collected for qPCR analysis 72 hours later; one biological replicate (n=3).
(L) Schematic for *SMARCD3* overexpression in *KP$^{f/f}$C* cells *in vitro*. *KP$^{f/f}$C* cell lines were transduced with *SMARCD3-GFP* or empty GFP lentiviral vectors; 72 hours post-transduction GFP+ CD133+ and GFP+ CD133- cells were plated in 3D sphere-forming conditions and counted 1 week later.
(M) *SMARCD3* overexpression enhances 3D growth of CD133- and CD133+ *KP$^{f/f}$C* cells *in vitro.* *KP$^{f/f}$C* cell lines were transduced with *SMARCD3-GFP* or empty GFP lentiviral vectors; 72 hours post-transduction GFP+ CD133+ and GFP+ CD133- cells were plated in 3D sphere-forming conditions and counted 1 week later (representative of 4 biological replicates; n=3-6 each).
(N) *SMARCD3* overexpression sustains CD133+ *KP$^{f/f}$C* cells *in vitro. KP$^{f/f}$C* cell lines were transduced with *SMARCD3-GFP* or empty GFP lentiviral vectors; 72 hours post-transduction GFP+ CD133+ cells were plated in 2D. The fraction of CD133+ cells after was assessed by FACS after 72 hours in culture representative of 3 biological replicates; n=3 each).

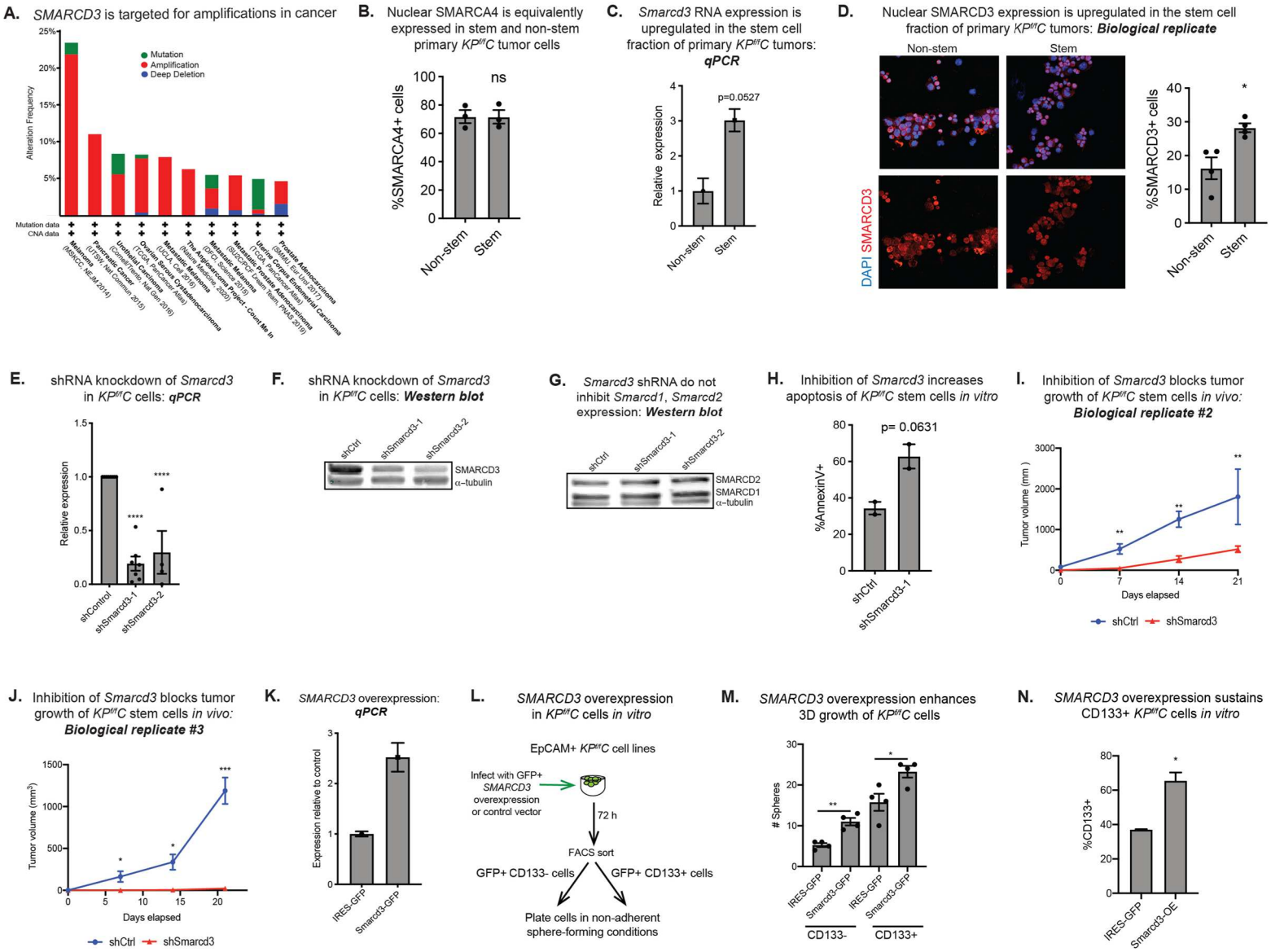
A. SMARCD3 is targeted for amplifications in cancer
Mutation
Amplification
Deep Deletion
Alteration Frequency
Mutation data
CNA data
B. Nuclear SMARCA4 is equivalently expressed in stem and non-stem primary KPfl/fl C tumor cells
%SMARCA4+ cells
ns
Non-stem
Stem
C. Smarcd3 RNA expression is upregulated in the stem cell fraction of primary KPfl/fl C tumors: qPCR
Relative expression
p=0.0527
D. Nuclear SMARCD3 expression is upregulated in the stem cell fraction of primary KPfl/fl C tumors: Biological replicate
Non-stem
Stem
DAPI SMARCD3
%SMARCD3+ cells
E. shRNA knockdown of Smarcd3 in KPfl/fl C cells: qPCR
Relative expression
shControl
shSmarcd3-1
shSmarcd3-2
F. shRNA knockdown of Smarcd3 in KPfl/fl C cells: Western blot
shCtrl
shSmarcd3-1
shSmarcd3-2
SMARCD3
α–tubulin
G. Smarcd3 shRNA do not inhibit Smarcd1, Smarcd2 expression: Western blot
shCtrl
shSmarcd3-1
shSmarcd3-2
SMARCD2
SMARCD1
α–tubulin
H. Inhibition of Smarcd3 increases apoptosis of KPfl/fl C stem cells in vitro
%AnnexinV+
p= 0.0631
shCtrl
shSmarcd3-1
I. Inhibition of Smarcd3 blocks tumor growth of KPfl/fl C stem cells in vivo: Biological replicate #2
Tumor volume (mm)
Days elapsed
shCtrl
shSmarcd3
J. Inhibition of Smarcd3 blocks tumor growth of KPfl/fl C stem cells in vivo: Biological replicate #3
Tumor volume (mm3)
Days elapsed
shCtrl
shSmarcd3
K. SMARCD3 overexpression: qPCR
Expression relative to control
IRES-GFP
Smarcd3-GFP
L. SMARCD3 overexpression in KPfl/fl C cells in vitro
EpCAM+ KPfl/fl C cell lines
Infect with GFP+ SMARCD3 overexpression or control vector
72 h
FACS sort
GFP+ CD133- cells
GFP+ CD133+ cells
Plate cells in non-adherent sphere-forming conditions
M. SMARCD3 overexpression enhances 3D growth of KPfl/fl C cells
Spheres
IRES-GFP
Smarcd3-GFP
IRES-GFP
Smarcd3-GFP
CD133-
CD133+
N. SMARCD3 overexpression sustains CD133+ KPfl/fl C cells in vitro
%CD133+
IRES-GFP
Smarcd3-OE

Figure 3.S2. Genetic inhibition of Smarcd3 impairs tumor growth (related to Figure 3.2), Continued
(A) *Smarcd3* deletion in the context of embryonic *Kras* mutation increases formation of fibrotic nodules. *Smarcd3^{WT}* (WT) and *Smarcd3^{KO}* (KO) *Kras$^{G12D/+}$;Ptf1a-Cre* (*KC*) mice were analyzed between 9-10 weeks of age. Pancreatic tissue was analyzed for gross morphological cysts or overt fibrotic nodules and collected for histological analysis and H&E (left, 10X); frequency of nodules and PanIN present in tissues from WT and KO *KC* mice are represented (right) as determined from gross morphological presentation of the pancreas (n=7-9 mice per genotype).
(B) *Smarcd3* deletion in the context of *Kras* mutation in adult mice increases ductal-driven and inhibits acinar-driven formation of fibrotic nodules. Adult (8 weeks of age) *Smarcd3^{WT}* (WT) and *Smarcd3^{KO}* (KO) *Kras$^{G12D/+}$;Sox9-CreER^{T2}* or *Kras$^{G12D/+}$; Ptf1a$^{CRE-ERTM}$* mice were treated with 150mg/kg tamoxifen (1 or 3 doses respectively) to induce recombination in pancreatic ductal cells or acinar cells respectively. 90 days later, pancreatic tissue was analyzed for gross morphological cysts or fibrotic nodules and collected for histological analysis and H&E; frequency of nodules present are represented as determined from gross morphological presentation of the pancreas (n=3-8 mice/genotype).
(C) Gating strategy for the analysis of *KP$^{f/f}$C* tumors. Representative FACS plots demonstrate the gating strategy used for the analysis of tumor (EpCAM-APC+) and CD133+ (CD133-PE+) and Msi2+ (Msi2-GFP+) tumor stem cells in primary and secondary *Smarcd3^{WT}* and *Smarcd3^{KO}-KP$^{f/f}$C* tumors. FACS plots for unstained tumor cells are shown as a control. Plots are shown for populations that were first gated through morphology (FSC-A/SSC-A), single cell (FSC-A/FSC-H) and live cell (Propidium iodide negative) gates (see also Fig. 2C,E). This gating strategy was also used to sort EpCAM-APC+ primary *KP$^{f/f}$C* tumor cells for secondary syngeneic transplants.
(D) Schematic for genetic deletion of *Smarcd3* in the *KPF* model using adenoviral Cre (adCre). *Smarcd3$^{f/f}$* mice were crossed to a dual-recombinase model of pancreatic cancer (*FSF-Kras$^{G12D/+}$,p53$^{FRT/FRT}$,Pdx-Flp; KPF*) driven by *Kras* mutation/*p53* deletion by a pancreas-specific flippase, enabling global *Smarcd3* deletion by delivering adenoviral Cre (adCre). End-stage *Smarcd3$^{f/f}$-KPF* tumors were isolated, dissociated, plated, and EpCAM-APC+ tumor cells were FACS sorted to derive primary *Smarcd3$^{f/f}$-KPF* tumor cell lines. Tumor cells were transduced with GFP-tagged adCre or adGFP, FACS sorted, and either plated in 3D sphere-forming conditions or transplanted in the flanks of NSG recipients. Spheres were counted 1 week after plating; tumor burden was analyzed 5 weeks after transplant.
(E) *Smarcd3$^{f/f}$* allele is completely recombined by adCre delivery *in vitro. Smarcd3$^{f/f}$-KPF* cells were transduced with adGFP or adCre and sorted 72 hours later for functional assays and lysis for genotyping PCR to analyze recombination.
(F) Relative effect of Cre transduction on sphere formation in *KPF* cells. *Smarcd3^{WT}-KPF* (WT) and *Smarcd3$^{f/f}$-KPF* (KO) cells were transduced with adGFP or adCre *in vitro*; 72 hours post-transduction GFP+ cells were sorted plated in sphere forming conditions. Spheres were counted 1 week later; counts were normalized to adGFP to account for varying sphere numbers across cell lines (representative of n=3-5 biological replicates; n=3-6 technical replicates each)
(G) *Smarcd3* deletion depletes CD133+ *KPF* stem cells *in vitro. Smarcd3$^{f/f}$-KPF* cells were transduced with adGFP or adCre *in vitro*; 72 hours post-transduction GFP+ CD133+ transduced cells were sorted by FACS and plated in 2D culture. Frequency of CD133+ stem cells was assessed by FACS after 72 hours in culture (representative of n=3 biological replicates; n=3 technical replicates each).
(H) Genetic *Smarcd3* deletion with adCre blocks flank tumor growth *in vivo. Smarcd3* deletion with adCre reduces tumor burden 5 weeks post-transplant. Tumors were isolated, weighed, and dissociated for cell count* and EpCAM+* and EpCAM+CD133+* analysis by FACS (representative of n=2 biological replicates, n=4-5 technical replicates each, *1 outlier removed, Grubbs alpha=0.05).
(I) *Smarcd3$^{f/f}$* allele is recombined upon tamoxifen treatment *in vivo*. *Smarcd3$^{f/f}$-KPF-R26-CreER^{T2}* tumor-bearing NSG mice were treated with tamoxifen (100mg/kg, 5 consecutive days); tumors were isolated for analysis 3 weeks after the first tamoxifen dose and dissociated. EpCAM+ tumor cells were then sorted for lysis and PCR analysis for recombination.
(J) SMARCD3 is re-expressed in *KPF* transplant after inducible deletion *in vivo.* Representative images of immunofluorescent staining for SMARCD3 (red) in epithelial tumor cells (pan-keratin+, green) of *Smarcd3$^{f/f}$-KPF-R26-CreER^{T2}* flank transplant treated with tamoxifen; nuclei stained with DAPI (blue). One of three tamoxifen-treated transplants re-expressed SMARCD3.

A. *Smarcd3* deletion in the context of embryonic *Kras* mutation increases formation of fibrotic nodules

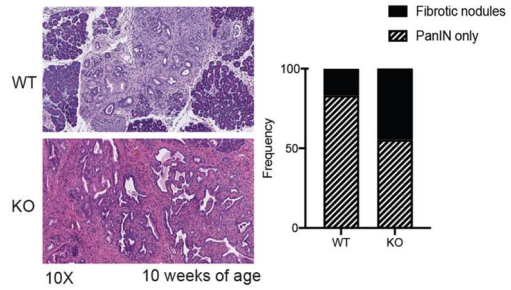

B. *Smarcd3* deletion in the context of *Kras* mutation in adult mice increases ductal-driven and inhibits acinar-driven formation of fibrotic nodules

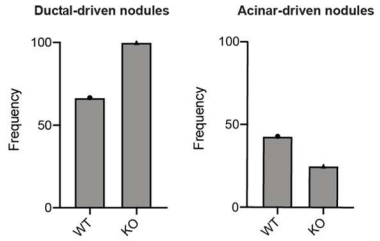

C. Gating strategy for the analysis of primary and secondary *KP^{fl}C* tumors

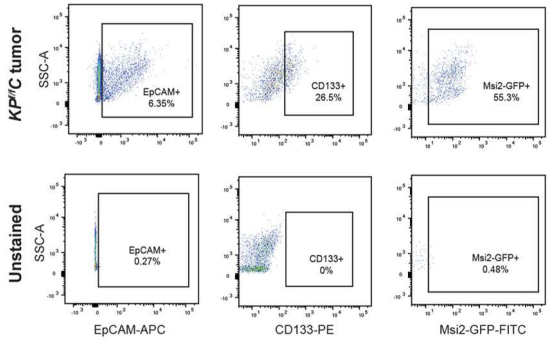

D. Genetic deletion of *Smarcd3* in the *KPF* model using adenoviral Cre

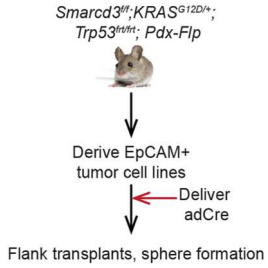

E. *Smarcd3^{fl}* allele is completely recombined by adCre delivery *in vitro*

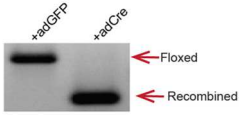

F Relative effect of Cre transduction on sphere formation *KPF* tumor cells

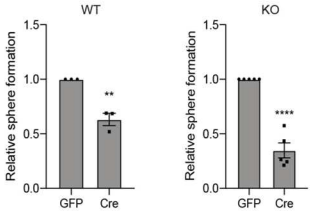

G. *Smarcd3* deletion depletes CD133+ *KPF* stem cells *in vitro*

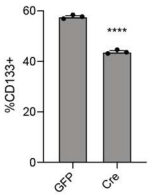

H. Genetic *Smarcd3* deletion with adCre blocks flank tumor growth *in vivo*

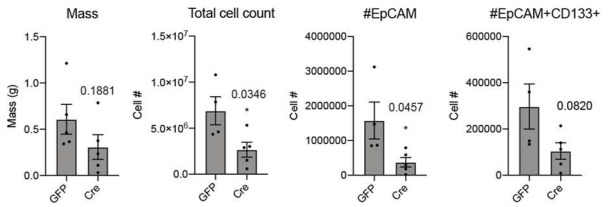

I. *Smarcd3^{fl}* allele is recombined upon tamoxifen treatment *in vivo*

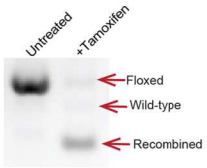

J. Re-expression of SMARCD3 in *KPF* transplant after inducible deletion *in vivo*

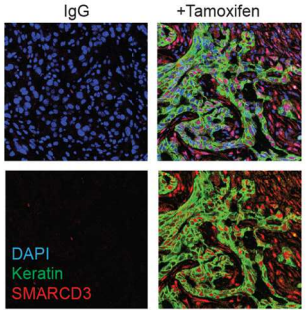

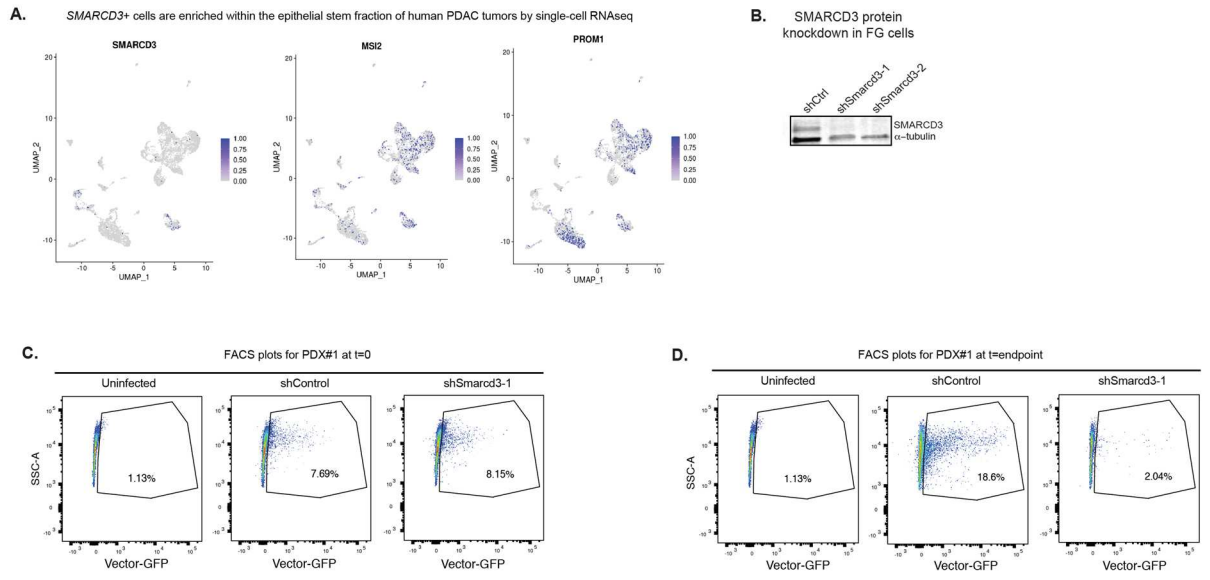

Figure 3.S3. SMARCD3 inhibition blocks tumor growth in human models of PDAC (related to Figure 3.3)

(A) The frequency of *SMARCD3*+ cells is increased in the stem fraction of primary human PDAC tumors by single-cell RNA-seq. After gating on EpCAM+ tumor cells, plots are shown for *SMARCD3*, *PROM1* (CD133+), and *MSI2* expressing cells by single-cell RNA-seq.

(B) Inhibition of *SMARCD3* using shRNA. Human FG PDAC cells were transduced with GFP-tagged shRNA against *SMARCD3* or control, GFP+ cells were sorted and plated in 2D, and cells were collected 72 hours later for analysis by western blot (α-tubulin used as loading control).

(C) PDX tumors are transduced equivalently with shControl and shSMARCD3 lentivirus at t=0. The frequency of transduced GFP+EpCAM+ PDX tumor cells was analyzed by FACS 48 hours post-transduction (t=0). Representative plots are shown for PDX#1; frequency of GFP+ cells at t=0 are plotted and are gated though live, single EpCAM-PE+ cells (see also Fig. 3k).

(D) Inhibition of *SMARCD3* using shRNA blocks *in vivo* growth of patient-derived xenograft PDAC tumors. At endpoint (12 weeks), xenograft tumors were isolated, dissociated, and analyzed by FACS. Representative plots are shown for PDX#1; frequency of GFP+ tumor cells at endpoint are plotted and are gated though live, single EpCAM-PE+ cells.

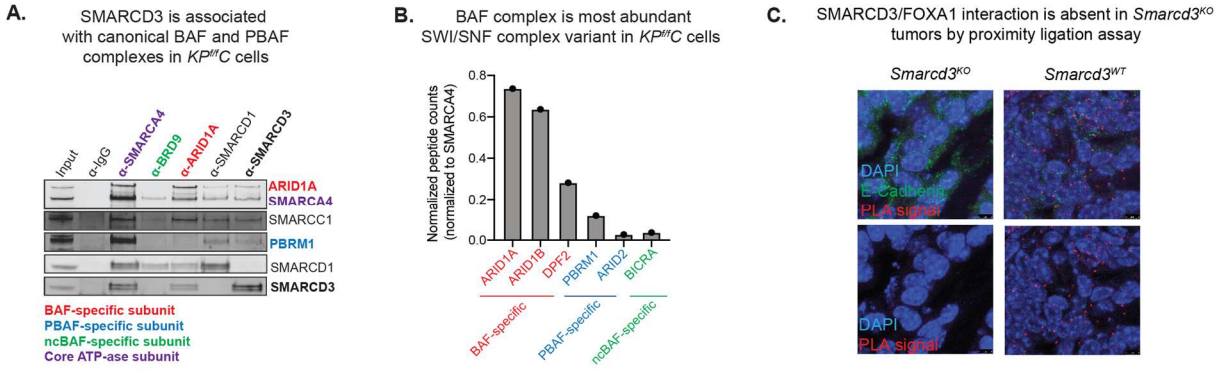

Figure 3.S4. SMARCD3 regulates the epigenetic landscape and BAF complex binding at FOXA1 binding sites in mouse pancreatic cancer cells (related to Figure 3.4)
(A) SMARCD3/Baf60c is associated with canonical BAF and PBAF complexes in *KP$^{f/f}$C* cells. Immunoprecipitation (IP) was followed by western blot using antibodies against variant-specific SWI/SNF complex subunits in *KP$^{f/f}$C* lysates to determine which SWI/SNF complex variants incorporate SMARCD3. Probing for SMARCD3 interactions with ncBAF (BRD9), canonical BAF (ARID1A) and PBAF (PBRM1) -specific subunits showed that SMARCD3 is associated with BAF and PBAF as well as the core ATP-ase subunit SMARCA4 in *KP$^{f/f}$C* cells. SMARCD3 does not associate with ncBAF.
(B) BAF complex is the most abundant SWI/SNF complex variant in *KP$^{f/f}$C* cells. Primary *KP$^{f/f}$C* cells were derived by dissociating end-stage *KP$^{f/f}$C* tumors, then FACS sorting and plating EpCAM+ tumor cells. *KP$^{f/f}$C* cells were collected and SMARCA4 was immunoprecipitated (IP) from the lysates; lysate from this IP was used for mass spectrometry (MS) analysis of proteins associated with SMARCA4. Counts were normalized to bait (SMARCA4); BAF complex members ARID1A, ARID1B, and DPF2 were more abundant than PBAF complex members PBRM1/ARID2 or ncBAF member BICRA.
(C) SMARCD3/FOXA1 interaction is absent in *Smarcd3^{KO}* tumors by proximity ligation assay. Using proximity ligation assay with antibodies against FOXA1 and SMARCD3, we found positive PLA signals (red) in the nuclei (DAPI, blue) of *KP$^{f/f}$C* tumor cells (E-Cadherin, green) *in vivo*, representing associations between both FOXA1 and SMARCD3 in mouse pancreatic tumor tissue. The PLA signal was absent in *Smarcd3^{KO}-KPF* tumor cells, serving as a control (representative images from n=2 mice, n=5 frames/tumor)

Figure 3.S5: SMARCD3 regulates transcriptional networks implicated in lipid metabolism (related to Figure 3.5)
(A) Genes down-regulated by *Smarcd3* inhibition are enriched within FOXA-regulated gene sets. Gene set enrichment analysis (GSEA) on our RNA-seq dataset revealed a significant enrichment for 2 FOXA1-regulated gene sets within genes down-regulated by *Smarcd3* inhibition (fdr<0.15).
(B) Total free fatty acid levels are reduced in *Smarcd3$^{f/f}$-KPF-R26-CreER^{T2}* tumors treated with tamoxifen. *Smarcd3$^{f/f}$-KPF-R26-CreER^{T2}* tumors treated with vehicle or tamoxifen were dissociated, and EpCAM+ tumor cells were sorted by FACS and flash frozen for free fatty acid analysis by GC-MS (n=3 tumors per group).
(C) GC-MS profiling of free fatty acids in *Smarcd3$^{f/f}$-KPF-R26-CreER^{T2}* tumors. *Smarcd3$^{f/f}$-KPF-R26-CreER^{T2}* tumors treated with vehicle or tamoxifen were dissociated, and EpCAM+ tumor cells were sorted by FACS and flash frozen for free fatty acid analysis by GC-MS (n=3 tumors per group).
(D) Expression of SMARCA4 and SMARCD3 in the normal adult mouse pancreas. Representative images of immunofluorescent staining for SMARCA4 or SMARCD3 (red) in epithelial tumor cells (pan-keratin+, yellow) of adult mouse pancreatic tissue (8 weeks old); nuclei stained with DAPI (blue), pancreatic structures denoted with white labels and arrows (representative images from n=2 mice).
(E) Expression of chromatin-remodeler associated genes in primary stem vs non-stem *KP$^{f/f}$C* cells. Relative expression (normalized read counts per gene) of chromatin-remodeler associated genes in primary stem (Msi2-GFP+) versus non-stem (Msi2-GFP-) EpCAM+ *KP$^{f/f}$C* tumor cells by RNA-seq (no cutoff on fold change or adjusted p value).
(F) SMARCD3 expression is significantly associated with the presence of tertiary lymphoid structures (TLT) in PDAC patients. SMARCD3 expression was assessed by IHC in a cohort of 104 PDAC patients; samples were scored as positive (any SMARCD3+ cells) or negative (no SMARCD3+ cells). ~30% of SMARCD3+ tumor samples also scored positive for the presence of TLT, while only ~9% of SMARCD3- tumor samples scored positive for the presence of TLT (p=0.0058).
(G) SMARCD3 expression is sensitive to glucose. *KP$^{f/f}$C* cells were cultured to >75% confluency in 2D on chamber slides; full growth media was replaced with media containing 1mM or 10mM glucose and slides were collected and fixed for immunofluorescent imaging 24 hours later. The frequency of nuclear (DAPI, blue) SMARCD3+ (red) cells was analyzed in ImageJ (representative images, n=3 frames).
Data represented as mean ± SEM. $^{*}p < 0.05$, $^{**}p < 0.01$, $^{***}p < 0.001$ by Student's t test or One-way ANOVA.

A. Results of GSEA analysis suggest SMARCD3 regulates FOXA1-dependent genes and programs involved in cell cycle, translation, and metabolism

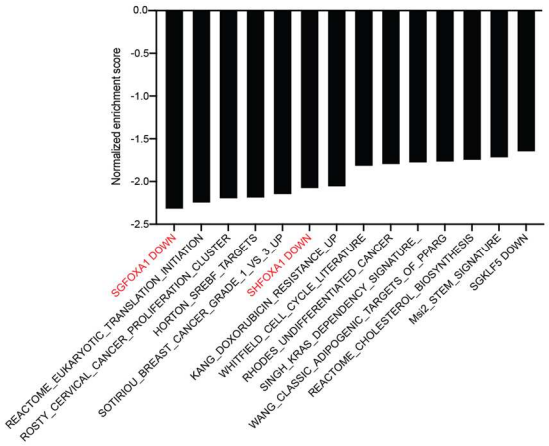

B. Total free fatty acids are down in *Smarcd3-KPF-R26-CreER*^{T2} tumors treated with tamoxifen

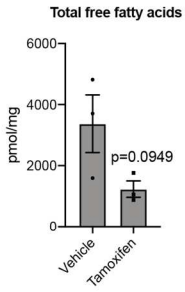

C. GC-MS profiling of free fatty acids in *Smarcd3-KPF-R26-CreER*^{T2} tumor cells *in vivo*

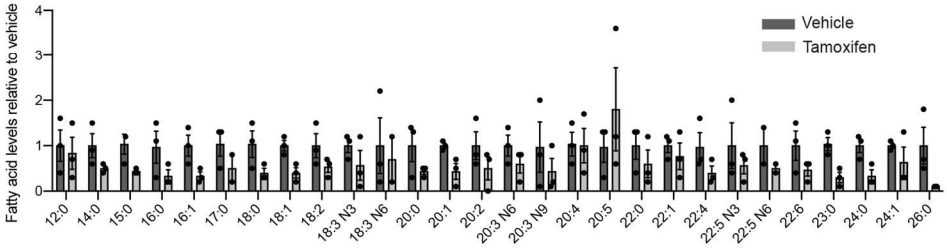

D. Expression of SMARCA4 and SMARCD3 in the normal adult mouse pancreas

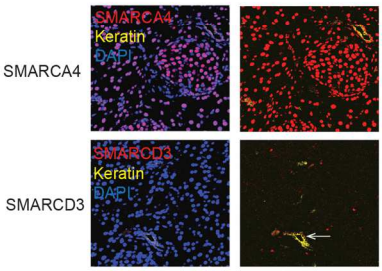

F. SMARCD3 expression is significantly associated with the presence of tertiary lymphoid structures in PDAC patients

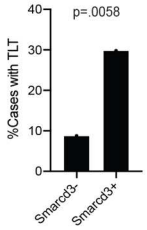

E. Expression of chromatin remodeling-associated genes in primary stem vs non-stem *KP*$^{fl/fl}$*C* tumor cells

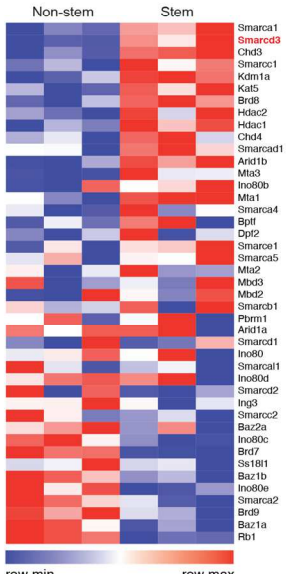

G. SMARCD3 expression in *KP*$^{fl/fl}$*C* cells is sensitive to glucose *in vitro*

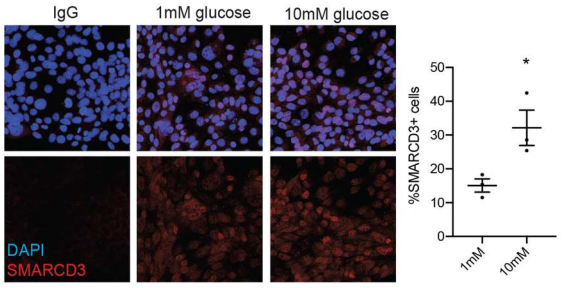

3.9. Supplemental information

Table 3.1. Node genes within each cluster hub of the RNA-seq network

Chapter 4. Targeting pancreatic cancer stem cells with clinical inhibitors

4.1. Abstract

Pancreatic cancer is projected to become the second leading cause of cancer-related deaths by 2030. Despite some recent advances in systemic therapy, survival remains dismal in large part due to the aggressive nature of this disease. To identify new therapeutic targets for cancer we have focused on stem cell programs that are reactivated in cancer progression. Through this work, we discovered that the fate determinant Musashi2 (Msi2) is a key stem cell signal that is aberrantly upregulated in many cancers as they progress to higher grades. Utilizing a genetic reporter, we showed that *Msi2* marks a molecularly distinct population of therapy-resistant pancreatic cancer stem cells, suggesting that targeting *Msi2*+ cancer cells could provide new strategies for therapy. Here, we use a high-throughput screen to identify small molecule inhibitors of *Msi2* expression, ultimately finding that clinical inhibitors of MEK signaling suppressed *Msi2* and blocked cancer stem cell growth *in vivo*. Through genomic and functional characterization of *Msi2*+ cancer cells, we also previously identified the nuclear receptor RORγ as a novel dependency in PDAC stem cells. We provide new preclinical evidence that clinical grade RORγ inhibitors can block pancreatic cancer growth and deplete cancer stem cells *in vivo.* These studies reveal new candidate strategies for the clinical targeting of CSCs in pancreatic cancer that could have important implications for therapy.

4.2. Introduction

Despite therapeutic gains in many cancers with advances in targeted therapy, pancreatic ductal adenocarcinoma (PDAC) has seen limited progress in clinical outcomes. The five-year survival rate for this disease remains at only 10%, with high mortality driven largely by late detection, early metastasis, and therapy resistance[1]. Almost all patients are diagnosed

with late-stage disease that is characteristically resistant to a wide range of systemic therapies[2]. Even immunotherapy, which has shown promising results in many cancers has yet to be used to effectively treat pancreatic cancer[3]. An important factor underlying therapy resistance in pancreatic cancer and others is the existence of intrinsically resistant cancer cell subpopulations enriched for self-renewal and the activation of classic developmental signals. These aggressive cancer stem cells (CSCs) preferentially contribute to resistance and metastasis and therefore represent an important target for new therapies[4,5]. Ablation of these resistant cells could sensitize tumors to current therapies and inhibit tumor progression. Thus, to identify new therapeutic targets for cancer, we have focused on stem cell programs that are reactivated in cancer. Through this work, we discovered that the stem cell signal Musashi (Msi) is required for the growth and maintenance of many liquid and solid cancers[6,7,8]. In prior work, we showed that pancreatic cancer stem cells, a population identified by high expression of the stem cell signal Musashi, are particularly aggressive with preferential capacity to drive lethality and therapy resistance[8]. These data collectively raise the possibility that targeting Msi may provide a new strategy for therapy in a broad array of malignancies.

As a tool to isolate and study Msi-expressing cells, our lab previously developed a genetic GFP knock-in reporter for *Msi2*[8]. Crossing this reporter line into the autochthonous *KP$^{f/f}$C* mouse model of pancreatic cancer enabled us to both isolate *Msi2*-expressing cells and track *Msi2* transcriptional activity in cancer cells via GFP expression. Leveraging this model system, we used *Msi2-GFP KP$^{f/f}$C* cells to screen for compounds that reduce *Msi2* expression or block the growth of *Msi2*-expressing CSCs by conducting an automated high-content image-based assay. 90 hit compounds were identified in this pilot screen, including several targeted and chemotherapeutic agents that have not been considered for pancreatic adenocarcinoma. Using functional and qPCR validation, we determined that hit compounds from the screen both blocked the 3D growth of *Msi2*+ *KP$^{f/f}$C* stem cells and resulted in the transcriptional

suppression of *Msi2* expression. Of the hit compounds we identified, MEK inhibitors were the most potent suppressors of *Msi2* expression and cancer stem cell growth. Using the clinically available MEK inhibitor, trametinib, we showed that MEK inhibition could deplete CSCs *in vivo* as a single agent or as a maintenance regimen combined with chemotherapy. These results suggest a unique dependence of cancer stem cells on MEK signaling, and provide preliminary evidence that clinical MEK inhibition could directly target the chemo-resistant CSC fraction.

To further identify networks critical for the maintenance and function of *Msi2*+ cancer stem cells we used the *Msi2-GFP KP$^{f/f}$C* model to conduct RNA-Seq, ChIP-seq and a genome-wide CRISPR screen. An integrated computational analysis of this functional genomic data revealed an unexpected dependency of pancreatic cancer stem cells on immunoregulatory networks generally known to be utilized by immune cells (described in detail in Chapter 2)[9]. Within these networks, ROR gamma (RORγ), a member of the Retinoic acid receptor-related orphan receptor (ROR) family critical in Th17 differentiation, emerged as a key dependency. We showed that RORγ inhibition in mouse or human pancreatic cancer cells reduced PDAC sphere-forming ability *in vitro* as well as tumor growth *in vivo*. These studies identified RORγ as a critical vulnerability that could be exploited to improve therapeutic targeting of aggressive, drug-resistant pancreatic cancer cells. Because several clinical grade RORγ inhibitors have been tested in other indications[10], we focused on developing the preclinical data needed to position these agents (AZD-0284, JTE-151) for trials in pancreatic cancer. We found that drugs against RORγ have activity against both PDAC mouse models and patient-derived organoids and xenografts. These findings are novel and have significant implications for strengthening the case for anti-RORγ agents in context of clinical trials.

4.3. Results

Image-based screen for transcriptional inhibitors of *Msi2*

To identify compounds that target *Msi2* directly, we used *Msi2-GFP KP$^{f/f}$C* pancreatic tumor cells to conduct a high-content image-based screen for inhibitors of *Msi2* expression. *Msi2-GFP*+ tumor cells were seeded in 384-well optical plates and treated with three compound libraries (Epigenetics, EMD, Selleckchem, and Cayman Kinase Libraries, Prestwick Chemical Library); cells were imaged at 24, 48, and 72 hours after treatment for GFP, DAPI (nuclei), and cell area (CellMask) (Figure 4.1. A). Images collected from the screen were analyzed for overall cell count and mean GFP (*Msi2*) intensity per cell to assess compound impact on both cell growth and *Msi2* expression respectively. Cell area was used to normalize GFP intensity in order to remove artifactual hits that could be attributed to changes in cell size. Out of 2168 compounds, we identified 90 unique hit compounds that reduced *Msi2* expression as measured by a reduction in GFP intensity of 20% or more (Figure 4.1. B-D, Table 4.1). GFP- cells served as a control for autofluorescence or background signal (Figure 4.2. A), while DMSO-treated *Msi2-GFP*+ cells were used as a baseline to assess the inhibitory effect of compounds on cell growth and *Msi2* expression (Figure 4.2. B). Serving as a control for cell growth, treatment with the chemotherapeutic agent gemcitabine induced high cell death over time, but had no effect on *Msi2-GFP* expression (Figure 4.2. C). In contrast, the hit compound trametinib both reduced cell growth and *Msi2-GFP* signal over time (Figure 4.2. D). To identify emergent pathways upstream of *Msi2* expression, we plotted the distribution of the different programs targeted by hit compounds (Figure 4.2. E). Although hit compounds targeted a wide range of interesting molecules, we found that histone deacetylase (HDAC), phosphatidylinositol-3-kinase (PI3K)/mammalian target of rapamycin (mTOR), mitogen-activated protein kinase kinase (MEK), and cyclin-dependent kinase (CDK) inhibitors were most commonly associated with *Msi2* downregulation in our screen. Strikingly, MEK inhibitors also accounted for 8 of the top 20 most powerful compounds in terms of impact on *Msi2* expression (Figure 4.2. F, red). Consistent with an important functional role for the MEK

pathway in *Msi2*+ cells, we identified several effectors of the MEK pathway, *Fos, Jun, Ets1*, and *Ets2* as super enhancers in *Msi2*+ tumor cells[9].

To verify the results of the screen, we selected hit compounds from several commonly targeted pathways for further functional validation *in vitro.* These compounds included the mTOR inhibitor INK-28, MEK inhibitors (AZD8330, Tak-733, trametinib), and HDAC inhibitors (abexinostat, belinostat). We found that although all of these compounds significantly blocked the 3D growth of *Msi2*+ *KP$^{f/f}$C* tumor cells *in vitro*, mTOR and MEK inhibitors had the deepest impact on the self-renewal of mouse pancreatic cancer cells (Figure 4.3. A). Furthermore, treatment with inhibitors of both mTOR and MEK significantly blocked the expression of *Msi2* in *KP$^{f/f}$C* cells *in vitro* (Figure 4.3. B). Next, we treated human MiaPaCa2 pancreatic cancer cells with INK-28 or AZD8330, finding that AZD8330 most potently blocked the growth of MiaPaCa2 cells in 3D culture (Figure 4.3 C). Together, these results suggested that MEK inhibition may be an effective strategy for blocking *Msi2* expression and self-renewal in pancreatic cancer cells.

Figure 4.1. Image-based screen for transcriptional inhibitors of Msi2
(A) Schematic shows workflow for the high content imaging screen for inhibitors of Msi2. End-point pancreatic tumors from *Msi2-GFP KP$^{f/f}$C* mice were dissociated, plated, and FACS sorted on EpCAM to derive primary *Msi2-GFP KP$^{f/f}$C* cell lines. Tumor cells from an early-passage line with *Msi2-GFP* >95% were plated 1500 cells in 50uL media per well in 384 well plates. Cells were treated with three compound libraries at 0.5 or 5 uM in 10uL, 0.5% DMSO final; libraries used were Prestwick chemical library (1,200 compounds), Epigenetics library (261 compounds), and Kinase libraries (EMD, Selleckchem, and Cayman, 752 total compounds). Cells were treated for 24, 48, or 72 hours and then fixed with PFA. Fixed cells were stained with DAPI and CellMask deep red and images were collected. Images were then analyzed to count total nuclei per well, cell area per cell, and Msi2-GFP intensity. Hit compounds were selected by calculating Z-score in GFP intensity inhibition relative to *Msi2-GFP+ KP$^{f/f}$C* cells treated with DMSO alone. Msi2-GFP- KP$^{f/f}$C cells were used as a GFP- control. Further, Msi2-GFP intensity was normalized to cell area to remove artifactual candidate hits that were due to increasing cell area; 113 hit compounds were identified.
(B) Screen results at 72 hours across all compound libraries and concentrations. Distribution of mean Msi2-GFP intensity is shown for each treated well, visualizing *Msi2* inhibition across libraries. Compound treated wells are shown in black, Msi2-GFP- negative control wells are shown in navy, and Msi2-GFP+ wells treated with DMSO are shown in teal.
(C-D) Msi2 inhibition over time. Mean Msi2-GFP per cell is plotted for all compounds and concentrations (blue) at 24, 48, and 72 hours after treatment relative to Msi2-GFP- negative control wells (red) and and Msi2-GFP+ wells treated with DMSO (yellow); Msi2-GFP is normalized to DMSO control GFP intensity on each plate (C); zoom to show inhibitors (D). Mean Msi2-GFP per cell is plotted for all compounds at 0.5uM (light blue) and 5uM (dark blue) at 24, 48, and 72 hours after treatment relative to Msi2-GFP- negative control wells (red) and Msi2-GFP+ wells treated with DMSO (yellow); Msi2-GFP is normalized to DMSO control and GFP- intensity (-100) on each plate. Msi2-GFP intensity below -20 (indicated with black dashed line) represents candidate hit compounds. Dot size is scaled to normalized nuclei count per well, demonstrating the distribution of hits that both reduced cell count and Msi2 expression at each time point.

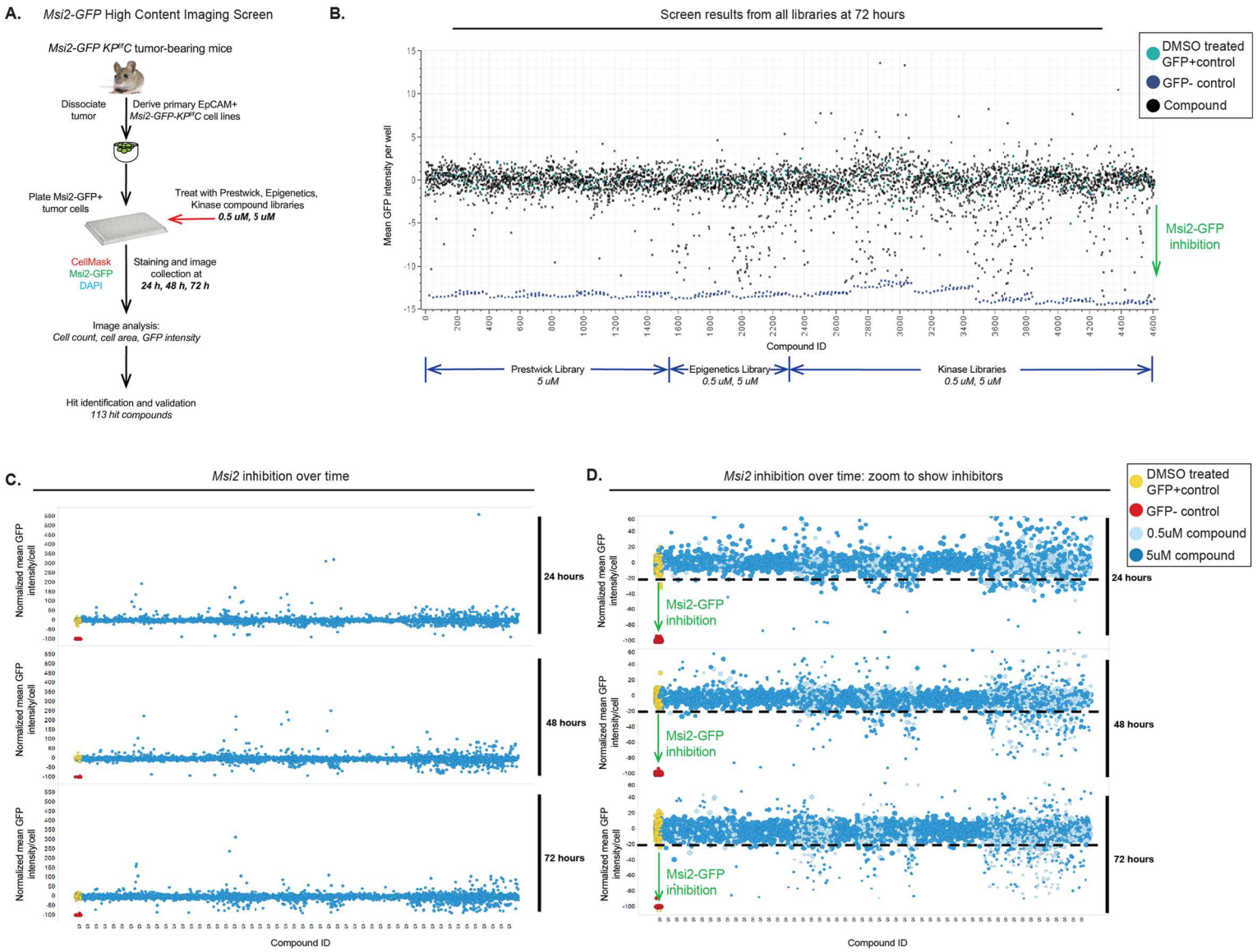
A.
Msi2-GFP High Content Imaging Screen
Msi2-GFP KPfl/fl C tumor-bearing mice
Dissociate tumor
Derive primary EpCAM+ Msi2-GFP-KPfl/fl C cell lines
Plate Msi2-GFP+ tumor cells
Treat with Prestwick, Epigenetics, Kinase compound libraries
0.5 uM, 5 uM
CellMask
Msi2-GFP
DAPI
Staining and image collection at
24 h, 48 h, 72 h
Image analysis:
Cell count, cell area, GFP intensity
Hit identification and validation
113 hit compounds
B.
Screen results from all libraries at 72 hours
DMSO treated GFP+control
GFP- control
Compound
Mean GFP intensity per well
Msi2-GFP inhibition
Compound ID
Prestwick Library
5 uM
Epigenetics Library
0.5 uM, 5 uM
Kinase Libraries
0.5 uM, 5 uM
C.
Msi2 inhibition over time
Normalized mean GFP intensity/cell
24 hours
48 hours
72 hours
Compound ID
D.
Msi2 inhibition over time: zoom to show inhibitors
DMSO treated GFP+control
GFP- control
0.5uM compound
5uM compound
Normalized mean GFP intensity/cell
Msi2-GFP inhibition
24 hours
48 hours
72 hours
Compound ID

Figure 4.2. Hit compound identification from image-based screen for transcriptional inhibitors of Msi2
(A) Example of imaging data and analysis for Msi2-GFP- control wells over time. Well images (above) show DAPI (blue) and GFP (green) in Msi2-GFP- cells at 24, 48, and 72 hours. Line plots (below) show GFP intensity (green), cell count (blue), and cell area (red) over time.
(B) Example of imaging data and analysis for Msi2-GFP+ DMSO-treated control wells over time. Well images (above) show DAPI (blue) and GFP (green) in Msi2-GFP+ cells at 24, 48, and 72 hours. Line plots (below) show GFP intensity (green), cell count (blue), and cell area (red) over time.
Figure 4.2. Hit compound identification from image-based screen for transcriptional inhibitors of Msi2, Continued
(C) Example of imaging data and analysis for high cell death hit compound gemcitabine. Well images (above) show DAPI (blue) and GFP (green) in Msi2-GFP+ cells treated with 0.5 uM gemcitabine at 24, 48, and 72 hours. Line plots (below) show GFP intensity (green), cell count (blue), and cell area (red) over time.
(D) Example of imaging data and analysis for Msi2 inhibition hit compound trametinib. Well images (above) show DAPI (blue) and GFP (green) in Msi2-GFP+ cells treated with 0.5 uM trametinib at 24, 48, and 72 hours. Line plots (below) show GFP intensity (green), cell count (blue), and cell area (red) over time.
(E) Distribution of pathways targeted by hit compounds. Pie chart demonstrates the diverse functional pathways targeted by hit Msi2 inhibitory compounds. Pathways most commonly targeted by hit compounds included HDAC (24 hits), PI3K/mTOR (17 hits), MEK (8 hits), and CDK (7 hits). All other pathways were targeted by 3 or fewer hit compounds.
(F) Top 20 Msi2 inhibitory hit compounds ranked by fold change reduction in GFP intensity. The top 20 hit compounds by rank are shown, with MEK inhibitors highlighted in red; compounds that have FDA approval are denoted with an asterik*.

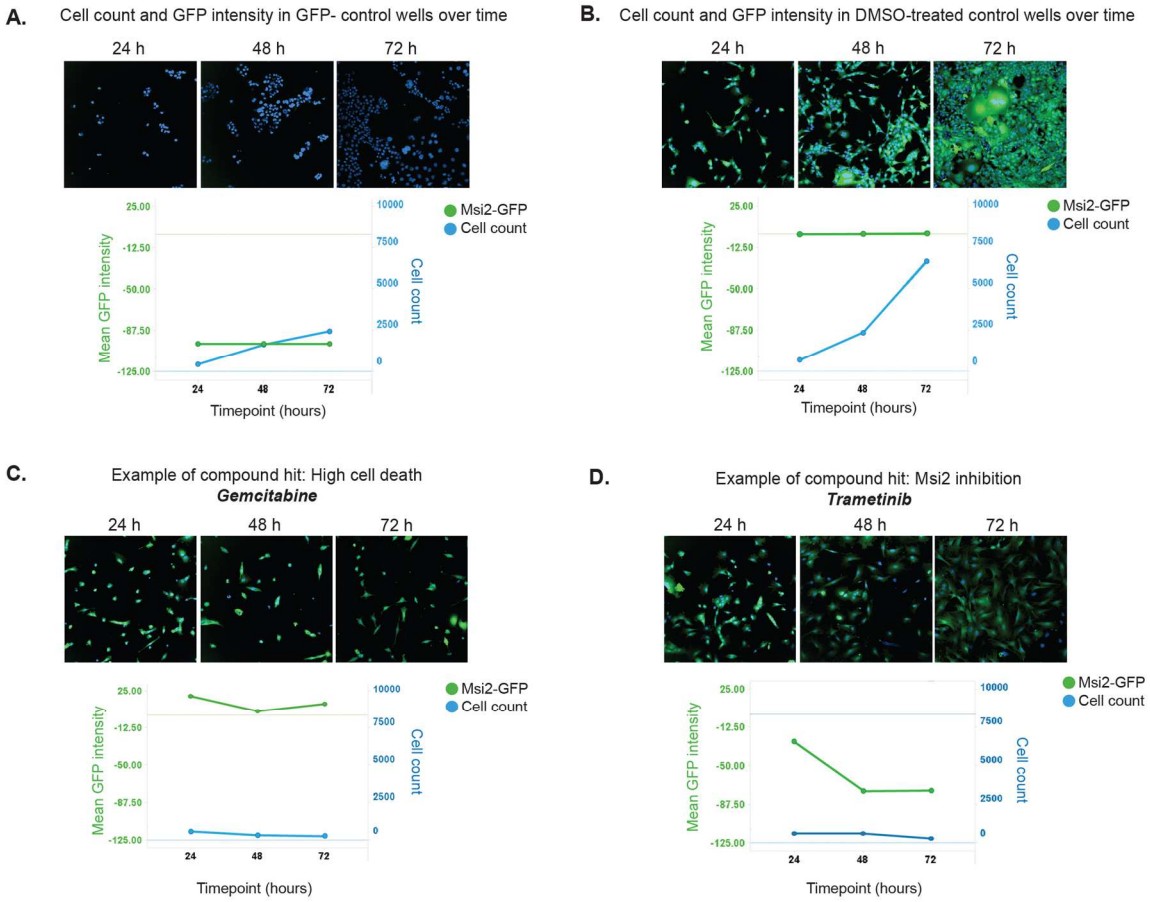
A.
Cell count and GFP intensity in GFP- control wells over time
24 h
48 h
72 h
Msi2-GFP
Cell count
Mean GFP intensity
Cell count
Timepoint (hours)
B.
Cell count and GFP intensity in DMSO-treated control wells over time
C.
Example of compound hit: High cell death
Gemcitabine
D.
Example of compound hit: Msi2 inhibition
Trametinib

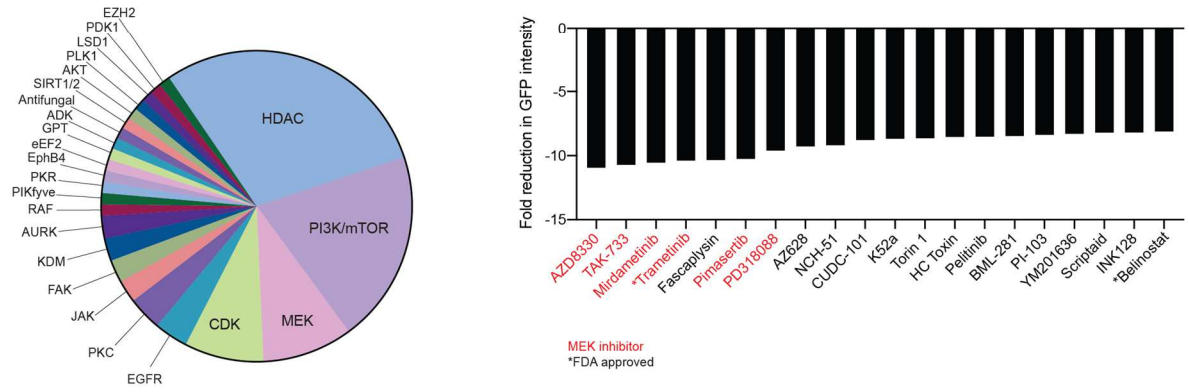
E.
Distribution of pathways targeted by hit compounds
HDAC
PI3K/mTOR
MEK
CDK
EGFR
PKC
JAK
FAK
KDM
AURK
RAF
PIKfyve
PKR
EphB4
eEF2
GPT
ADK
Antifungal
SIRT1/2
AKT
PLK1
LSD1
PDK1
EZH2
F.
Top 20 Msi2 inhibitors by fold change
Fold reduction in GFP intensity
AZD8330
TAK-733
Mirdametinib
*Trametinib
Fascaplysin
Pimasertib
PD318088
AZ628
NCH-51
CUDC-101
K52a
Torin 1
HC Toxin
Pelitinib
BML-281
PI-103
YM201636
Scriptaid
INK128
*Belinostat
MEK inhibitor
*FDA approved

To determine if MEK inhibition could target cancer stem cells *in vivo*, we tested the impact of the clinical MEK inhibitor (trametinib) on autochthonous *KP$^{f/f}$C* tumor growth. *KP$^{f/f}$C* mice were enrolled in treatment at 8.5 weeks of age with trametinib or vehicle for two weeks (3 mg/kg, three doses/week) (Figure 4.3. D). Trametinib treatment significantly reduced overall tumor mass and cell count, also driving a trend in reduced EpCAM+ tumor cells (Figure 4.3. E). Most notably, both the frequency and total number of CD133+ cancer stem cells were reduced by just two weeks of single agent trametinib treatment (Figure 4.3. E). These promising results suggested that MEK inhibition may target CSCs *in vivo* in mouse models. To extend these studies, we tested the impact of trametinib on the overall survival of *KP$^{f/f}$C* mice in a small pilot study. Although non-significant, single-agent trametinib treatment almost doubled median survival after enrollment from 33 to 59 days (Figure 4.3. F). Despite evidence of a real effect as a single agent, trametinib would be administered alongside or following standard of care chemotherapy in the clinical setting. Thus, we tested the impact of trametinib on tumor growth in the context of a maintenance therapy regimen *in vivo.* At 8 weeks of age, *KP$^{f/f}$C* mice were given two doses of standard of care chemotherapy (80 mg/kg gemcitabine + 60 mg/kg abraxane) followed by 2 weeks of maintenance trametinib therapy (3 mg/kg, 3 doses/week) (Figure 4.3. G). Although trametinib still significantly reduced tumor mass and cell number in the context of chemotherapy, the impact on the frequency and total number of CD133+ tumor cells was less pronounced in the maintenance setting (Figure 4.3. H). This could be due in part to a selection for resistant cancer stem cells in the context of standard of care chemotherapy. Nonetheless, these results suggest that further *in vivo* investigation may be warranted to determine how MEK inhibitors may be used to effectively reduce cancer stem cell content *in vivo,* especially in combination with other therapies.

Figure 4.3. Functional validation for hit compounds shows that MEK inhibition can target cancer stem cells *in vivo*

(A) Functional validation of hit compounds *in vitro*. *Msi2* inhibitors identified as hit compounds in the screen inhibit the growth of *Msi2*+ *KP$^{f/f}$C* tumor cells in a 3D sphere-forming assay *in vitro. Msi2*+ *KP$^{f/f}$C* tumor cells were sorted and plated at single cell in sphere-forming growth conditions and treated with mTOR (INK-128), MEK (AZD8330, Tak-733, trametinib), and HDAC (abexinostat, belinostat) inhibitors or vehicle (0nM, DMSO) at the concentrations noted. Spheres were counted 1 week later.

Figure 4.3. Functional validation for hit compounds shows that MEK inhibition can target cancer stem cells *in vivo*, Continued

(B) Hit compounds inhibit *Msi2* expression *in vitro* in *KP$^{f/f}$C* cells. *KP$^{f/f}$C* tumor cells were plated in 2D culture and treated with 500nM of each compound or vehicle (DMSO). After 48 hours, cells were collected and RNA was isolated for analysis of *Msi2* expression by qPCR. *Msi2* expression was normalized to *Gapdh* and is shown relative to DMSO control.

(C) Function validation of hit compounds *in vitro* in human MiaPaCa2 cells. Human MiaPaCa2 pancreatic cancer cells were plated in a soft agar colony formation assay in 3D and treated with 1nM, 5nM, or 10nM AZD8330 or INK-128, or vehicle (DMSO). Colonies were counted one week later.

(D) Schematic for single agent trametinib in *KP$^{f/f}$C* mice *in vivo. KP$^{f/f}$C* mice (8.5 weeks of age) were enrolled in treatment with 3 mg/kg trametinib or vehicle (corn oil) 3x weekly. After 2 weeks of treatment, tumors were isolated and dissociated for analysis by FACS.

(E) Single agent trametinib in *KP$^{f/f}$C* mice *in vivo.* Single agent trametinib reduced tumor burden in *KP$^{f/f}$C* mice; trametinib treatment reduced tumor mass, total cell number, EpCAM+ tumor cell number, and the fraction of CD133+ EpCAM+ tumor cells by 2-fold. The total number of CD133+ tumor stem cells was also reduced by over 5-fold.

(F) Survival in *KP$^{f/f}$C* mice *in vivo* treated with single agent trametinib. *KP$^{f/f}$C* mice (8.5 weeks of age) were enrolled in treatment with 3 mg/kg trametinib or vehicle (corn oil) 3x weekly until humane endpoint. Trametinib treatment improved overall survival of *KP$^{f/f}$C* mice from 33 to 59 days.

(G) Trametinib maintenance therapy in *KP$^{f/f}$C* mice *in vivo. KP$^{f/f}$C* mice (8 weeks of age) were treated with two doses of 60 mg/kg abraxane and 80 mg/kg gemcitabine followed with two weeks of single agent trametinib (3 mg/kg) or vehicle, 3x weekly. After two weeks of maintenance therapy tumors were isolated and dissociated for analysis by FACS.

(H) Trametinib maintenance therapy in *KP$^{f/f}$C* mice *in vivo*. Chemotherapy followed by maintenance therapy with trametinib reduced tumor burden in *KP$^{f/f}$C* mice; trametinib treatment reduced tumor mass about 2-fold. Total cell number and EpCAM+ tumor cell number were also significantly reduced; however, the fraction of CD133% EpCAM+ tumor cells was not reduced by maintenance trametinib treatment. The total number of CD133+ EpCAM+ tumor cells was also trending down in the context of trametinib therapy.

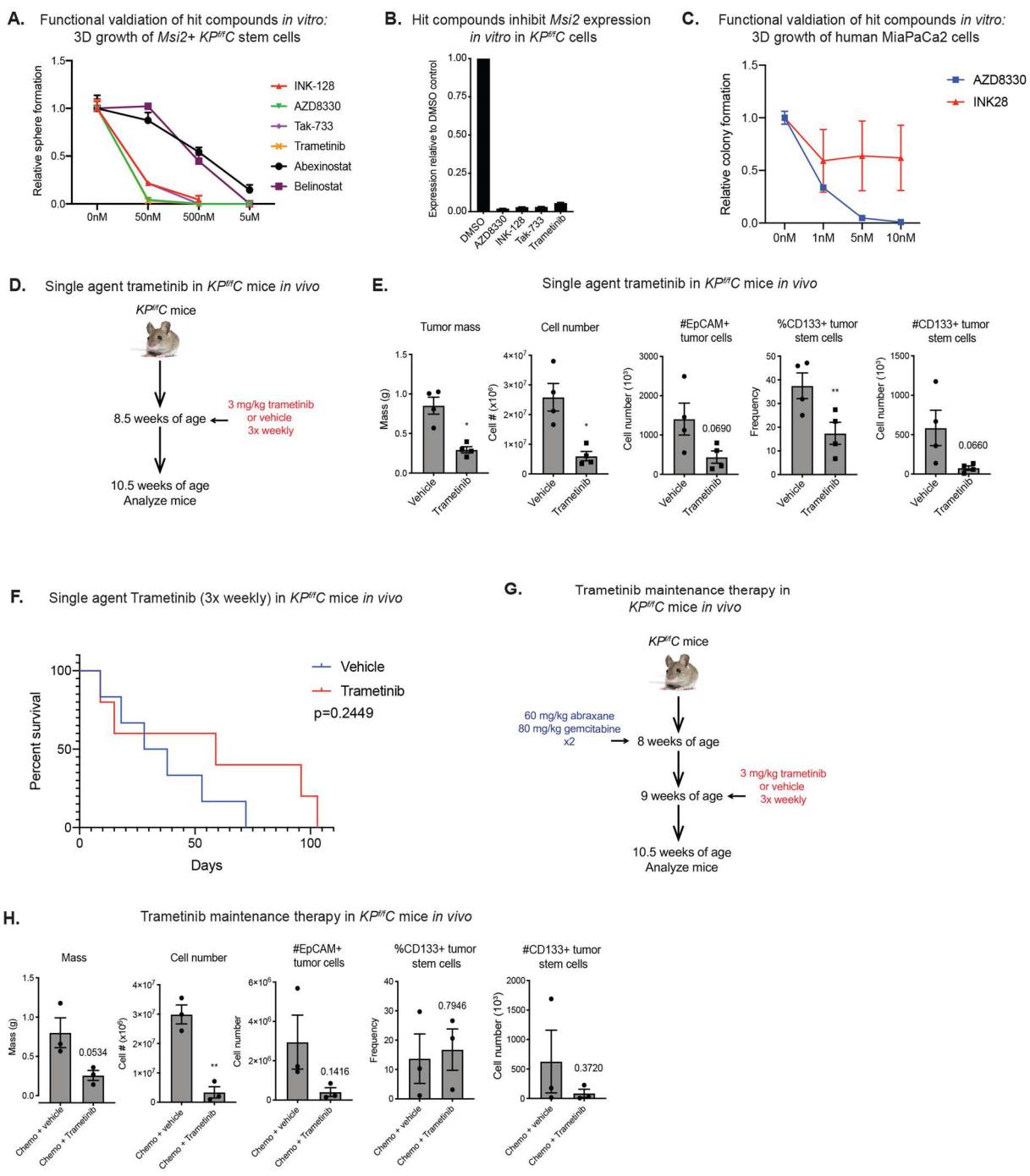
A.
Functional valdiation of hit compounds in vitro:
3D growth of Msi2+ KPf/fC stem cells
Relative sphere formation
INK-128
AZD8330
Tak-733
Trametinib
Abexinostat
Belinostat
0nM
50nM
500nM
5uM
B.
Hit compounds inhibit Msi2 expression
in vitro in KPf/fC cells
Expression relative to DMSO control
DMSO
AZD8330
INK-128
Tak-733
Trametinib
C.
Functional valdiation of hit compounds in vitro:
3D growth of human MiaPaCa2 cells
Relative colony formation
AZD8330
INK28
0nM
1nM
5nM
10nM
D.
Single agent trametinib in KPf/fC mice in vivo
KPf/fC mice
8.5 weeks of age
3 mg/kg trametinib
or vehicle
3x weekly
10.5 weeks of age
Analyze mice
E.
Single agent trametinib in KPf/fC mice in vivo
Tumor mass
Cell number
#EpCAM+
tumor cells
%CD133+ tumor
stem cells
#CD133+ tumor
stem cells
Mass (g)
Cell # (x10⁶)
Cell number (10³)
Frequency
0.0690
0.0660
Vehicle
Trametinib
F.
Single agent Trametinib (3x weekly) in KPf/fC mice in vivo
Percent survival
Vehicle
Trametinib
p=0.2449
Days
G.
Trametinib maintenance therapy in
KPf/fC mice in vivo
KPf/fC mice
60 mg/kg abraxane
80 mg/kg gemcitabine
x2
8 weeks of age
9 weeks of age
3 mg/kg trametinib
or vehicle
3x weekly
10.5 weeks of age
Analyze mice
H.
Trametinib maintenance therapy in KPf/fC mice in vivo
Mass
Cell number
#EpCAM+
tumor cells
%CD133+ tumor
stem cells
#CD133+ tumor
stem cells
0.0534
0.1416
0.7946
0.3720
Chemo + vehicle
Chemo + Trametinib

Pharmacological inhibition of RORG in pancreatic cancer

In prior work, we identified RORγ as a critical dependency that could be exploited to target aggressive pancreatic cancer stem cells[9]. Clinical RORγ antagonists have already been tested in early phase clinical trials for autoimmune indications, positioning these drugs to more easily move forward into trials for cancer[10]. To determine if pharmacological RORγ inhibition might be effective in pancreatic cancer, we tested the impact of two clinical RORγ inhibitors (AZD-0284 and JTE-151) on tumor growth *in vitro* and *in vivo*, using mouse and patient-derived models. In line with our previous results[9], we found that both AZD-0284 (sourced from MedChem Express, Figure 4.4. A) and JTE-151 (sourced from JT Therapeutics, Figure 4.4. B) significantly blocked the growth of $KP^{f/f}C$ organoids *in vitro,* an effect that was further enhanced by inclusion of the chemotherapy gemcitabine (Figure 4.4. A). To move these preclinical studies forward, we tested the impact of AZD-0284 on autochthonous tumor growth in $KP^{f/f}C$ mice *in vivo* (Figure 4.4. C). Cohorts of mice were treated with either vehicle, AZD-0284, or AZD-0284 plus gemcitabine. AZD-0284 was administered by oral gavage (90 mg/kg) daily based on pilot dosing studies; gemcitabine was administered i.p. (25 mg/kg) weekly. Drugs were provided for a total of 3 weeks prior to assessment of any impact on tumor growth. Overall, we observed a consistent drop in cell number and loss of EpCAM+ tumor epithelial cells as well as CD133+ cancer stem cells in mice that were treated with AZD-0284 relative to controls (Figure 4.4. D). While gemcitabine alone had a significant effect on these parameters as well, the impact of AZ-0284 alone was 3-fold greater than that of gemcitabine. In parallel, we tested the impact of JTE-151 on $KP^{f/f}C$ mice *in vivo* (Figure 4.4. E). Using the same schema, 8 week old $KP^{f/f}C$ mice were enrolled in treatment with either 30 mg/kg or 90 mg/kg JTE-151 daily for 3 weeks. Even at 30 mg/kg JTE-151 potently reduced the number of EpCAM+ tumor cells as well as CD133+ cancer stem cells (Figure 4.4. F), supporting RORγ inhibition as an effective strategy for targeting cancer stem cell *in vivo* in genetically engineered mouse

models. As a putative biomarker for drug activity, we used ELISA to test for serum IL-17 levels in *KP$^{f/f}$C* mice treated with both RORγ inhibitors. Reduced levels of IL-17, a known downstream target of RORγ, indicated successful inhibition of RORγ activity in our model system (Figure 4.4. G).

These promising results in mouse models set the stage for us to test whether these clinical-grade RORγ antagonists could also be effective against primary human pancreatic cancer cells. Organoid tumor cells derived from primary patient-derived xenografts were plated as single cells and treated with AZD-0284 in the presence or absence of gemcitabine for one week before analysis of organoid growth (Figure 4.5. A). AZD-0284 significantly impaired the growth of 2 independent patient-derived organoid lines; moreover, the combination of AZD-0284 and gemcitabine blocked the growth of primary patient-derived organoids more effectively than either drug alone (Figure 4.5. B,C). Based on these data, we tested the impact of JTE-151 on patient-derived organoids in parallel and observed impaired growth in all four independent patient-derived samples (Figure 4.5. D-H). In line with earlier studies, treatment with a combination of JTE-151 and gemcitabine had a greater effect than either agent alone (Figure 4.5. F,G). These results are exciting because they show for the first time that a clinical grade RORγ antagonist can block the growth of primary patient-derived pancreatic cancer cells.

Figure 4.4. Clinical grade RORγ inhibitors block the growth of *KP$^{f/f}$C* tumor cells *in vitro* and *in vivo.*
(A) AZD-0284 blocks *KP$^{f/f}$C* organoid growth +/- gemcitabine. *KP$^{f/f}$C* organoids dissociated to single cells and plated in Matrigel domes in a 48-well plate; organoids were treated with 6uM AZD-0284 or vehicle +/- 0.025nM gemcitabine. After 4 days in culture with the inhibitor, organoid wells were imaged and organoid volume was analyzed in ImageJ.
(B) JTE-151 blocks *KP$^{f/f}$C* organoid growth *in vitro*. *KP$^{f/f}$C* organoids dissociated to single cells and plated in Matrigel domes in a 48-well plate; organoids were treated with 0.003uM, 0.03uM, 0.3uM, 3uM, 6uM, or 9uM JTE-151 or vehicle. After 4 days in culture with the inhibitor, organoid wells were imaged and organoid volume was analyzed in ImageJ.
(C) Acute AZD-0284 treatment in *KP$^{f/f}$C* mice. *KP$^{f/f}$C* mice (8 weeks of age) were enrolled into treatment with 90 mg/kg AZD-0284 or vehicle (daily, oral gavage) +/- 25 mg/kg gemcitabine (weekly). After three weeks of treatment, tumors were isolated and dissociated for analysis.
(D) AZD-0284 blocks *KP$^{f/f}$C* tumor growth *in vivo.* Although therapy had no significant effect on tumor mass and modestly reduced total cell count, treatment with AZD-0284 +/- gemcitabine reduced EpCAM+ tumor cell number and CD133+ tumor stem cell number, with AZD-0284 more deeply reducing both EpCAM+ tumor cell and CD133+ tumor stem cell numbers than gemcitabine alone.
(E) Acute JTE-151 treatment in *KP$^{f/f}$C* mice. *KP$^{f/f}$C* mice (8 weeks of age) were enrolled into treatment with 30 mg/kg or 90 mg/kg JTE-151 or vehicle (daily, oral gavage). After three weeks of treatment, tumors were isolated and dissociated for analysis.
(F) JTE-151 blocks growth of autochthonous *KP$^{f/f}$C* tumors *in vivo.* Treatment with 30 mg/kg or 90 mg/kg JTE-151 significantly ablated both EpCAM+ tumor cells and CD133+ tumor stem cells by over 2-fold in *KP$^{f/f}$C* mice.
(G) Pharmacological RORγ inhibition blocks IL-17 levels in *KP$^{f/f}$C* mice. *KP$^{f/f}$C* mice treated with both AZD-0284 and JTE-151 were analyzed for serum IL-17 levels by ELISA to assess inhibition of this known downstream target of RORγ. Reductions in serum IL-17 by AZD-0284 and JTE-151 treatment indicate effective RORγ inhibition by both clinical inhibitors in this model system.

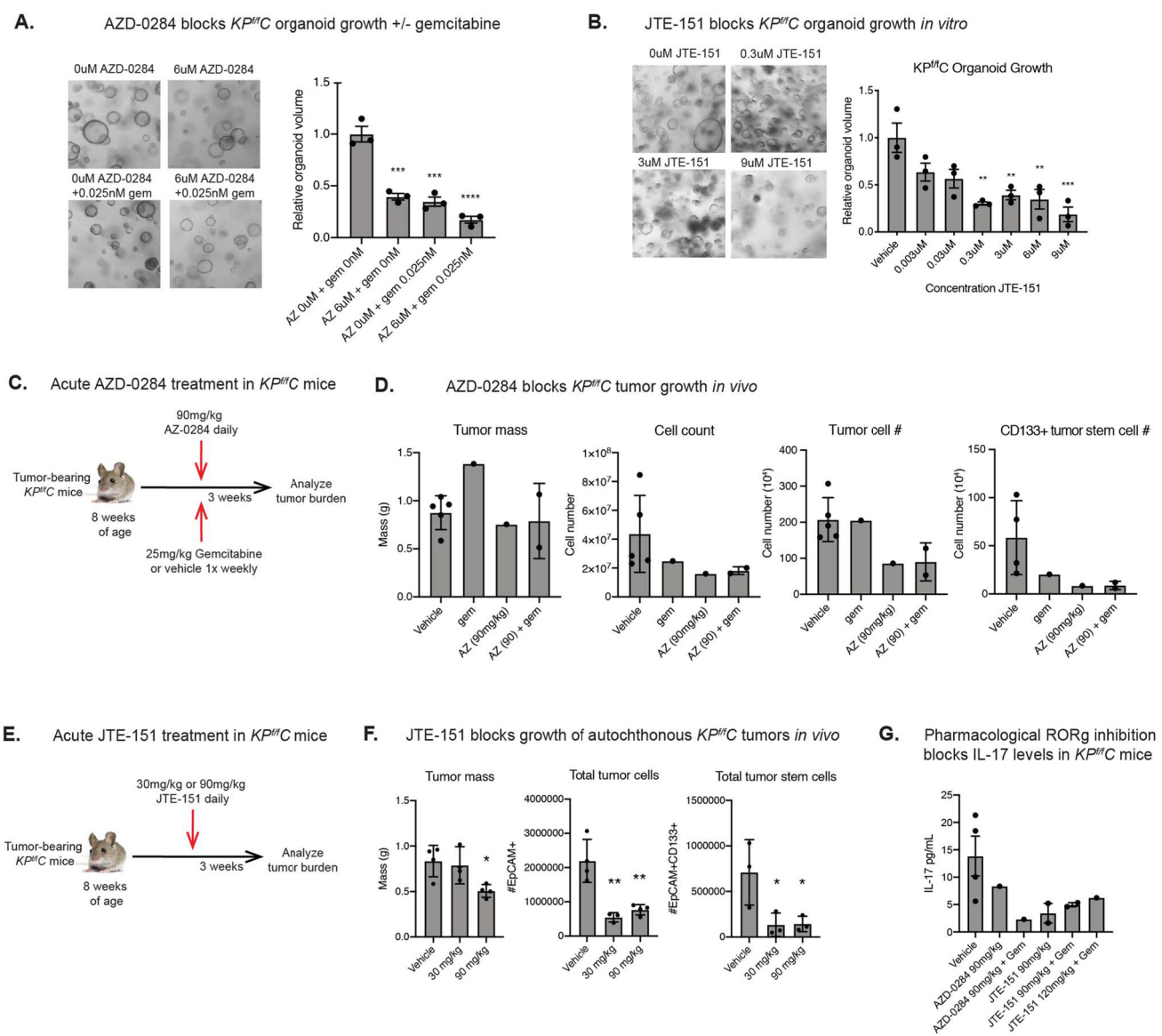
A.
AZD-0284 blocks KP^f/fC organoid growth +/- gemcitabine
0uM AZD-0284
6uM AZD-0284
0uM AZD-0284 +0.025nM gem
6uM AZD-0284 +0.025nM gem
Relative organoid volume
AZ 0uM + gem 0nM
AZ 6uM + gem 0nM
AZ 0uM + gem 0.025nM
AZ 6uM + gem 0.025nM
B.
JTE-151 blocks KP^f/fC organoid growth in vitro
0uM JTE-151
0.3uM JTE-151
3uM JTE-151
9uM JTE-151
KP^f/fC Organoid Growth
Relative organoid volume
Vehicle
0.003uM
0.03uM
0.3uM
3uM
6uM
9uM
Concentration JTE-151
C.
Acute AZD-0284 treatment in KP^f/fC mice
90mg/kg AZ-0284 daily
Tumor-bearing KP^f/fC mice
8 weeks of age
3 weeks
Analyze tumor burden
25mg/kg Gemcitabine or vehicle 1x weekly
D.
AZD-0284 blocks KP^f/fC tumor growth in vivo
Tumor mass
Mass (g)
Cell count
Cell number
Tumor cell #
Cell number (10^4)
CD133+ tumor stem cell #
Cell number (10^4)
Vehicle
gem
AZ (90mg/kg)
AZ (90) + gem
E.
Acute JTE-151 treatment in KP^f/fC mice
30mg/kg or 90mg/kg JTE-151 daily
Tumor-bearing KP^f/fC mice
8 weeks of age
3 weeks
Analyze tumor burden
F.
JTE-151 blocks growth of autochthonous KP^f/fC tumors in vivo
Tumor mass
Mass (g)
Total tumor cells
#EpCAM+
Total tumor stem cells
#EpCAM+CD133+
Vehicle
30 mg/kg
90 mg/kg
G.
Pharmacological RORg inhibition blocks IL-17 levels in KP^f/fC mice
IL-17 pg/mL
Vehicle
AZD-0284 90mg/kg
AZD-0284 90mg/kg + Gem
JTE-151 90mg/kg
JTE-151 90mg/kg + Gem
JTE-151 120mg/kg + Gem

Figure 4.5. Clinical grade RORγ inhibitors block the growth of patient-derived pancreatic cancer organoids *in vitro,* Continued
(B and C) AZD-0284 blocks PDX organoid growth in organoid line PDX#1356 (B) and PDX#1535 (C), with or without gemcitabine. Two independent patient-derived organoid lines were treated with 6uM AZD-0284 or vehicle +/- 0.05nM gemcitabine; AZD-0284 or gemcitabine monotherapy reduced organoid growth by ~2-fold in both organoid lines. Combination treatment with AZD-0284 and gemcitabine blocked organoid growth more effectively than either agent alone.
(D-G) JTE-151 blocks PDX organoid growth in four independent patient-derived organoid lines, PDX#202 (D), PDX#204 (E), PDX#1356 (F), and PDX#1535. Patient-derived organoids were treated with 3uM JTE-151 or vehicle +/- 0.05nM gemcitabine. JTE-151 monotherapy reduced organoid growth in all four organoid lines, and combination treatment with JTE-151 and gemcitabine blocked organoid growth more effectively than either agent alone in PDX#1356 (F) and PDX#1535 (G).
(H) JTE-151 blocks growth of PDX organoids. Data is shown compiled across all four independent patient-derived organoid lines, showing a deep impact of 3uM JTE-151 on organoid growth across samples.

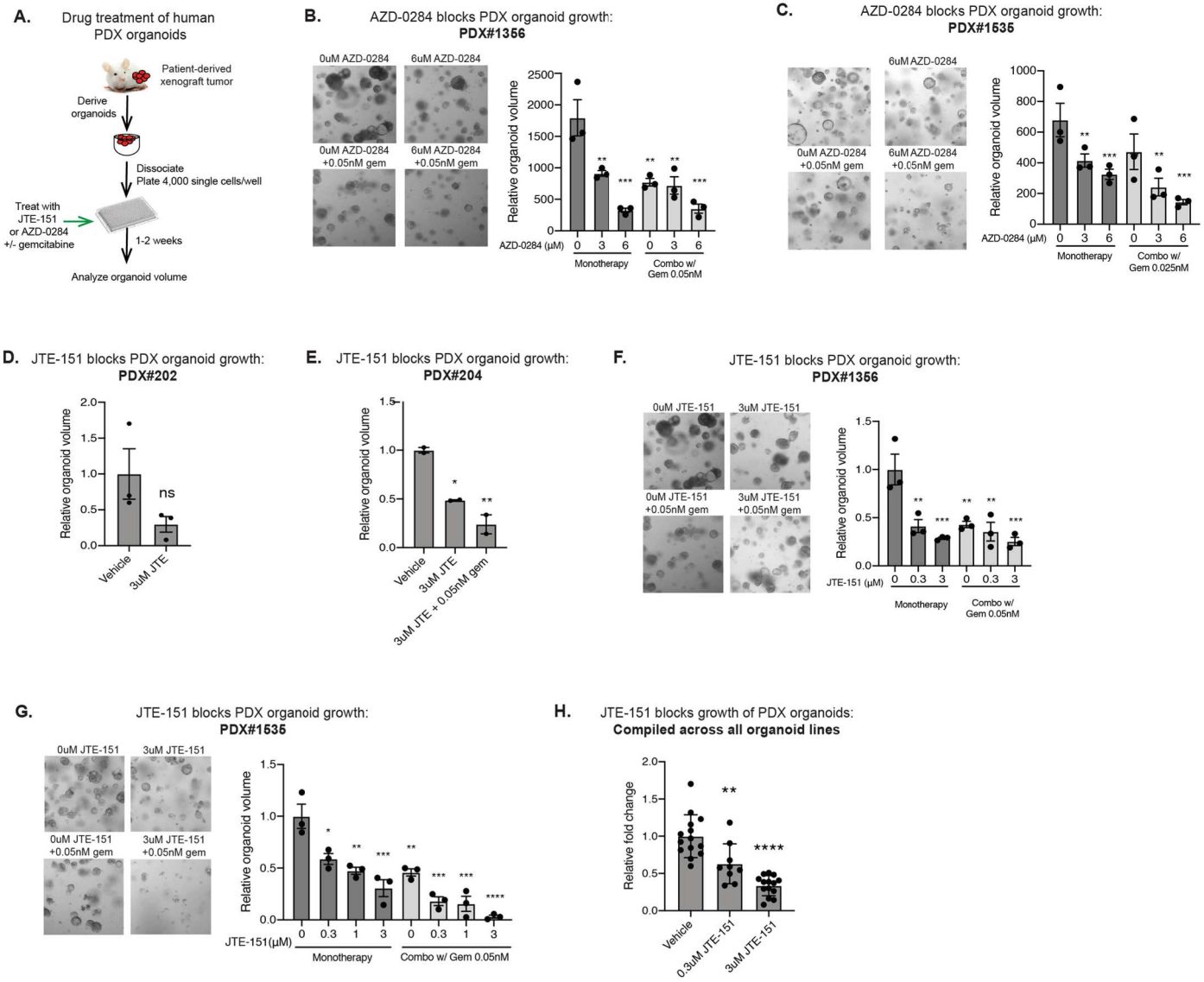
A.
Drug treatment of human PDX organoids
Patient-derived xenograft tumor
Derive organoids
Dissociate
Plate 4,000 single cells/well
Treat with JTE-151 or AZD-0284 +/- gemcitabine
1-2 weeks
Analyze organoid volume
B.
AZD-0284 blocks PDX organoid growth:
PDX#1356
0uM AZD-0284
6uM AZD-0284
0uM AZD-0284 +0.05nM gem
6uM AZD-0284 +0.05nM gem
Relative organoid volume
AZD-0284 (μM) 0 3 6 0 3 6
Monotherapy
Combo w/ Gem 0.05nM
C.
AZD-0284 blocks PDX organoid growth:
PDX#1535
6uM AZD-0284
0uM AZD-0284 +0.05nM gem
6uM AZD-0284 +0.05nM gem
Relative organoid volume
AZD-0284 (μM) 0 3 6 0 3 6
Monotherapy
Combo w/ Gem 0.025nM
D.
JTE-151 blocks PDX organoid growth:
PDX#202
Relative organoid volume
ns
Vehicle
3uM JTE
E.
JTE-151 blocks PDX organoid growth:
PDX#204
Relative organoid volume
Vehicle
3uM JTE
3uM JTE + 0.05nM gem
F.
JTE-151 blocks PDX organoic growth:
PDX#1356
0uM JTE-151
3uM JTE-151
0uM JTE-151 +0.05nM gem
3uM JTE-151 +0.05nM gem
Relative organoid volume
JTE-151 (μM) 0 0.3 3 0 0.3 3
Monotherapy
Combo w/ Gem 0.05nM
G.
JTE-151 blocks PDX organoid growth:
PDX#1535
0uM JTE-151
3uM JTE-151
0uM JTE-151 +0.05nM gem
3uM JTE-151 +0.05nM gem
Relative organoid volume
JTE-151(μM) 0 0.3 1 3 0 0.3 1 3
Monotherapy
Combo w/ Gem 0.05nM
H.
JTE-151 blocks growth of PDX organoids:
Compiled across all organoid lines
Relative fold change
Vehicle
0.3uM JTE-151
3uM JTE-151

Finally, we tested whether RORγ antagonists could have activity in primary patient-derived xenograft (PDX) models *in vivo*. Following subcutaneous transplantation of PDX tumor cells into immunodeficient recipients, mice were treated with either vehicle, AZD-0284, or JTE-151 once tumors were established. Tumor burden and cellular content and composition were analyzed by FACS after three weeks of treatment (Figure 4.6 A). Although transplant number was limited for some of these studies, we observed a striking decrease in total numbers of EpCAM+ tumor cells as well as the numbers of EpCAM+CD133+ tumor stem cells in AZD-0284 and JTE-151 treated mice (Figure 4.6 B-E). When taken together, treatment with JTE-151 was sufficient to significantly reduce both tumor cell and tumor stem cell content in PDX models *in vivo.* These data provide compelling evidence that clinical-grade RORγ antagonists can have activity in primary patient-derived PDAC models *in vivo*, and support further investigation into these inhibitors for their potential use in treating pancreatic cancer by targeting the stem cell compartment.

Figure 4.6. Clinical grade RORγ inhibitors block the growth of patient-derived xenografts *in vivo*
(A) Drug treatment of human PDX organoids. Patient-derived organoids were derived by dissociating patient-derived xenograft (PDX) tumors and plating single cells in Matrigel in organoid culture conditions. Patient-derived organoids were then passaged, dissociated to single cell, and plated at 4,000 cells per well in 20uL Matrigel domes in a 48-well plate. Organoid media containing JTE-151, AZD-0284, or vehicle (DMSO) +/- gemcitabine was added to each well, Wells were imaged and organoid volume was calculated after 1-2 weeks of drug treatment *in vitro.*
Figure 4.6. Clinical grade RORγ inhibitors block the growth of patient-derived xenografts *in vivo,* Continued
(A) Drug treatment of human PDX flank tumors *in vivo.* Patient-derived xenograft (PDX) tumors were dissociated and re-transplanted subcutaneously into the flanks of NSG mice. After tumor establishment (3-8 weeks post-transplant), mice were enrolled into daily treatment with AZD-0284, JTE-151, or vehicle. Tumors were isolated and dissociated after 3 weeks of drug treatment.
(B) AZD-0284 blocks growth of PDX tumors *in vivo.* Although tumor number was limiting, preliminary evidence showed that daily 90 mg/kg AZD-0284 treatment reduced the number of EpCAM+ tumor cells and CD133+ tumor stem cells in one PDX sample *in vivo.*
(C-E) JTE-151 blocks growth of PDX tumors *in vivo.* Daily treatment with 90 mg/kg JTE-151 reduced the number of EpCAM+ tumor cells and CD133+ tumor stem cells in three independent PDX samples *in vivo;* PDX#1424 (C), PDX#1535 (D), and PDX#1356 (E).
(F) JTE-151 blocks growth of PDX flank tumors. Data is shown compiled across all three independent patient-derived xenograft tumors samples and normalized to vehicle, showing a deep impact of JTE-151 treatment on the growth of patient-derived xenograft tumors *in vivo.*

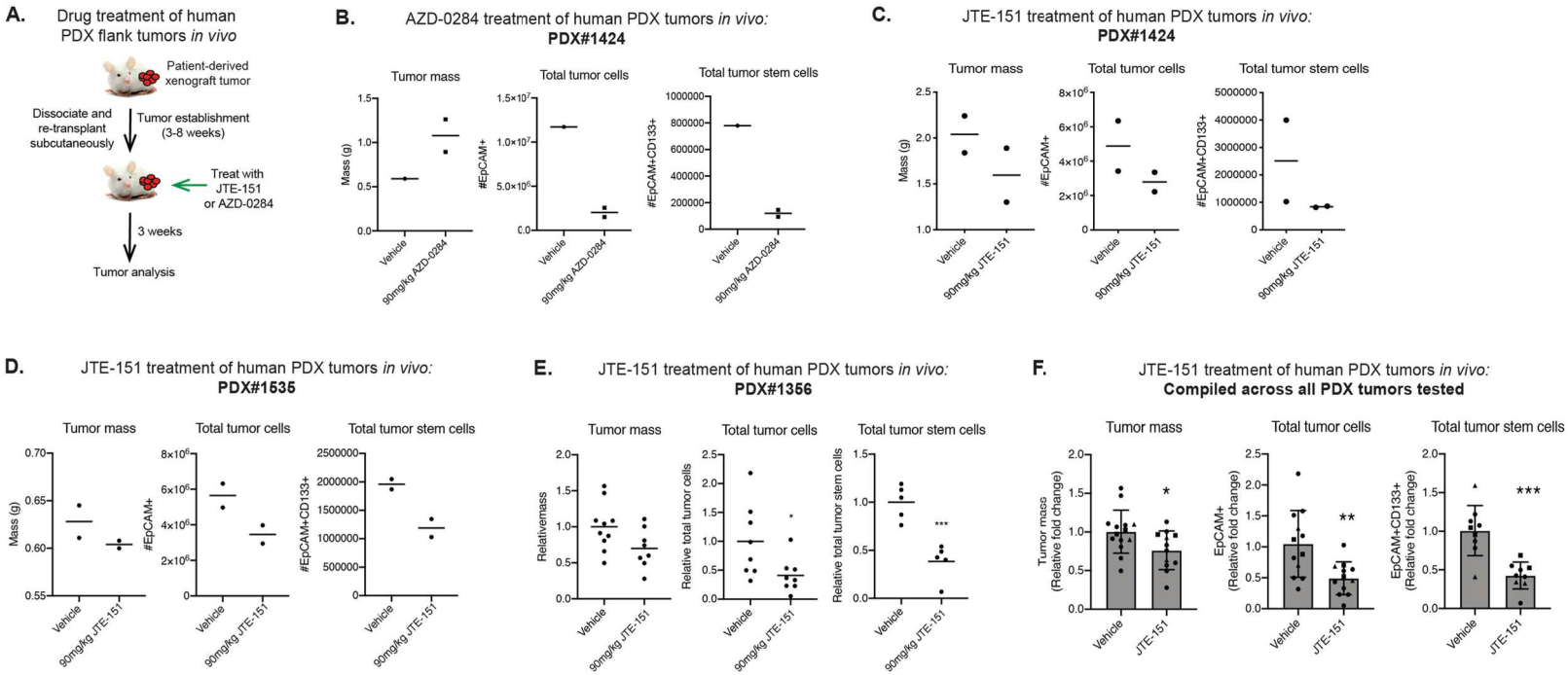
A.
Drug treatment of human PDX flank tumors in vivo
Patient-derived xenograft tumor
Dissociate and re-transplant subcutaneously
Tumor establishment (3-8 weeks)
Treat with JTE-151 or AZD-0284
3 weeks
Tumor analysis
B.
AZD-0284 treatment of human PDX tumors in vivo:
PDX#1424
Tumor mass
Total tumor cells
Total tumor stem cells
Mass (g)
#EpCAM+
#EpCAM+CD133+
Vehicle
90mg/kg AZD-0284
C.
JTE-151 treatment of human PDX tumors in vivo:
PDX#1424
Tumor mass
Total tumor cells
Total tumor stem cells
Mass (g)
#EpCAM+
#EpCAM+CD133+
Vehicle
90mg/kg JTE-151
D.
JTE-151 treatment of human PDX tumors in vivo:
PDX#1535
Tumor mass
Total tumor cells
Total tumor stem cells
Mass (g)
#EpCAM+
#EpCAM+CD133+
Vehicle
90mg/kg JTE-151
E.
JTE-151 treatment of human PDX tumors in vivo:
PDX#1356
Tumor mass
Total tumor cells
Total tumor stem cells
Relativemass
Relative total tumor cells
Relative total tumor stem cells
Vehicle
90mg/kg JTE-151
F.
JTE-151 treatment of human PDX tumors in vivo:
Compiled across all PDX tumors tested
Tumor mass
Total tumor cells
Total tumor stem cells
Tumor mass (Relative fold change)
EpCAM+ (Relative fold change)
EpCAM+CD133+ (Relative fold change)
Vehicle
JTE-151

4.4. Discussion

The results outlined here demonstrate the utility of the genetic *Msi2-GFP* stem cell reporter in screening for dependencies and inhibitors of cancer stem cell function. Using this reporter in context of the *KP$^{f/f}$C* model of pancreatic cancer, we were able to identify inhibitors of both *Msi2* specifically, and *Msi2*+ stem cell function. First, in using *Msi2-GFP*+ *KP$^{f/f}$C* cells for an image-based screen, we identified a range of compounds that inhibit *Msi2* transcription. Not only do these compounds reveal new potential strategies to target cancer stem cell function, but they suggest pathways upstream of *Msi2* regulation in cancer. Of all the hit compounds identified, we found that the most common targets included HDAC, PI3K/mTOR, MEK, and CDK. Confirming the utility of our screen in identifying stem cell dependencies, these core pathways have all been associated with stem cell function in cancer. CDK activity has been tied to cancer stem cells in breast[11] and pancreatic cancer[12], and epigenetic regulatory factors including HDACs are known to be important in cancer stem cells[13]. In fact, HDAC inhibitors have been shown to target cancer stem cell populations[14] in many cancers[15,16,17,18,19,20,21,22] including PDAC[23]. Our data that various HDAC inhibitors block *Msi2* expression supports the epigenetic regulation of *Msi2*, and a functional dependence on histone acetylation in line with the literature. Although PI3K/mTOR[24,25] and MEK signaling[26] have also been linked to CSC function in pancreatic cancer, our results also suggest a link between Ras activation and *Msi2* transcription through these two Ras effector pathways[27].

Our image-based screen also strikingly revealed MEK inhibition as a potent suppressor of *Msi2* expression and CSC growth *in vivo* in GEMMs. These preclinical results support a role for the MEK pathway in cancer self-renewal and suggest that MEK inhibition could be a useful strategy for targeting CSCs clinically. However, given the role of the MEK pathway as a powerful downstream effector of Ras, clinical trials have already been conducted to assess the impact of MEK inhibitors in pancreatic cancer, without yielding significant sucess[28,29,30,31,32,30,33].

More recent evidence suggests that clinical MEK inhibitors may be more efficacious in combination with other therapeutics[34,35,36], and clinical investigation into combination therapies is ongoing[37]. Our results suggest that by targeting CSCs, MEK inhibition may indeed be a promising strategy to consider, perhaps in a maintenance setting in combination with cytotoxic drugs and/or inhibitors of pathways associated with MEK inhibitor resistance. In fact, other *Msi2* inhibitors identified here could be interesting targets for combination MEK inhibitor therapy. There is some evidence that epigenetic drugs can synergize with MEK inhibition in cancer[38,39]; perhaps dual targeting of CSCs with MEK and HDAC inhibitors could improve therapeutic response in pancreatic cancer.

In addition to leveraging our *Msi2-GFP* reporter *KP$^{f/f}$C* model to screen for *Msi2* inhibitors, we used primary cells from this model to extensively characterize the transcriptomic/epigenomic landscape and functional dependencies of *Msi2*+ cancer cells (discussed in detail in Chapter 2)[9]. These studies revealed a unique dependency of pancreatic CSCs on the nuclear receptor RORγ. Because RORγ inhibitors have been tested clinically in non-cancer indications[10], these drugs could be promising candidates to consider for clinical trials in pancreatic cancer. In a series of preclinical studies, we profiled the impact of the RORγ inhibitors AZD-0284 and JTE-151 on pancreatic cancer growth using mouse and patient-derived models. Although batch to batch variability in these compounds was not tested, we provide substantial evidence that these clinical inhibitors can effectively deplete pancreatic cancer stem cells *in vivo* in the autochthonous *KP$^{f/f}$C* model. Importantly, these inhibitors also blocked the growth of patient-derived xenograft cells *in vitro* and *in vivo*, demonstrating that RORγ inhibition is also effective in more genetically and molecularly diverse patient-derived samples. Together, these data provide compelling evidence that clinical RORγ inhibition may be a promising strategy to block pancreatic cancer growth and target CSCs. Additional

preclinical development of these RORγ inhibitors is warranted, and could recommend RORγ inhibition as a candidate strategy to move forward into clinical development.

4.5. Methods

Image-based screen in *Msi2-GFP* reporter *KP$^{f/f}$C* cells

The high content image-based screen for *Msi2* inhibitors was conducted at the Sanford Burnham Prebys Medical Discovery Institute (La Jolla, CA). DSMO or compounds were dispensed at 10uL per well in a 384 well plate, for a final concentration of 0.5% DMS0. 1,500 *Msi2-GFP*+ or *Msi2-GFP- KP$^{f/f}$C* tumor cells were then seeded at a final of volume of 50uL per well and incubated for 24, 48, or 72 hours in a tissue culture incubator at 37 degrees Celsius. At each analysis timepoint, cells were fixed using PFA and stained using DAPI and HCS CellMask (Deep Red). After staining, plates were sealed and imaged using an Opera Phenix confocal 20X H_2O objective (1.0 NA). *Msi2-GFP-* cells were used as a baseline control for background GFP signal. The compound libraries screened were the Prestwick Chemical Library (screened at 5uM), Epigenetics Library (screened at 0.5 and 5uM) and the EMD, Cayman, and SelleckChem Kinase Libraries (screened at 0.5 and 5uM). For analysis, DAPI was used to stain nuclei and count cells, and CellMask deep red was used to calculate cell area, which was used to normalize the GFP signal in each cell. DMSO treated *Msi2-GFP+* wells were used as a baseline control to calculate fold change in cell count and GFP intensity. After removing artifacts due to toxicity or increasing cell area, we 90 unique hit compounds where identified GFP intensity was reduced by 20% or more.

Image-based screen functional validation

To validate the functional impact of hit compounds identified in the image-based screen, *Msi2-GFP*+ *KP$^{f/f}$C* tumor cells were sorted and plated in 3D sphere-forming conditions

plus vehicle (DMSO) or inhibitor. This pancreatic sphere formation assay was modified from Rovira et al. 2010[40]. Briefly, *KP$^{f/f}$C* cells lines were plated at 350 single cells were per well in an ultra-low attachment 96-well plate in sphere media: 100 µl DMEM F-12 (Gibco, Life Technologies) containing 1x B-27 supplement (Gibco, Life Technologies), 3% FBS, 100 µM B-mercaptoethanol (Gibco, Life Technologies), 1x non-essential amino acids (Gibco, Life Technologies), 1x N2 supplement (Gibco, Life Technologies), 20 ng/ml EGF (Gibco, Life Technologies), and 20 ng/ml bFGF2 (Gibco, Life Technologies). Cells were plated at 90uL per well; the next day 10uL of DMSO vehicle or inhibitor (INK-128, AZD8330, Tak-733, trametinib, abexinostat, belinostat; SelleckChem) was added to a final concentration of 0nM, 50nM, 500nM, or 5uM in each well and cells were incubated at 37°C for 7 days, at which point the number of spheres per well as counted. The inhibitors AZD8330 and INK-128 were additionally tested for their functional impact on human MiaPaCa2 pancreatic cancer cells. MiaPaCa2 cells (ATCC) were plated in a colony assay; 24-well plates were first coated with 0.6% agarose in DMEM without supplements. Cells were plated at a density of 2,000 cells per well in 0.3% agarose containing DMEM, 10% FBS, NEAA, penicillin and streptomycin, and Glutamax and DMSO vehicle or inhibitor at a final concentration of 0nM, 1nM, 5nM, or 10nM. Growth medium also containing a final concentration of 0nM, 1nM, 5nM, or 10nM inhibitor was placed over the solidified agarose layers. Colonies were counted 7 days after plating.

Image-based screen qPCR validation

50,000 *Msi2-GFP+ KP$^{f/f}$C* tumor cells were plated in 2D culture and treated with 500nM inhibitors or vehicle (DMSO) for 48 hours. Cells were then collected for RNA isolation and qPCR. GAPDH was used as a housekeeping gene for qPCR analysis.

Trametinib treatment *in vivo*

For single agent trametinib treatment *in vivo*, *KP$^{f/f}$C* mice were enrolled in 3 mg/kg 3x weekly trametinib or vehicle (corn oil) at 8.5 weeks of age. After 2 weeks of treatment, tumors were dissociated and analyzed by FACS for mass, cell count, EpCAM expression, and CD133 expression. For survival studies, *KP$^{f/f}$C* mice were enrolled in 3 mg/kg 3x weekly trametinib or vehicle (corn oil) treatment at 8.5 weeks and monitored until humane endpoint. A maintenance therapy regimen for trametinib was also tested in *KP$^{f/f}$C* mice; 8 week old mice were treated with one dose of 60 mg/kg abraxane and 80 mg/kg gemcitabine followed by 2 weeks of treatment with 3 mg/kg trametinib or vehicle. Tumors were then dissociated and analyzed by FACS for mass, cell count, EpCAM expression, and CD133 expression as described below.

RORγ inhibitor treatment *in vitro*

Mouse primary pancreatic cancer organoids were established from end-stage *KP$^{f/f}$C* mice as follows: tumors from endpoint mice (10-12 weeks of age) were isolated and dissociated into single cell suspension as follows. Mouse pancreatic tumors were washed in MEM (GIBCO, Life Technologies) and cut into 1-2 mm pieces immediately following resection. Tumor pieces were collected into a 50 mL Falcon tube containing 10 mL Gey's balanced salt solution (Sigma), 5 mg Collagenase P (Roche), 2 mg Pronase (Roche), and 0.2 µg DNase I (Roche). Samples were incubated for 20 minutes at 37°C, then pipetted up and down 10 times and returned to 37°C. After 15 more minutes, samples were pipetted up and down 5 times, then passaged through a 100 µm nylon mesh (Corning). Red blood cells were lysed using RBC Lysis Buffer (eBioscience) and the remaining tumor cells were washed, and plated in 20uL in Matrigel as a dome in a pre-warmed 48 well plate. After incubation at 37°C for 5 min, domes were covered with 300 µL PancreaCult Organoid Growth Media (StemCell Technologies, Inc.). *KP$^{f/f}$C* organoids were passaged at ~1:2 as previously described[14]. Briefly, organoids were isolated using Cell Recovery Solution (Corning 354253), then dissociated using Accumax Cell

Dissociation Solution (Innovative Cell Technologies AM105), and plated in 20 µL matrigel (BD Biosciences, 354230) domes on a pre-warmed 48-well plate. After incubation at 37°C for 5 min, domes were covered with 300 µL PancreaCult Organoid Growth Media (StemCell Technologies, Inc.). AZD-0284 or JTE-151 were resuspended in DMSO and further diluted in PancreaCult Organoid Media (StemCell Technologies, Inc.) to the indicated dilutions. Organoids were grown in the presence of vehicle or drug for 4 days, then imaged and quantified.

Primary patient organoids were established and provided by Dr. Andrew Lowy. Briefly, patient-derived xenografts were washed in MEM (GIBCO, Life Technologies) and cut into 1-2 mm pieces immediately following resection. Tumor pieces were collected into a 50 mL Falcon tube containing 10 mL Gey's balanced salt solution (Sigma), 5 mg Collagenase P (Roche), and 0.2 µg DNase I (Roche). Samples were incubated for 10 minutes at 37°C, then pipetted up and down 10 times and returned to 37°C. After 10 more minutes, samples were pipetted up and down 5 times, then passaged through a 100 µm nylon mesh (Corning). Red blood cells were lysed using RBC Lysis Buffer (eBioscience) and the remaining tumor cells were washed, and then resuspended in Matrigel and plated in pre-warmed 24-well plate in 25uL Matrigel domes. After 15 minutes, domes were covered in human organoid growth media containing: Advanced DMEM/F12, 10mM HEPES (pH 7.2-7.5), 1X GlutaMAX, 100 ug/mL primocin, 50% Wnt3a conditioned media, 10% R-Spondin1-conditioned media, 1X-B27 supplement, 10mM nicotinamide, 1.25 mM N-acetyl cysteine, 100 ng/mL murine noggin, 50 ng/mL human-EGF, 100 ng/mL human-FGF, 10 nM human gastrin, 500 nM A-83-01, and 10.5 uM Rho Kinase inhibitor (SelleckChem, Y-27632). Organoids were passaged and maintained as previously described[41–43]. For drug studies, cells were split 1:2 into 20 µL domes plated on pre-warmed 48 well plates. Domes were incubated at 37°C for 5 min, then covered with human complete organoid feeding media[14] containing the indicated doses of AZD-0284, JTE-151, or

gemcitabine and refreshed every 3 days. Organoids were grown in the presence of vehicle or drug for 7 days, then imaged and quantified. All images were acquired on a Zeiss Axiovert 40 CFL. Organoids were counted and measured using ImageJ 1.51 s software.

RORγ inhibitor treatment *in vivo*

The clinical grade RORγ inhibitors AZD-0284 and JTE-151 were resuspended as follows. Approximately 10 mg of compound was weighed and poured into an agate mortar. Using the agate pestle, the powder was ground into a very fine layer. 20 uL of 0.5% methylcellulose was then added to the center of the agate mortar; the pestle was used to continue grinding the methylcellulose into the powder until it appeared shiny. Another 20 uL of methylcellulose was added, repeating the same step until well mixed. Next, 50 uL of methylcellulose was added, continuing to grind until well mixed. This step was repeated until a total of 1 mL 0.5% methylcellulose was fully incorporated with the compound. When fully suspended, the drug was returned to a 5 mL polystyrene tube and a fresh volume of methylcellulose was added to the agate mortar and ground, repeating several times, to collect all of the compound suspension into the 5 mL tube. Finally, the drug suspension was vortexed for 1 minute and sonicated in a water bath for 5 minutes. Gemcitabine (Sigma, G6423) was resuspended in PBS at 20 mg/ml. $KP^{f/f}C$ autochthonous tumor-bearing mice were treated with either vehicle (PBS) or gemcitabine (25 mg/kg i.p., 1x weekly) alone or in combination with vehicle, AZD-0284 (30 mg/kg p.o. daily), or JTE-151 (30 or 90 mg/kg p.o. daily) for 3 weeks. After 3 weeks of therapy, tumors were removed, weighed, and dissociated for FACS analysis as described below. For drug-treated PDX tumor transplants $1x10^6$ patient-derived xenograft cells were resuspended in 50 µL culture media, then mixed 1:1 with Matrigel (BD Biosciences). Cells were injected subcutaneously into the left or right flank of 5-8 week-old NSG recipient mice. When measurable tumors could be detected, tumors were measured and mice were

randomly enrolled in treatment groups and treated for 3 weeks. After 3 weeks of therapy, tumors were removed, weighed, and dissociated for FACS analysis as described below.

FACS analysis of tumors

Mouse pancreatic tumors or human PDX tumors were dissociated to single cell suspension as described above. Analysis and cell sorting were carried out on a FACS Aria III machine (Becton Dickinson), and data were analyzed with FlowJo software (Tree Star). For analysis of cell surface markers by flow cytometry, $5x10^5$ cells were resuspended in HBSS containing 2.5% FBS and 2 mM EDTA, then stained with FC block followed by 0.5 µL of each antibody. The following rat antibodies were used: anti-mouse EpCAM-APC (eBioscience), anti-mouse CD133-PE (eBioscience), anti-human EpCAM-PE (ThermoFisher #12-9326-42) and CD133-BV421 (BD Biosciences, #566598) or CD133-APC (Miltenyi #130-113-746). Propidium-iodide (Life Technologies) was used to stain for dead cells.

4.6. Acknowledgements

Chapter 4 is co-authored with Chambers KC, McDermott ML, Fisher C, Heyen-Genel S, and Jackson M, and Reya TR. The dissertation author was primary author of this chapter. KC helped conduct many *in vitro* and *in vivo* studies testing clinical RORγ inhibitors. MLM assisted with analysis of PDX transplants treated with RORγ inhibitors. CF, SHG, and MJ conducted and analyzed the results of the image-based screen for *Msi2* inhibitors a the Sanford Burnham Prebys Medical Discovery Institute.

4.7. References

1. Mizrahi, J. D., Surana, R., Valle, J. W. and Shroff, R. T. Pancreatic cancer. *Lancet* **395**, 2008–2020 (2020).

2. Kleeff, J., Korc, M., Apte, M., La Vecchia, C., Johnson, C.D., Biankin, A.V., Neale,

R.E., Tempero, M., Tuveson, D.A., Hruban, R.H. and Neoptolemos, J.P. Pancreatic cancer. *Nat. Rev. Dis. Prim. 2016 21* **2**, 1–22 (2016).

3. Morrison, A. H., Byrne, K. T. and Vonderheide, R. H. Immunotherapy and prevention of pancreatic cancer. *Trends in Cancer* **4**, 418–428 (2018).

4. Reya, T., Morrison, S. J., Clarke, M. F. and Weissman, I. L. Stem cells, cancer, and cancer stem cells. *Nature* **414**, 105–111 (2001).

5. Batlle, E. & Clevers, H. Cancer stem cells revisited. *Nat. Med.* **23**, 1124–1134 (2017).

6. Fox, R. G., Park, F. D., Koechlein, C. S., Kritzik, M. and Reya, T. Musashi signaling in stem cells and cancer. *Annu. Rev. Cell Dev. Biol.* **31**, 249-267 (2015).

7. Kudinov, A. E., Karanicolas, J., Golemis, E. A. annd Boumber, Y. Musashi RNA-binding proteins as cancer drivers and novel therapeutic targets. *Clin. Cancer Res.* **23**, 2143–2153 (2017).

8. Fox, R.G., Lytle, N.K., Jaquish, D.V., Park, F.D., Ito, T., Bajaj, J., Koechlein, C.S., Zimdahl, B., Yano, M., Kopp, J.L. and Kritzik, M. Image-based detection and targeting of therapy resistance in pancreatic adenocarcinoma. *Nature* **534**, 407–411 (2016).

9. Lytle, N.K., Ferguson, L.P., Rajbhandari, N., Gilroy, K., Fox, R.G., Deshpande, A., Schürch, C.M., Hamilton, M., Robertson, N., Lin, W., Noel, P. A., Wartenberg, M., Zlobec, I., Eichmann, M., Galván, J. A., Karamitopolous, E., Gilderman, T., Esparza, L. A., Shima, Y., Spahn, P., French, R., Lewis, N. E., Fisch, K. M., Sasik, R., Rosenthal S. B., Kritzik, M., Von Hoff, D., Han, H., Ideker, T., Desphande A. J., Lowy, A. M., Adams, P. D., and Reya T. A multiscale map of the stem cell state in pancreatic adenocarcinoma. *Cell* **177**, 572-586 (2019).

10. Sun, N., Guo, H. and Wang, Y. Retinoic acid receptor-related orphan receptor gamma-t (RORγt) inhibitors in clinical development for the treatment of autoimmune diseases: a patent review (2016-present). *Expert Opin. Ther. Pat.* **29,** 663-674 (2019).

11. Dai, M., Zhang, C., Ali, A., Hong, X., Tian, J., Lo, C., Fils-Aimé, N., Burgos, S.A., Ali, S. and Lebrun, J.J. CDK4 regulates cancer stemness and is a novel therapeutic target for triple-negative breast cancer. *Sci. Reports* **6**, 1–15 (2016).

12. Wijnen, R., Pecoraro, C., Carbone, D., Fiuji, H., Avan, A., Peters, G.J., Giovannetti, E. and Diana, P. Cyclin dependent kinase-1 (CDK-1) inhibition as a novel therapeutic strategy against pancreatic ductal ddenocarcinoma (PDAC). *Cancers (Basel).* **13**, 4389 (2021).

13. Wainwright, E. N. & Scaffidi, P. Epigenetics and cancer stem cells: Unleashing, hijacking, and restricting cellular plasticity. *Trends in Cancer* **3**, 372–386 (2017).

14. Keyvani-Ghamsari, S., Khorsandi, K., Rasul, A. and Zaman, M. K. Current understanding of epigenetics mechanism as a novel target in reducing cancer stem cells resistance. *Clin. Epigenetics* **13**, 1–31 (2021).

15. Di Pompo, G., Salerno, M., Rotili, D., Valente, S., Zwergel, C., Avnet, S., Lattanzi, G., Baldini, N. and Mai, A. Novel histone deacetylase inhibitors induce growth arrest,

apoptosis, and differentiation in sarcoma cancer stem cells. *J. Med. Chem.* **58**, 4073–4079 (2015).

16. Salvador, M.A., Wicinski, J., Cabaud, O., Toiron, Y., Finetti, P., Josselin, E., Lelièvre, H., Kraus-Berthier, L., Depil, S., Bertucci, F. and Collette, Y. The histone deacetylase inhibitor abexinostat induces cancer stem cells differentiation in breast cancer with low Xist expression. *Clin. Cancer Res.* **19**, 6520–6531 (2013).

17. Schech, A., Kazi, A., Yu, S., Shah, P. and Sabnis, G. Histone deacetylase inhibitor entinostat inhibits tumor-initiating cells in triple-negative breast cancer cells. *Mol. Cancer Ther.* **14**, 1848–1857 (2015).

18. Guzman, M.L., Yang, N., Sharma, K.K., Balys, M., Corbett, C.A., Jordan, C.T., Becker, M.W., Steidl, U., Abdel-Wahab, O., Levine, R.L. and Marcucci, G. Selective activity of the histone deacetylase inhibitor AR-42 against leukemia stem cells: a novel potential strategy in acute myelogenous leukemia. *Mol. Cancer Ther.* **13**, 1979–1990 (2014).

19. Kumar, B., Yadav, A., Lang, J. C., Teknos, T. N. and Kumar, P. Suberoylanilide hydroxamic acid (SAHA) reverses chemoresistance in head and neck cancer cells by targeting cancer stem cells via the downregulation of nanog. *Genes Cancer* **6**, 169 (2015).

20. Hii, L.W., Chung, F.F.L., Soo, J.S.S., Tan, B.S., Mai, C.W. and Leong, C.O. Histone deacetylase (HDAC) inhibitors and doxorubicin combinations target both breast cancer stem cells and non-stem breast cancer cells simultaneously. *Breast Cancer Res. Treat.* **179**, 615–629 (2019).

21. Ceccacci, E. & Minucci, S. Inhibition of histone deacetylases in cancer therapy: lessons from leukaemia. *Br. J. Cancer 2016 1146* **114**, 605–611 (2016).

22. Reddy, R. G., Bhat, U. A., Chakravarty, S. and Kumar, A. Advances in histone deacetylase inhibitors in targeting glioblastoma stem cells. *Cancer Chemother. Pharmacol.* **86**, 165–179 (2020).

23. Meidhof, S., Brabletz, S., Lehmann, W., Preca, B.T., Mock, K., Ruh, M., Schüler, J., Berthold, M., Weber, A., Burk, U. and Lübbert, M. ZEB1-associated drug resistance in cancer cells is reversed by the class I HDAC inhibitor mocetinostat. *EMBO Mol. Med.* **7**, 831–847 (2015).

24. Mueller, M.T., Hermann, P.C., Witthauer, J., Rubio–Viqueira, B., Leicht, S.F., Huber, S., Ellwart, J.W., Mustafa, M., Bartenstein, P., D'Haese, J.G. and Schoenberg, M.H. Combined targeted treatment to eliminate tumorigenic cancer stem cells in human pancreatic cancer. *Gastroenterology* **137**, 1102-1113 (2009).

25. Matsubara, S., Ding, Q., Miyazaki, Y., Kuwahata, T., Tsukasa, K. and Takao, S. mTOR plays critical roles in pancreatic cancer stem cells through specific and stemness-related functions. *Sci. Reports* **3**, 1–10 (2013).

26. Walter, K., Tiwary, K., Trajkovic-Arsic, M., Hidalgo-Sastre, A., Dierichs, L., Liffers, S.T., Gu, J., Gout, J., Schulte, L.A., Münch, J. and Seufferlein, T. MEK inhibition targets cancer stem cells and impedes migration of pancreatic cancer cells in vitro and in vivo. *Stem Cells Int.* (2019).

27. Takács, T., Kudlik, G., Kurilla, A., Szeder, B., Buday, L. and Vas, V. The effects of mutant Ras proteins on the cell signalome. *Cancer Metastasis Rev.* **39**, 1051–1065 (2020).

28. Trujillo, J. I. MEK inhibitors: a patent review (2008 – 2010). *Expert Opin. Ther. Pat.* ***21,*** 1045-1069 (2011).

29. Mahapatra, D. K., Asati, V. and Bharti, S. K. MEK inhibitors in oncology: a patent review (2015-Present). *Expert Opin. Ther. Pat.* **27**, 887–906 (2017).

30. Cheng, Y. & Tian, H. Current development status of MEK inhibitors. *Mol. A J. Synth. Chem. Nat. Prod. Chem.* **22**, (2017).

31. Huang, L., Jiang, S. & Shi, Y. Tyrosine kinase inhibitors for solid tumors in the past 20 years (2001–2020). *J. Hematol. Oncol.* **13**, 1–23 (2020).

32. Van Cutsem, E., Hidalgo, M., Canon, J.L., Macarulla, T., Bazin, I., Poddubskaya, E., Manojlovic, N., Radenkovic, D., Verslype, C., Raymond, E. and Cubillo, A. Phase I/II trial of pimasertib plus gemcitabine in patients with metastatic pancreatic cancer. *Int. J. Cancer* **143**, 2053–2064 (2018).

33. Qian, Y., Gong, Y., Fan, Z., Luo, G., Huang, Q., Deng, S., Cheng, H., Jin, K., Ni, Q., Yu, X. and Liu, C. Molecular alterations and targeted therapy in pancreatic ductal adenocarcinoma. *J. Hematol. Oncol.* **13**, 1–20 (2020).

34. Manchado, E., Weissmueller, S., Morris, J.P., Chen, C.C., Wullenkord, R., Lujambio, A., de Stanchina, E., Poirier, J.T., Gainor, J.F., Corcoran, R.B. and Engelman, J.A. A combinatorial strategy for treating KRAS-mutant lung cancer. *Nature* **534**, 647–651 (2016).

35. Weisner, J., Landel, I., Reintjes, C., Uhlenbrock, N., Trajkovic-Arsic, M., Dienstbier, N., Hardick, J., Ladigan, S., Lindemann, M., Smith, S. and Quambusch, L. Preclinical efficacy of covalent-allosteric AKT inhibitor borussertib in combination with trametinib in KRAS-mutant pancreatic and colorectal cancer. *Cancer Res.* **79**, 2367–2378 (2019).

36. Walters, D.M., Lindberg, J.M., Adair, S.J., Newhook, T.E., Cowan, C.R., Stokes, J.B., Borgman, C.A., Stelow, E.B., Lowrey, B.T., Chopivsky, M.E. and Gilmer, T.M. Inhibition of the growth of patient-derived pancreatic cancer xenografts with the MEK inhibitor trametinib is augmented by combined treatment with the epidermal growth factor receptor/HER2 inhibitor lapatinib. *Neoplasia* **15**, 143–155 (2013).

37. Kun, E., Tsang, Y. T. M., Ng, C. W., Gershenson, D. M. and Wong, K. K. MEK inhibitor resistance mechanisms and recent developments in combination trials. *Cancer Treat. Rev.* **92**, (2021).

38. Peng, D.H., Kundu, S.T., Fradette, J.J., Diao, L., Tong, P., Byers, L.A., Wang, J., Canales, J.R., Villalobos, P.A., Mino, B. and Yang, Y. ZEB1 suppression sensitizes KRAS mutant cancers to MEK inhibition by an IL17RD-dependent mechanism. *Sci. Transl. Med.* **11**, (2019).

39. Wang, Z., Hausmann, S., Lyu, R., Li, T.M., Lofgren, S.M., Flores, N.M., Fuentes, M.E.,

Caporicci, M., Yang, Z., Meiners, M.J. and Cheek, M.A. SETD5-coordinated chromatin reprogramming regulates adaptive resistance to targeted pancreatic cancer therapy. *Cancer Cell* **37**, 834-849 (2020).

40. Rovira, M., Scott, S.G., Liss, A.S., Jensen, J., Thayer, S.P. and Leach, S.D. Isolation and characterization of centroacinar/terminal ductal progenitor cells in adult mouse pancreas. *Proc. Natl. Acad. Sci. U. S. A.* **107**, 75–80 (2010).

41. Baker, L., Tiriac, H., Corbo, V. and Young, C. M. *Tuveson Laboratory Murine and Human Organoid Protocols*. (2017).

42. Boj, S.F., Hwang, C.I., Baker, L.A., Chio, I.I.C., Engle, D.D., Corbo, V., Jager, M., Ponz-Sarvise, M., Tiriac, H., Spector, M.S. and Gracanin, A. Organoid models of human and mouse ductal pancreatic cancer. *Cell* **160**, 324–338 (2015).

43. Huch, M., Bonfanti, P., Boj, S.F., Sato, T., Loomans, C.J., Van De Wetering, M., Sojoodi, M., Li, V.S., Schuijers, J., Gracanin, A. and Ringnalda, F. Unlimited in vitro expansion of adult bi-potent pancreas progenitors through the Lgr5/R-spondin axis. *EMBO J.* **32**, 2708–2721 (2013).

4.8. Supplemental information

Table 4.1. Hit compounds from image-based screen for *Msi2* inhibitors

Conclusions

Unfortunately, the most common outcome for pancreatic cancer patients following therapy is not cure but eventual disease progression. The high mortality in this disease is driven by aggressive therapy resistance and metastasis, and can be attributed in part to cancer stem cells, a subpopulation with the tumor bulk enriched for developmental signals and self-renewal[10,11,12,13,14,15]. The studies outlined here have allowed us to develop a comprehensive molecular map of the core dependencies of pancreatic cancer stem cells by integrating their epigenetic, transcriptomic, and functional genomic landscape. This dataset provides a novel resource for understanding therapeutic resistance and for discovering new pancreatic cancer vulnerabilities. This dataset also led us to identify the immune-regulatory nuclear receptor RORγ as a key dependency in pancreatic cancer stem cells. Clinical inhibitors of RORγ have already been developed, suggesting that these agents could be repositioned as pancreatic cancer therapies. To expand preclinical efforts to this end, we tested the clinical RORγ inhibitors JTE-151 and AZD-0284 in mouse and patient-derived models of pancreatic cancer, providing additional evidence that RORγ inhibition can target cancer stem cells *in vivo.*

The comprehensive map of the cancer stem cell state generated above also allowed us to identify and investigate epigenetic regulators of stem cell fate in pancreatic cancer. Using this dataset and a curated screen, we identified SMARCD3 as a stem cell-enriched epigenetic dependency in PDAC. SMARCD3 is a subunit of SWI/SNF, a nucleosome remodeling complex with core functions in development and cancer[27,29,44]. Here, we used a diverse set of genetic models to show that SMARCD3 is uniquely enriched in the stem cell fraction of pancreatic tumors, and a critical functional dependency of established cancer stem cells *in vivo,* providing an important complement to emerging studies showing that the SWI/SNF ATP-ase SMARCA4 supports stem function in glioma[23,24] and in leukemia[26]. Integrating RNA-seq and ChIP-seq via network analysis we found that *Smarcd3* inhibition drove losses in BAF complex binding and

H3K27-acetylation at active enhancers co-bound by FOXA1, controlling the landscape of lipid metabolism in pancreatic cancer cells. Collectively, our results position SMARCD3 as an oncogenic SWI/SNF subunit that could drive important metabolic functions in aggressive cancer cells and serve as a potential target for new therapies.

Furthering our effort to identify clinical inhibitors of cancer stem cell function, we also conducted an image-based screen for inhibitors of the stem cell signal *Msi2*. Using a genetically encoded GFP reporter for *Msi2* expression, we found that small molecules targeting HDAC, PI3K/mTOR, MEK, and CDK could inhibit *Msi2*. Strikingly, the top hit compounds from this screen were enriched for MEK inhibitors, and we found that the clinical MEK inhibitor trametinib could target cancer stem cells *in vivo.* Although MEK inhibitors have not yet yielded clinical success in pancreatic cancer, these studies support a role for MEK signaling in cancer stem cells and suggest that combination MEK inhibitor therapy could be considered for further development in the context of targeting CSCs.

Together, the studies outlined here provide a comprehensive framework for understanding the unique molecular features and susceptibilities of pancreatic cancer stem cells, revealing new clinically-targetable pathways that may be exploited for pancreatic cancer treatment in the future. Combined with a high-throughput screen for *Msi2* inhibitors, this work offers insight into diverse mechanisms that might be utilized to inhibit cancer stem cell function. Furthermore, this work allowed us to unravel the role of Smarcd3, a SWI/SNF subunit, in the epigenetic regulation of pancreatic cancer stem cells. Our work outlines a pro-tumorigenic function for Smarcd3 in established tumors, supporting context-specific functions for SWI/SNF in cancer outside of its role as a tumor suppressor; this work suggests that some accessory subunits like Smarcd3 may in fact be interesting targets for future therapy.